

ABSTRACT

DU, YAO. Molecular Dynamics Simulation in Plasma Etching. (Under the direction of Steven C. Shannon).

In plasma etching for microelectronics fabrication, one of the objectives is to produce high aspect ratio (HAR) via and trench structures. A principal contributor to the HAR feature shape is the manner in which energetic ions interact with sidewalls inside the feature. The scattering angle and energy loss of ions reflecting from sidewalls determines the sidewall slope and can lead to defects such as microtrenching and bowing. Understanding how ions interact with sidewalls can improve our control of the critical dimensions of HAR features. Ions accelerated in the plasma sheath arrive in the feature with energies as large as a few keV and initially strike the sidewalls at glancing-angles. These scattering events extend to the photolithographic mask. Scattering from the mask at glancing angles can produce ions incident into the underlying feature with a broader angular distribution, leading to less desirable feature properties. In this work, results are discussed from Molecular Dynamics (MD) simulations of glancing-angle scattering of argon ions from three materials common to HAR etch: polystyrene (as a photoresist surrogate), amorphous carbon (a hard mask material) and SiO₂ (a common insulating material used in microelectronics devices). Results from the simulations reveal a transition from specular scattering to diffuse scattering as the angle of the incident ion decreases (90 degrees being glancing incidence) and incident energy increases. Scattering from polystyrene is more diffuse compared to amorphous carbon and SiO₂ for identical incident ion conditions.

In the latter half of this work we investigate the formation of fluorocarbon polymer film on the HAR surfaces. During a plasma etching process using fluorocarbon gases such as CF₄ and C₄F₈, the formation of fluorocarbon polymers can occur due to chemical reactions and modifications of the reactive radicals in the plasma with the substrate material being etched, usually on its surface. These polymer films typically consist of a complex mixture of chemical compounds, primarily containing carbon and fluorine with a PTFE-like structure, but may also include other elements from the substrate materials, such as silicon, oxygen, and hydrogen. These polymer films can have both positive and negative effects. On one hand, it can act as a protective layer to protect the underlying material from being etched. On the other hand, the buildup of excessive unwanted polymers can result in process contamination, reduce etch selectivity, slow down the etch rate, and negatively impact the final feature profile. With the help of reactive molecular dynamics simulations, the impact

of different conditions on the formation of the fluorocarbon polymer can be investigated in nanoscale, the atomic structure of the formed polymer films can be well captured, and the accuracy of modeling chemical reactions in plasma-surface interactions can be improved. In this work, we discuss results from reactive MD simulations of fluorocarbon polymer formation on HAR sidewalls in plasma etching processes by depositing CF_x ($x = 1 \sim 3$) radicals onto amorphous SiO_2 and Si substrates. The results show that the film thickness strongly depends on the incident species as fluorine deficient species tend to grow thicker polymers. The film thickness also strongly depends on the substrate materials as polymer on Si crystal can grow much thicker than on amorphous SiO_2 . It was also found that carbon could potentially play a role in forming thick polymer films.

Measuring sticking coefficients for various plasma species on different HAR feature materials in fluorocarbon plasma etching processes is a natural outcome of studying the fluorocarbon polymer formation. Measuring sticking coefficients on varying substrate surface conditions as a function of time can help in understanding the time-dependent behavior of polymer growth on substrate surfaces. On the other hand, measuring sticking coefficients can also benefit other rigorous computational models by delivering more accurate and flexible data which are essential for developing such models. It can be expected that in experimental works, sticking coefficients are generally difficult to measure, and are usually estimated indirectly from other results such as feature profile shape and radicals' density within the plasma. With the help of MD simulations, the sticking coefficients can be measured directly at atomic scale, and the conditions of the incident species and the substrate surfaces can be precisely manipulated so that the effect of each factor can be measured independently. In this work, the sticking coefficients of CF_x ($x = 0 \sim 4$) and SiF_x ($x = 0 \sim 4$) species on substrate materials such as amorphous SiO_2 and Si crystal were measured using reactive MD simulations. The sticking coefficients were measured both on the bare material surfaces and on the material surfaces with growing polymer layers. An analytical model was derived and fitted to the measured data using a two-segment regression scheme, and good match was achieved. The analytical model makes it possible to conveniently incorporate the measured sticking coefficients data into any rigorous models to accurately predict the sticking coefficients for varying surface conditions.

© Copyright 2023 by Yao Du

All Rights Reserved

Molecular Dynamics Simulation in Plasma Etching

by
Yao Du

A dissertation submitted to the Graduate Faculty of
North Carolina State University
in partial fulfillment of the
requirements for the Degree of
Doctor of Philosophy

Nuclear Engineering

Raleigh, North Carolina
2023

APPROVED BY:

Jacob Eapen

Mark Kushner

Yaroslava Yingling

Mohamed Bourham

Steven C. Shannon
Chair of Advisory Committee

BIOGRAPHY

Yao Du was born in 1994 in Shaanxi, China. After obtaining a bachelor's degree from the University of Science and Technology of China in 2016, he came to NC State and started doctoral study in the department of Nuclear Engineering. In 2017, he joined the 4-STAR research group led by Professor Shannon and focused on developing simulations and models for low-temperature plasmas, including molecular dynamics, particle-in-cell and magnetohydrodynamics.

ACKNOWLEDGEMENTS

I would like to express my deep appreciation and gratitude to the following individuals and organizations without whom this research would not have been possible.

Firstly, I would like to express my deepest gratitude to my advisor, Dr. Shannon, for his invaluable guidance, support, and patience throughout the entirety of my research. His commitment to my academic growth and development has been instrumental in shaping the outcome of this work, and his feedback and suggestions have helped me to refine my work and stay on track. Not only is he a fantastic advisor, but he's also an amazing friend. I've lost count of the number of times his passion for both research and social networking has inspired me to keep pushing forward, particularly during the most challenging times when the pandemic has upended everything.

I am also grateful to the members of my thesis committee, Dr. Eapen, Dr. Kushner, Dr. Yingling and Dr. Bourham, for their valuable feedback and insights on this research. I owe much of my success to the valuable guidance and support of my committee members. Dr. Eapen's expertise in Molecular Dynamics simulations was instrumental in my rapid learning and progress in this field. When I encountered confusion, Dr. Kushner's insightful suggestions always steered me in the right direction with his expertise in plasma modeling. Dr. Yingling's input from a Material Science perspective enhanced the solidity of my work. Additionally, Dr. Bourham provided much-needed assistance in being the last committee member for my prelim exam when there was an issue in the procedure only a few weeks before the exam, and he has continuously been a supportive presence throughout both my qualifier and prelim exams.

I am also thankful to the faculty members and staff of the Department of Nuclear Engineering, for their encouragement, support, and feedback during the various stages of this research. Their willingness to share their expertise and resources has been of immense help.

I would like to express my sincere gratitude to all the past and present members of the 4-STAR research group, as well as faculty and students from other plasma groups, for their insights and helpful discussions on all kinds of research projects. When I joined the department in 2016, there was only one plasma group with one or two faculty members. Today, we have over six plasma faculties leading various fascinating plasma research projects. This growth and success could not have been possible without the collaborative efforts of everyone involved. I look forward to witnessing more groundbreaking plasma research

conducted within the department, and perhaps one day, we can establish a large plasma center on-site.

Furthermore, I would like to acknowledge the support and encouragement of my family and friends who have been a constant source of motivation throughout this journey. To my family, I am eternally grateful for your sacrifices, unwavering love, and endless support. Although we have not been able to see each other in person since the summer of 2018, and all the planned trips and gatherings had to be canceled since the spring of 2020, I remain hopeful that the situation will improve this year and that we can soon reunite. To all my friends, who have listened to me ramble on about my research and shared in my successes and failures, I cannot thank you enough. Thank you for all the foods we shared, all the trips we took, all the movies we watched, all the games we played, all the jokes we told, all the difficulties we faced ... Even though we may or may not have the opportunity to create more memories in the future, I am grateful for the good times we have shared and hope that they will remain a cherished memory forever.

I would also like to acknowledge the invaluable contributions of the many open source software developers, online course platforms as well as the course instructors that have provided me with the tools and knowledge necessary for my research. Their work has enabled me to conduct my research more efficiently and effectively, and has contributed to the advancement of science and technology.

Lastly, I would like to thank the funding support from Samsung Electronics, Mechatronics Research and Development Division and the state of North Carolina, which made it possible for me to conduct this research. Their investment in my education and research is deeply appreciated. I also appreciate the computing resources provided by North Carolina State University High Performance Computing Services Core Facility. Most of the Molecular Dynamics simulations were performed on this platform.

Thank you all for your contributions, support, and encouragement. This thesis would not have been possible without your help.

TABLE OF CONTENTS

List of Tables	vii
List of Figures	viii
Chapter 1 Introduction	1
1.1 Low temperature plasmas	1
1.2 Plasma sheath	3
1.3 Plasma etching	6
1.3.1 Photolithography	8
1.4 Passivation layer	10
1.5 Molecular dynamics in plasma etching	12
1.6 Selected research topics	13
1.6.1 Glancing-angle scatterings	13
1.6.2 Fluorocarbon polymer formation	17
1.6.3 Sticking coefficient	20
1.7 Dissertation outline	22
Chapter 2 Methods	23
2.1 Classical Molecular Dynamics	23
2.2 LAMMPS	25
2.2.1 Nose-Hoover thermostat and barostat	26
2.2.2 <i>fix deposit</i> command	27
2.3 Interatomic potentials	29
2.3.1 Tersoff potential	29
2.3.2 TraPPE potential	30
2.3.3 ZBL potential	34
2.3.4 ReaxFF potential	35
Chapter 3 Glancing-angle scatterings	41
3.1 Abstract	41
3.2 Materials preparation	42
3.3 Ions scattering	46
3.4 Validation of the materials properties	49
3.5 Angular distribution of ion scattering	54
3.6 Analytical distribution	61
3.6.1 Second layer of fitting	64
3.7 Near-normal scatterings	70
3.8 Threshold energy	74
Chapter 4 Fluorocarbon polymer formation	78
4.1 Abstract	78

4.2	Prepare ReaxFF parameter set	79
4.3	Validation of combined ReaxFF parameter set	84
4.3.1	Si-C system	84
4.3.2	F-C system	88
4.3.3	Si-F system	93
4.4	Deposition of CF_x radicals on amorphous SiO_2	99
4.4.1	Material preparation and simulation setup	99
4.4.2	A general test case for CF_x radicals deposition	102
4.4.3	Substrate temperature dependency	104
4.4.4	CF_x incident energy and angle dependency	105
4.4.5	Effects of energetic Ar ions	107
4.5	Effects of different incident species	108
4.6	Effects of different substrate materials	113
4.7	Effects of adding carbon atoms	117
4.7.1	Comparison of depositing carbon atoms on different substrate materials	119
4.7.2	Combining incidence of CF_x radicals with carbon atoms	121
4.8	Alternative approach: use PTFE as a surrogate	124
Chapter 5	Sticking coefficient	130
5.1	Abstract	130
5.2	Material preparation and simulation setup	131
5.3	Sticking coefficients measurements	132
5.3.1	On bare surface - static	132
5.3.2	On growing surface - dynamic	140
5.4	Analytical model	149
5.4.1	Model derivation	150
5.4.2	Regression scheme	153
5.4.3	Regression results	154
Chapter 6	Conclusions and Future Work	158
6.1	Conclusions	158
6.2	Future Work	160
6.2.1	Refinement of the ReaxFF parameter set	160
6.2.2	Use available polymer structures as surrogates	160
6.2.3	Expand the dataset to include other molecules and materials	161
6.2.4	Larger scale parametric studies on more powerful HPC	161
6.2.5	More investigations in modeling carbon systems using ReaxFF	161
References	162
APPENDICES	171
Appendix A	ReaxFF parameter files	172
Appendix B	LAMMPS input files and Python scripts	185

LIST OF TABLES

Table 2.1	Coefficients for the TraPPE force field for an atactic polystyrene system	33
Table 3.1	Optimized values of (σ, k, θ_0) presented in a look-up table form	64
Table 3.2	Bivariate linear fitting parameters for all three materials	66
Table 4.1	Comparison of the general parameters of all the ReaxFF parameter sets referenced in this work	83
Table 4.2	Comparison of coordination numbers for Si atoms in the manufactured Si-F random system, using both ReaxFF parameter sets	95
Table 4.3	Comparison of the peak locations of the bond length and the bond angle distributions presented in Fig. 4.12 for the three ReaxFF parameter sets, and the corresponding experimental data are also included	97
Table 4.4	Comparison of number of attached C atoms for different deposition cases, normalized with respect to the substrate surface area.	115
Table 4.5	Comparison of number and percentage of C hybridization on SiO_2 and Si substrates.	121
Table 4.6	Comparison of number and percentage of C hybridization on Si substrate for different incident energies.	121
Table 5.1	The experimentally measured bond length (Chemist 2023) and the characteristic cutoff values used for different bond types	135
Table 5.2	Number of attached molecules on the substrate materials surface with a total incidence of 2000 molecules	136
Table 5.3	The experimentally measured bond energies (Chemist 2023) for different bond types related to this work	137
Table 5.4	Number of Si atoms and O atoms left in the system at the end of the simulation for different incident cases	149
Table 5.5	Fitting parameters obtained from the two-segment regression for CF_x species incident on Si crystal	155
Table 5.6	Fitting parameters obtained from the two-segment regression for CF_x species incident on amorphous SiO_2	155

LIST OF FIGURES

Figure 1.1	A typical setup of a capacitively coupled plasma (CCP) chamber	3
Figure 1.2	A simple illustration of plasma sheath formation: (a) Prior to sheath formation, quasi-neutrality is valid everywhere, and bulk plasma extends to the walls (electrodes) and has an uniform potential of 0 with respect to the walls; (b) After sheath formed and positively charged, a potential difference is generated across the sheath, and quasi-neutrality is only valid within the bulk plasma. Figures taken from Chapter 1 of Lieberman and Lichtenberg (2005)	5
Figure 1.3	Plasma etch (anisotropic) vs. wet etch (isotropic). Diagrams reproduced from Chapter 1 of [Végh (2007)]	6
Figure 1.4	Diagrams representing four basic plasma etching processes: (a) sputtering; (b) chemical etching; (c) ion energy-driven etching; (d) ion-enhanced inhibitor etching. Diagrams reproduced from Chapter 15 of [Lieberman and Lichtenberg (2005); Flamm and Manos (1989)]	7
Figure 1.5	Diagrams representing key steps in photolithography: (a) substrate coated with photoresist (PR); (b) photomask aligned and PR partially exposed to ultraviolet (UV) light; (c) degradation occurred within the exposed PR and PR selectively removed by a special solution called "developer"; (d) pattern transferred to PR after development and target material ready to be etched by plasma	9
Figure 1.6	Illustration of Bosch method: (a) sidewalls and bottom of HAR trench passivated with C_4F_8 ; (b) etching with SF_6 gas; (c) SEM image of HAR trenches; (d) zoom-in view which shows nanoscallops on sidewall. Figures reproduced from Wu et al. (2010) and permission granted by Journal of Applied Physics.	11
Figure 1.7	Cross section view of a typical HAR feature with a multi-layer structure.	16
Figure 1.8	Formation of fluorocarbon polymer film on Si crystal with CF radicals deposition (red=Si, yellow=C, pink=F): (a) initial Si crystal; (b) after 1000 CF radicals incidence; (c) after 1000 CF radicals incidence	19
Figure 1.9	Measuring the sticking coefficients on bare substrate surface (red=Si, blue=O, yellow=C, pink=F): (a) 5 CF_3 radicals incident on Si crystal surface; (b) 5 SiF_4 molecules incident on amorphous SiO_2 surface	21
Figure 2.1	Diagrams showing how bonded potential usually represented in a Molecular Dynamics simulation. Images were taken from (Kouza 2013)	31
Figure 2.2	Monomer of polystyrene shown in a) Typical model with both C and H atoms, b) United atom model	34
Figure 2.3	Summary of different energy terms in ReaxFF total energy equation in Eq. 2.9. (Figure taken from Senftle et al. (2016) and permission gained from Creative Commons Attribution 4.0 International License.)	38

Figure 2.4	Bond order calculation (uncorrected) of a C-C bond as a function of interatomic distance. (Figure taken from Van Duin et al. (2001) and permission gained from American Chemical Society Publications.) .	39
Figure 3.1	Equilibrated state of amorphous SiO ₂ at 300 K, the final size of the simulation box is (35.18 Å) ³ , corresponding to a density of 2.288 g/cm ³ .	43
Figure 3.2	Examples of C atoms deposited on a Si substrate a) initial Si substrate, b) 1000 C deposited and c) 2000 deposited. The computational domain is 23 × 23 × 120 Å ³	45
Figure 3.3	Monomer of PS shown in a) Typical model with both C and H atoms, b) United atom model	46
Figure 3.4	Structure of PS with 10 chains each containing 40 monomers. (a) Initial structure, unwrapped at the periodic boundaries (b) Equilibrated state at 300 K. The chains are colored separately.	47
Figure 3.5	Schematic showing the ion scattering geometry.	47
Figure 3.6	Front view of the simulation cells prior to ions scattering: (left) SiO ₂ with width 35.18 Å, (middle) AC with width 23 Å and (right) PS with width 40.27 Å.	48
Figure 3.7	Radial distribution function $g(r)$ for SiO ₂ glass (this work, simulation results from [Munetoh et al. (2007)] and experimental data from [Johnson et al. (1983)]).	50
Figure 3.8	Radial distribution function $g(r)$ for AC (this work, simulation results from [Bhattarai and Drabold (2017)] and experimental data from [O'Malley et al. (1998)]).	51
Figure 3.9	Structural and thermodynamic studies of PS: (a) Density and length (of simulation box) as a function of temperature; (b) Diffusion constant as a function of temperature reciprocal in semi-log plot; (c) Radial distribution function $g(r)$ (this work and simulation results from [(Srivastava 2010)]).	53
Figure 3.10	Specific volume as a function of temperature for PS, where the intersecting point of linear fittings gives glass transition temperature T_g	54
Figure 3.11	Invariant RDFs for SiO ₂ , AC and PS (top to bottom) in cell size tests.	55
Figure 3.12	Comparison of $f_{E_{\text{in}}, \theta_{\text{in}}}(E_{\text{out}}, \theta_{\text{out}})$ for different materials, incident energies and incident angles (x axis → θ_{out} , y axis → E_{out} , color scale → magnitude), presented in matrix form: (Upper matrix) Constant incident energy $E_{\text{in}} = 316$ eV at $\theta_{\text{in}} = 75^\circ, 79^\circ, 85^\circ, 89^\circ$ (left to right) for SiO ₂ , AC and PS (top to bottom) (Lower matrix) Constant incident angle $\theta_{\text{in}} = 79^\circ$ at $E_{\text{in}} = 20, 79, 316, 1257$ eV (left to right) for SiO ₂ , AC and PS (top to bottom).	56

Figure 3.13	Fractional retained energy vs. E_{in} for SiO ₂ , AC and PS (top to bottom). The data presented are quantiles of E_{out} normalized by E_{in} : solid line is median (50% quantile) and shaded area (colored correspondingly) is from 25% quantile to 75% quantile.	59
Figure 3.14	Rate of reflection (color scale, also numbered in each bin) as a function of E_{in} (x axis) and θ_{in} (y axis) for SiO ₂ , AC and PS (top to bottom).	60
Figure 3.15	Illustration of the three characteristic parameters in the analytical form	62
Figure 3.16	Comparison between (left) collected distribution and (right) fitted distribution, the fitted distribution was normalized so that the two distributions have the same volume	63
Figure 3.17	Bivariate linear fitting for shape parameters ($\sigma, \theta_0, \ln k$) for SiO ₂ (blue circle → original, orange triangle → predicted)	65
Figure 3.18	Scattering distributions for SiO ₂ : (left) original distribution, (middle) analytical distribution with look-up table values and (right) analytical distribution with bivariate linear fitting predicted values	67
Figure 3.19	Scattering distributions for AC: (left) original distribution, (middle) analytical distribution with look-up table values and (right) analytical distribution with bivariate linear fitting predicted values	68
Figure 3.20	Scattering distributions for PS: (left) original distribution, (middle) analytical distribution with look-up table values and (right) analytical distribution with bivariate linear fitting predicted values	69
Figure 3.21	Comparison of collected and predicted scattering distributions for AC at $\theta_{\text{in}} = 0^\circ$ and $E_{\text{in}} = 20$ or 316 eV	71
Figure 3.22	Decouple the full distribution for SiO ₂ at $\theta_{\text{in}} = 70^\circ$ and $E_{\text{in}} = 630$ eV, using a cutoff energy $E_{\text{cut}} = 0.1 E_{\text{in}}$	73
Figure 3.23	Decouple the full distribution for SiO ₂ at $\theta_{\text{in}} = 55^\circ$ and $E_{\text{in}} = 158$ eV, using a threshold energy $E_{\text{thre}} = 35$ eV	75
Figure 3.24	Number of scattered ions with energies above the threshold energy (35 eV) for SiO ₂ , AC, and PS. Total number of incident ions is 2000, table row names are θ_{in} in degree and column names are E_{in} in eV.	76
Figure 4.1	ReaxFF development tree, where parameter sets on the same development branch can be directly combined. (Figure taken from Senftle et al. (2016) and permission gained from Creative Commons Attribution 4.0 International License.)	80
Figure 4.2	Molecular structure of 3C-SiC crystal (red=Si, blue=C) in a 8.752 Å long (2 times lattice constant) cubic simulation box	85
Figure 4.3	Comparison of partial RDFs for 3C-SiC crystal, using ReaxFF parameters from (a) Ref.2, (b) the combined parameter set	86
Figure 4.4	Comparison of results from bond analysis for 3C-SiC crystal, using ReaxFF parameters from both Ref.2 and the combined parameter set	87

Figure 4.5	Molecular structure of fluorographene sheet (red=C, blue=F) (a) in a $81.1158 (x) \times 82.1773 (y) \times 100.032 (z)$ Å ³ horizontally periodical simulation box; (b) zoom-in front view.	89
Figure 4.6	Comparison of partial RDFs for fluorographene, using ReaxFF parameters from (a) Ref.3, (b) the combined parameter set	90
Figure 4.7	Molecular structure of CF ₄ molecules, with 10 molecules in a periodical simulation box (red=C, blue=F): (a) initial setup with 20 Å in cubic box length; (b) after 0.5 ns box shrank to 10.34 Å in cubic box length.	91
Figure 4.8	Partial RDF for CF ₄ , using ReaxFF parameters from the combined parameter set	92
Figure 4.9	Molecular structure of the manufactured Si-F random system, using ReaxFF parameters from (a) Ref.7, (b) the combined parameter set	94
Figure 4.10	Comparison of partial RDFs for the manufactured Si-F random system, using ReaxFF parameters from (a) Ref.7, (b) the combined parameter set	95
Figure 4.11	Molecular structure of thermally equilibrated SiF ₄ molecules at 120 K, with 10 molecules in a periodical simulation box (red=Si, blue=F), using parameter set respectively from: (a) Ref.4; (b) Ref.7; (c) the combined system.	96
Figure 4.12	Comparison of results from bond analyses for SiF ₄ molecules, using ReaxFF parameter sets from both Ref.4, Ref.7 and the combined system	98
Figure 4.13	Preparation and validation of amorphous SiO ₂ : (a) amorphous SiO ₂ equilibrated at 300 K using ReaxFF potential; (b) correspondingly partial RDFs.	100
Figure 4.14	Diagram presenting the computational setup of the amorphous SiO ₂ deposition simulations.	101
Figure 4.15	Deposition of CF _x radicals onto amorphous SiO ₂ substrate (red=Si, blue=O, yellow=C, pink=F), presented here are snapshots at timestep of: (a) 0; (b) 2E5; (c) 4E5.	103
Figure 4.16	Number of attached C and F atoms on SiO ₂ substrate as a function of timestep.	103
Figure 4.17	Comparison of number of attached atoms as a function of timestep for different substrate temperature, presented here are for: (a) C atoms; (b) F atoms.	104
Figure 4.18	Comparison of number of attached atoms as a function of timestep for different CF _x incident energies, presented here are for: (a) C atoms; (b) F atoms.	105
Figure 4.19	Deposition of 25 eV CF _x radicals onto amorphous SiO ₂ substrate (red=Si, blue=O, yellow=C, pink=F), presented here are snapshots at timestep of: (a) 0; (b) 1E6; (c) 2E6; (d) 3E6; (e) 4E6	106

Figure 4.20 Comparison of number of attached atoms as a function of timestep for different CF_x incident energies where the incident angle was randomly sampled, presented here are for: (a) C atoms; (b) F atoms.	107
Figure 4.21 Comparison of number of attached atoms as a function of timestep for different Ar ions incident energies where the incident angles were 75° with respect to surface normal, presented here are for: (a) C atoms; (b) F atoms.	109
Figure 4.22 Comparison of number of attached C atoms as a function of timestep for different CF incident energies as well as different Ar ions incident energies, presented here are separated by CF incident energy of: (a) 1 and 5 eV; (b) 10 eV.	110
Figure 4.23 Comparison of number of attached atoms as a function of timestep for different incident energies of C_2F_4 and Ar, presented here are for: (a) C atoms; (b) F atoms.	111
Figure 4.24 Number of attached C and F atoms as a function of timestep for C_4F_4 species incident on amorphous SiO_2 substrate.	112
Figure 4.25 Molecular structures of: (a) C_4F_8 (gray=C, green=F; obtained from PubChem online database); (b) C_4F_4 (yellow=C, pink=F; generated from this work).	113
Figure 4.26 Deposition of 1 eV CF radicals onto Si crystal substrate (red=Si, yellow=C, pink=F), presented here are snapshots at timestep of: (a) 0; (b) 2.5E5; (c) 5E5; (d) 7.5E5; (e) 1E6.	114
Figure 4.27 Number of attached C and F atoms as a function of timestep for CF species incident on Si crystal substrate.	115
Figure 4.28 Deposition of 5 eV C_4F_4 radicals onto Si crystal substrate (red=Si, yellow=C, pink=F), presented here are snapshots at timestep of: (a) 0; (b) 4E5; (c) 8E5; (d) 1.2E6; (e) 1.6E6.	116
Figure 4.29 Number of attached C and F atoms as a function of timestep for C_4F_4 species incident on Si crystal substrate.	117
Figure 4.30 Deposition of 1 eV C atoms onto amorphous SiO_2 substrate (red=Si, blue=O, yellow=C), presented here are snapshots at timestep of: (a) 0; (b) 3E5; (c) 6E5; (d) 9E5; (e) 1.2E6.	118
Figure 4.31 Deposition of 1 eV C atoms onto substrate materials of (red=Si, blue=O, yellow=C): (a) amorphous SiO_2 ; (b) Si crystal.	119
Figure 4.32 Histograms of the z position (with respect to substrate bottom plane where $z = 0$) of C atoms on substrates: (a) amorphous SiO_2 ; (b) Si crystal.	120
Figure 4.33 Deposition of combining CF_x and C flux onto amorphous SiO_2 substrate (red=Si, blue=O, yellow=C, pink=F), presented here are snapshots at the same timestep of 1E6 for different $N_{\text{C}}/N_{\text{CF}_x}$ ratios of: (a) 0.1; (b) 0.4; (c) 0.6; (d) 0.8; (e) 1.0.	122

Figure 4.34 Comparison of number of attached atoms as a function of timestep for different N_C/N_{CF_x} ratios, presented here are for: (a) C atoms; (b) F atoms.....	123
Figure 4.35 Preparation of PTFE using ReaxFF: (a) single polymer chain of PTFE; (b) 10 polymer chains of PTFE, where each chain has 40 monomers, are randomly oriented and placed into a simulation box with periodical boundaries in all three directions, and the initial density was 0.05 g/cm ³ ; (c) thermal equilibrated at 300 K and final density reached 2.2 g/cm ³ (d) same results as in (c) but chains are colored separately and unwrapped at periodical boundaries.....	125
Figure 4.36 Partial RDF for PTFE, categorized by different types of atom pairs: (a) short-range part; (b) zoomed in to emphasize the long-range part. . .	127
Figure 4.37 Stack PTFE (yellow=C, pink=F) on top of SiO ₂ (red=Si, blue=O): (a) initial structure; (b) PTFE swollen vertically after 2.5 ps; (c) after 5 ps	128
Figure 5.1 Measure sticking coefficient on bare surface (red=Si, blue=O, yellow=C, pink=F): (a) CF ₃ radicals incident on Si crystal; (b) SiF _x molecules incident on amorphous SiO ₂	133
Figure 5.2 Incident CF ₃ radicals attached to Si crystal with molecules dissociation (red=Si, yellow=C, pink=F)	134
Figure 5.3 Top layer zoom in view of (red=Si, blue=O): (a) Si crystal; (b) amorphous SiO ₂	137
Figure 5.4 Plots of the data in Table 5.2, categorized by incident species as: (a) CF _x ; (b) SiF _x	138
Figure 5.5 Trajectory plots showing that an attached C atom left the SiO ₂ substrate surface in the form of CO (red=Si, blue=O, yellow=C), presented here are snapshots at timesteps of: (a) 5000; (b) 5700; (c) 6800.	139
Figure 5.6 CF _x molecules dissociated on Si crystal (red=Si, yellow=C, pink=F), presented here are: (a) CF ₂ ; (b) CF ₃ ; (c) CF ₄	140
Figure 5.7 SiF _x molecules retained molecular structure on Si crystal (red=Si, pink=F), presented here are: (a) SiF ₂ ; (b) SiF ₃ ; (c) SiF ₄	141
Figure 5.8 Measure sticking coefficient on growing surface (CF radicals incident on Si crystal; red=Si, yellow=C, pink=F): (a) after 0 molecules incidence; (b) after 1000 radicals incidence; (c) after 3000 radicals incidence.	143
Figure 5.9 Number of attached C and F atoms as a function of timestep, for substrate material of Si crystal and incident species of: (a) CF; (b) CF ₂ ; (c) CF ₃ ; (d) CF ₄	145
Figure 5.10 Number of attached C and F atoms as a function of timestep, for substrate material of amorphous SiO ₂ and incident species of: (a) CF; (b) CF ₂ ; (c) CF ₃ ; (d) CF ₄	146

Figure 5.11	Zoom-in view of the top layer of CF radicals deposited on substrate materials (red=Si, blue=O, yellow=C, pink=F): (a) Si crystal; (b) amorphous SiO ₂	148
Figure 5.12	Zoom-in view of the top layer of CF ₄ molecules incident on amorphous SiO ₂ (red=Si, blue=O, yellow=C, pink=F).	150
Figure 5.13	Diagram showing that there are two characteristic regions where the polymer growth behaves differently.	151
Figure 5.14	Number of attached C atoms as a function of number of inserted molecules, with fitting lines overlaid. Presented here are curves for simulation cases as: (a) CF on Si; (b) CF ₂ on Si; (c) CF ₃ on Si; (d) CF ₄ on Si; (e) CF on SiO ₂ ; (f) CF ₂ on SiO ₂ ; (g) CF ₃ on SiO ₂	157

CHAPTER

1

INTRODUCTION

1.1 Low temperature plasmas

Plasmas are ionized gases and are categorized as the fourth state of matter. From solid state to liquid state and further to gas state, the temperature of the matter is generally increased. When the temperature is further increased from gas state, the molecules decompose into atoms and further decompose into charged particles such as ions and electrons, and the matter enters plasma state. In plasma state, ions, electrons, neutral gas particles, and radicals coexist, therefore in addition to the thermodynamic interactions, the system now is also governed by electromagnetic forces. Other mechanisms such as excitation and deexcitation of atoms, recombination of ions and electrons as well as the photon-particle interaction should also be considered, which makes plasma very complex and significantly different than gas state.

Based on the power being delivered to the plasma and some other conditions such as the gas pressure, the RF frequency and the gas species being fed, plasma can be generated as low temperature plasma or high temperature plasma. Low temperature plasmas are

often weakly ionized, meaning the fractional ionization of plasma

$$x_{iz} = \frac{n_i}{n_g + n_i} \quad (1.1)$$

is much less than unity, where n_i is the ion density and n_g is the neutral gas density. For weakly ionized plasmas, the interactions between charged particles and neutral gas molecules are important, the plasmas are sustained in a steady state through balancing ionization of neutral particles and recombination of ions and electrons, and the electrons are not in thermal equilibrium with the ions and are usually with much higher temperature.

When low temperature plasmas are used for semiconductor etching, they are generally produced using plasma sources such as capacitively coupled plasma (CCP) or inductively coupled plasma (ICP). Capacitively coupled plasma system, as the name suggests, delivers energy to plasma using two RF-driven electrodes, working like a giant capacitor. A typical setup of a capacitively coupled plasma chamber is presented in Fig. 1.1, where a gas is fed into the plasma chamber through inlet, RF power is applied on the electrodes, and plasmas are generated between the electrodes. There are two different regions for the generated plasmas, bulk plasma and plasma sheath, which are important for plasma etching and will be discussed later within this chapter. Substrates are generally put on top of the bottom electrode and will be etched by the directional ion beams accelerated in the plasma sheath. Pumps are located in the gas outlet, which are used to purge the air as well as some volatile etch products and keep the chamber pressure at a fairly low level (mTorr to μ Torr).

For inductively coupled plasma system, an induction coil is implemented outside the cylindrical chamber and RF current is applied on the coil so that the RF power is delivered to the plasma in a inductor way.

For both capacitively and inductively coupled plasma systems, in a typical plasma discharge, an oscillating external electromagnetic (EM) field will first be generated within the plasma chamber. Since there are always some free electrons (only a very small amount) even the substance is in gas state, those free electrons will be preferentially accelerated by the EM field and thus lead to an increase in the electron temperature. Those heated-up electrons will then collide with the neutral gas atoms/molecules and produce ions, radicals and more free electrons. The generated ions and electrons will also be preferentially accelerated by the EM field, inducing even more collisions and more ionizations. This whole process is called electron avalanche and is the key mechanism of producing plasma.

This process cannot go indefinitely. In reality, generating plasma is a competition process among different physical mechanisms such as ionization, recombination, excitation and de-

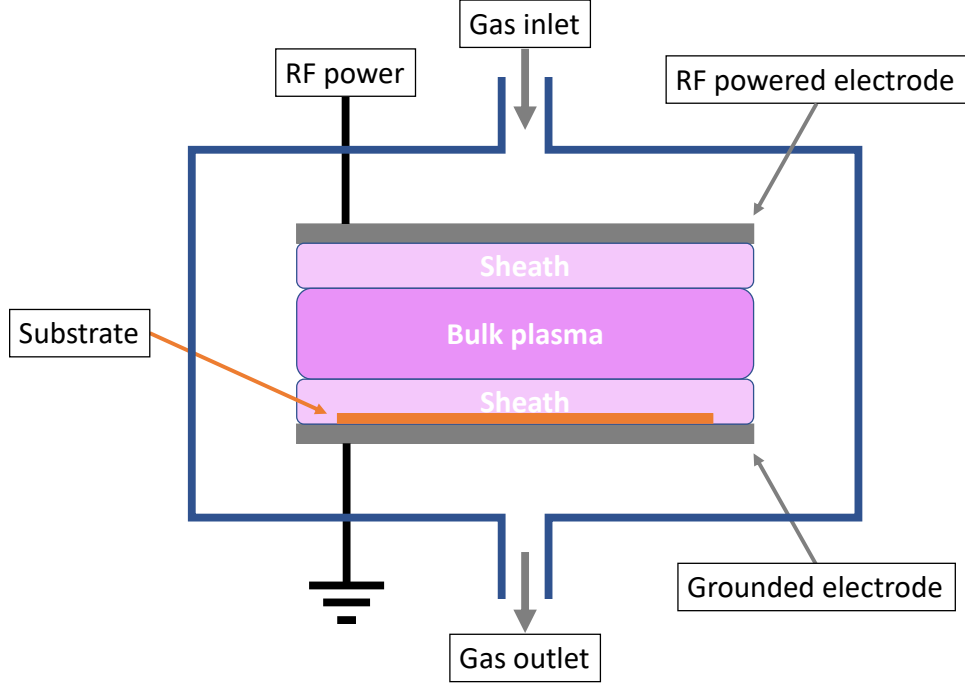


Figure 1.1: A typical setup of a capacitively coupled plasma (CCP) chamber

excitation. For example, when the fractional ionization of plasma x_{iz} increases, it also means the rate of recombination will increase since there will be more free ions and electrons which can be paired. The plasma will reach a steady state when the gain terms (ionization, ...) equal to the loss terms (recombination, ...). And the balance point in plasma conditions will be determined by the experimental conditions such as RF power and frequency, gas type, pressure, pump speed and gas feed speed, etc.

1.2 Plasma sheath

Plasma sheath is defined as the thin layer region which is located between the bulk plasma and the wall surfaces (both electrodes in Fig. 1.1). In plasma sheath, unlike in bulk plasma, the quasi-neutrality ($n_i \approx n_e$) cannot be maintained and generally it is positively charged, which is essentially due to the massive difference in mobility of positively charged ions and electrons. Since the electron mass m is much less than the ion mass M ($m \ll M$) and the temperature of electrons is generally higher than the temperature of ions ($T_e \geq T_i$) in

plasma, the thermal velocities of electrons and ions

$$v_e = \sqrt{\frac{e T_e}{m}} \quad (1.2a)$$

$$v_i = \sqrt{\frac{e T_i}{M}} \quad (1.2b)$$

will have $v_e \gg v_i$ (at least 100 times greater). In Fig. 1.2(a), consider a plasma with quasi-neutrality ($n_i \approx n_e$) is confined between two absorbing walls (grounded electrodes), thus the electrical potential Φ should be uniformly equal to the wall potential, as shown in the bottom figure of Fig. 1.2(a). Due to $v_e \gg v_i$ and the electrical field $\vec{E} = 0$, the electrons are not confined and therefore will have a much higher chance than ions to hit the wall and get absorbed. Thus, a positively charged ($n_i > n_e$) thin layer region is formed, known as plasma sheath, which is presented in Fig. 1.2(b). This is also a competition process. When sheath is formed, the difference between n_i and n_e gets bigger when closer to the walls, therefore the electrical field \vec{E} points outwards towards the walls and the bulk plasma has a positive electrical potential (known as plasma potential V_p) with respect to the walls, as shown in the bottom figure of Fig. 1.2(b). Thus, more electrons getting absorbed by the walls will make the sheath thicker and more positively charged, while thicker sheath or higher plasma potential V_p will make the electrons more difficult to reach the walls.

In reality, since RF power is being applied on the plasma chamber, the sheath conditions are not constant but rather some time-dependent periodic values, with frequencies equal to the RF frequency. The magnitude of those sinusoidal values however should be at steady state for a stable plasma.

Due to the potential gradient formed across the sheath, as shown in the bottom figure of Fig. 1.2(b), positively charged ions will experience force $q\vec{E}$ along the same direction as \vec{E} and be accelerated towards the walls/electrodes. Since the pressure in the plasma chamber is sufficiently low and the ion density n_i is even lower in the sheath, those ions are less likely to collide with each other and with the background gas molecules. Therefore the ions will form an ion beam which is both energetic and directional (perpendicular to the material surface). If a substrate is placed on top of the electrode, as shown in Fig. 1.1, the directional ion beam will strike the substrate surface at normal angle and etch the material in a desired way. This step plays the key role for plasma etching in semiconductor manufacture, and will be discussed in next section.

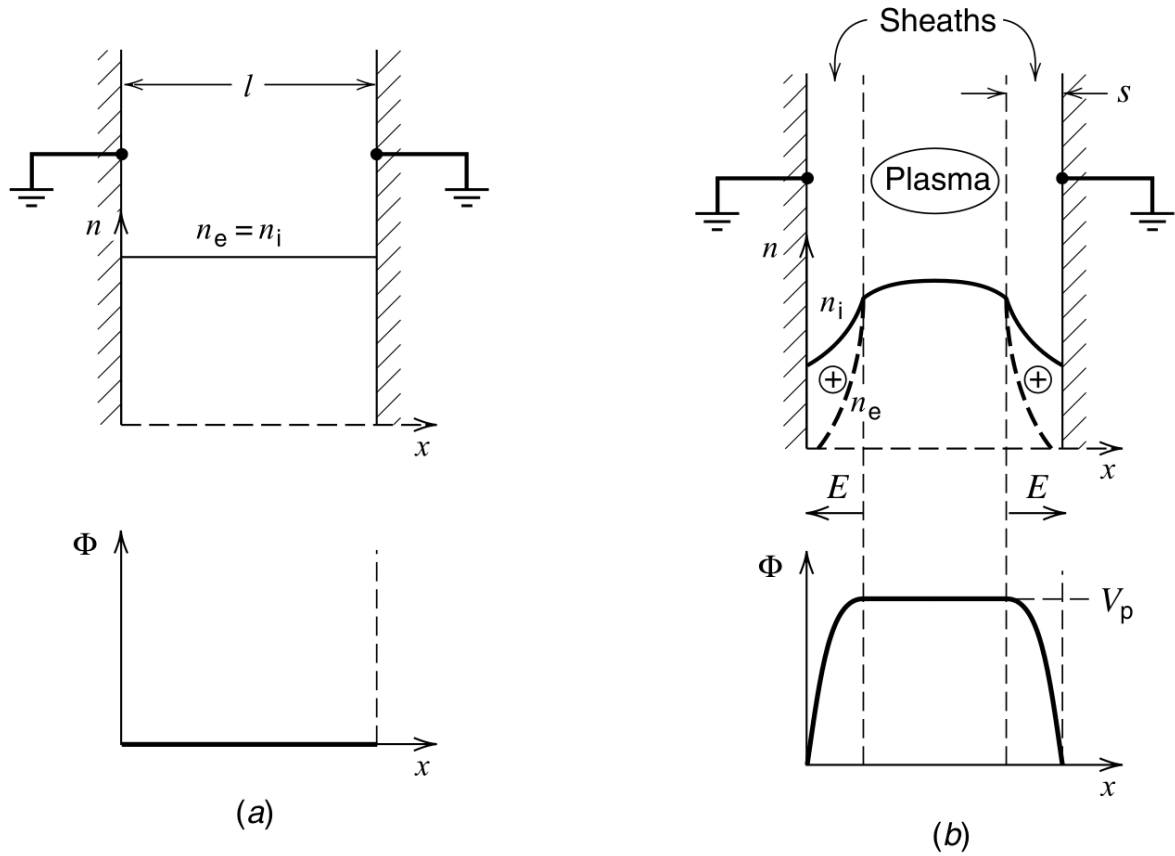


Figure 1.2: A simple illustration of plasma sheath formation: (a) Prior to sheath formation, quasi-neutrality is valid everywhere, and bulk plasma extends to the walls (electrodes) and has an uniform potential of 0 with respect to the walls; (b) After sheath formed and positively charged, a potential difference is generated across the sheath, and quasi-neutrality is only valid within the bulk plasma. Figures taken from Chapter 1 of Lieberman and Lichtenberg (2005)

1.3 Plasma etching

Plasma etching is a process used to remove material from surfaces. Plasma etching involves both physical and chemical reactions, and involves a mixture of particles such as neutral molecules or atoms, ions, electrons, radicals and photons. Plasma etching is popular in semiconductor manufacturing especially for its chemical selectivity and anisotropy, meaning that plasma etching can be designed to preferentially remove some types of material as well as preferentially remove the material at the bottom of a high aspect ratio (HAR) trench. In contrast, wet etching uses liquid-phase etchants and the target material is immersed in a bath of the etchants during etching (that is why plasma etching is also called dry etching). However, one major drawback of wet etching is that it is isotropic. See Fig. 1.3 for a comparison of plasma etching and wet etching. Anisotropy is one of the most important requirements for fabricating high quality integrated circuits (IC) and therefore plasma etching is preferred for modern semiconductor manufacturing.

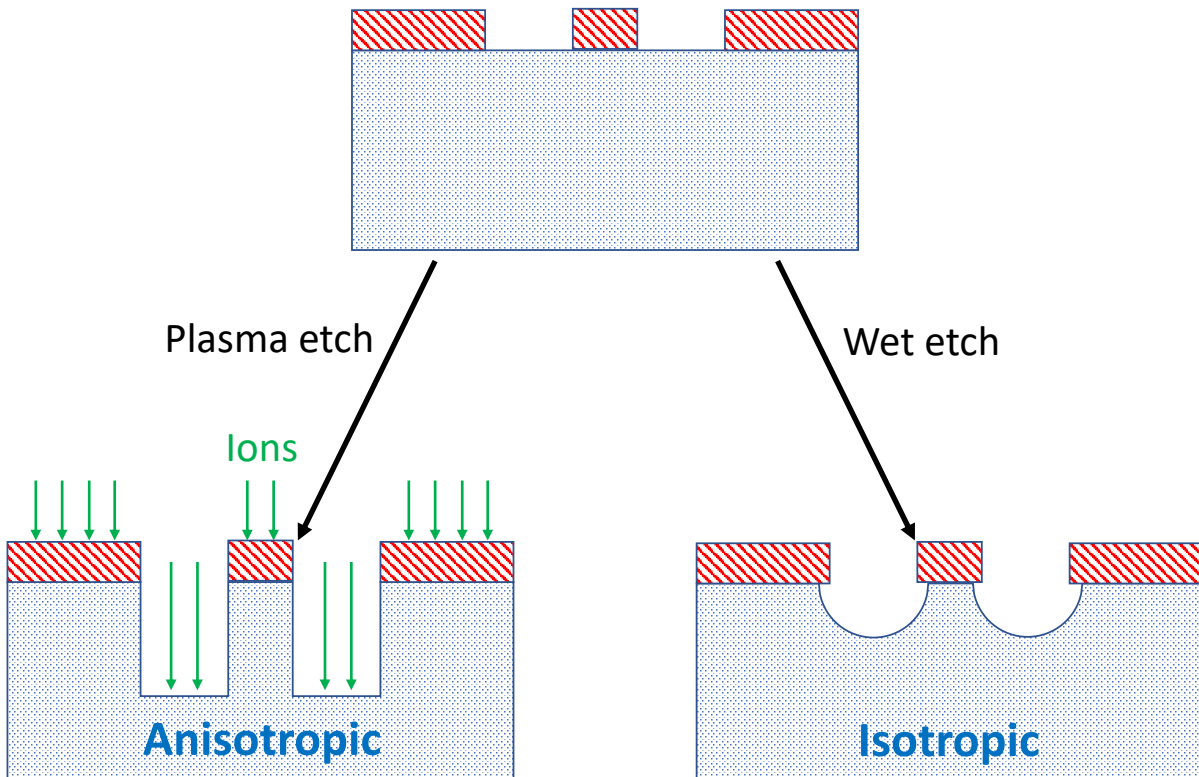


Figure 1.3: Plasma etch (anisotropic) vs. wet etch (isotropic). Diagrams reproduced from Chapter 1 of [Végh (2007)]

There are four basic plasma etching processes in which plasma can interact with the surface of the target material and are illustrated in Fig. 1.4 as: (a) sputtering; (b) chemical etching; (c) ion energy-driven etching; (d) ion-enhanced inhibitor etching.

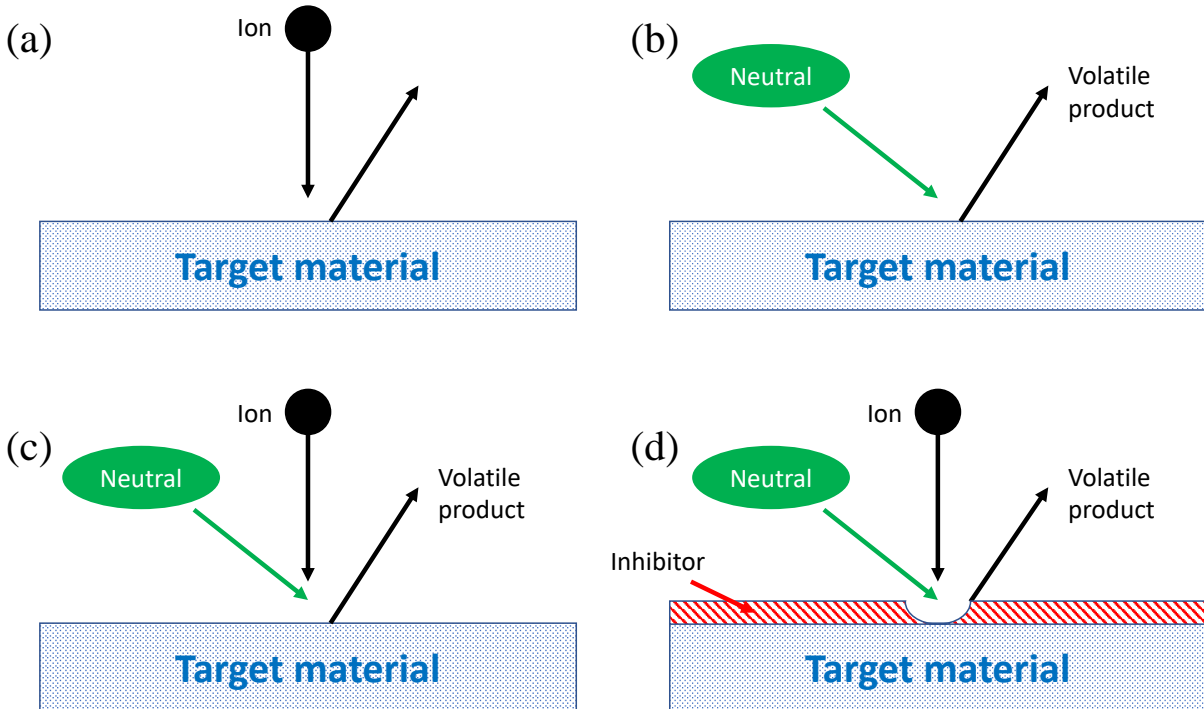


Figure 1.4: Diagrams representing four basic plasma etching processes: (a) sputtering; (b) chemical etching; (c) ion energy-driven etching; (d) ion-enhanced inhibitor etching. Diagrams reproduced from Chapter 15 of [Lieberman and Lichtenberg (2005); Flamm and Manos (1989)]

Sputtering, illustrated in Fig. 1.4(a), is defined as the energetic ions accelerated across the plasma sheath bombard the target material and remove some atoms. Sputtering is highly anisotropic and strongly depends on the incident angle. For example, sputtering yield usually increases when increasing incident angle from 0° (normal incidence) and starts to decrease after some critical angle θ_{\max} , and eventually decreases to zero at 90° (grazing incidence). (Here sputtering yield is defined as the average number of atoms knocked off from the target material per incident ion.) Sputtering yield is generally low and therefore it is necessary to combine sputtering with some chemical reactions in order to increase the etch rate.

Chemical etching, illustrated in Fig. 1.4(b), is defined as the plasma generated reactive

molecules or radicals interact with the target material through chemical reactions and form volatile gas-phase products. Those etchants are usually electrically neutral and are not accelerated when crossing the plasma sheath. Therefore the angular distribution is relatively uniform and the kinetic energy is quite low (near thermal equilibrium with 300K background gas), which makes the etching highly isotropic, similar to wet etching. However, the etch rate of chemical etching can be much higher than sputtering.

Ion energy-driven etching, illustrated in Fig. 1.4(c), combines the effects of sputtering and chemical etching. Both reactive molecules/radicals and directional energetic ions are supplied by the plasma to the target material, and the etch rate can be much higher than either of the etching processes and was experimentally demonstrated in [Coburn and Winters (1979)]. A simple explanation of the increase in etch rate is that the reactive species will first come to the target material, chemically react with the material and reproduce some new but weaker bonds, and form some cluster of atoms which are weakly attached to the material surface. The energetic non-reactive ions (such as Ar^+ with $E_{\text{Ar}} \approx 10^{3\sim 4}$ eV) will now bombard the target material and remove clusters of atoms at a much higher etch rate ($\approx 10^{1\sim 2}$ per incidence). However, the detailed mechanism for this is not well understood, and hopefully can be better explained throughout this work.

Ion-enhanced inhibitor etching, illustrated in Fig. 1.4(d), is similar to ion energy-driven etching but also includes the mechanism of depositing inhibitor species on the target material surface to form some kind of protective layers. This protective layer is also called passivation layer and usually has a polymer like structure. The inhibitor species used in production are usually some CF_x ($x = 1 \sim 3$) and CCl_x ($x = 2 \sim 3$) radicals and therefore the formed passivation layers are usually some fluoro/chloro-carbon polymer films. For example, when CF_x ($x = 1 \sim 3$) radicals are used, the formed polymer film has a molecular structure similar to polytetrafluoroethylene (PTFE). Passivation layer is generally used for optimizing the anisotropy of the etching, and will be discussed in details in next section.

In summary, four basic plasma etching processes have been briefly introduced here and in reality, they are always combined with each other by the process engineers to design a combined plasma etching process which can optimize the HAR profile.

1.3.1 Photolithography

Plasma etching does not naturally form patterns on the target material surface. In fact, if the target material is uniform along horizontal directions, plasma etching generally has the same etch rate across the whole surface. In order to selectively etch the material following

some designed patterns, a patterned mask material need to placed on top of the target material first, see Fig. 1.3 for an example and the mask layer (red colored) has a predefined pattern. The general process to transfer a pattern to a substrate material is called lithography. In particular, UV light is the most popular technique used in semiconductor industry for transferring patterns and therefore it is called photolithography.

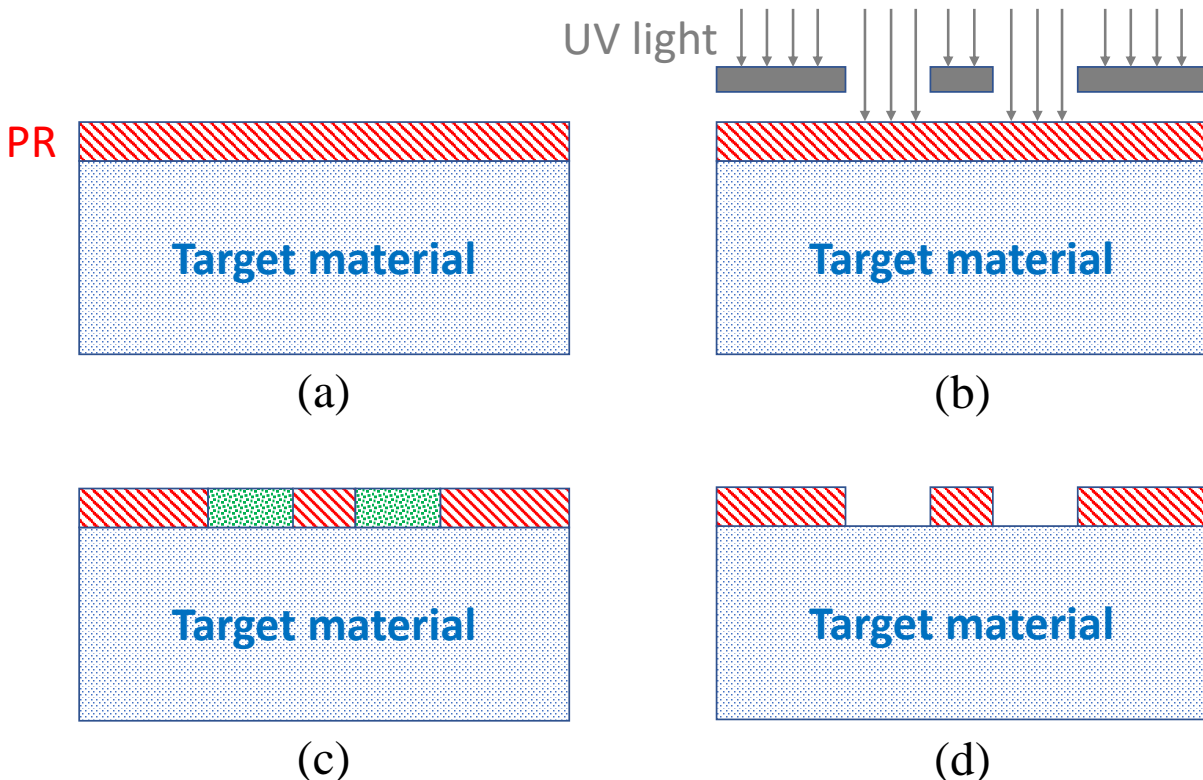


Figure 1.5: Diagrams representing key steps in photolithography: (a) substrate coated with photoresist (PR); (b) photomask aligned and PR partially exposed to ultraviolet (UV) light; (c) degradation occurred within the exposed PR and PR selectively removed by a special solution called "developer"; (d) pattern transferred to PR after development and target material ready to be etched by plasma

In Fig. 1.5 the key steps in a photolithography process are illustrated. The target material first need to be spin-coated with a thin layer of material called photoresist (PR), see Fig. 1.5(a). The actual materials used for photoresist are generally hydrocarbon (sometimes with oxygen atoms too) polymers (Oehrlein et al. 2011; Engelmann et al. 2007) and are sensitive to ultraviolet (UV) lights. Thus, by aligning a mold material called photomask (which

has the designed pattern already and should be irresponsive to UV lights) on top of the PR, the PR is selectively exposed to the UV light, see Fig. 1.5(b). The exposure causes local degradation within the material and makes the material soluble in some special solution called developer, see Fig. 1.5(c). The whole material is then immersed in the developer and ideally only the exposed PR is selectively removed while leaving the unexposed PR and the target material unaffected, see Fig. 1.5(d). After this step, the desired pattern has been successfully transferred to the PR and the target material is now ready to be etched by the plasma.

During plasma etching process, the patterned PR acts as a mask layer as shown in Fig. 1.3, therefore one of the key properties of PR material is that it should effectively resist ion bombardment, chemical reactions with the reactive neutrals as well as high temperature caused by the plasma. Other key properties include: (a) resolution, which defines the smallest distance one feature is differentiable from a neighboring feature; (b) contrast, which quantifies the difference between exposed and unexposed PR; (c) sensitivity, which defines the minimum energy required by the PR to respond to the UV light and form some well-defined features in the development step. A good quality PR material generally requires high resistance, high resolution, high contrast and high sensitivity. However, in reality, these properties are usually correlated so one may need to sacrifice one property in order to improve another, and some other properties may also need to be considered. Thus, choosing what material to use for PR is generally a complex problem and need to be individually optimized for different processes.

1.4 Passivation layer

As introduced in Fig. 1.4(d), ion-enhanced inhibitor etching uses a protective layer called passivation layer to protect the sidewalls of the HAR trench from being etched by the reactive species and energetic ions in plasma etching, and therefore high anisotropic trench profile could be achieved. The passivation layer is generally formed on the material surface through deposition of reactive radicals such as CF_x ($x = 1 \sim 3$) and CCl_x ($x = 2 \sim 3$), and the molecular structure of the passivation layer is usually polymer-like. The passivation layer is formed on both the sidewalls and the bottom of the HAR trench, however, the etch rate on the bottom is much higher than on the sidewalls due to the directional energetic ions bombardment. Thus, the deposition rate and the etch rate should be balanced in a way that on the trench bottom, the etch rate is higher and continuous etching is able to occur,

while on the sidewalls, the deposition rate and the etch rate should be fairly close so that a thin passivation layer can be formed in steady state which could effectively protect the underlying materials but does not grow too thick which may interfere the etching on the bottom.

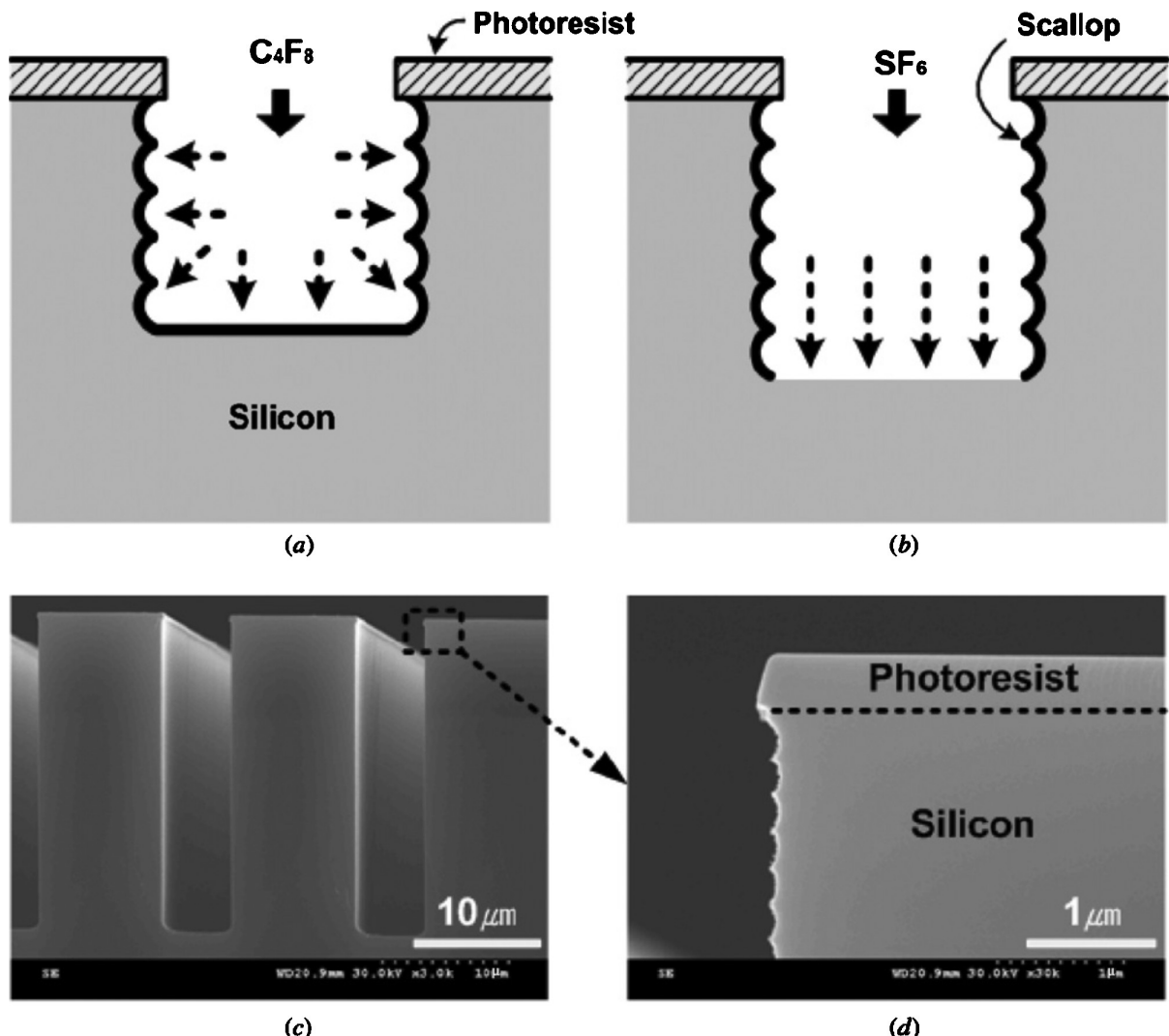


Figure 1.6: Illustration of Bosch method: (a) sidewalls and bottom of HAR trench passivated with C₄F₈; (b) etching with SF₆ gas; (c) SEM image of HAR trenches; (d) zoom-in view which shows nanoscallops on sidewall. Figures reproduced from Wu et al. (2010) and permission granted by Journal of Applied Physics.

Deposition and etching can be either simultaneous or alternating. It was found that by

alternating sidewall passivation and etch steps, the balance between lateral and vertical etch rates can be optimized and high anisotropic HAR trench can be achieved.

The first alternating process for HAR plasma etching was invented by Laemer and Schilp in 1996 (Laermer and Schilp 1996), and it is known as the Bosch method. Schematic illustration as well as some scanning electron microscope (SEM) images for HAR feature etching using the Bosch method are presented in Fig. 1.6, where it can be seen that the Bosch method can produce trenches with high aspect ratios and the sidewalls are generally smooth despite there are some periodic nanoscallops, see Fig. 1.6(c) and (d). Therefore the Bosch method has been widely used and well studied in semiconductor industry.

The original Bosch method used SF_6 for the etch gas and CHF_3 and Ar for the passivation gas. Some other options for the etch gas include NF_3 and CF_4 , and CHF_3 was later replaced by C_4F_8 for better passivation performance. In this work, we mainly investigate the polymerization of fluorocarbon radicals CF_x ($x = 1 \sim 3$) for sidewall passivation, and the effects of energetic Ar^+ ions are also considered. The formed polymer film has a molecular structure similar to polytetrafluoroethylene (PTFE), and the ratio of F:C atoms is generally between 1 and 2.

1.5 Molecular dynamics in plasma etching

Molecular dynamics (MD) is a simulation method used to model the time evolution of a system of some number of atoms/molecules moving through their interatomic potentials and external forces (if present). The detailed introduction of MD as well as all the interatomic potentials used in this work will be thoroughly covered in Chapter 2. Here we briefly introduce how MD was used to study the dynamics of the etching process at atomistic level in the context of plasma etching.

In a broader aspect of ion-material interactions, MD simulations have been extensively used for investigating how ions interact with materials across a broad spectrum of applications, spanning radiation damage in nuclear materials (Sarkar et al. 2016) and radiation interaction with biological systems (Zhigilei et al. 2003). In the context of plasma etching specifically, MD simulations have been used to investigate plasma assisted processes (Oehrlein et al. 2011) such as etching of conductors and dielectrics, Ar^+ and Cl^+ processes for etching silicon (Helmer and Graves 1998), reactive ion etching of Si and SiO_2 by fluorine-rich ion species (Tinacba et al. 2019; Gou et al. 2008) and SF_5^+ ions (Tinacba et al. 2021), near-surface modification of polystyrene by argon ions (Vegh et al. 2007), scattering

distributions of Cl^+ and Br^+ ions after reflected on Si crystal surfaces (Mori et al. 2021), and the surface reaction kinetics of etch byproduct for SiCl_x^+ ions incident on Si(100) surfaces (Nakazaki et al. 2014). The emphasis has been on how energetic ions erode or modify the material being processed, as well as the synergistic interaction of the ions, reactive species, and plasma facing surfaces.

MD simulations can also be used to study the effects of different parameters on the etching performance, such as the ion flux, the temperature, the chemistry of the etchant species, and the pick of the etching materials. This can be helpful for optimizing the etching process by adjusting those parameters as well as for developing new etching techniques.

MD simulations can also be used to estimate the value of the parameters that are necessary for some feature profile simulators, such as the scattering distribution of the incident ions after collision with the etching material, the etching rate for certain etchant species and target materials, and the sticking coefficients of the etching products on HAR sidewalls. These parameters are essential for feature profile simulators using Monte Carlo method, and can sometimes be difficult (if not impossible) to measure in experiments due to the extremely small length scale and short time scale as well as the complexity for keeping the input conditions (such as incident energies and species) to be constant when measuring the data. Therefore, MD simulations could be a good resource to generate these data, which compensate the gap between experiment data and rigorous feature profile simulators. Solid MD simulation data can help the development of feature profile simulators by improving the accuracy of some intrinsic parameters, which therefore can be helpful for optimizing the etching process as well as for developing new etching techniques.

In summary, MD simulations can be used to study the behavior of individual etchant species (atoms, molecules, ions, and radicals) and bulk etching materials in a plasma etching process, and can provide insight into designing etching processes as well as generate invaluable data for the development of feature profile simulators, which can help, both directly and indirectly, in optimizing the etching process as well as for developing new etching techniques.

1.6 Selected research topics

1.6.1 Glancing-angle scatterings

As characteristic dimensions of integrated circuits approach single atomic layers, improving device performance now depends on combining device scale length reduction, new mate-

rials, and new device geometries, including stacking of planar devices (i.e., 3-dimensional structures) (Subramanian et al. 2020). This is particularly the case in fabrication of high density memory in which up to 512 alternating layers of, for example, SiO_2 and Si_3N_4 form the material basis of the device (Kim et al. 2017). Fabrication requires plasma etching of high aspect ratio (HAR) vias through this stack. Aspect ratio (AR), is the ratio of the height to the width of the feature. A via is a vertical, cylindrical hole. The AR of such vias can exceed 100:1 in 3D-NAND memory devices (Lee et al. 2014; Kanarik 2020).

The fabrication of HAR vias and trenches is typically performed using plasma etching in capacitively coupled plasmas (Conrads and Schmidt 2000; Donnelly and Kornblit 2013). Acceleration of ions in the plasma sheath at the surface of the wafer produces an anisotropic angular distribution of ions incident onto the wafer (angular spread less than a few degrees) with energies as large as a few keV. The narrow angular distribution is intended to enable energetic ions to exclusively strike the bottom of the feature (Zhang et al. 2015; Huang et al. 2019). However, for any finite angular spread, there will be an AR for which ions collide with the interior sidewalls of the feature, typically at glancing-angles. (Here, a 90 degree angle of incidence is glancing to the surface; a 0 degree angle of incidence is normal to the surface.) Smaller angles of incidence may result from charging of surfaces inside the feature, producing lateral electric fields that deflect ions whose subsequent collisions with surfaces distort the feature's cross section profile. Near specular glancing-angle scattering may produce microtrenching as ion energy is focused near the sidewalls at the bottom of the feature (Ruixue et al. 2009; Min et al. 2005). (In this discussion ion refers to both the incident particle and the hot neutral particle after an ion neutralizes upon striking a surface.) With multiple sidewall scattering events, ion energy may be reduced to the point that etching cannot be activated, thereby terminating the etch process at some critical depth (Jin and Sawin 2003; Lee et al. 2010; Eriguchi et al. 2014). Understanding how ions interact with the sidewalls of HAR features at glancing-angle is important to optimizing plasma etching processes.

Optimizing the fabrication of HAR vias and trenches require an understanding of how ions propagate through these HAR features. Ion bombardment of the mask material causes mask erosion. Consecutive scattering events with the sidewalls can modify both the trajectory and energy of the ion as it moves deeper into the HAR feature. The selectivity between etching the underlying material and the mask defining the feature is finite (typically from 5-20). As a result, mask materials may themselves have AR of 5-20 in order that they do not erode prior to finishing etching an AR=100 feature in the underlying materials. The AR of the mask is large enough that ion scattering may occur from the sidewalls of the mask before

the ions reach the underlying materials. These sequential sidewall scatterings from both the mask and from the feature material will broaden the angular distribution and lower the ion energy. Of particular interest is the evolution of ion trajectories and energies from the mask where erosion may produce sloping sidewall angles and/or the mask intentionally has a sidewall slope.

Profile simulators (models which predict the evolution of features given the incident reactive fluxes from the plasma) address scattering from sidewalls inside features with varying degrees of sophistication, accounting for specular and diffusive scattering, and energy loss. A better understanding of these scattering processes, incorporated into profile simulations, will improve predictions of the energy and angle distributions of ions as they traverse HAR features. Profile simulations will then have improved capability to predict fabrication of HAR features and so guide process development. In the results discussed in this work, molecular dynamic simulations were employed to study these glancing angle scattering processes to improve this predictive capability and guide the evolution of HAR process conditions for increasingly challenging aspect ratio features.

A typical HAR feature consists of a mask layer and the etch layer. The mask layer may consist of a top layer of photoresist (PR), typically a radiation sensitive hydrocarbon polymer that is used to establish patterns in optical or beam driven lithographic processes (Hua et al. 2006). (See Fig. 1.7.) The PR may sit on top of a dielectric intended to mitigate light reflection during optical lithography patterning of the polymer layer (an anti-reflection coating) or on top of a more etch resistant "hard mask" that provides additional definition to the etch layer during pattern formation (Armacost et al. 1999). The etch layer is the material in which the feature is being fabricated, generally classified as dielectric (e.g., SiO₂, Si₃N₄), and or conductor (e.g., Si, Ge) (Cardinaud et al. 2000). In 3D devices, such as NAND memory, the etch layer can consist of layers of different materials such as silicon dioxide and silicon nitride that are used to eventually form vertical stacks of memory cells (Ho et al. 2008).

Materials used in MD simulations are typically either the actual material or a surrogate material that has well understood atomic scale properties while being representative of the composition and properties of the actual material. For example, previous modeling efforts (Vegh et al. 2007; Oehrlein et al. 2011; Scheer et al. 2005) used polystyrene (PS) as a representative material of 248 nm photoresist for its simpler chemical composition and for being well studied in MD community. Amorphous carbon (AC) is a common hard mask material in microelectronics manufacturing processes while also having reliable mechanical, chemical and electronic properties (Kim et al. 2013; Robertson 2002). Dielectrics in plasma etching

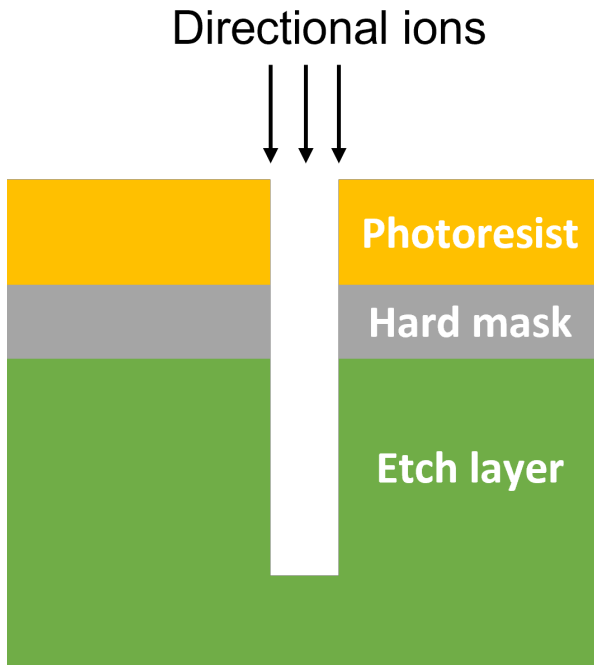


Figure 1.7: Cross section view of a typical HAR feature with a multi-layer structure.

often contains silicon compounds (Donnelly and Kornblit 2013) such as SiO_2 and Si_3N_4 both of which have well validated atomic scale models for molecular dynamic simulations (Nakano et al. 1995).

In this work, we discuss results from MD simulations of glancing-angle scattering of ions from materials of interest to HAR plasma etching processes. Specifically, PS (as a surrogate for photoresist), AC (as a hard mask candidate) and SiO_2 (as a dielectric etch layer) were investigated. Validation of computationally synthesized material structures for the simulations was performed by comparing structural and thermodynamic properties of the materials with previous computational and experimental studies with there being overall good agreement. Results of the simulations showed a transition from nearly elastic specular scattering to inelastic diffuse scattering as the incident angle of the ions became more normal to the surface and as the incident energy of the ion increased. Overall more diffuse scattering occurred for scattering from PS surfaces compared to AC and SiO_2 . The MD simulations were performed using the Large-scale Atomic/Molecular Massively Parallel Simulator (Thompson et al. 2021) (LAMMPS).

1.6.2 Fluorocarbon polymer formation

As introduced in Section 1.4, during a fluorocarbon plasma etching such as CF_4 and C_4F_8 , formation of fluorocarbon polymers can occur due to the chemical reactions and modifications in the plasma (Labelle et al. 2004; Li et al. 2002). For example, when a CF_4 plasma is created, it contains a mixture of fluorocarbon compound such as CF_x ($x = 1 \sim 3$) radicals (Booth 1999). These radicals can react with each other and with other species in the plasma to form larger molecules which generally has a back-bond carbon chain (d'Agostino et al. 1983). On the other hand, the energetic electrons and ions in the plasma can collide with those formed larger molecules and break them into smaller fragments, which furthermore increase the complexity of the species in the plasma and create more opportunities for different fluorocarbon polymers to form.

Fluorocarbon polymers can also form as a result of reactive radicals interacting with the substrate material being etched, most likely on the material surface (Metzler et al. 2014). These reactive radicals, generally with kinetic energy much lower than the energetic ions, can deposit on the surface of the substrate and polymerize, creating a thin film of polymer. This polymer film typically comprise a complex mixture of chemical compounds mainly containing carbon and fluorine with a PTFE-like structure (Booth 1999), but can still contain other elements from the substrate materials such as silicon, oxygen, and hydrogen.

It's important to note that the fluorocarbon polymer formed on the substrate material surface during plasma etching can have both positive and negative effects. On one hand, as shown for the Bosch method in Section 1.4, the polymer film can act as a sacrificial layer during an alternative etching process, where a thin layer of polymer film is deposited on the substrate surface prior to actually etching, to protect the underlying material (especially on the HAR sidewalls) from being etched. On the other hand, the build-up of excessive unwanted polymers can also lead to process contamination, reduce etch selectivity, reduce etch rate, and affect the final feature profile. Thus, the plasma conditions such as gas flow rate, pressure and power need to be carefully controlled, and the etching strategies need to be well designed, to mitigate the side-effects of the fluorocarbon polymer formation and optimize the etching performance.

The formation of fluorocarbon polymer on substrate surface has been observed and studied in previous experimental works. For example, Standaert et al. (2004) studied how the film thickness affects the total etch rate and showed that fluorocarbon polymer with different steady-state thickness formed on different substrate materials such as Si, Si_3N_4 , SiO_2 and SiCH within the same duration in a C_4F_8 discharge. Metzler et al. (2014) showed

that in a cyclic Ar/C₄F₈ discharge, when SiO₂ substrate was covered with fluorocarbon polymer, thicker polymer (5-10 Å) would first help in low energy ions etching the under-layer material. However, as the polymer thickness exceeded a critical thickness, the ions would only etch the over-layer polymer during the whole etch cycle and the under-layer material would be unreachable by the ions.

Computational efforts have also been carried out on this topic. For example, Huard et al. (2018) used a Monte Carlo type feature profile simulator, MCFPM (Zhang et al. 2017), to study the transient behavior of fluorocarbon polymer in Ar/C₄F₈ plasma etching of SiO₂ and Si₃N₄. Rauf et al. (2007) used a molecular dynamics model to study the deposition of a thin fluorocarbon polymer layer on SiO₂ surface using CF_x⁺ ions, as well as the reactive ion etching with the addition of Ar⁺ ions.

It should be noted that in the experimental works, due to the complexity of the nature of the plasma and the variety in substrate surface conditions, the contribution of a single species in a plasma to the polymer growth cannot be separated from the overall results. In addition, the controllable parameters in experiments are generally in large scale (such as the bias voltage in [Standaert et al. (2004)] and the C₄F₈ pulse time in [Metzler et al. (2014)]), but the nanoscale parameter dependencies and the atomic structure of the fluorocarbon polymer are quite difficult to capture. On the other hand, Monte Carlo type feature profile simulators would require some predefined rate coefficients to model the polymer growth. These rate coefficients are generally empirically equations measured previously, and the accuracy can be improved using modern atomic simulation tools. In addition, previous molecular dynamics works (Rauf et al. 2007; Végh 2007) focused mainly on etching of the substrate with the presence of fluorocarbon film, while information about formation of the fluorocarbon polymer and the corresponding molecular structure are still lacked. Moreover, the simulation accuracy could be improved by using an bond-order reactive potential such as ReaxFF, especially for surface-radical interactions where lots of chemical reactions take place.

Therefore, an extensive parametric study of the formation of the fluorocarbon polymer using molecular dynamics simulation would definitely help the researchers to determine which of these nanoscale conditions can affect the results. The atomic structure of the polymer film can also be well captured, which could be used to differentiate the roles of different plasma species play on the polymer formation. Compared to other computational works, a reactive molecular dynamics simulation not only can provide various rate coefficients needed by feature profile simulations, but also it can improve the accuracy in modeling chemical reactions.

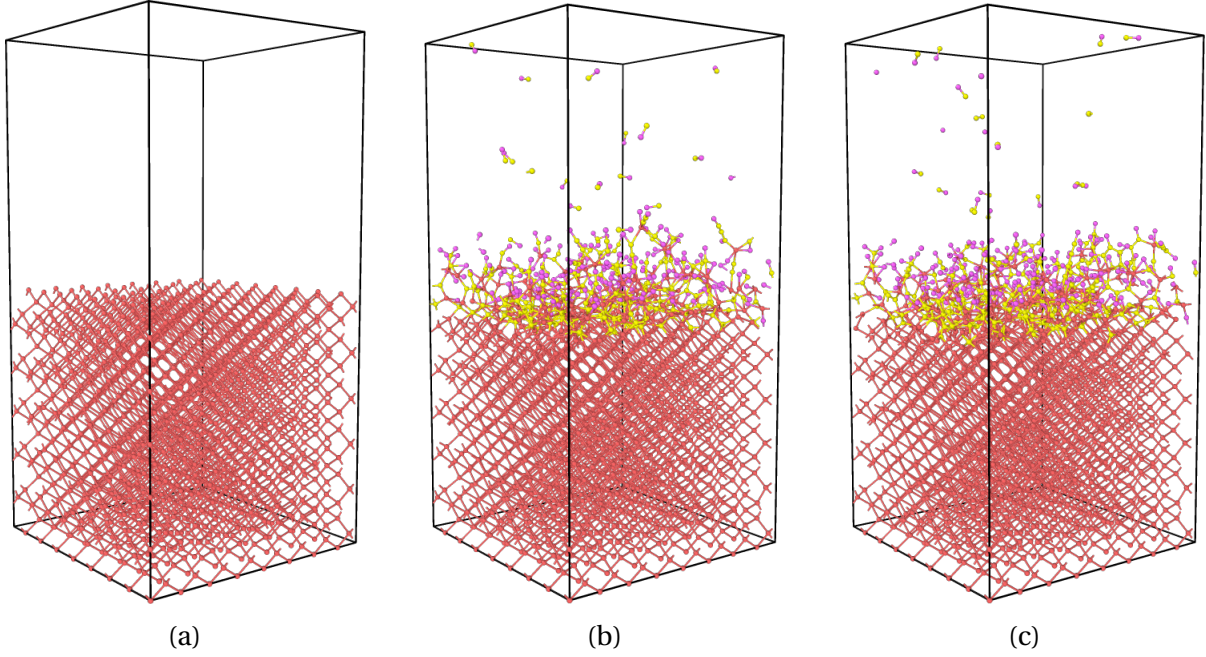


Figure 1.8: Formation of fluorocarbon polymer film on Si crystal with CF radicals deposition (red=Si, yellow=C, pink=F): (a) initial Si crystal; (b) after 1000 CF radicals incidence; (c) after 1000 CF radicals incidence

In this work, we discuss results from MD simulations of fluorocarbon polymer formation on HAR sidewalls in plasma etching processes. Specifically, amorphous SiO_2 and Si were used as the substrate material, and CF_x ($x = 1 \sim 3$) radicals were used to as the incident molecules to grow a polymer film on top of the substrate. See Fig. 1.8 for an example of growing fluorocarbon polymer film on Si crystal through the deposition of CF radicals. In order to perform reactive MD simulations, a parameter file for ReaxFF interatomic potential was carefully prepared using the datasets from previous ReaxFF works. Validations of the prepared parameter file itself as well as the computationally synthesized material structures were carried out by comparing structural and thermodynamic properties of the materials with previous computational and experimental studies. Results of the simulations showed that the film thickness (or grow rate) strongly depends on the incident species. A fluorine rich species such as CF_3 is very likely to form a thin monolayer on the substrate surface and then saturates, while a fluorine deficient species such as CF can grow a much thicker polymer and has the potential of continued growing. The film thickness also strongly depends on the substrate material, where it was observed that fluorocarbon polymer on Si crystal can grow a much thicker film than on amorphous SiO_2 , during the same period of

radicals deposition. It was also found that carbon could potentially play a role in forming the multi-chain polymer structure on the substrate surface. The MD simulations were performed using LAMMPS with ReaxFF potential, and the details and features about ReaxFF potential will be covered in Chapters 2 and 4.

1.6.3 Sticking coefficient

Measuring sticking coefficients for various plasma species on different HAR materials in fluorocarbon plasma etching processes is a natural outcome of studying the fluorocarbon polymer formation. A high growth rate of the polymer film indicates a large value in sticking coefficient, and the time-dependent behavior of polymer growth can be explained by quantitatively measuring the sticking coefficients on varying substrate surface conditions as a function of time. On the other hand, measuring sticking coefficients can also benefit computational models such as feature profile simulators or other rigorous models, as those models generally treat plasma-surface interactions as individual computational events with some predefined probabilities, and sticking coefficients are among the key design parameters.

The term "sticking coefficient" is used to characterize the ratio of the number of particles (atoms, molecules, or radicals) that stick to a target material surface upon collision, to the total number of incident particles during the same period of time. It is commonly used in describing the behavior of gas-surface interactions in surface science. Since it is a measure of probability, sticking coefficient is dimensionless and generally has value between 0 and 1, where a value of 0 means none of the particles stick to the target surface and a value of 1 means all the particles stick. The value of the sticking coefficient is not always the same for the same incident particle and target material, in fact, it depends on various factors such as the pressure, the temperature, the surface roughness of the target material and the incident energy and angle of the incident particles.

It can be expected that in the experimental works, sticking coefficients are generally difficult to measure, and are usually estimated indirectly from other results. For example, in an experimental work by Izawa et al. (2007), they estimated the sticking coefficients of radicals CF_x and C_x by comparing the measured HAR profile with a calculated profile. It can be found that this estimated value represents an overall effect where the sticking coefficients of different radical species such as CF and CF_3 , which we expect to have a significant difference, cannot be individually measured. Moreover, the estimated value is based on the HAR profile at the end of the plasma etching process, meaning that it assumes

the sticking coefficient is uniform during the whole etching process but not time dependent, while what could really happen is that the sticking coefficient could decrease (or increase) in time as more and more radicals are deposited on the substrate and modify the surface condition. In another experimental work by Cunge et al. (2010), the sticking coefficients of SiCl and SiCl₂ on SiOCl layer were estimated using UV light emitting diodes and absorption spectroscopy. They measured the SiCl and SiCl₂ densities in the afterglow of Ar/SiCl₄/Cl₂ plasma as a function of time. And the sticking coefficients were estimated by assuming the decay in radical densities were mostly due to radicals sticking to the plasma chamber walls, which are precious information but once again show the limitation of experiments for estimating sticking coefficients.

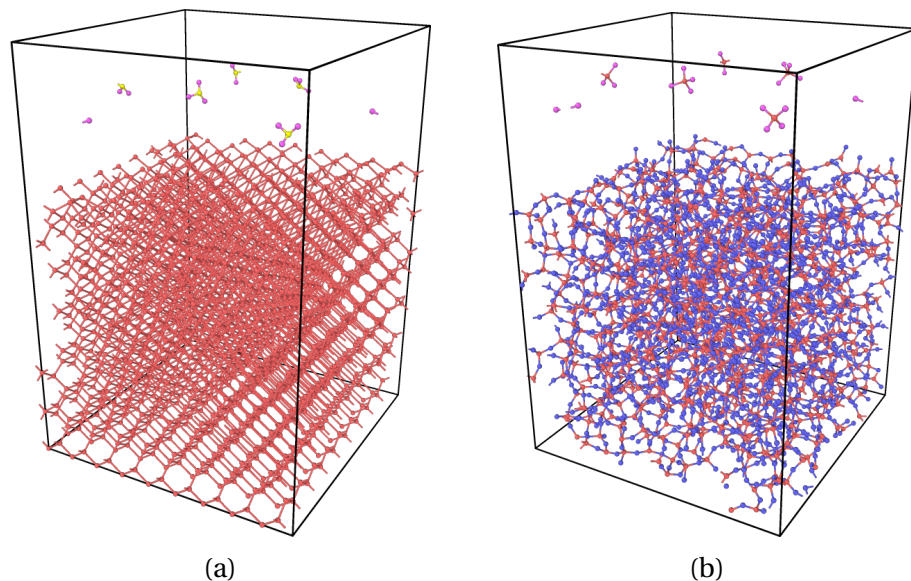


Figure 1.9: Measuring the sticking coefficients on bare substrate surface (red=Si, blue=O, yellow=C, pink=F): (a) 5 CF₃ radicals incident on Si crystal surface; (b) 5 SiF₄ molecules incident on amorphous SiO₂ surface.

In this work, we discuss results from MD simulations of measuring the sticking coefficients of molecules/radicals on some general HAR materials' surface in plasma etching processes. Specifically, amorphous SiO₂ and Si were used as the substrate materials, and CF_x ($x = 1 \sim 4$) and SiF_x ($x = 1 \sim 4$) were used to as the incident molecules/radicals. The sticking coefficients were measured directly from the ratio of the number of attached molecules to the number of incident molecules, independently for each plasma species.

The sticking coefficients were measured in two ways. Firstly, the sticking coefficients were measured on bare material surfaces, where the material surfaces were reset to the initial state (bare surface) every five incidences so no accumulation effect was taken into account. And the sticking coefficients were measured after many repetitions of these five-incidence cases. See Fig. 1.9 for an example. Secondly, the sticking coefficients were measured in a growing manner (no reset, with accumulation), which is quite similar to fluorocarbon polymer formation. Constant fluxes were used so that the number of attached molecules can be measured as a function of the number of incidence, and the sticking coefficients can be measured from the slope of such curves. An analytical model was also derived and fitted to the measured data using two-segment regression, and good match was achieved between the analytical model and the measured results which makes it possible to incorporate the simple model into any rigorous models to conveniently predict the variation in sticking coefficients as a function of surface conditions. Details will be covered in Chapters 5.

1.7 Dissertation outline

The computational methods and procedures are discussed in Chapter 2. Results regarding to glancing-angle scatterings are discussed in Chapter 3. Results regarding to fluorocarbon polymer formation are discussed in Chapter 4. Results regarding to sticking coefficient are discussed in Chapter 5. Conclusions are summarized and future works are discussed in Chapter 6. The ReaxFF parameter files used in this work are listed in Appendix A. Some of the LAMMPS input files and Python scripts, which are vital for simulation preparing and data post-processing, are selectively listed in Appendix B.

CHAPTER

2

METHODS

2.1 Classical Molecular Dynamics

Molecular dynamics (MD), as the name suggests, models the time evolution of a system of some number of atoms/molecules moving through their interatomic potentials and external forces (if present). One way to describe the motion of particles in a force field is by using Newton's Second Law (Law of motion), thus such simulations are called classical Molecular Dynamics. In contrast, if the system is described by quantum mechanics (QM) by solving Schrödinger equation, such simulations are called *ab initio* Molecular Dynamics. One popular application of *ab initio* MD is the density-functional theory (DFT), where many physical quantities of the system are solved in the form of functional of densities and the complicated higher-order QM equations can be significantly simplified, which makes it feasible to solve a more complex system. However, even with DFT, the system size is still quite small. For comparison, the molecular systems in this work usually have a few thousand particles, which can be solved on a 4-core desktop within a feasible amount of time using classical MD, while the system size would be less than 100 particles for a DFT program to run on a similar setup with even longer simulation time. In order to model the

surface interactions in plasma etching, a larger system size is required as the local structures (such as amorphous structure and polymer structure) are usually non-uniform and more particles are needed to better represent the real material and to reduce statistical error, and a longer simulation time is required since some reactions (such as sticking and sputtering) would need extra time steps for the materials to thermalize and equilibrate. Thus, classical MD was selected for modeling all the plasma-surface interactions in this work.

A complete mathematical description of classical MD can be briefly summarized as

$$\vec{F}_{ij} = -\nabla_r V(\vec{r}_{ij}) \quad (2.1a)$$

$$\frac{\sum_{j,j \neq i} \vec{F}_{ij}}{m_i} = \frac{d^2 \vec{r}_i}{dt^2} \quad (2.1b)$$

$$(\vec{r}_1, \dots, \vec{r}_N, \vec{p}_1, \dots, \vec{p}_N, t) \rightarrow (\vec{r}_1, \dots, \vec{r}_N, \vec{p}_1, \dots, \vec{p}_N, t + \Delta t) \quad (2.1c)$$

where \vec{F}_{ij} is the interatomic force between two particles i and j , which can be obtained by calculating the spatial gradient of the corresponding interatomic potential $V(\vec{r}_{ij})$. Note for some more complicated interatomic potentials, 3-body interactions are also included when computing interatomic forces. In such cases, both \vec{F}_{ij} and \vec{F}_{ijk} (or some equivalent terms) need to be calculated in order to calculate the force \vec{F}_i exerted on a single atom. See Sec. 2.3.1 for Tersoff potential for an example. All the interatomic forces can be added up and plugged into the Newton's Law of motion, as shown in Eq. 2.1b. The positions \vec{r}_i and momenta \vec{p}_i of all the particles in the system can be obtained for the next time step $t + \Delta t$ using some sort of time integrator, as shown in Eq. 2.1c. Different numerical constraints can be enforced to different parts of the system when performing the time integration step, essentially matching real physical conditions. For example, constant pressure, constant temperature condition is usually required when preparing the material using MD in order to reduce internal stress and keep the material stable. More details about the constraints will be covered in Sec. 2.2.1.

The direct output of classical MD simulations are the positions, momenta of all the particles as a function of time, which can then be post-processed to obtain the thermodynamic and structural properties of the system. For example, thermodynamic properties such as temperature and pressure can be measured using the concept of ensemble average in statistical mechanics, shown in Eq. 2.2, and structural properties such as crystal structure and radial distribution function (RDF) can also be estimated using the positions information.

$$\langle G \rangle = \frac{\int \int G(\vec{r}_1, \dots, \vec{r}_N, \vec{p}_1, \dots, \vec{p}_N) \exp\{(-\beta E(\vec{r}_1, \dots, \vec{r}_N, \vec{p}_1, \dots, \vec{p}_N))\} d\vec{r}_1 \dots d\vec{r}_N d\vec{p}_1 \dots d\vec{p}_N}{\int \int \exp\{(-\beta E(\vec{r}_1, \dots, \vec{r}_N, \vec{p}_1, \dots, \vec{p}_N))\} d\vec{r}_1 \dots d\vec{r}_N d\vec{p}_1 \dots d\vec{p}_N} \quad (2.2)$$

As can be seen from Eq. 2.1, it is the interatomic potential $V(\vec{r}_{ij})$ that characterize different elemental systems. Thus, determining the interatomic potentials is the vital part in classical MD simulations. Generally, researchers will first bring up some analytical empirical functions based on some existed data or model that can apply to the desired physical scenario. For instance, a screened Coulomb potential is suitable for modelling high-energy collisions, and a bond-order potential may be needed when chemical interactions need to be taken into account. Those analytical empirical functions will then be trained with some validated data, either from experiments or from DFT, and the coefficients can be optimized with respect to different types of atoms or molecules. Details about all the interatomic potentials used in this work will be covered in Sec. 2.3.

2.2 LAMMPS

A classical molecular dynamics simulation code, LAMMPS, was used to perform all the MD simulations in this work. LAMMPS stands for Large-scale Atomic/Molecular Massively Parallel Simulator, and was originally developed at Sandia National Laboratories (Thompson et al. 2021). LAMMPS is a open-source code, which means the users can easily view the source code and learn the physics in detail or make changes as desired. LAMMPS supports a lot of different interatomic potentials (force fields) and can model a MD system with dimensions up to 3 and with a wide range of system scale (number of particles). LAMMPS is written in C++ with an object-oriented style, thus, it is fairly easy to modify or extend the current existed functions to include new capabilities. LAMMPS can be compiled with either Open MPI (Gabriel et al. 2004) or MPICH (MPICH 2022) to support the MPI message-passing library. LAMMPS can also be compiled with OpenMP package (OpenMP 2022) for multi-threading support. Having all of these accelerator packages complied, LAMMPS can be run on a small desktop with only a few cores or a high-performance server with thousands of cores. In this work, LAMMPS was run on different computational platforms including a 4-core (8 threads, Intel Core i7-6700 CPU) Linux desktop, a 36-core Linux desktop (72 threads, 2 of Intel Xeon Gold 6240 CPUs), and NC State High Performance Computing (HPC) servers (different architectures on different nodes) with multiple parallel jobs. Consistency

in simulation results was observed among different platforms, and performance increase was achieved when increasing the number of cores.

Most of the LAMMPS usage and documentation can be found on the official LAMMPS manual website (LAMMPS 2022) or on the MATSCI website (MATSCI 2022). Here, we will briefly cover some main functions heavily used in this work, as shown in the next two subsections.

2.2.1 Nose-Hoover thermostat and barostat

In order to match different experimental conditions in a MD simulation, several numerical constraints can be applied to different parts of the system. For example, in a plasma etching process, the target materials are usually at room temperature (300K) with pressure close to vacuum (≈ 0), and the incident particles are treated free of constraints (energy conserved) prior to striking, both of which can be achieved using LAMMPS *fix npt/nvt/nve* commands. Specifically, *fix npt/nvt* commands perform time integration on Nose-Hoover style non-Hamiltonian equations of motion (Evans and Holian 1985; Nose 1990; Martyna et al. 1994) for thermostating and barostating, and the atoms in the group controlled by the commands will have positions and velocities which are consistent with the canonical (nvt), isothermal-isobaric (npt) ensembles. The equations of motion used by LAMMPS for these Nose-Hoover style thermostat and barostat were taken from the paper by Shinoda et al. (2004). On the other hand, *fix nve* command performs plain time integration for the specified group of particles (similar to Eq. 2.1b and 2.1c, so no constraints), which is consistent with the microcanonical ensemble (nve).

```

1 # set constant temperature at 300K and constant pressure at 0
2 fix      3    mobile_group npt temp 300.0 300.0 $(100.0*dt) x 0.0
   0.0 $(1000.0*dt) y 0.0 0.0 $(1000.0*dt)
3 run      10000
4 unfix   3
5
6 # set constant temperature at 300K and constant volume
7 fix      3    mobile_group nvt temp 300.0 300.0 $(100.0*dt)
8
9 # set no constraints
10 fix     7    addatoms nve

```

Listing 2.1: *fix npt/nvt/nve* commands example

A snippet of code is listed in List. 2.1 for an example. In the first *fix npt* command, the temperature of all the atoms within group "mobile_group" is set at 300 K constant and the pressure is set at 0 constant for *x* and *y* directions. The temperature is controlled by rescaling the velocity vectors of the specified atoms and the pressure is controlled by rescaling the simulation box size in the corresponding directions. If the current system state deviates from the target state, the temperature and pressure will be adjusted each timestep with damping rates of "100.0*dt" and "1000.0*dt" respectively ("dt" is the current timestep unit). In the second *fix nvt* command, the temperature is treated constant with the same approach while the pressure is free of constraint, so constant simulation box size. In the third *fix nve* command, no constraints are applied to all the atoms within group "addatoms" and therefore energy will be conserved. This is useful when modeling atoms deposition or the atoms on the material surface need to move freely.

2.2.2 *fix deposit* command

fix deposit command can be used for inserting atoms or molecules into the simulation domain with some predefined velocities. In this work, *fix deposit* command was used for all the Ar ions scattering simulations, for depositing carbon atoms on silicon crystal surface to generate amorphous carbon layer, and for depositing CF_x ($x = 1, 2$) radicals on amorphous SiO_2 surface to generate passivation layer.

A snippet of code is listed in List. 2.2 for an example. The region for inserting the particles is predefined as *deposit_slab*. The total number of incidence, the interval between two successive incidence, the incident angle and incident energy can all be dynamically defined using LAMMPS *variable* keyword. The *fix deposit* command is then called for setting up the deposition environment, and the final *run* command is called to actually start the simulation.

```

1 # create deposition block for Ar
2 region deposit_slab block EDGE EDGE EDGE EDGE $((zhi-zlo)*0.9+zlo)
   $((zhi-zlo)*0.95+zlo) units box
3
4 # define number of incidence, incident interval and random seed for
   reproducibility
5 variable num_of_insert equal 10 #
6 variable delta_step_insert equal 2000 # 2000fs=2ps
7 variable randomSeedForDeposit equal 1234
8
9 # define incident angle and energy and convert to velocity vectors

```

```

10 variable in_angle_degree equal 75 # degree
11 variable in_energy equal 100 # eV
12 variable in_angle equal v_in_angle_degree/180*3.1415926 # rad
13 variable in_velocity equal sqrt(2*v_in_energy*1.602E-19/6.633E-26)
   /100/1000 # Angstrom/fs
14 variable in_vz equal -v_in_velocity*cos(v_in_angle)
15 variable in_vy equal v_in_velocity*sin(v_in_angle)
16
17 # define the group for incident atoms and call the "fix deposit"
   command
18 group addatoms type 5
19 fix 5 addatoms nve
20 fix 6 addatoms deposit ${num_of_insert} 5 ${delta_step_insert} ${
   randomSeedForDeposit} region deposit_slab near 1.0 id next vz ${
   in_vz} ${in_vz} vy ${in_vy} ${in_vy} units box
21
22 # actually start the simulation
23 variable run_step equal (${num_of_insert}+5)*${delta_step_insert}
24 run      ${run_step}

```

Listing 2.2: *fix deposit* command example

Note that in MD simulations, the real flux values usually cannot be achieved due to the limitations of the time scale and the system size scale, i.e., the system size scale in MD simulations is so small that the number of time steps between two consecutive incidence need to be fairly large in order to represent a reasonable flux value, thus the computational time would be too long to achieve if a significant number of incidence need to be simulated in order to reduce statistical errors. Instead, most of the MD simulations would use a much smaller value for the number of time steps between two consecutive incidence, essentially increasing the flux value. This can be justified by assuming that the two consecutive incidence are independent events when decreasing the time interval, which can be observed by monitoring the thermodynamic properties of the target material surface during the scattering/deposition process. In this work, the temperature and pressure of the target material surface were monitored, and thermodynamic equilibrium was reached between two consecutive incidence, indicating that the independence was achieved.

2.3 Interatomic potentials

2.3.1 Tersoff potential

Tersoff potential, first introduced by J. Tersoff in 1988 (Tersoff 1988, 1989), is a 3-body potential which has been widely used in Si, Si_xO_y , Si_xC_y and Si_xN_y systems. See Eq. 2.3 for a complete mathematical description of Tersoff potential:

$$E = \frac{1}{2} \sum_i \sum_{j \neq i} V_{ij} \quad (2.3a)$$

$$V_{ij} = f_C(r_{ij} + \delta) [f_R(r_{ij} + \delta) + b_{ij} f_A(r_{ij} + \delta)] \quad (2.3b)$$

$$f_C(r) = \begin{cases} 1 & : r < R - D \\ \frac{1}{2} - \frac{1}{2} \sin\left(\frac{\pi}{2} \frac{r-R}{D}\right) & : R - D < r < R + D \\ 0 & : r > R + D \end{cases} \quad (2.3c)$$

$$f_R(r) = A \exp(-\lambda_1 r) \quad (2.3d)$$

$$f_A(r) = -B \exp(-\lambda_2 r) \quad (2.3e)$$

$$b_{ij} = (1 + \beta^n \zeta_{ij}^n)^{-\frac{1}{2n}} \quad (2.3f)$$

$$\zeta_{ij} = \sum_{k \neq i, j} f_C(r_{ik} + \delta) g[\theta_{ijk}(r_{ij}, r_{ik})] \exp[\lambda_3 m (r_{ij} - r_{ik})^m] \quad (2.3g)$$

$$g(\theta) = \gamma_{ijk} \left(1 + \frac{c^2}{d^2} - \frac{c^2}{[d^2 + (\cos \theta - \cos \theta_0)^2]} \right) \quad (2.3h)$$

where E is the total potential energy, V_{ij} is the interatomic potential between atoms i and j , r_{ij} is the interatomic distance, f_R and f_A are 2-body terms, b_{ij} includes 3-body interactions as shown in Eq. 2.3f, 2.3g and 2.3h, σ is an optional negative shift of the equilibrium bond length, and f_C is a smoothing function to smoothly transition the interatomic potential V_{ij} to 0 after the cutoff radius R within the width $2D$.

Different MD system would require different parametrization of Eq. 2.3. The two Tersoff parametrizations used in this work are from (Munetoh et al. 2007) and (Erhart and Albe 2005), which were used to simulate Si-O and Si-C systems respectively and both parameter files are available in the current LAMMPS version (under *potentials* folder and named *SiO.tersoff* and *SiC_Erhart-Albe.tersoff* respectively).

2.3.2 TraPPE potential

Transferable Potentials for Phase Equilibria-United Atom (TraPPE) force field, first introduced by JI Siepmann in 1998 (Martin and Siepmann 1998), has been widely used in polymer systems such as alkanes (Martin and Siepmann 1998), alkylbenzenes (Wick et al. 2000) and ketones (Stubbs et al. 2004). In contrast to the other nonbonded potentials used in this work (Tersoff and ZBL), TraPPE force field used explicit bonds to connect and constrain atoms in a polymer structure. See Fig. 2.1 for diagrams of how interaction between atoms in a bonded system are described in separate ways (also see Eq. 2.4a): (a) U_{bond} is a bond stretching interaction term which accounts for two atoms oscillating about the equilibrium bond length; (b) U_{angle} is a bond angle interaction term which accounts for the oscillation of 3 atoms about an equilibrium bond angle; (c) U_{torsion} is a dihedral torsion interaction term which accounts for torsional rotation of 4 atoms about a central bond; (d) U_{improper} is an improper dihedral interaction term which is used to maintain planarity of 4 atoms in a polymer structure; (e) $U_{\text{nonbonded}}$ is a non-bonded interaction term which is used to describe the interaction between two atoms which are not explicitly connected with bonds. The total interatomic potential of the system can be obtained by adding up all these individual interaction terms, as shown in Eq. 2.4a.

$$U_{\text{total}} = U_{\text{bond}} + U_{\text{angle}} + U_{\text{torsion}} + U_{\text{improper}} + U_{\text{nonbonded}} \quad (2.4a)$$

$$U_{\text{bond}} = K_r(r - r_0)^2 \quad (2.4b)$$

$$U_{\text{angle}} = K_\theta(\theta - \theta_0)^2 \quad (2.4c)$$

$$\begin{aligned} U_{\text{torsion}} = & \frac{1}{2}K_1[1 + \cos(\phi)] + \frac{1}{2}K_2[1 - \cos(2\phi)] + \\ & \frac{1}{2}K_3[1 + \cos(3\phi)] + \frac{1}{2}K_4[1 - \cos(4\phi)] \end{aligned} \quad (2.4d)$$

$$U_{\text{improper}} = K_\chi(\chi - \chi_0)^2 \quad (2.4e)$$

$$U_{\text{nonbonded}} = U_{\text{LJ}} = 4\epsilon \left[\left(\frac{\sigma}{r} \right)^{12} - \left(\frac{\sigma}{r} \right)^6 \right] \quad r < r_c \quad (2.4f)$$

Note that there are plenty of analytical forms for each individual potentials of U_{bond} , U_{angle} , U_{torsion} , U_{improper} and $U_{\text{nonbonded}}$, and different force fields might have one or two terms in common but with the other terms being different. Specifically, TraPPE force field used harmonic form for U_{angle} (see Eq. 2.4c) and U_{improper} (see Eq. 2.4e), and Lennard-Jones (LJ) potential for $U_{\text{nonbonded}}$ (see Eq. 2.4f). For U_{torsion} , it used this harmonic series form as shown

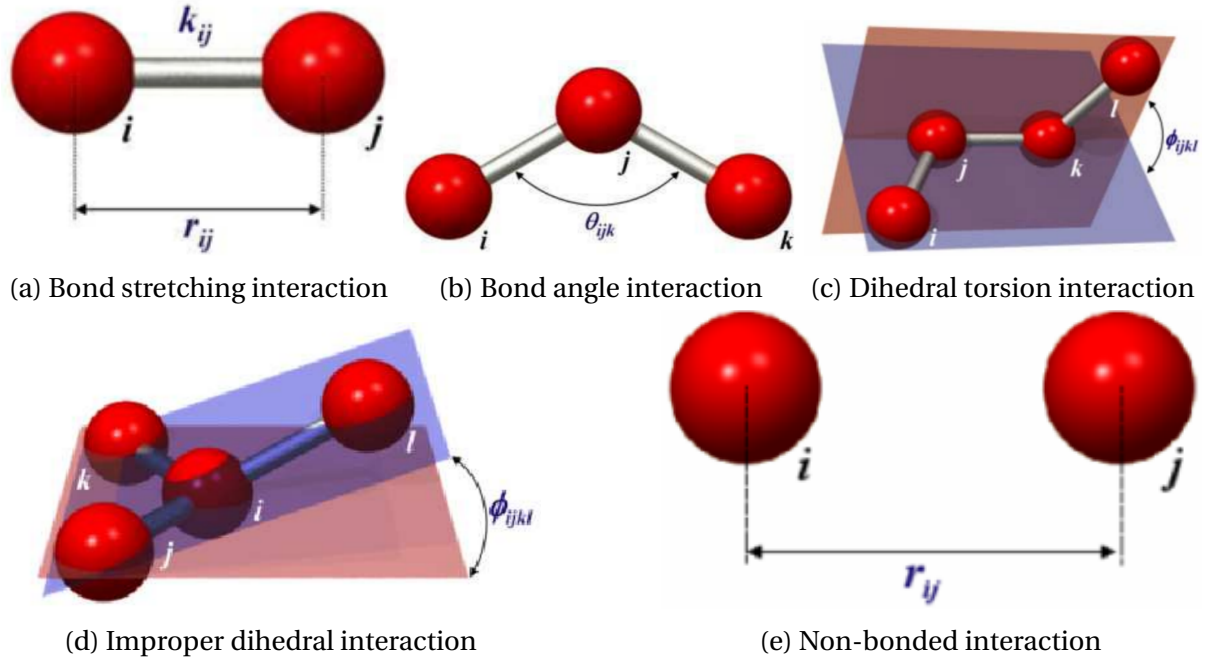


Figure 2.1: Diagrams showing how bonded potential usually represented in a Molecular Dynamics simulation. Images were taken from (Kouza 2013)

in Eq. 2.4d. And for U_{bond} , TraPPE force field actually assumed fix-length bond model, so the bond length will be constant and no oscillation will be allowed.

Some modifications need to be performed to the original TraPPE force field in order to apply it to LAMMPS:

(1) The original TraPPE force field usually has a factor of 1/2 before each harmonic interaction terms as

$$U_{\text{angle}} = \frac{1}{2} k_\theta (\theta - \theta_0)^2 \quad (2.5a)$$

$$U_{\text{improper}} = \frac{1}{2} k_\chi (\chi - \chi_0)^2 \quad (2.5b)$$

This usual 1/2 factor was incorporated into the K values in LAMMPS representations, see Eq. 2.4c and Eq. 2.4e;

(2) The original TraPPE force field used fix-length bond model, which cannot be achieved in the current LAMMPS version. A similar approach LAMMPS has to constrain bond length is the SHAKE algorithm (Ryckaert et al. 1977), but this algorithm can only be used for small clusters of atoms (less than 4 connected atoms). Thus, in order to apply the TraPPE force field to polymers with longer chains such as polystyrene, a harmonic bond stretching

interaction term was used instead as shown in Eq. 2.4b. The values of coefficients were taken from previously published data (Han and Boyd 1996);

- (3) The dihedral torsion interaction term in the original TraPPE force field

$$U_{\text{torsion}} = c_0 + c_1[1 + \cos(\phi)] + c_2[1 - \cos(2\phi)] + c_3[1 + \cos(3\phi)] \quad (2.6)$$

is slightly different from all the available dihedral styles in LAMMPS. The closest one can get is the *opls* dihedral style, as shown in Eq. 2.4d. So the 1/2 factor need to be taken care of and the K_4 coefficient in Eq. 2.4d need to be kept 0. Note the c_0 coefficient in Eq. 2.6 is always 0 for all the dihedral torsion interaction term considered in this work. If a non-zero c_0 is required in a future work, then the source code of LAMMPS need to be modified, for example, the *opls* dihedral style could be inherited and expanded. It is fairly easy to do so since LAMMPS is open-source and has been written in object-oriented style.

- (4) Units for all the values of the coefficients taken from reference data need to be converted to be compatible with LAMMPS. For example, the reference data used unit of kJ/mol for the K coefficients, while LAMMPS used kcal/mol in units style *real*. (Here units style *real* determines a set of units for some basic physical quantities, which is the same idea as SI units and cgs units.) So a conversion factor of 4.184kJ = 1kcal need to be applied when preparing the coefficients for the input file.

TraPPE force field is based on united-atom description, i.e., the lightweight "branch atoms" (such as H atoms) will be incorporated into heavier "stem atom" (such as C and N atoms) to form a pseudo macro atom. In this work for polystyrene, the H atoms were incorporated into their neighboring C atoms for both the carbon chain and the benzene ring, see Fig. 2.2 for an illustration, and macro atoms such as CH₃, CH₂, CH, C_{ar}H and C_{ar} were formed (C_{ar} means the carbon atoms on the aromatic ring).

In summary, the analytical equations of the modified TraPPE force field are listed in Eq. 2.4 and the values of the corresponding coefficients for an atactic polystyrene system are listed in Table 2.1.

Note that in Table 2.1, angle type is denoted as *i-j-k* where *j* being the central atom, dihedral type is denoted as *i-j-k-l* where *j* and *k* being the two central atoms, and improper type is denoted as *i-j-k-l* where *i* being the central atom and χ measures how far out-of-plane *i* is with respect to the plane of *j-k-l*. For nonbonded LJ parameters, certain mixing rules need to be applied if the interaction between two different atoms need to be calculated, and the LAMMPS default *geometric* mixing rule was used, see Eq. 2.7.

Table 2.1: Coefficients for the TraPPE force field for an atactic polystyrene system

Bond type	K_r (kcal/mol)	r_0 (\AA)
$\text{CH}_3/\text{CH}_2-\text{CH}$	79.2304	1.54
$\text{C}_{\text{ar}}-\text{CH}$	79.2304	1.50
$\text{C}_{\text{ar}}/\text{C}_{\text{ar}}\text{H}-\text{C}_{\text{ar}}\text{H}$	131.453	1.39

Angle type	K_θ (kcal/mol/rad ²)	θ_0 (degree)
$\text{CH}_3/\text{CH}_2-\text{CH}-\text{CH}_3/\text{CH}_2$	62.1415	112
$\text{CH}-\text{CH}_2-\text{CH}$	62.1415	114
$\text{C}_{\text{ar}}\text{H}-\text{C}_{\text{ar}}\text{H}-\text{C}_{\text{ar}}\text{H}/\text{C}_{\text{ar}}$	119.503	120
$\text{C}_{\text{ar}}\text{H}-\text{C}_{\text{ar}}-\text{CH}$	119.503	120

Dihedral(Torsion) type	K_1 (kcal/mol)	K_2 (kcal/mol)	K_3 (kcal/mol)	K_4 (kcal/mol)
$\text{CH}_3/\text{CH}_2-\text{CH}-\text{CH}_2-\text{CH}$	1.41109	-0.268642	3.14484	0

Improper type	K_χ (kcal/mol/rad ²)	χ_0 (degree)
$\text{C}_{\text{ar}}\text{H}-\text{C}_{\text{ar}}\text{H}-\text{C}_{\text{ar}}\text{H}-\text{C}_{\text{ar}}\text{H}$	20.0048	0
$\text{C}_{\text{ar}}-\text{C}_{\text{ar}}\text{H}-\text{C}_{\text{ar}}\text{H}-\text{CH}$	20.0048	0
$\text{CH}-\text{CH}_3/\text{CH}_2-\text{CH}_3/\text{CH}_2-\text{C}_{\text{ar}}$	40.0096	35.26

Nonbonded LJ parameters	ϵ (kcal/mol)	σ (\AA)
CH_3	0.195005	3.75
CH_2	0.091491	3.95
CH	0.019861	4.65
C_{ar}	0.059608	3.7
$\text{C}_{\text{ar}}\text{H}$	0.100311	3.695

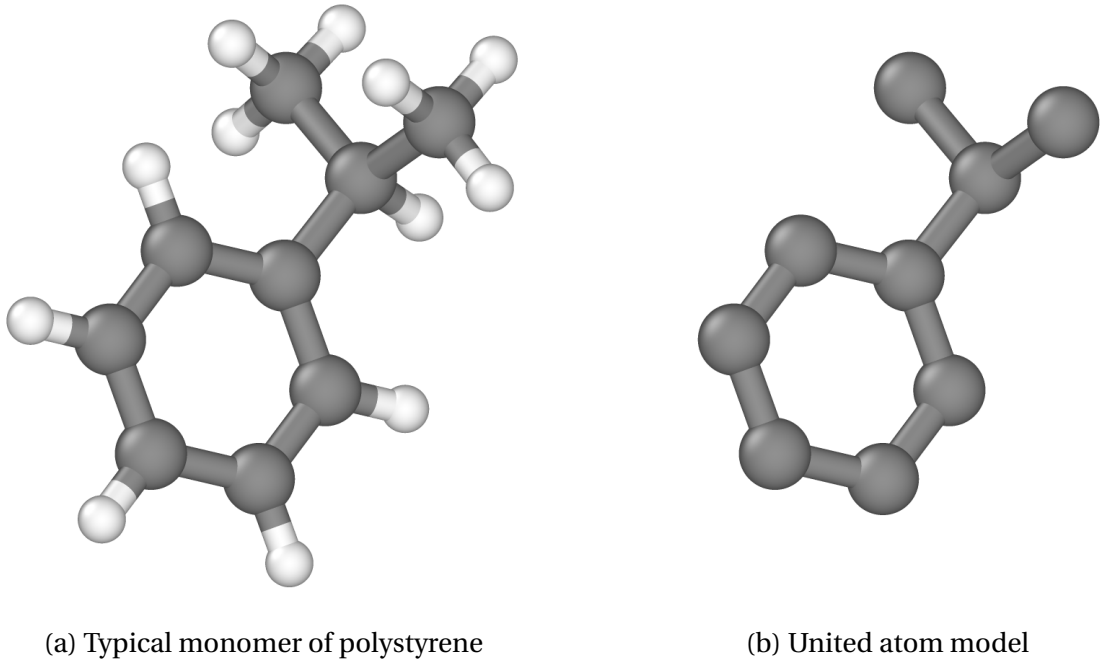


Figure 2.2: Monomer of polystyrene shown in a) Typical model with both C and H atoms, b) United atom model

$$\epsilon_{ij} = \sqrt{\epsilon_i \epsilon_j} \quad (2.7a)$$

$$\sigma_{ij} = \sqrt{\sigma_i \sigma_j} \quad (2.7b)$$

2.3.3 ZBL potential

Ziegler-Biersack-Littmark (ZBL) potential, first introduced by three researchers in 1985 (Ziegler and Biersack 1985), is commonly used in high energy particles or ions interacting with material surface. ZBL potential has the form of repulsive screened Coulomb potential for nuclei, as shown in Eq. 2.8:

$$E_{ij}^{ZBL} = \frac{1}{4\pi\epsilon_0} \frac{Z_i Z_j e^2}{r_{ij}} \phi(r_{ij}/a) + S(r_{ij}) \quad (2.8a)$$

$$a = \frac{0.46850}{Z_i^{0.23} + Z_j^{0.23}} \quad (2.8b)$$

$$\phi(x) = 0.18175e^{-3.19980x} + 0.50986e^{-0.94229x} + 0.28022e^{-0.40290x} + 0.02817e^{-0.20162x} \quad (2.8c)$$

$$S(r) = C \quad r < r_1 \\ S(r) = \frac{A}{3}(r - r_1)^3 + \frac{B}{4}(r - r_1)^4 + C \quad r_1 < r < r_c \quad (2.8d)$$

$$A = (-3E'(r_c) + (r_c - r_1)E''(r_c))/(r_c - r_1)^2 \\ B = (2E'(r_c) - (r_c - r_1)E''(r_c))/(r_c - r_1)^3 \\ C = -E(r_c) + \frac{1}{2}(r_c - r_1)E'(r_c) - \frac{1}{12}(r_c - r_1)^2 E''(r_c) \quad (2.8e)$$

where $e^2/(4\pi\epsilon_0 r_{ij})$ is the same term as in Coulomb potential for two charged particles, Z_i and Z_j are the atomic numbers (charge of the nuclei) of the two atoms, $S(r)$ is a switching function to smoothly transition the interatomic potential E_{ij}^{ZBL} and its first and second order derivatives to 0 between an inner and outer cutoff, and $\phi(r_{ij}/a)$ is the actual function that accounts for the screening effect characterized by the interatomic distance and the nuclear charges.

ZBL potential differentiates atoms only by their atomic numbers. It can be seen from Eq. 2.8 that no electronic charge term was included in ZBL potential, so ions and neutrals will be treated the same from an interatomic force standpoint. This can be justified by assuming that the incident ion will neutralize by Auger recombination prior to actually striking the surface. This assumption is consistent with published MD works (Graves and Brault 2009; Tinacba et al. 2019) in plasma etching.

2.3.4 ReaxFF potential

ReaxFF was first introduced by van Duin, Goddard and co-workers in 2001 (Van Duin et al. 2001). ReaxFF is a reactive force field which was designed with the ability to model chemical reactions as bonds break and form. Unlike the aforementioned potentials, the function form of ReaxFF also includes several connection-dependent terms, which makes it possible to directly describe bond breaking and forming in a relatively simple way. Specifically, ReaxFF uses the concept of bond order to model the chemical interactions in a classical MD system, where the bond order of an atom is empirically calculated using interatomic distances. Bond orders can be dynamically calculated for each individual atom during the simulation, therefore predefined reactive sites, usually used by some empirical potentials, are not needed and more accurate description of chemical reactions can be achieved. Similar to other interatomic potentials, ReaxFF assumes a set of general functions, which can be parameterized for different particles or interactions using validated quantum or experimental data. In particular, ReaxFF was designed with transferability across phases,

i.e., the same mathematical formalism will be used for an oxygen atom whether it is in gas phase as O₂, in liquid phase as in H₂O molecule, or in solid phase as in SiO₂ (Senftle et al. 2016). This transferability makes it more accurate and more convenient to model chemical reactions involving different phases such as the formation of SiO₂CF_x passivation layer when attaching bare amorphous SiO₂ surface with some CF_x gas molecules (radicals) in a plasma etching process. Overall, ReaxFF bridges the gap between empirical potentials and QM methods which improves the accuracy in describing chemical reactions without sacrificing too much computational performance.

The functional form of ReaxFF has been updated several times to increase the general compatibility. The most up-to-date form of ReaxFF and the detailed explanations can be found in the Supporting Information of Chenoweth et al. (2008). Here, an overview of different potential terms in a ReaxFF system will be covered and some of the key functional terms which make ReaxFF different from the aforementioned potentials will be addressed.

The overall system energy of a ReaxFF system is represented in Eq. 2.9 as

$$E_{\text{system}} = E_{\text{bond}} + E_{\text{lp}} + E_{\text{over}} + E_{\text{under}} + E_{\text{val}} + E_{\text{pen}} + E_{\text{coa}} + E_{\text{C2}} + E_{\text{triple}} \\ + E_{\text{tors}} + E_{\text{conj}} + E_{\text{H-bond}} + E_{\text{vdWaals}} + E_{\text{Coulomb}} \quad (2.9)$$

where the individual terms on the right hand side usually represent different physical interactions and the detailed explanations are listed below:

- E_{bond} : determine bond order and calculate bond energy; contributions from sigma bonds, pi bonds and double pi bonds are included and can be determined from the interatomic distance r_{ij}
- E_{lp} : determine the number of lone pairs around an atom; used to penalize the atoms with number of lone pairs deviated from the optimal number
- E_{over} : determine overcoordination energy; used as a penalty energy term imposed on those overcoordinated atoms
- E_{under} : determine undercoordination energy; used to include the energy contribution for the resonance of the π -electron between attached under-coordinated atoms
- E_{val} : determine valence angle energy; this term is similar to U_{angle} for determining equilibrium angle in bonded potentials such as TraPPE except the bond orders are also taken into account here

- E_{pen} : determine penalty energy for valence angle; used to reproduce stability in a system with valence angles in which two double bonds are sharing an centering atom
- E_{coa} : determine three-body conjugation term for valence angles; used to describe the stability of the $-\text{NO}_2$ -group
- E_{C_2} : determine energy correction for C_2 molecule; used specifically for C_2 molecule to fix an error within previous ReaxFF formalism where a very strong triple bond will be erroneously formed between two carbon atoms in a C_2 molecule
- E_{triple} : determine triple bond energy correction; used only for C-O bonded pairs to form the triple bond in carbon monoxide and make it stable
- E_{tors} : determine torsion angle energy; this term is similar to U_{torsion} for determining equilibrium torsional angle in bonded potentials such as TraPPE except the bond orders are also taken into account here
- E_{conj} : determine four-body conjugation term for torsion angles
- $E_{\text{H-bond}}$: determine the hydrogen bond term for a X-H—Z system which is also bond-order dependent
- E_{vdWaals} : determine the van der Waals interactions; a distance-corrected Morse potential was used
- E_{Coulomb} : determine the Coulomb interactions; a shielded Coulomb potential was used to account for orbital overlap between atoms at close distances

A schematic diagram of different energy terms in ReaxFF can also be found in Fig. 2.3, where the energy terms can mainly be categorized into bond-order dependent (blue color) and bond-order independent (orange color) groups.

As mentioned previously, one of the fundamental feature in ReaxFF which makes it capable of modeling chemical reactions more accurately is the use of bond order. The concept of bond order, first introduced by Linus Pauling, defines the number of electron pairs (covalent bonds) between two atoms. So for example, the C-C pair in molecule $\text{H}-\text{C} \equiv \text{C}-\text{H}$ has a bond order of 3 because of the triple bond, while the C-C pair in molecule $\text{H}_2-\text{C}=\text{C}-\text{H}_2$ has a bond order of 2 because of the double bond. In ReaxFF, bond order of a atom pair is determined by interatomic distance r_{ij} using an empirical equation presented in Eq. 2.10

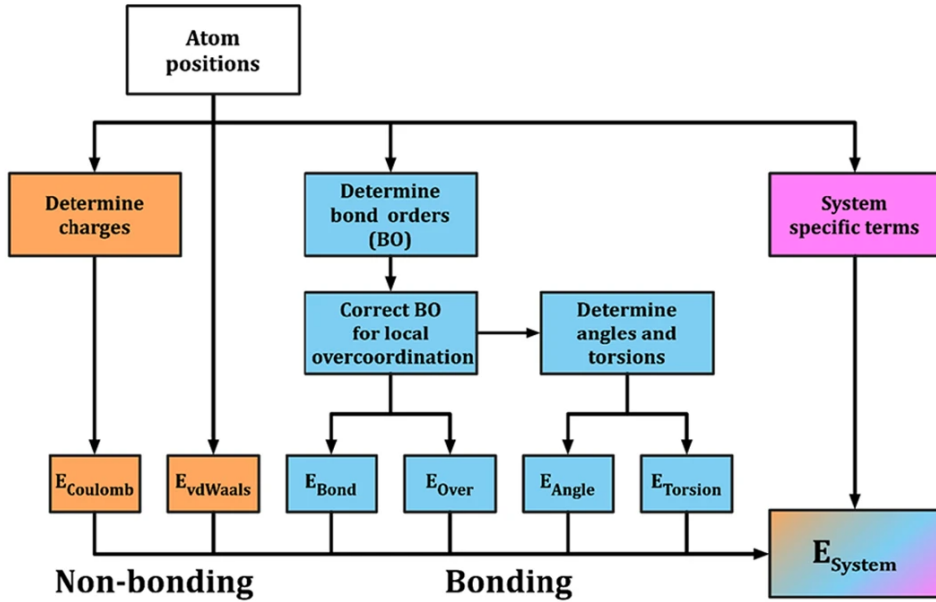


Figure 2.3: Summary of different energy terms in ReaxFF total energy equation in Eq. 2.9. (Figure taken from Senftle et al. (2016) and permission gained from Creative Commons Attribution 4.0 International License.)

$$\begin{aligned}
 BO'_{ij} &= BO_{ij}^{\sigma} + BO_{ij}^{\pi} + BO_{ij}^{\pi\pi} \\
 &= \exp\left[p_{bo,1} \cdot \left(\frac{r_{ij}}{r_o^{\sigma}}\right)^{p_{bo,2}}\right] + \exp\left[p_{bo,3} \cdot \left(\frac{r_{ij}}{r_o^{\pi}}\right)^{p_{bo,4}}\right] + \exp\left[p_{bo,5} \cdot \left(\frac{r_{ij}}{r_o^{\pi\pi}}\right)^{p_{bo,6}}\right]
 \end{aligned} \quad (2.10)$$

where the three exponential terms calculate the contributions from single (sigma bond), double (pi bond), and triple (double pi bond) bond respectively. The parameters $p_{bo,1-6}$ and $r_o^{\sigma, \pi, \pi\pi}$ are all fitting parameters which need to be specified for each element in a ReaxFF system. The bond order calculation of a C-C bond as a function of interatomic distance is presented in Fig. 2.4, where the bond starts to form at approximately 2.5 Å, reaches $BO'_{ij} = 1$ at around 1.5 Å for a single (sigma) bond, and eventually reaches $BO'_{ij} = 3$ for a triple bond such as in $\text{C}\equiv\text{C}$. The entire transition from a non-bonded interaction to a triple-bond interaction is smooth and continuous, and depends on all three bond types (sigma, pi, and double pi). The uncorrected bond order BO'_{ij} calculated from Eq. 2.10 need to be further corrected to obtain the corrected bond order BO_{ij} , which will then be used to calculate the bond energies as presented in Eq. 2.11

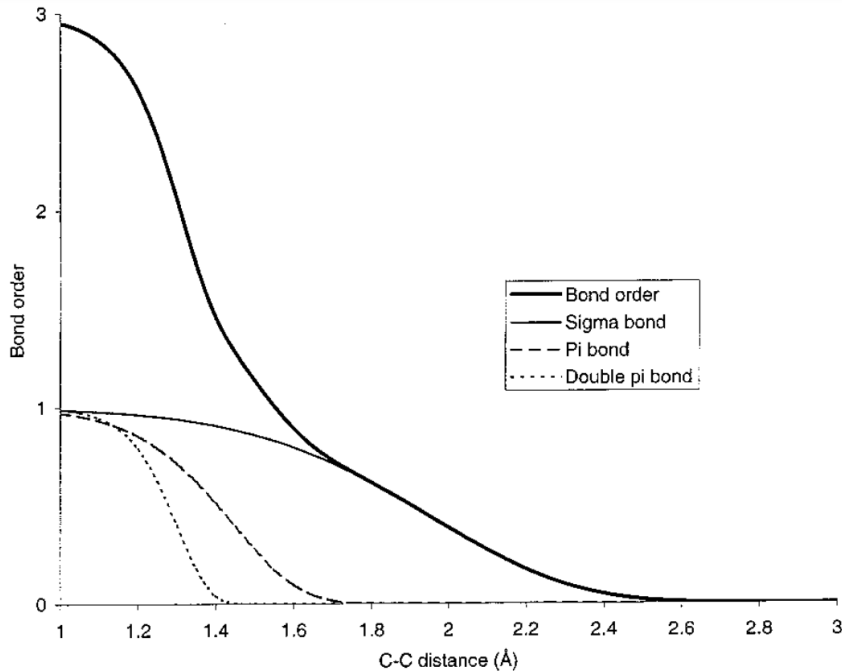


Figure 2.4: Bond order calculation (uncorrected) of a C-C bond as a function of interatomic distance. (Figure taken from Van Duin et al. (2001) and permission gained from American Chemical Society Publications.)

$$E_{bond} = -D_e^\sigma \cdot BO_{ij}^\sigma \cdot \exp\left[p_{be1}\left(1 - (BO_{ij}^\sigma)^{p_{be2}}\right)\right] - D_e^\pi \cdot BO_{ij}^\pi - D_e^{\pi\pi} \cdot BO_{ij}^{\pi\pi} \quad (2.11)$$

The corrected bond order BO_{ij} can also be used to calculate the corrected overcoordination Δ_i , as shown in Eq. 2.12

$$\Delta_i = -Val_i + \sum_{j=1}^{neighbours(i)} BO_{ij} \quad (2.12)$$

where Val_i is the number of bonding electrons atom i can have. So essentially corrected overcoordination Δ_i calculates the difference between the total bond order atom i currently has with its neighbouring atom(s) j and the number of bonding electrons atom i can optimally have. A positive value of Δ_i indicates atom i has formed more bonds than the maximum value, thus overcoordinated. An energy penalty term, E_{over} , is imposed on those overcoordinated atoms, as shown in

$$E_{\text{over}} = \frac{\sum_{j=1}^{nbond} p_{ovun1} \cdot D_e^\sigma \cdot BO_{ij}}{\Delta_i^{lpcorr} + Val_i} \cdot \Delta_i^{lpcorr} \cdot \left[\frac{1}{1 + \exp(p_{ovun2} \cdot \Delta_i^{lpcorr})} \right] \quad (2.13)$$

where D_e^σ and $p_{ovun1,2}$ are all fitting parameters, and Δ_i^{lpcorr} is used to take into account the effect of broken-up lone electron pair on overcoordination Δ_i . Undercoordination is also numerically addressed by calculating the undercoordination energy E_{under} .

Similarly, unlike the TraPPE potential using simple harmonic function forms, ReaxFF treats the angle and torsion interactions as bond order dependent, as shown in

$$E_{\text{val}} = f_7(BO_{ij}) \cdot f_7(BO_{jk}) \cdot f_8(\Delta_j) \cdot [p_{val1} - p_{val1} \exp(-p_{val2}(\Theta_o(BO) - \Theta_{ijk})^2)] \quad (2.14)$$

where $f_7(BO)$ and $f_8(\Delta)$ are bond order dependent functions for which the detailed definitions can be found in the Supporting Information of Chenoweth et al. (2008).

Overall, ReaxFF bridges the gap between empirical potentials and QM methods by improving the accuracy in describing chemical reactions. This improvement obviously comes with a price. As can be seen from previous definitions, the functional form of ReaxFF is much more complex than other non-reactive potentials. However, this sacrifice in computational cost is still acceptable as the modern computational resources are getting much more powerful.

CHAPTER

3

GLANCING-ANGLE SCATTERINGS

3.1 Abstract

In plasma etching for microelectronics fabrication, one of the objectives is to produce high aspect ratio (HAR) via and trench structures. A principal contributor to the HAR feature shape is the manner in which energetic ions interact with sidewalls inside the feature. The scattering angle and energy loss of ions reflecting from sidewalls determines the sidewall slope and can lead to defects such as microtrenching and bowing. Understanding how ions interact with sidewalls can improve our control of the critical dimensions of HAR features. Ions accelerated in the plasma sheath arrive in the feature with energies as large as a few keV and initially strike the sidewalls at glancing-angles. These scattering events extend to the photolithographic mask. Scattering from the mask at glancing angles can produce ions incident into the underlying feature with a broader angular distribution, leading to less desirable feature properties. In this work, results are discussed from Molecular Dynamics (MD) simulations of glancing-angle scattering of argon ions from three materials common to HAR etch: polystyrene (as a photoresist surrogate), amorphous carbon (a hard mask material) and SiO₂ (a common insulating material used in microelectronics devices). Results

from the simulations reveal a transition from specular scattering to diffuse scattering as the angle of the incident ion decreases (90 degrees being glancing incidence) and incident energy increases. Scattering from polystyrene is more diffuse compared to amorphous carbon and SiO₂ for identical incident ion conditions.

3.2 Materials preparation

In performing MD simulations, the material to be investigated must be prepared. This means that computational atoms composing the material (e.g., Si and O atoms for SiO₂) must be arranged in a manner that produces the desired stoichiometry and topology (e.g., crystalline vs amorphous, defect free or with defects). In this section, the methods and procedures for computationally preparing the materials and performing ions scattering simulations are discussed.

Amorphous SiO₂ was prepared using a quenching procedure (Munetoh et al. 2007). A system of 1000 Si atoms and 2000 O atoms were randomly distributed in a (35.1 Å)³ cubic box corresponding to a density of 2.307 g/cm³. Before quenching, the system was heated to 5000 K using an NPT (isothermal-isobaric) ensemble at 0 pressure for a total of 300 ps using the Nose-Hoover thermostat and barostat (Evans and Holian 1985; Nose 1990; Martyna et al. 1994). The NPT ensemble is a concept in statistical mechanics which describes a system where the number of particles(N), the pressure(P) and the temperature(T) of the system are kept constant. The temperature and pressure of the simulation cell are constrained by adjusting particle velocities and domain dimensions respectively. After the system was thermodynamically equilibrated, it was quenched to 300 K with a cooling rate of 1 K/ps. The system was then relaxed in an NPT ensemble to enable the system to freely expand or shrink, reducing both the internal stresses and energies. The final state of amorphous SiO₂, when the thermodynamic parameters have reached a steady state condition, is shown in Fig. 3.1. The simulations were performed with periodic boundary conditions using an integration time step of 1 fs. For SiO₂, we used the interatomic potential developed by Munetoh et al. (2007), which is a Tersoff potential parameterized specifically for Si-O system.

For AC, the simulation cell was prepared following the procedure used in a previous work (Wang and Komvopoulos 2020) by growing an AC layer. The AC growth was simulated with a carbon deposition procedure on a 23 × 23 × 59.7 Å³ silicon(100) crystal substrate. With a lattice constant of 5.4307 Å, a Si substrate structure was first simulated using 1584 Si atoms. The substrate was equilibrated at 300 K in an NVT (canonical, same as the NPT ensemble

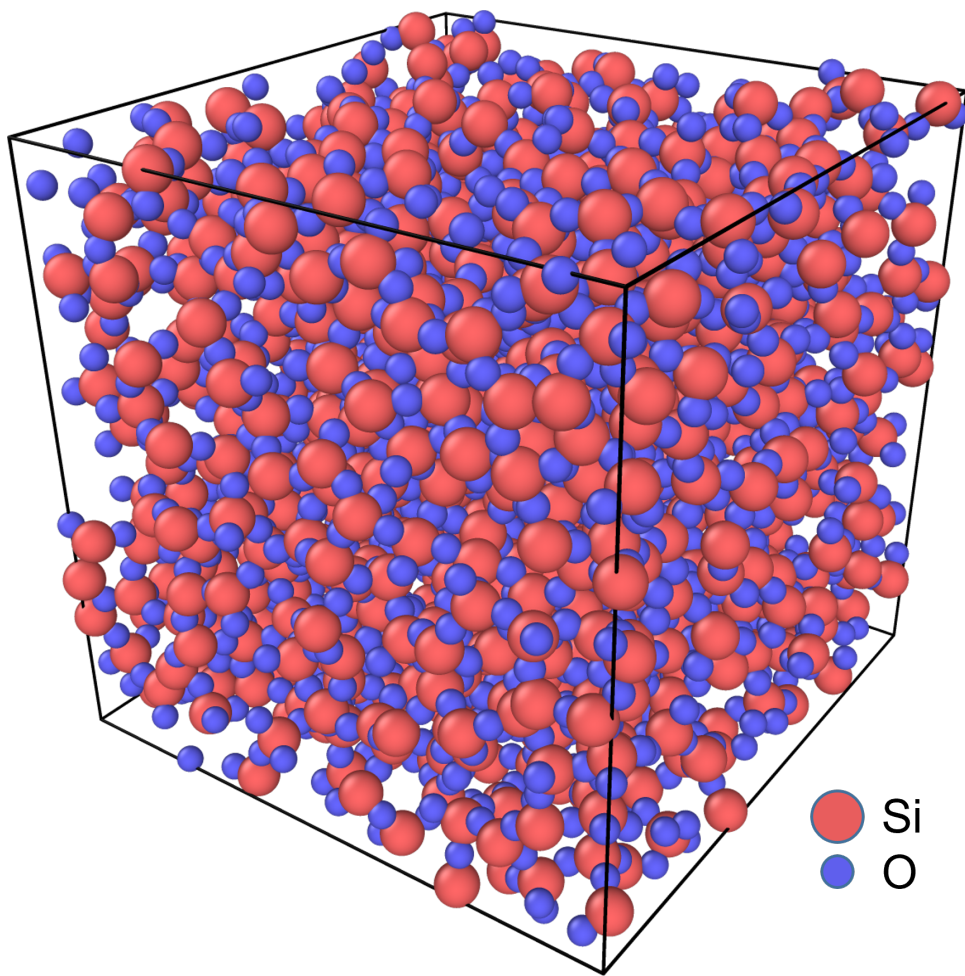


Figure 3.1: Equilibrated state of amorphous SiO_2 at 300 K, the final size of the simulation box is $(35.18 \text{ \AA})^3$, corresponding to a density of 2.288 g/cm^3 .

except volume(V) is kept constant instead of pressure(P)) ensemble for 30 ps. Following equilibration, 2000 carbon atoms were deposited randomly and sequentially on top of the silicon substrate surface. C atoms were directed onto the surface at normal incidence with an energy of 1 eV. During the deposition the substrate was maintained at 300 K using a time step of 0.5 fs in an NVT ensemble. The time interval between launching C atoms was 2 ps to allow the substrate to fully relax after the previous atom interacted with the substrate. The sequential deposition of C atoms is shown in Fig. 3.2. To simulate a semi-infinite large substrate, periodic boundary conditions were enforced along the lateral directions while the bottom two layers of silicon atoms were fixed. The interatomic potential used in this Si-C system was developed by Erhart and Albe (2005), which is a Tersoff parameterized specifically for silicon, carbon, and silicon carbide system.

PS is somewhat more complex to model. The Transferable Potentials for Phase Equilibria-United Atom (TraPPE) force field (Wick et al. 2000) was used to describe this hydrocarbon polymer. The values of parameters in TraPPE force field used in this work were taken from [Srivastava (2010); Harmandaris et al. (2006)]. Due to limitations in LAMMPS, a harmonic bond potential (Han and Boyd 1996) was used in place of fixed-length bonds as used in the original work (Wick et al. 2000). With TraPPE force fields, bonds, angles and dihedrals interactions are explicitly defined. The carbon atoms are connected to the neighboring hydrogen atoms to form macro-atoms as shown in Fig. 3.3. The system was constructed with 10 chains of PS with each chain containing 40 monomers so that the molecular weight of the polymer chain is consistent with commercial photoresists and published results (Vegh et al. 2007; Kim et al. 2018; Srivastava 2010; Harmandaris et al. 2006).

The chains were randomly placed and oriented in a box with periodic boundary conditions with the help of an online polymer builder (Haley et al. 2010). The initial structure of PS is shown in Fig. 3.4a, where the chains were colored separately and the structure was unwrapped at the periodic boundaries for better illustration. Several post-processing steps were needed to properly define the united-atom model and the topology required by TraPPE force field. The initial size of the simulation box was $(51.7 \text{ \AA})^3$ (51.7 \AA on a side) which corresponds to a density of $\sim 0.5 \text{ g/cm}^3$. The system was then heated to 600 K using an NPT ensemble at atmosphere pressure, maintaining temperature and pressure for 4 ns using a timestep of 2 fs. After equilibration, the system was steadily cooled to 300 K and further equilibrated for 2 ns. The final system was stable and denser than prior to equilibration with a density closely matching typical PS ($\sim 1.0 \text{ g/cm}^3$). The final state of the polymer system is shown in Fig. 3.4b.

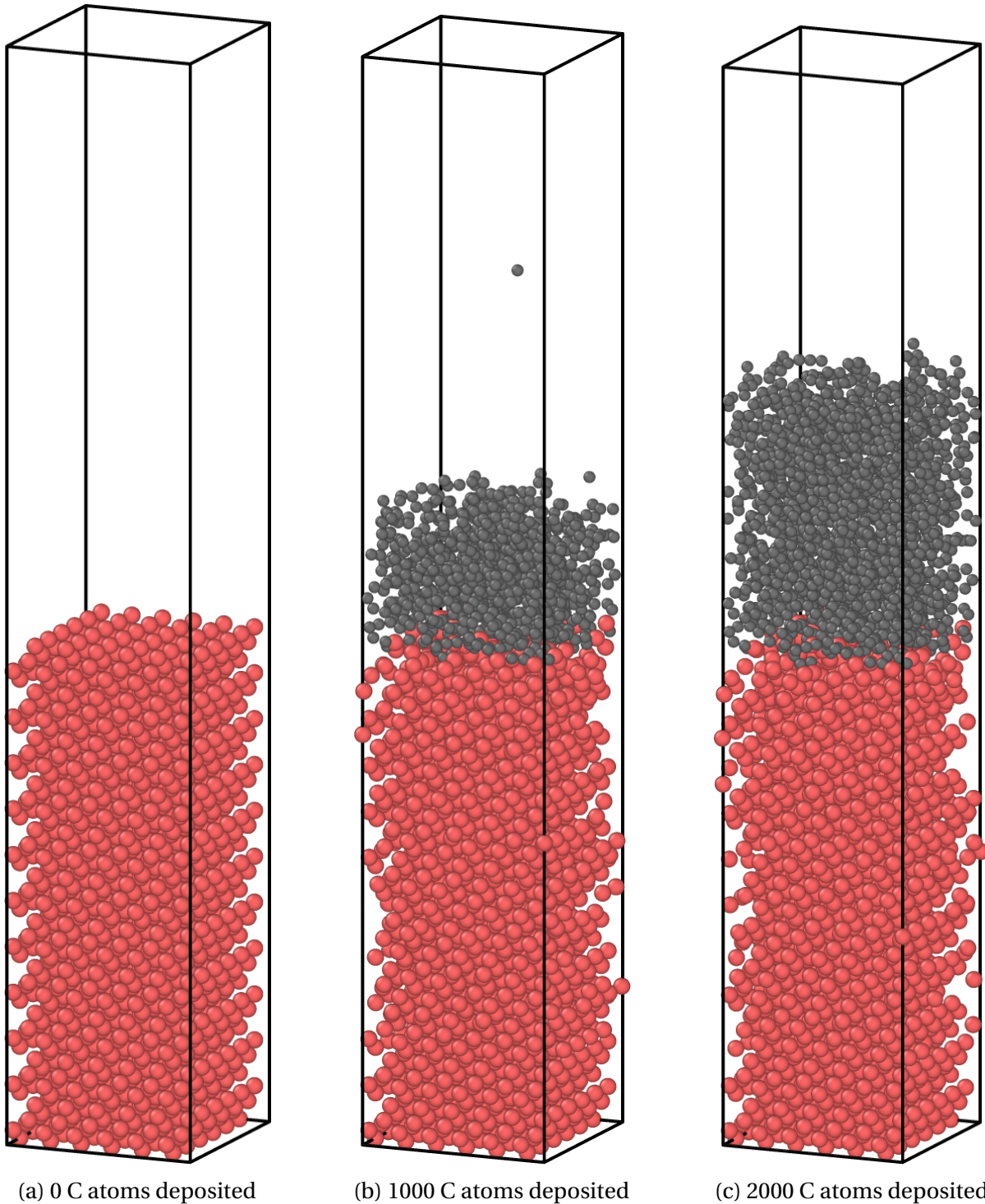


Figure 3.2: Examples of C atoms deposited on a Si substrate a) initial Si substrate, b) 1000 C deposited and c) 2000 deposited. The computational domain is $23 \times 23 \times 120 \text{ \AA}^3$.

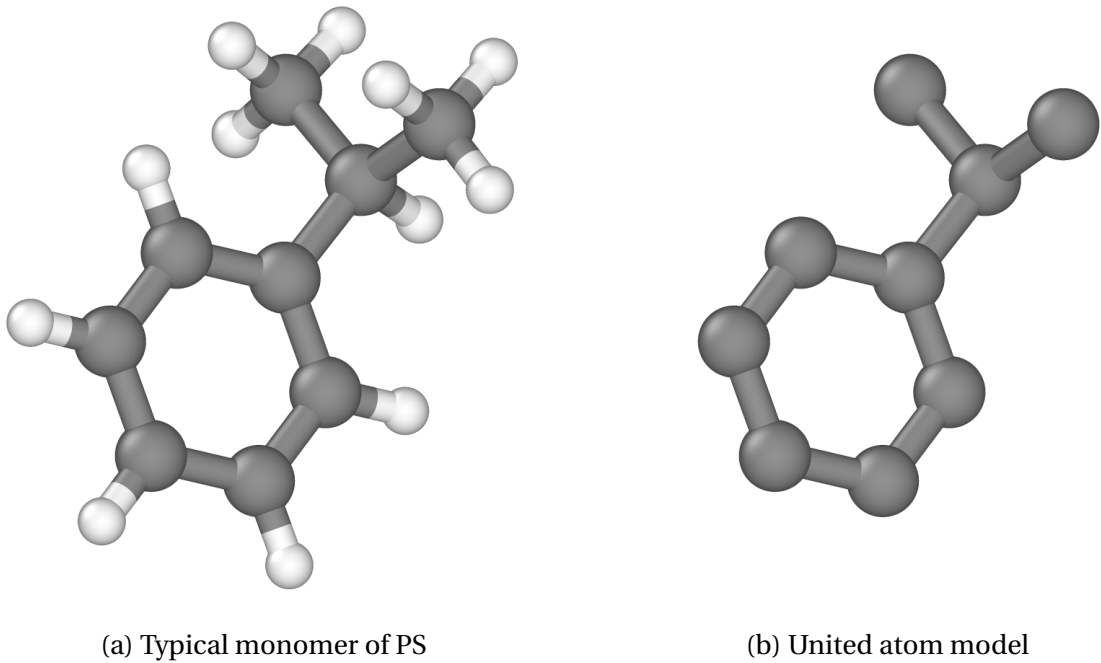


Figure 3.3: Monomer of PS shown in a) Typical model with both C and H atoms, b) United atom model

3.3 Ions scattering

After producing the three etching-layer structures for SiO_2 , PS and AC, ion scattering was simulated from the top surface of each material, as shown schematically in Fig. 3.5. Ions with energy E_{in} were incident on the surface of the MD generated structure at an angle of incidence θ_{in} defined as the angle between the surface normal and incident ion velocity vector. The exit energy E_{out} and exit angle θ_{out} for the scattered ions were recorded. Some modifications to the computational domain were also made to facilitate these scattering simulations. The boundary condition in the z (vertical) direction was changed from periodic to finite to allow reflected ions to leave the simulation domain. The boundary conditions in the x and y directions (horizontal) were kept periodic. A thin layer was removed from the top of the material to smooth the surface. The atomic positions in the bottom layers of the simulation cell ($\sim 20\%$ of the total volume) were fixed to simulate a semi-infinite large substrate. A final equilibration step was then performed to ensure that the simulation cell was stable. The equilibrated structures used for ion scattering are shown in Fig. 3.6.

This study focuses primarily on physical ion interactions more so than reactive sur-

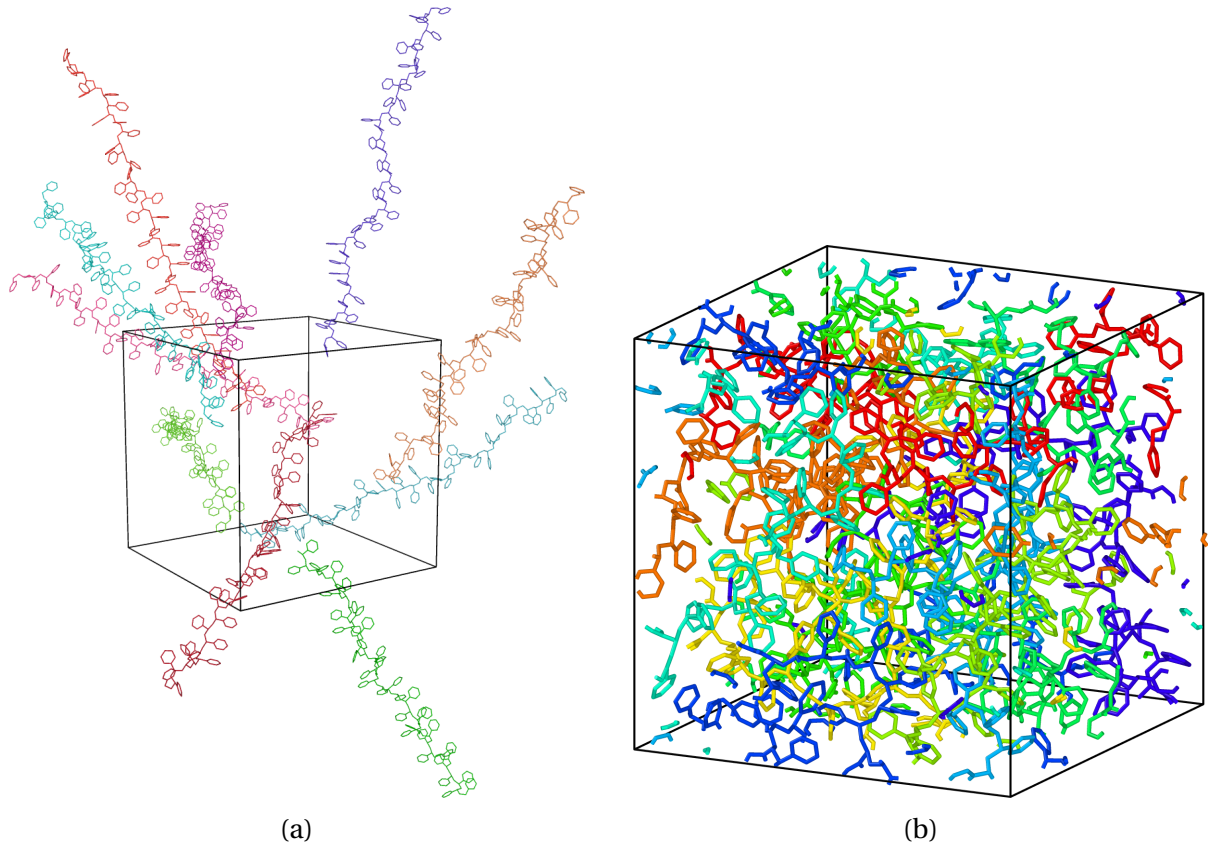


Figure 3.4: Structure of PS with 10 chains each containing 40 monomers. (a) Initial structure, unwrapped at the periodic boundaries (b) Equilibrated state at 300 K. The chains are colored separately.

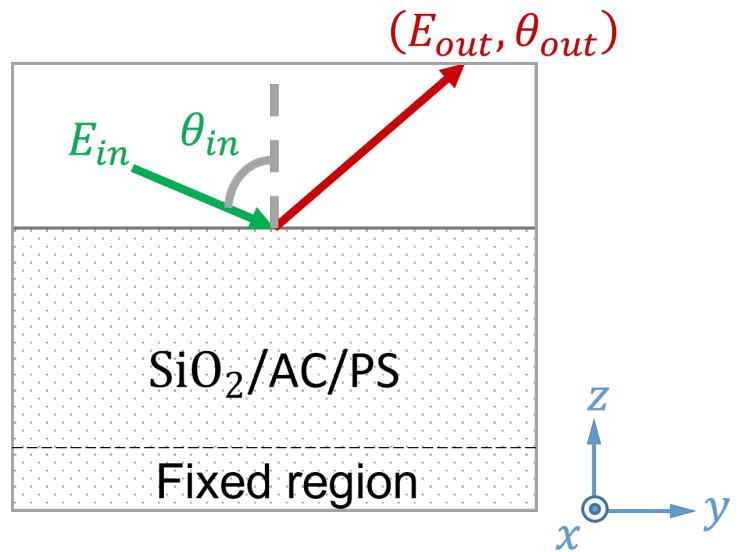


Figure 3.5: Schematic showing the ion scattering geometry.

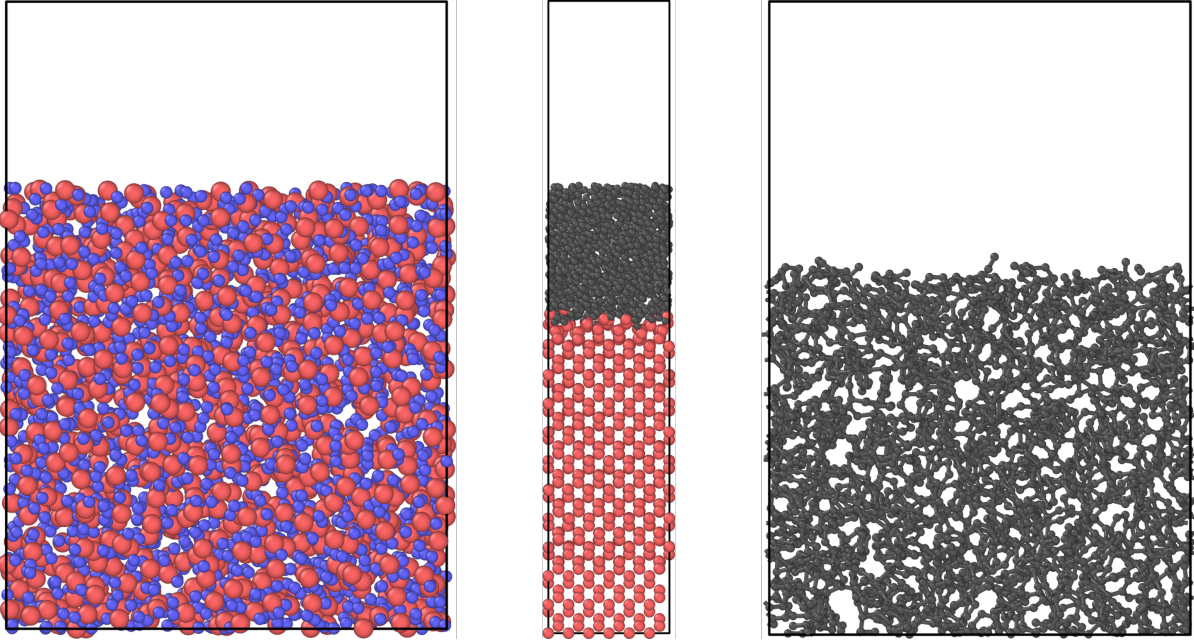


Figure 3.6: Front view of the simulation cells prior to ions scattering: (left) SiO_2 with width 35.18 Å, (middle) AC with width 23 Å and (right) PS with width 40.27 Å.

face modifications that would be more impacted by ion selection, particularly a reactive species such as chlorine. Thus, singly ionized argon ions were used to investigate glancing-angle scattering. The Ziegler-Biersack-Littmark (ZBL) screened nuclear repulsion potential (Ziegler and Biersack 1985) was used to describe the interaction between the argon ions and the target atoms (Ar-Si, Ar-O, Ar-C). The ZBL potential has been widely used in ion induced modification of materials and is commonly combined with other interatomic potentials such as EAM, SW and Tersoff (Kammara et al. 2016; Sycheva et al. 2018; Prskalo et al. 2010). The ZBL potential between two particles i and j is given by

$$E_{ij}^{ZBL} = \frac{1}{4\pi\epsilon_0} \frac{Z_i Z_j e^2}{r_{ij}} \phi(r_{ij}/a) + S(r_{ij}) \quad (3.1)$$

where ϵ_0 is the permittivity of vacuum, Z_i and Z_j are the atomic numbers, e is the elementary charge, r_{ij} is the interatomic distance, ϕ is a screening parameter defined by a scale length a , and $S(r_{ij})$ is a switching function for smoothly transitioning the whole function to 0 after the cutoff distance. For PS, the total atomic number of each macro-atom is used in the ZBL potential. It can be seen from Eq. 3.1 that no electronic charge term was included in ZBL potential, so ions and neutrals will be treated the same from an interatomic force standpoint. This can be justified by assuming that the incident ion will neutralize by

Auger recombination prior to actually striking the surface. This assumption is consistent with published MD works (Graves and Brault 2009; Tinacba et al. 2019) in plasma etching.

Ions are introduced at random (x, y) positions along a plane parallel to the surface at a distance that exceeds the cutoff of the ZBL potential. 2000 Ar ions are directed towards the surface for each incident energy E_{in} and angle, θ_{in} . The target material was allowed to equilibrate between collisions. To minimize the effect of cumulative damage to the surface, the target configuration was reset to its initial state after every 10 collisions. In a typical plasma etching process, the surface conditions will be affected by several surface processes such as chemical etch, polymer deposition, roughening, striations, mask reticulation, etc. In this work, we chose to focus on pristine surfaces to generate ions scattering data relatively independently. The results from this work could be further incorporated in the future into profile simulators where the surface damage effect has been included. The energy and angle of each scattered ion (E_{out} and θ_{out}) were recorded after the scattered ion leaves the simulation domain.

The parametric study consisted of θ_{in} ranging from 65° to 89° (every 2°) and E_{in} ranging from 10 eV to 5000 eV, using 10 energies evenly spread on a log scale for E_{in} . The results from each individual ($E_{\text{in}}, \theta_{\text{in}}$) were then used to construct a two-dimensional distribution of ($E_{\text{out}}, \theta_{\text{out}}$).

3.4 Validation of the materials properties

In this section, the methods for validating the prepared target materials are discussed. The structural and thermodynamic properties were validated with those from previous studies and comparison to published experimental data. Overall, the current results show good agreement with the published data.

The structures for SiO₂, AC, and PS were validated using the radial distribution function (RDF). For SiO₂, the amorphous structure was benchmarked against previous simulation data (Munetoh et al. 2007) using classical MD, as well as with experiment data (Johnson et al. 1983) obtained from neutron scattering, as shown in Fig. 3.7. The location of the first two major peaks in the RDF, corresponding to the Si-O and O-O separation distances, respectively, in a [SiO₄] tetrahedral structure, match the two reference results. The second peak in the simulations shows a split, which is a signature of a disordered structure. The location of the third and fourth peaks also agree with nearly the same magnitude. The partial RDFs (not shown) also have good agreement with the reference results (Munetoh

et al. 2007). The density calculated from the simulations is 2.288 g/cm^3 , which is close to the experimental value of 2.203 g/cm^3 . Overall, the interatomic potential used in the simulation is able to predict the amorphous state of silica well.

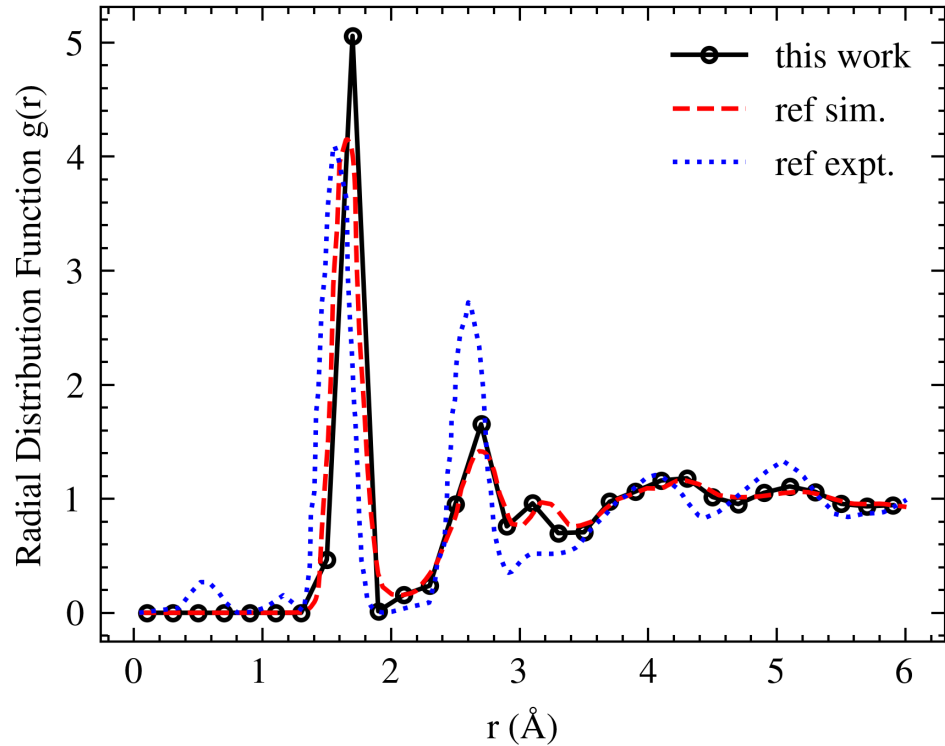


Figure 3.7: Radial distribution function $g(r)$ for SiO_2 glass (this work, simulation results from [Munetoh et al. (2007)] and experimental data from [Johnson et al. (1983)]).

Similarly, the RDF was used for validating the properties of AC. As shown in Fig. 3.8, the RDF of the simulated structure agrees well with that from previous ab initio MD results (Bhattarai and Drabold 2017), as well as with experiment data from electron-microscopy. Both the peak locations and the overall shape of the RDF are in reasonable agreement with the reference results. The first and second peaks are sharper in the simulations while they are more diffuse in the experiments. The simulated results are in better agreement with the ab initio MD data. Note that the simulated density of 2.25 g/cm^3 is larger than the experimental value 1.55 g/cm^3 . It is known that carbon atoms can form numerous atomic structures with densities ranging from below 1 g/cm^3 to above 3 g/cm^3 . Previous research(McCulloch et al. 2000) showed that although the density of AC does not affect the

shape of the RDF significantly, the locations of the RDF peaks shift slightly to the right with increasing density.

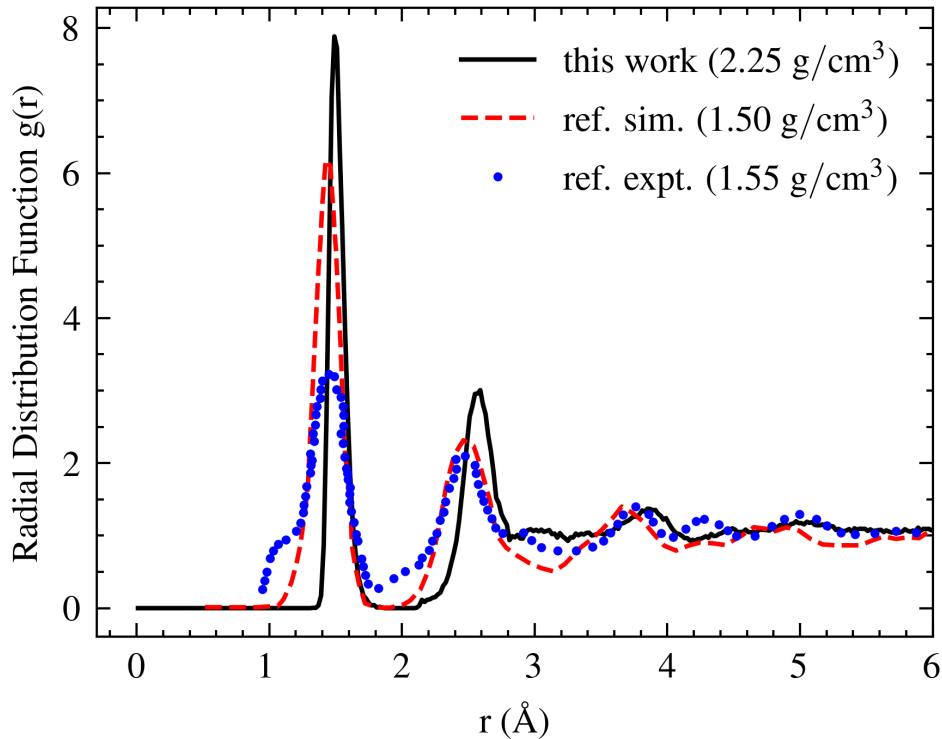


Figure 3.8: Radial distribution function $g(r)$ for AC (this work, simulation results from [Bhattarai and Drabold (2017)] and experimental data from [O’Malley et al. (1998)]).

In addition to the RDF, the fraction of carbon atoms with sp^3 hybridization was also evaluated for validation. The sp^3 fraction is generally positively correlated to the density of the system. In one study (McCulloch et al. 2000), it was reported that a density of $2.0\text{ g}/\text{cm}^3$ corresponds to a sp^3 fraction of 6.4% while a density of $2.6\text{ g}/\text{cm}^3$ corresponds to 43.2%. The estimated sp^3 fraction of 13.3% with a density of $2.25\text{ g}/\text{cm}^3$ obtained from current work is consistent with these previous estimates. In another study, (Bhattarai and Drabold 2017) a lower density (below $1.6\text{ g}/\text{cm}^3$) was shown to correspond to less than 10% sp^3 fraction. This estimate is also in agreement with the data obtained in this work.

For PS, additional validation was performed due to the more complex structure of the polymer. A parametric study of temperature, ranging from 300 K to 800 K with a step of 50 K, was conducted using an NPT ensemble, and the density, dimensions and diffusion constant

of the system were calculated. The density of the PS and the length of the periodic simulation box are plotted as a function of temperature in Fig. 3.9a. A typical experimental value for the density of PS is 1.05 g/cm^3 at room temperature – and results from the simulations agree with this value. The computed linear thermal expansion coefficient is

$$\alpha_L = \frac{1}{L} \frac{\mathrm{d}L}{\mathrm{d}T} \quad (3.2)$$

where L is the length of the simulation box and T is the temperature. Results from the model produce $\alpha_L = 270 \times 10^{-6} \text{ K}^{-1}$ while typical experimental measurements(Inc. 2021) have a range of $(30 \sim 210) \times 10^{-6} \text{ K}^{-1}$, indicating that the simulated PS is softer. The diffusion constant is plotted as a function of reciprocal temperature on a semi-log plot in Fig. 3.9b, which is intended to show an Arrhenius relationship. An Arrhenius relationship describes the temperature dependence of a transport coefficient or rate constant, k , in terms of an activation energy, E_a , as follows

$$k = A \exp\left(-\frac{E_a}{RT}\right) \quad (3.3)$$

where R is the universal gas constant, T is the temperature and A is a constant. The derived diffusion coefficient is shown in Fig. 3.9b indicates a single activation energy (straight line) and diffusion is a simple linear process. The simulated RDF for PS is compared with previous MD simulation results (Srivastava 2010) using the same TraPPE united-atom model in Fig. 3.9c. Both the overall shape and the positions of the peaks obtained from these simulations match previous results.

The glass transition temperature T_g for PS was also measured. The procedures used was followed from Lyulin and Michels (2002). The system was first heated to 600K and kept stable for 5ns. Then it was steadily cooled down to 100K with a cooling rate of 50K/ns. The specific volume was measured as a function of temperature for the entire cooling step, see Fig. 3.10. Two linear fittings were then performed to the lower part (100K 300K) and the higher part(450K 600K) of the data respectively. And the intersecting point was then measured, which is supposed to be T_g . The result gives T_g of 370.8K, which matches the simulation data ($\approx 370 \text{ K}$) and experimental measurements($\approx 100 \text{ }^\circ\text{C}$) very well.

Cell size tests were also performed for all the MD systems described in this work. The total number of atoms for SiO_2 was varied from 3000 to 10000 while keeping the same Si:O ratio. For AC, the horizontal dimension of the crystalline silicon and the number of deposited carbon atoms were scaled up with the same ratio (from 1.0 to 2.0). The number

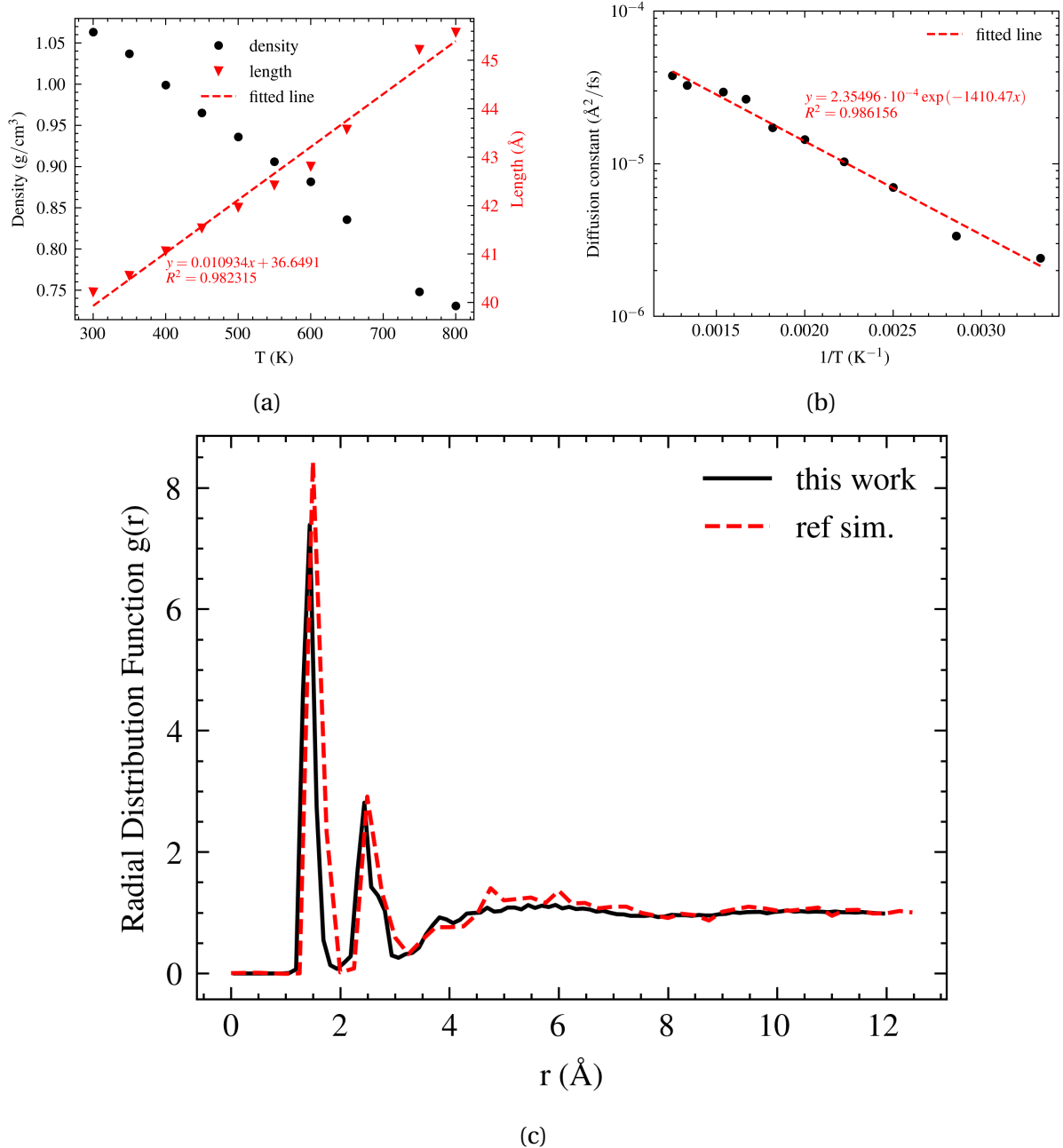


Figure 3.9: Structural and thermodynamic studies of PS: (a) Density and length (of simulation box) as a function of temperature; (b) Diffusion constant as a function of temperature reciprocal in semi-log plot; (c) Radial distribution function $g(r)$ (this work and simulation results from [(Srivastava 2010)]).

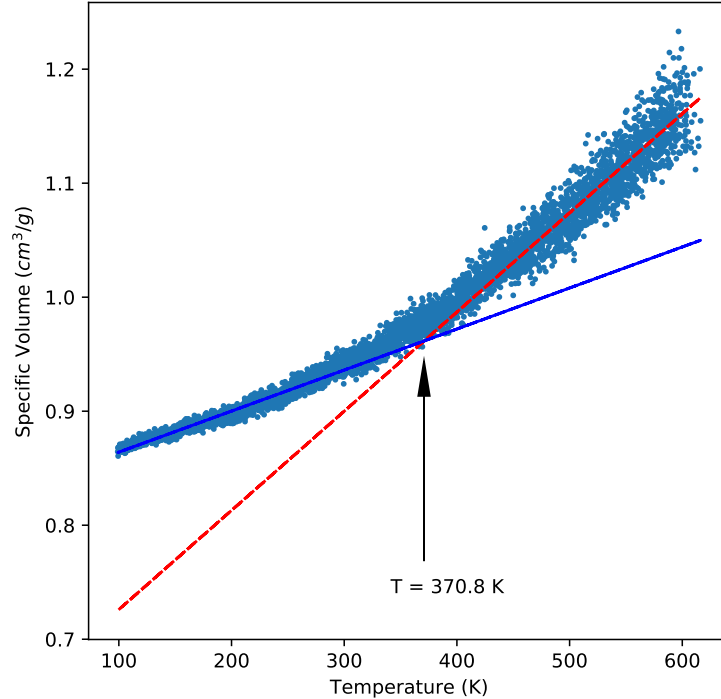


Figure 3.10: Specific volume as a function of temperature for PS, where the intersecting point of linear fittings gives glass transition temperature T_g .

of chains for PS was also varied from 10 to 20. The size of the simulation box was adjusted accordingly. The results show that the RDFs are invariant with respect to system sizes over the range investigated, see Fig. 3.11, indicating that the chosen system sizes for all the three materials were adequate for generating accurate MD results.

3.5 Angular distribution of ion scattering

In this section, results from the simulations for glancing-angle scattering of argon ions from PS, AC and SiO_2 are discussed. A parametric study of incident angle θ_{in} (75° to 89°) and incident energy E_{in} (10 to 5000 eV) was conducted. The after scattering probability distribution $f_{E_{\text{in}}, \theta_{\text{in}}}(E_{\text{out}}, \theta_{\text{out}})$ for angle θ_{out} and energy E_{out} were collected on a grid of 20×20 equal-size bins in a range of $[0, 90^\circ] \times [0, E_{\text{in}}]$. $f_{E_{\text{in}}, \theta_{\text{in}}}(E_{\text{out}}, \theta_{\text{out}})$ was normalized so that the probability distributions integrate to unity. These $f_{E_{\text{in}}, \theta_{\text{in}}}(E_{\text{out}}, \theta_{\text{out}})$ are shown in Fig. 3.12 for a constant incident energy $E_{\text{in}} = 316$ eV at $\theta_{\text{in}} = 75^\circ, 79^\circ, 85^\circ, 89^\circ$ (left to right) for SiO_2 , AC and PS (top to bottom). Results are also shown for constant incident angle $\theta_{\text{in}} = 79^\circ$ at $E_{\text{in}} = 20, 79, 316, 1257$ eV (left to right) for SiO_2 , AC and PS (top to bottom).

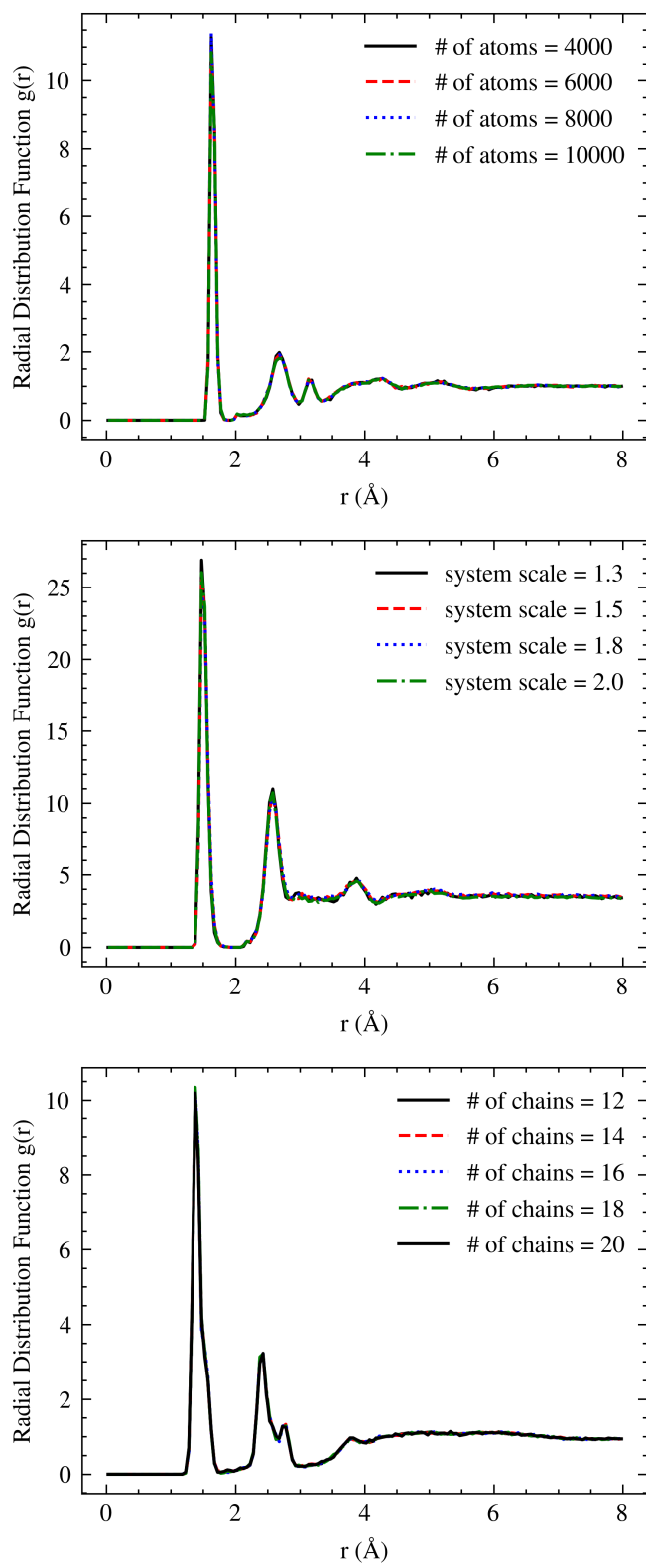


Figure 3.11: Invariant RDFs for SiO_2 , AC and PS (top to bottom) in cell size tests.

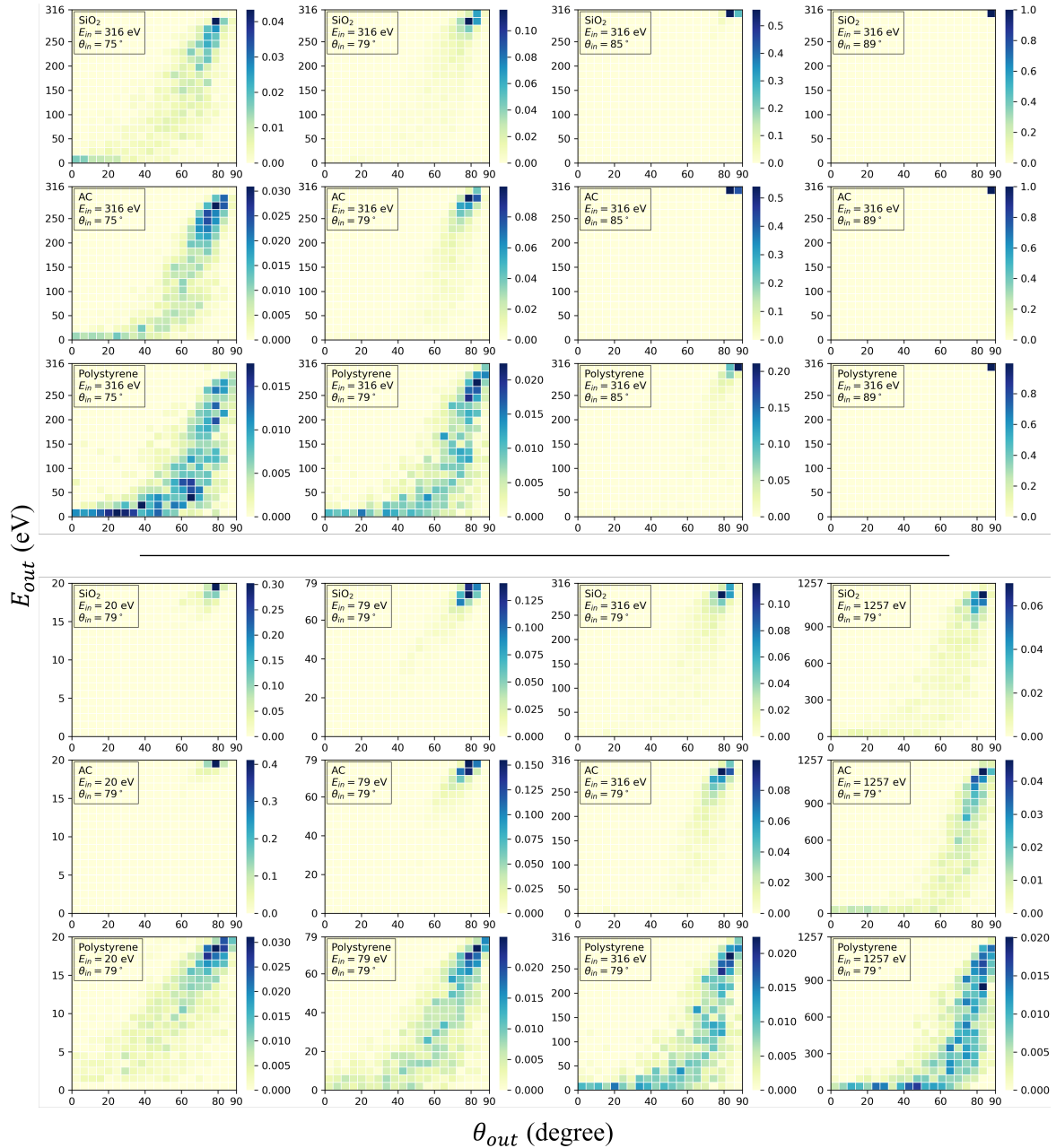


Figure 3.12: Comparison of $f_{E_{in}, \theta_{in}}(E_{out}, \theta_{out})$ for different materials, incident energies and incident angles (**x axis** → θ_{out} , **y axis** → E_{out} , **color scale** → magnitude), presented in matrix form: (**Upper matrix**) Constant incident energy $E_{in} = 316 \text{ eV}$ at $\theta_{in} = 75^\circ, 79^\circ, 85^\circ, 89^\circ$ (left to right) for SiO_2 , AC and PS (top to bottom) (**Lower matrix**) Constant incident angle $\theta_{in} = 79^\circ$ at $E_{in} = 20, 79, 316, 1257 \text{ eV}$ (left to right) for SiO_2 , AC and PS (top to bottom).

The distributions $f_{E_{\text{in}}, \theta_{\text{in}}}(E_{\text{out}}, \theta_{\text{out}})$ generally peak at the position of $(E_{\text{in}}, \theta_{\text{in}})$, and extend to the lower right half of the domain, which shows a transition from specular, elastic reflection to diffuse reflection with a commensurate loss in energy. The scattering is more specular for larger values of θ_{in} and lower values of E_{in} ; and more diffusive otherwise. A low-energy tail in the after scattering distribution occurs in highly diffusive cases, especially for PS. This is because in such cases the close-to-normal scattering with high incident energy results in large fraction of ions penetrating the material and then exiting the material after many collisions and scattering events, resulting in substantial energy loss compared to E_{in} .

The distributions $f_{E_{\text{in}}, \theta_{\text{in}}}(E_{\text{out}}, \theta_{\text{out}})$ shown in Fig. 3.12 can be summarized by their first and second moments as a function of incident ion parameters. The fractional retained energy of the scattered ions as a function of E_{in} and θ_{in} is shown in Fig. 3.13. The solid lines are the 50% quantile (median) of normalized E_{out} with the shaded areas extending from the 25% quantile to the 75% quantile. The incident energy is mostly retained for ions having larger values of θ_{in} and lower values of E_{in} . For example, for $\theta_{\text{in}} = 89^\circ$, the incident energy was nearly 100% retained for all materials across the incident energy range. For incident ions at $\theta_{\text{in}} = 75^\circ$ and $E_{\text{in}} > 1000$ eV, more than 50% of the ions lost at least half of their incident energy regardless of the material. In some generally more diffuse cases, the fractional retained energies seem to have minimum values as a function of E_{in} . One possible explanation is that it is expected to see more surface damage in such cases even after a few ion incidences, which could affect the scattering distributions. Another possible reason is that the span of the incident energy for the last few data points is much wider and the number of collected reflected ions is much smaller in such cases, which could lead to overall significant statistical errors.

There is material dependence on the scattering distributions, particularly for PS compared to AC and SiO₂. The scattering distributions $f_{E_{\text{in}}, \theta_{\text{in}}}(E_{\text{out}}, \theta_{\text{out}})$ are more diffuse for PS compared to either SiO₂ or AC. This can be explained by estimating the total interatomic force an incident ion will experience as well as the structural uniformity for different materials. The ZBL potential was used to describe the interatomic forces between Ar ions and the target atoms. The ZBL potential differentiates atoms only by their atomic numbers (see Eq. 3.1). SiO₂ and AC have similar amorphous structure, and the number density of SiO₂ (0.0689 \AA^{-3}) is 50% lower than AC (0.1133 \AA^{-3}), while the atomic numbers of Si(14) and O(8) atoms are higher than for C(6) atoms. Thus, it is expected to see the same level of interatomic forces being experienced by the ions when interacting with those two materials, therefore giving similar scattering results. The structure of PS contains multiple molecular chains, producing a structure less uniform and more anisotropic compared to

the amorphous structure for SiO_2 and AC. This nonuniformity affects the surface roughness at an atomic level and makes the scatterings significantly more diffuse.

The rate of reflection was also investigated as a function of E_{in} and θ_{in} , with the results shown in Fig. 3.14. The rate of reflection was estimated by the total number of the ions leaving the simulation box through the top boundary. The remaining ions were either embedded into the material, or the ions slowed due such a degree that they did not leave the simulation domain within the simulation time (~ 5 ps for the last incident ion). These slow ions typically have energies below the thresholds for etching. The rate of reflection follows the transition from specular, elastic reflection to diffuse reflection. Those ions with larger values of θ_{in} (more parallel to the surface) and lower values of E_{in} are more likely to be reflected. This suggests that for an ion interacting with a surface at these glancing angles, the transition from specular to diffuse reflection is related to the number of target atoms the ion collides with. For ions with higher incident energy and lower incident angle, the depth into the material that the ion can penetrate is larger and the number of target atoms the ions can interact with increases. These interactions are cumulative resulting in greater energy loss and deviation from the angle of incidence. For the same incident ($E_{\text{in}}, \theta_{\text{in}}$), more ions are embedded into PS than SiO_2 and AC, which is consistent with PS(1.05 g/cm³) having a lower mass density than SiO_2 (2.288 g/cm³) and AC(2.25 g/cm³).

These results were compared with published data (Helmer and Graves 1998; Abrams and Graves 1998) by D. B. Graves et al. They have performed MD simulations of Ar^+ and Cl^+ impacting onto Si and SiO_2 surfaces, with incident energies below 200 eV and with a wide range of incident angle. Apart from the incident energy, there are differences between their work and our simulations. First, their SiO_2 was initially crystalline, with ion bombardment being used to increase roughness. In this work, we used amorphous SiO_2 with the top surface being smoothed prior to ion scattering. Second, Graves et al. simulated scattering of 300-800 ions while retaining the material damage during the scattering process. In this work, the material was restored to its initial smooth state after every 10 incidence ions, which was intended to reduce the effect of material damage induced by high energy ions. Therefore, it is expected to see more specular scattering for the same incident conditions in this work than in the results of Graves et al. Qualitatively, the shape of the distribution $f_{E_{\text{in}}, \theta_{\text{in}}}(E_{\text{out}}, \theta_{\text{out}})$ for θ_{in} of 75° and 85° with E_{in} below 200 eV, and the transition from diffuse to specular scattering when increasing θ_{in} , are consistent with Graves et al. The reflection rates in their work for θ_{in} of 75° and 85° and E_{in} of 100 eV are about 0.8 and 1.0 respectively, which are slightly lower than the rate in this work as expected. A low energy tail was also observed in their work for normal incidence. In this work, the low energy tail appeared for

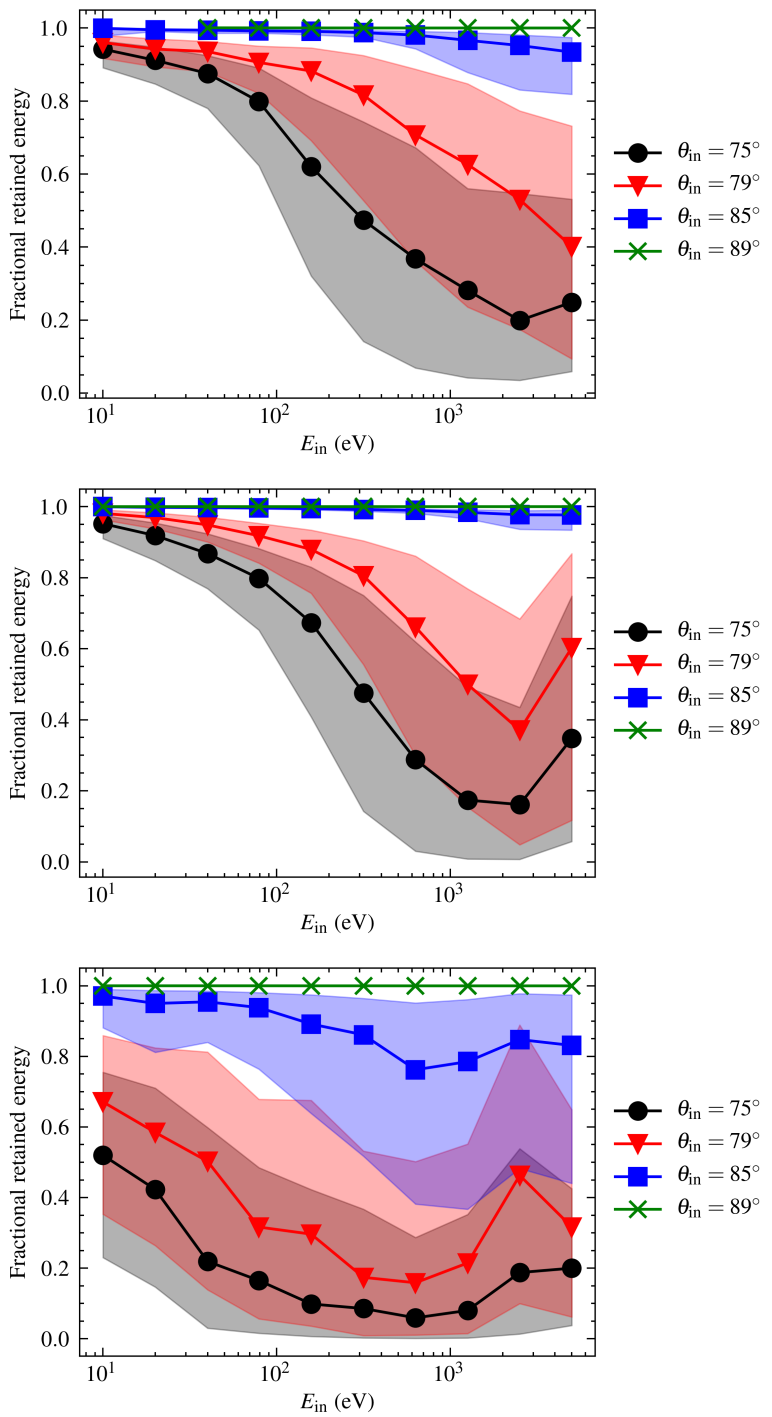


Figure 3.13: Fractional retained energy vs. E_{in} for SiO₂, AC and PS (top to bottom). The data presented are quantiles of E_{out} normalized by E_{in} : solid line is median (50% quantile) and shaded area (colored correspondingly) is from 25% quantile to 75% quantile.

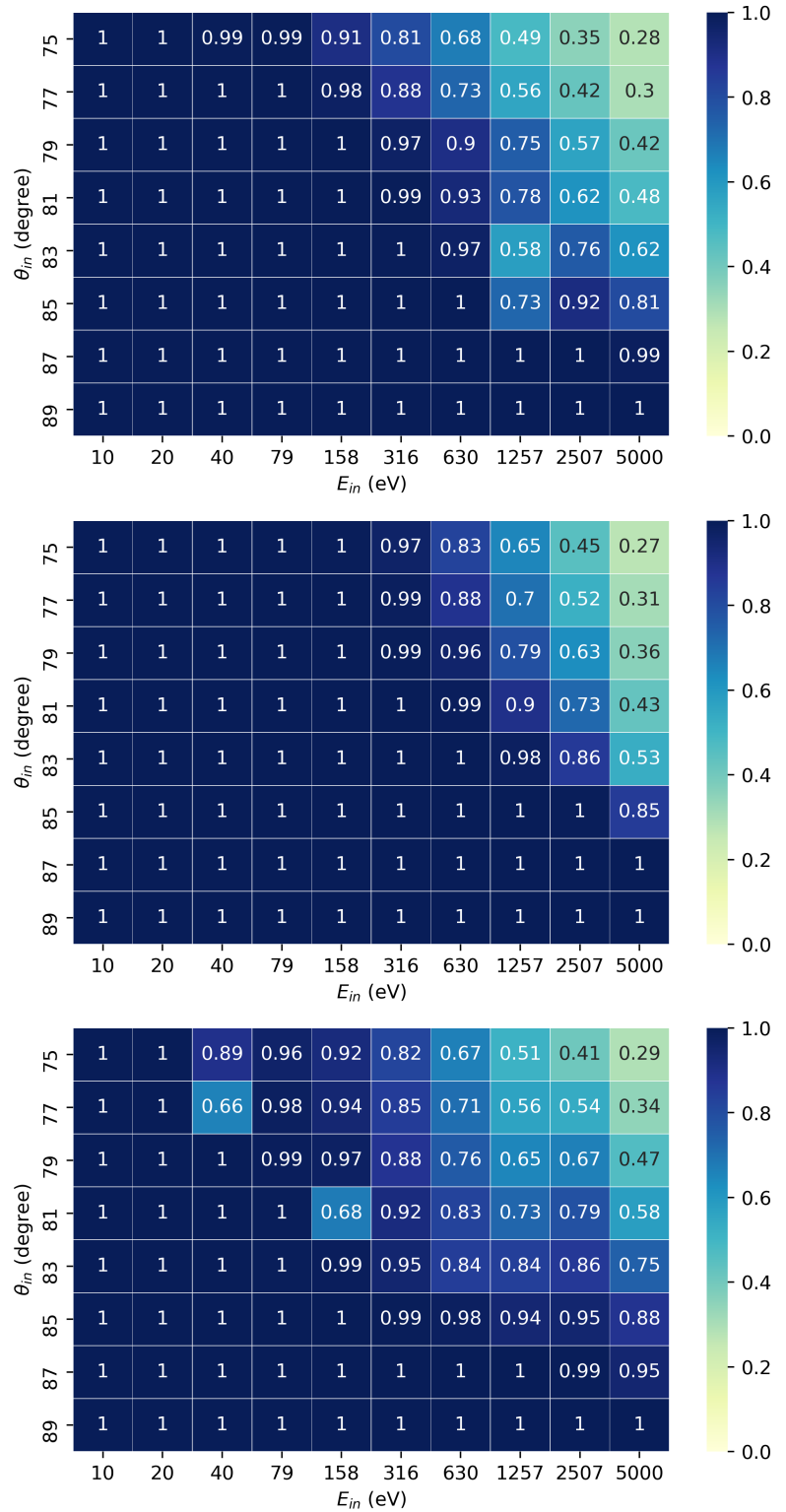


Figure 3.14: Rate of reflection (color scale, also numbered in each bin) as a function of E_{in} (x axis) and θ_{in} (y axis) for SiO₂, AC and PS (top to bottom).

high incident energies while the mechanism behind is the same.

3.6 Analytical distribution

To incorporate the glancing-angle scattering data from MD simulations into a feature profile simulator, an empirical analytical function was proposed, which can be used to predict the scattering distribution $f(\theta, E)$ characterized by incident angle θ_{in} and incident energy E_{in} , as shown in Eq. 3.4,

$$f_{\theta_{in}, E_{in}}(\theta, E) = \frac{1}{\sigma\sqrt{2\pi}} \exp\left\{\left[-\frac{1}{2}\left(\frac{\theta-\mu}{\sigma}\right)^2\right]\right\} \times \exp\left\{\left(\frac{E-E_{in}}{kE_{in}}\right)\right\} \quad (3.4)$$

where

$$\mu = \theta_{in} \frac{E}{E_{in}} + \theta_0 \left(1 - \frac{E}{E_{in}}\right) \quad (3.5)$$

Here variables θ and E are the scattered angle and energy of the ions, which were denoted by θ_{out} and E_{out} in previously sections. The analytical distribution was constructed in the form of an univariate normal distribution with center μ multiplied by an exponentially decaying term. The full distribution is an integral of multiple cross-sectional distributions as a function of E , and each cross-sectional distribution is an univariate normal distribution along the axis of θ . The analytical distribution was also designed to peak at the position of (θ_{in}, E_{in}) , which was intended to reproduce what we observed from the scattering results. There are three characteristic parameters (k , θ_0 and σ) in this analytical form, which can be intuitively illustrated by the three characteristic lines in Fig. 3.15. The rate of decrease of the green line is determined by k , as shown in the decaying term in Eq. 3.4. This decaying term describes how the magnitude of $f_{\theta_{in}, E_{in}}(\theta, E)$ drops as E decreases from the incident energy E_{in} . Other than the exponential form used here, other options such as square function or cubic function have also been tested. It was found that the exponential form not only fits the data very well but also can remain positive as E decreases, which is a natural requirement for probability distributions and will significantly reduce the amount of work and the level of inaccuracy when trying to reproduce the distribution numerically. The position of the red line reaching the θ axis ($E = 0$) is determined by θ_0 , which was designed to characterize the direction of the center of the cross-sectional distributions moving as a function of E . The width of the distribution along the θ axis is determined by σ , shown as the yellow line in Fig. 3.15. σ is the standard deviation in an univariate normal distribution, and it was kept constant (with respect to E) in the current design. It is possible to fit a linear function

to σ if the distribution shows significantly varying width with respect to E , see Eq. 3.5 for an example of a linear fitting of μ .

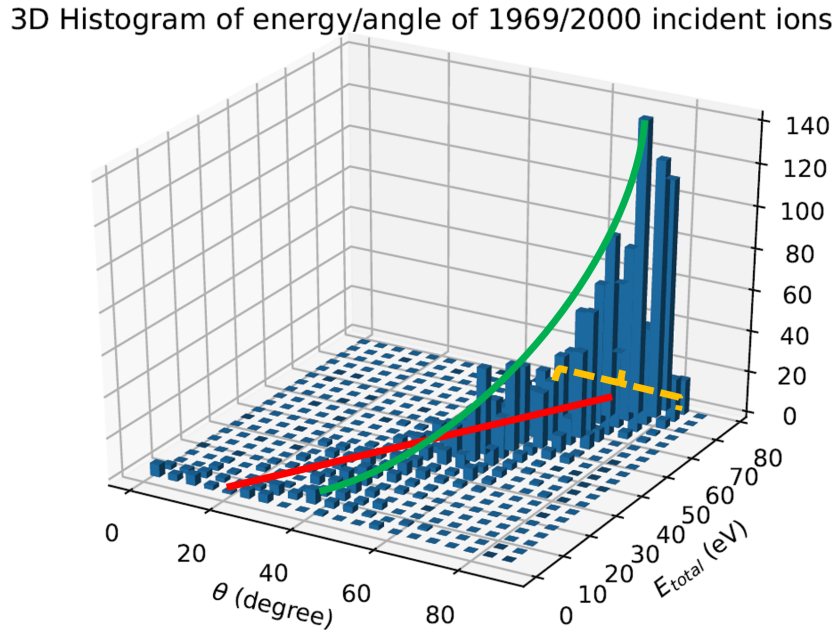


Figure 3.15: Illustration of the three characteristic parameters in the analytical form

Among the three characteristic parameters, it was found that the distribution $f_{\theta_{in}, E_{in}}(\theta, E)$ is most sensitive to the value of k and least sensitive to the value of θ_0 .

This analytical form can capture the general trends of the scattering distribution very well, see Fig. 3.16 for an example. Both the peak position and the tail shape were reproduced in the fitted distribution. The peak magnitude deviates from the collected distribution. However, since it is the integral of a probability distribution within some range that gives the actual probability, this deviation in peak magnitude should not affect the results too much as long as the bin width is small. Least square method was used to optimize the values of (σ, k, θ_0) so that a distribution $f_{\theta_{in}, E_{in}}(\theta, E)$ that most closely fit to the original distribution $f_{\text{original}}(\theta, E)$ can be obtained, as shown in Algorithm 1.

For each incident case with condition (θ_{in}, E_{in}) , the optimized values of characteristic parameters (σ, k, θ_0) can be obtained. Thus, the whole parametric study ($75-89^\circ$, 10-5000 eV) can give us three look-up tables (one for each material), as illustrated in Table 3.1. The actual values of (σ, k, θ_0) are not shown here in the table since a second layer of fitting was

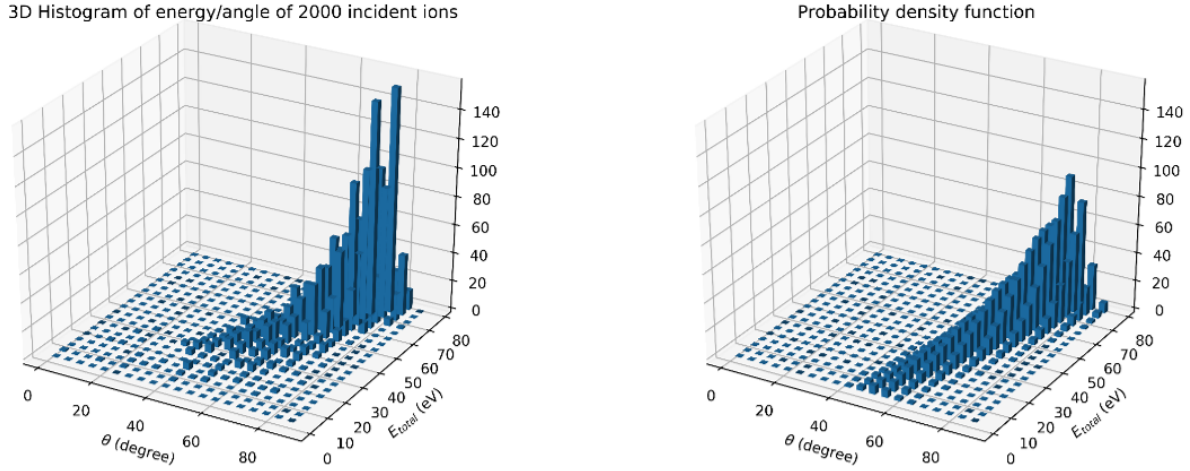


Figure 3.16: Comparison between (left) collected distribution and (right) fitted distribution, the fitted distribution was normalized so that the two distributions have the same volume

Algorithm 1 Least square method to determine k , θ_0 and σ

```

for all  $(\theta_{in}, E_{in})$  cases do
    for all  $\theta_0$  and all  $k$  and all  $\sigma$  do
        calculate  $f_{\sigma,k,\theta_0}(\theta, E)$  and normalize
        calculate  $SSE = \sum_{\text{all bins}} [f_{\sigma,k,\theta_0}(\theta, E) - f_{\text{original}}(\theta, E)]^2$ 
        find the  $(\sigma, k, \theta_0)$  values that give the least SSE
    end for
end for

```

also performed which could reduce the large fitting data (3 large look-up tables) to small tables, see next section.

Table 3.1: Optimized values of (σ, k, θ_0) presented in a look-up table form

$\theta_{\text{in}}(^{\circ})$	$E_{\text{in}}(\text{eV})$	σ	k	θ_0
75	10	-	-	-
75	...	-	-	-
75	5000	-	-	-
76	10	-	-	-
...	...	-	-	-
89	5000	-	-	-

3.6.1 Second layer of fitting

A second layer of fitting was performed to the previously obtained look-up tables, mainly due to two reasons: 1. the look-up tables data were on discrete points ($\theta_{\text{in}} = 80^{\circ}$ and $E_{\text{in}} = 20 \text{ eV}$ for example) while in the actual simulation case these incident conditions would be at somewhere in between, thus certain interpolation steps need to be done prior to using the table data in any etching profile simulators; 2. for demonstration and application purposes, an analytical form is much better than having data table for each material.

In order to extract information from the look-up tables, a bivariate linear regression with a crossing term was used to fit the characteristic parameters (σ, k, θ_0) as a function of incident angle θ_{in} and incident energy E_{in} , shown in Eq. 3.6

$$\left. \begin{array}{l} \sigma \\ \theta_0 \\ \ln k \end{array} \right\} = f(\theta_{\text{in}}, \ln E_{\text{in}}) = a\theta_{\text{in}} + b \ln E_{\text{in}} + c \theta_{\text{in}} \ln E_{\text{in}} + d \quad (3.6)$$

where log form of E_{in} was used since the incident energy ranges widely from 10 to 5000 eV, and log form of k was used since it ranges widely from 0.01 to 25 and the shape of the distribution is very sensitive to k when the value of k is small. For each characteristic parameter within (σ, k, θ_0) , the fitting parameters (a, b, c, d) were calculated, and the discrete look-up table form was fitted into continuous bivariate analytical form. After the second layer of fitting, the characteristic parameters (σ, k, θ_0) can then be predicted as a function

of the incident conditions ($\theta_{\text{in}}, E_{\text{in}}$), given the bivariate linear fitting parameters (a, b, c, d). Those bivariate linear fitting parameters (a, b, c, d) were independently determined for each characteristic parameter. So for each material, there will be three pairs of (a, b, c, d).

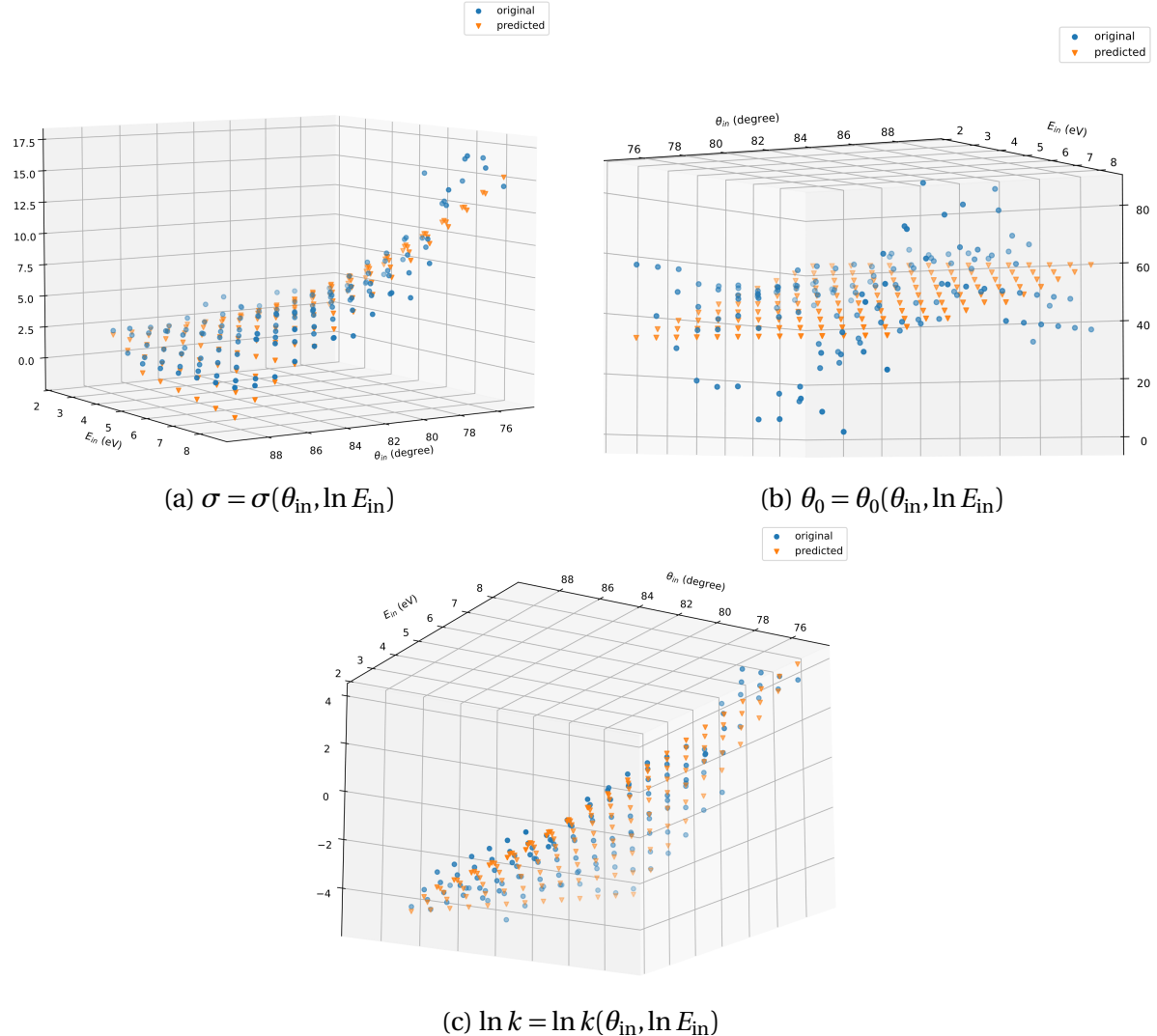


Figure 3.17: Bivariate linear fitting for shape parameters ($\sigma, \theta_0, \ln k$) for SiO_2 (blue circle → original, orange triangle → predicted)

The bivariate linear fitting results are plotted in Fig. 3.17 for SiO_2 , where the predicted values (from bivariate linear fitting) of (σ, k, θ_0) are compared against the optimized values (from the look-up table). The predicted values of σ and $\ln k$ match the optimized values

very well. While for θ_0 , the optimized data points are more scattered and the fitting can only capture the general trend. Since the distribution $f_{\sigma,k,\theta_0}(\theta, E)$ is least sensitive to the value of θ_0 , it can be seen from the following distribution comparison results that the fitting of θ_0 here is capable of reproducing the shape of the original distributions. The same bivariate linear fitting was also performed for AC and PS, and the predicted values match the optimized values well.

The fitting parameters (a, b, c, d) for all three materials are presented in Table 3.2. Using the data from Table 3.2 as well as the general analytical forms Eq. 3.4, Eq. 3.5 and Eq. 3.6, one can conveniently reproduce the scattering distribution $f_{\theta_{in},E_{in}}(\theta, E)$ with a certain degree of accuracy.

Table 3.2: Bivariate linear fitting parameters for all three materials

SiO₂	a	b	c	d
σ	0.1339	9.5686	-0.1065	-11.4593
θ_0	-3.6841	-34.1894	0.5025	303.7449
k	-0.1335	4.4684	-0.0486	5.8509

AC	a	b	c	d
σ	0.1016	8.5444	-0.0939	-9.2958
θ_0	-4.5886	-43.4925	0.6337	373.8219
k	-0.1817	3.5199	-0.0384	10.2898

PS	a	b	c	d
σ	-0.5229	3.3393	-0.0349	46.0859
θ_0	-3.5006	-34.3652	0.4327	336.3185
k	-0.0085	7.1230	-0.0799	-3.6708

The original MD collected distributions were compared against analytical distributions with both look-up table values and bivariate linear fitting predicted values for several incident cases, presented in Fig. 3.18, Fig. 3.19 and Fig. 3.20 for SiO₂, AC and PS respectively. It can be seen that the general analytical form can reproduce the scattering distributions well. Both the peak positions and the general shapes were predicted in the fitted distributions with a certain degree of accuracy, especially for the cases with less diffuse scatterings. For those cases that are more diffuse, (SiO₂, 75°, 630 eV) in Fig. 3.18a for example, the analytical

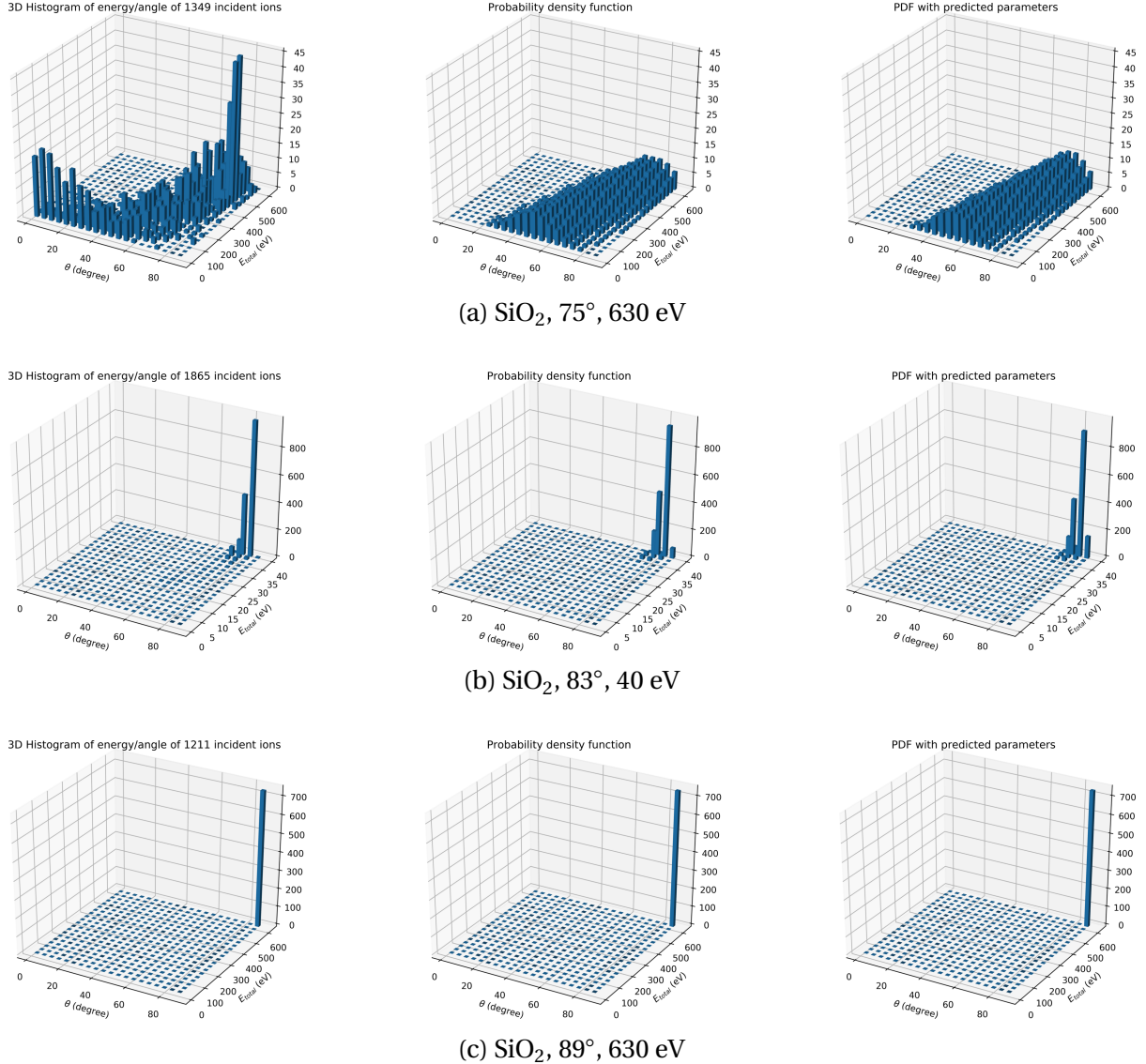


Figure 3.18: Scattering distributions for SiO_2 : (left) original distribution, (middle) analytical distribution with look-up table values and (right) analytical distribution with bivariate linear fitting predicted values

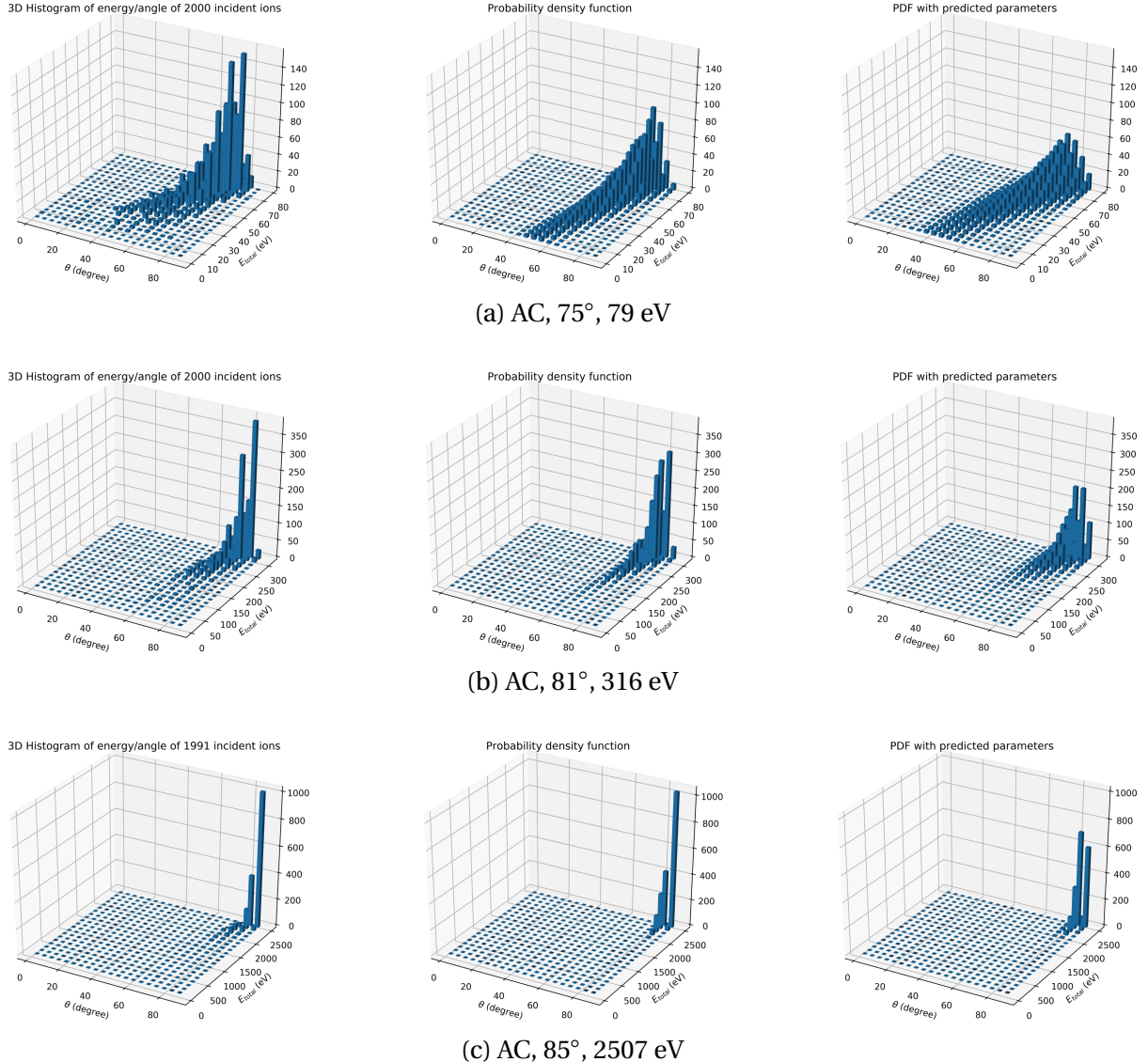


Figure 3.19: Scattering distributions for AC: (left) original distribution, (middle) analytical distribution with look-up table values and (right) analytical distribution with bivariate linear fitting predicted values

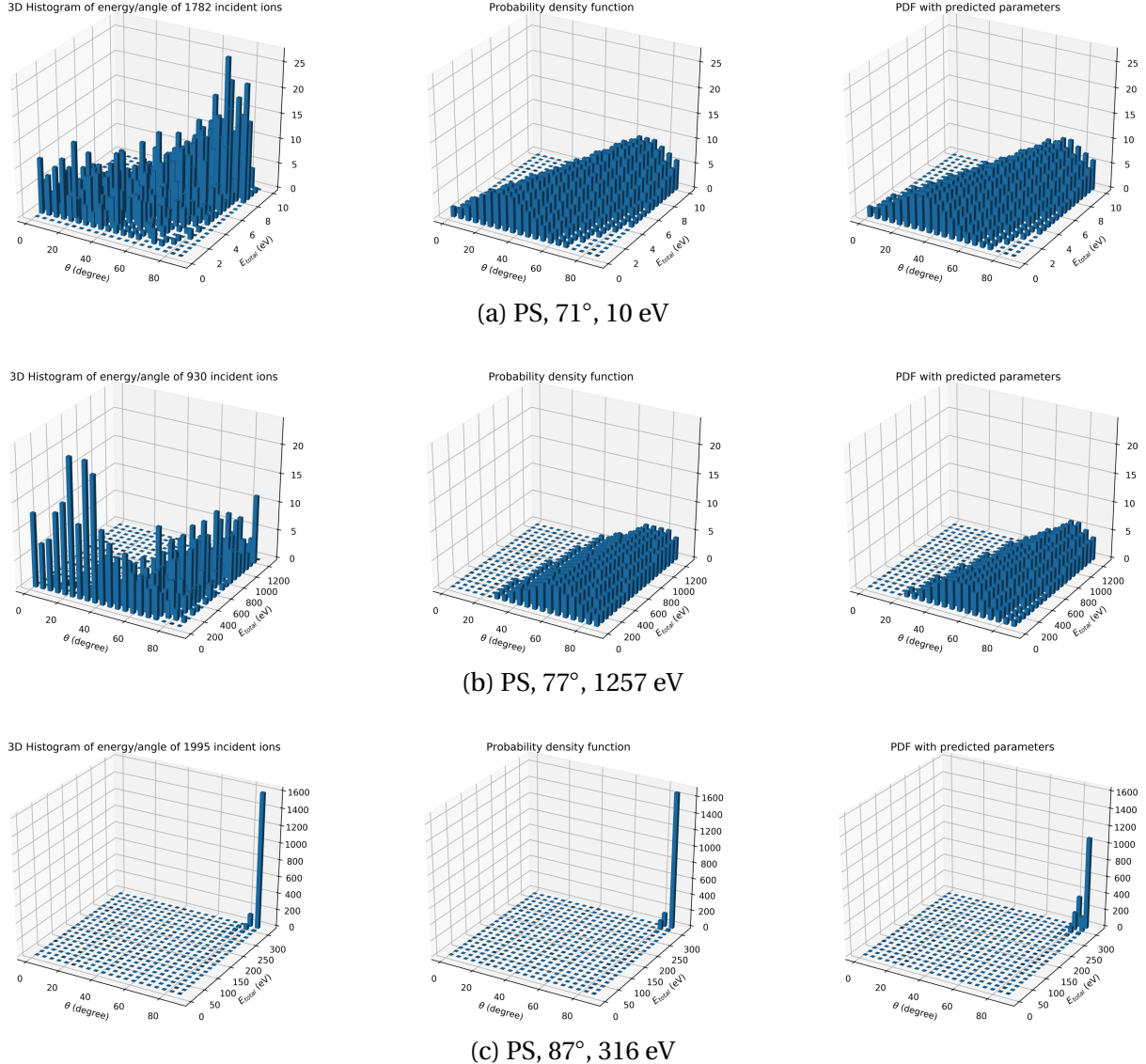


Figure 3.20: Scattering distributions for PS: (left) original distribution, (middle) analytical distribution with look-up table values and (right) analytical distribution with bivariate linear fitting predicted values

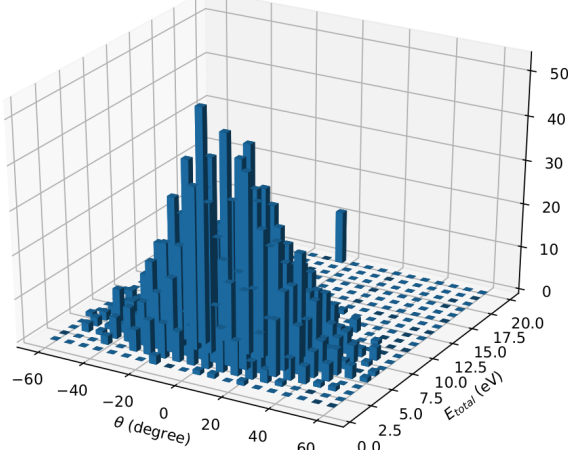
distribution can capture the major part of the scattering distribution while failed to predict the protruding peak (for specular scattering) and the low-energy tail (near thermal energy). On the other hand, for cases that are less diffuse, most cases with $\theta_{\text{in}} > 80^\circ$ for example, both the two analytical distributions match the original scattering distribution very well, indicating that the two layers of fitting process can significantly simplify the problem without sacrificing too much accuracy. The protruding peak could be better fitted when some other decaying functions are used in Eq. 3.4. The low-energy tail, which is more significant in the scattering cases for PS (see Fig. 3.20), can be accounted for when the threshold energy is considered, which will be covered in later section.

3.7 Near-normal scatterings

The scatterings with incident angles that are close to material surface normal were also investigated. It was found in such cases the shape of the distributions were significantly different than for glancing-angle scatterings. The scattering distributions with incident conditions (0° , 20 eV) and (0° , 316 eV) for AC are presented here in Fig. 3.21. It can be seen from Fig. 3.21a and Fig. 3.21b that the collected distributions now have a bell shape centered around 0° , which is closer to a 2d normal distribution. Unlike the glancing-angle scattering distributions which peaked at the position of $(\theta_{\text{in}}, E_{\text{in}})$, the peak position is now at much lower energy, indicating the reflected ions have lost most of their incident energy. See Fig. 3.21b for an example, the incident energy was 316 eV while the scattered ions mostly had energies within the first bin, (0, 15.8 eV), on energy axis.

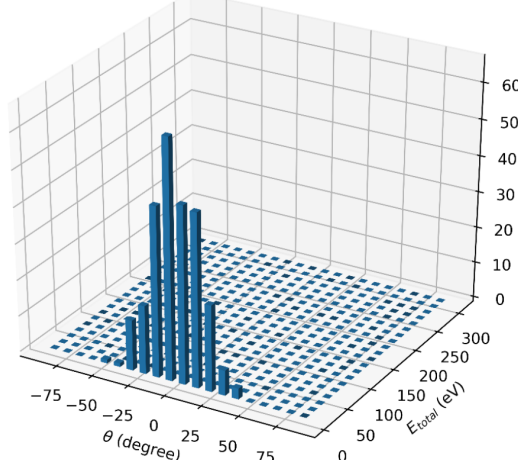
It is also worth noting that for the normal scattering cases, most of the incident ions were captured by the material for higher incident energy cases. Out of the 2000 incident ions, 1954 ions were reflected and collected for incident case $E_{\text{in}} = 20$ eV, while only 279 ions were collected for incident case $E_{\text{in}} = 316$ eV. In conclusion, both the shape of the scattering distribution and the number of collected ions suggest that for near-normal scatterings, lower incident angle (with respect to surface normal) results in large fraction of ions penetrating deeply into the material and then exiting the material (more likely to be trapped) after many collisions and scattering events, resulting in substantial energy loss compared to E_{in} . This matches what we observed for higher incident energy cases. This energy-loss effect by multiple collisions is even more significant for near-normal scatterings as most of the ions are essentially thermalized by the material regardless of their incident energies.

3D Histogram of energy/angle of 1954 incident ions



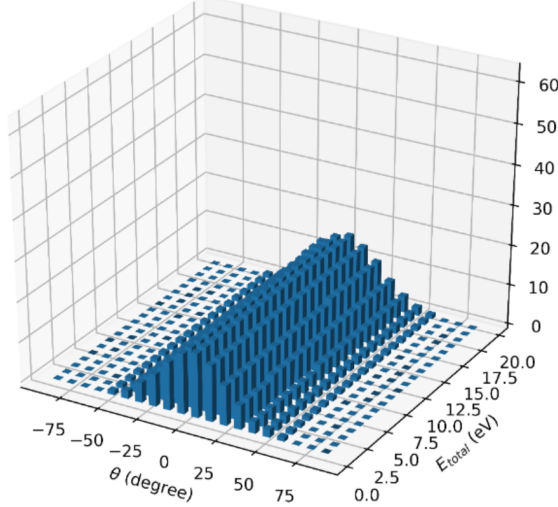
(a) Collected, AC, 0° , 20 eV

3D Histogram of energy/angle of 279 incident ions



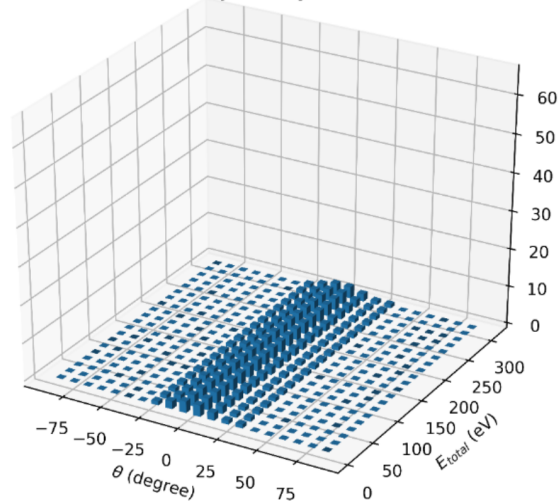
(b) Collected, AC, 0° , 316 eV

Probability density function



(c) Predicted, AC, 0° , 20 eV

Probability density function



(d) Predicted, AC, 0° , 316 eV

Figure 3.21: Comparison of collected and predicted scattering distributions for AC at $\theta_{\text{in}} = 0^\circ$ and $E_{\text{in}} = 20$ or 316 eV

As expected, our proposed analytical function failed to reproduce the scattering distributions in such incident conditions, as shown in Fig. 3.21c and Fig. 3.21d. This is due to the analytical function intrinsically assume the peak position is at (θ_{in}, E_{in}) and the distribution has a long decaying tail towards the low-energy end, which obviously do not apply for the distributions collected for near-normal scatterings. It is possible to propose a new analytical function based on a 2d normal distribution, which could be used to approximate these bell-shape distributions for near-normal scatterings.

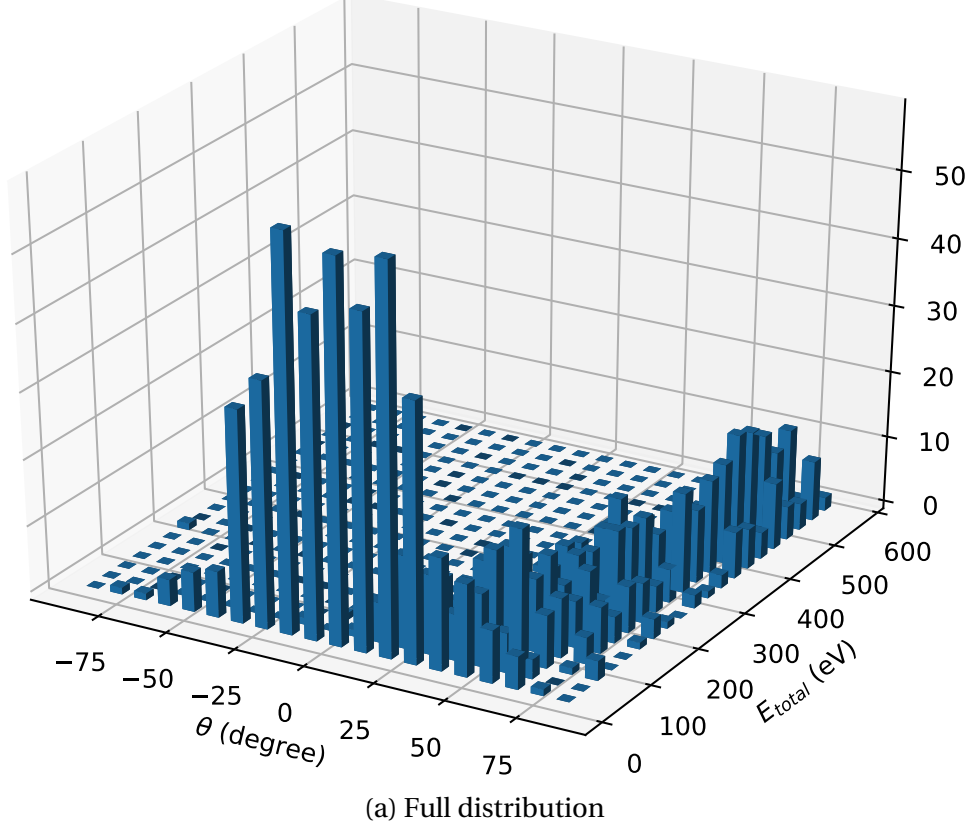
For those cases with mixed effects from both glancing-angle scattering distribution (skewed, shown in Eq. 3.4) and near-normal scattering distribution (bell shaped), i.e., cases with high E_{in} and not so high θ_{in} , it is possible to decouple the full distribution into two partial distributions for different energy ranges. See Fig. 3.22 for an example. The scattering distribution for SiO₂ at $\theta_{in} = 70^\circ$ and $E_{in} = 630$ eV was decoupled using a cutoff energy $E_{cut} = 0.1E_{in}$. The high-energy partial distribution shows the major trend of a glancing-angle scattering distribution which peaked around (θ_{in}, E_{in}) and has a long tail extending to the lower right half of the histogram domain. On the other hand, the low-energy partial distribution is more like the near-normal scattering distribution which has a bell shape centered around 0° , regardless of the incident angle. We can also see that the majority of the low-energy partial distribution is much lower than the cutoff energy (63 eV) and is actually within the first bin, (0, 3.15 eV), indicating that those ions were effectively thermalized and may not be significant for sputtering simulations.

It can therefore be assumed that the actual scattering process involves two mechanisms: (1) The ions may only interact with a few surface atoms and do not go deeply into the material, so that they can still maintain a fair amount of the incident energy and the scattered angle will depend on the incident angle. The scattering distribution is skewed with a long tail, as described by Eq. 3.4; (2) The ions may also penetrate deeply into the material, get captured and then get re-emitted. It involves many collisions and scattering events so that the final ions will be thermalized and the scattered angle will not depend on the incident angle. The scattering distribution has a bell shape centered around 0° , and with scattered energy much lower than the incident energy (close to thermal energy). Transition from mechanism (1) to (2) will occur as the incident angle gets lower (closer to surface normal) or as the incident energy gets higher.

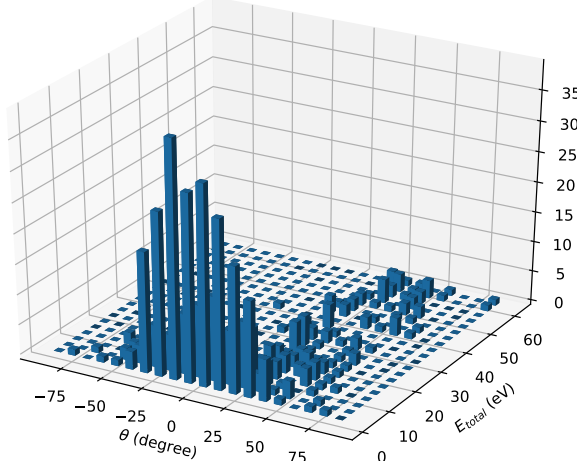
A linear combination of both the distributions could be used to quantify the transition from mechanism (1) to (2), such as in Eq. 3.7

$$f_{\theta_{in}, E_{in}}^{\text{total}}(\theta, E) = a f_{\theta_{in}, E_{in}}^{\text{glancing}}(\theta, E) + (1-a) f_{\theta_{in}, E_{in}}^{\text{normal}}(\theta, E) \quad (3.7)$$

3D Histogram of energy/angle of 1125 incident ions



3D Histogram of energy/angle of 507.0 incident ions



3D Histogram of energy/angle of 608.0 incident ions

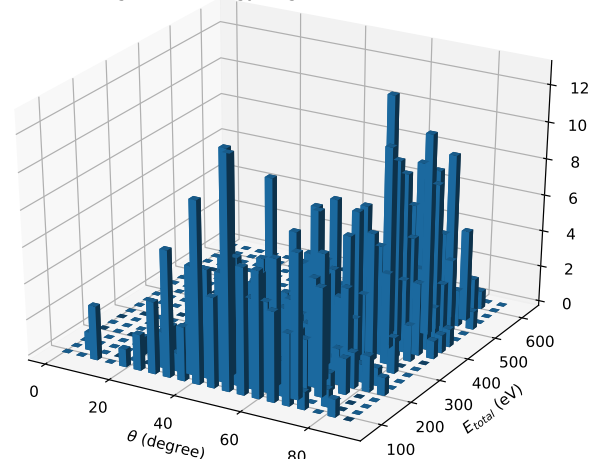


Figure 3.22: Decouple the full distribution for SiO_2 at $\theta_{in} = 70^\circ$ and $E_{in} = 630 \text{ eV}$, using a cutoff energy $E_{cut} = 0.1 E_{in}$

where a is a coefficient which could also be approximated using the bivariate linear fitting technique as a function of $(\theta_{in}, \ln E_{in})$, as used previously in Eq. 3.6. We did not perform the linear combination in this work since those near-normal scatterings are not the major concern for studying ions interaction with sidewalls and in fact those thermalized ions can be excluded when threshold energy is taken into account. However, one is encouraged to do so if the transition is a major concern or the thermalized ions cannot be excluded, for example, when studying ions interaction with feature bottom.

3.8 Threshold energy

In a feature profile simulator in plasma etching simulation, threshold energy is introduced so that particles with kinetic energy below the threshold produce no sputtering on the materials and thus can be safely removed from the simulation domain. Since the threshold energy is determined by the significance of sputtering, it is thus a material dependent quantity. In Monte Carlo Feature Profile Model (MCFPM) (A feature profile simulator module developed by Kushner's group used by the Hybrid Plasma Equipment Model (HPEM).), the threshold energy was defined as 70 eV for SiO_2 , ≈ 35 eV for Si crystal, 10 eV for passivated SiCl_3 , etc. In this project, since we modelled a lot of Si related materials, a universal threshold energy of 35 eV was used. In fact, as observed in last section, even a threshold energy of 10 eV should be enough to exclude the low-energy bell shaped part from the total scattering distribution. An example is presented in Fig. 3.23, where a full distribution and a partial distribution above the threshold energy of 35 eV were compared for the incident case of $(\text{SiO}_2, \theta_{in} = 55^\circ, E_{in} = 158 \text{ eV})$. As expected, a threshold energy of 35 eV effectively removed the low-energy bell shaped part from the total scattering distribution, giving a distribution which can be well fitted and predicted by the proposed analytical function in Eq. 3.4.

Using the threshold energy of 35 eV, the number of collected scattered ions with energies above the threshold can be counted, giving an estimate of the probability of the ions still being important to monitor after this scattering event from a sputtering modeling perspective. These results are listed in Fig. 3.24 for SiO_2 , AC, and PS for all the incident conditions simulated, where the total number of incident ions is 2000, the table row names are θ_{in} in degree and the column names are E_{in} in eV. The table cells are color coded: (1) all the red colored cells have number of collected ions less than 100, meaning that for these incident conditions, less than 5% of chance the ions will still need to be considered for their consecutive behaviors in a sputtering simulation after this first-time scattering event; (2)

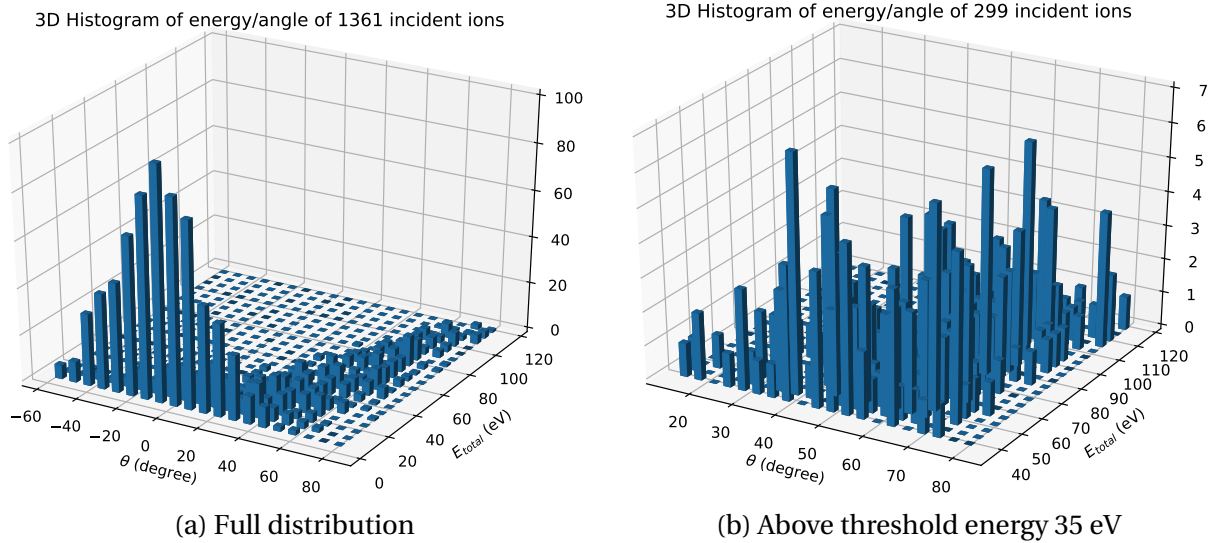


Figure 3.23: Decouple the full distribution for SiO₂ at $\theta_{\text{in}} = 55^\circ$ and $E_{\text{in}} = 158 \text{ eV}$, using a threshold energy $E_{\text{thre}} = 35 \text{ eV}$

all the other cells were linearly grayscale colored so that from the lightest to the darkest the cell color can conveniently represent the increase of the number (probability) of collected scattered ions from 100 (5%) to 2000 (100%). From Fig. 3.24 it can be seen that if we use the cutoff probability of 5% to differentiate the incident conditions for which the scattered ions are still worth monitoring after their first-time scattering events, the distinction significantly and almost uniformly depends on the incident angle θ_{in} . For example, for SiO₂ with θ_{in} below 50°, for AC with θ_{in} below 55° and for PS with θ_{in} below 65° (did not perform extra simulation cases for PS with θ_{in} below 65°, but the trends are quite obvious), the probability of scattered ions with energies above the threshold energy are less than 5% and gets even lower when θ_{in} gets lower (closer to surface normal), these are the incident conditions regions we define as *sputtering dominated*, i.e., we only consider the physical quantities related to sputtering events such as removal rates, yields and type of etch byproducts, but do not take into account the ions scattering distributions since not only the scattering probability is low but also ions kinetic energy after scattering is too low to play a role in a sputtering simulation. On the other hand, for the incident cases with higher θ_{in} (grayscale colored cells in Fig. 3.24), these are the incident conditions regions we define as *scattering dominated*, i.e., the significance of scattering event is higher than our predefined level (5%) so that we cannot ignore the consecutive behaviors of the ions after this scattering event. Thus, both the sputtering related mechanisms and the scattering distributions need to be

	10	20	40	79	158	316	630	1257	2507	5000	
0	0	0	0	0	0	1	2	5	32	19	
5	0	0	0	0	0	1	3	7	27	22	
10	0	0	0	0	0	2	1	6	34	27	
15	0	0	0	0	0	1	2	19	34	17	
20	0	0	0	0	3	4	4	15	36	14	
25	0	0	0	0	5	9	1	12	43	25	
30	0	0	0	2	12	19	12	18	59	24	
35	0	0	0	6	27	37	20	13	34	42	
40	0	0	0	27	61	51	30	25	56	42	
45	0	0	0	69	107	99	49	43	65	57	
50	0	0	0	125	200	129	114	86	105	72	
55	0	0	0	225	299	233	161	114	130	83	
60	0	0	9	420	486	415	278	175	170	102	
65	0	0	31	677	743	591	425	275	267	143	
70	0	0	194	1159	1151	960	669	422	348	188	
	10	20	40	79	158	316	630	1257	2507	5000	
0	0	0	0	0	0	0	0	0	0	1	33
5	0	0	0	0	0	0	0	0	0	3	20
10	0	0	0	0	0	0	0	0	0	1	35
15	0	0	0	0	0	0	0	0	0	1	39
20	0	0	0	0	0	0	0	0	0	1	37
25	0	0	0	0	0	1	2	0	0	2	47
30	0	0	0	0	0	0	0	2	0	3	52
35	0	0	0	1	0	5	4	1	0	3	50
40	0	0	0	10	6	8	10	7	1	12	61
45	0	0	0	13	26	38	21	14	6	14	85
50	0	0	0	18	95	93	49	27	22	18	84
55	0	0	0	21	231	202	127	83	46	48	112
60	0	0	0	16	465	447	275	179	116	108	161
	10	20	40	79	158	316	630	1257	2507	5000	
65	0	0	67	835	744	532	324	221	202	213	
67	0	0	87	964	895	633	465	310	272	250	
69	0	0	167	1180	1097	881	600	385	309	299	
71	0	0	331	1385	1270	1013	740	480	431	348	
73	0	0	594	1620	1476	1214	868	694	517	366	
75	0	0	951	1823	1738	1504	1169	892	652	468	
77	0	0	1279	1932	1927	1729	1395	1094	801	548	
79	0	0	1641	1964	1987	1919	1693	1334	1017	625	
81	0	0	1867	1994	1997	1997	1898	1648	1287	771	
83	0	0	1968	1999	2000	2000	1989	1926	1634	1022	
85	0	0	2000	2000	2000	2000	2000	2000	1999	1984	1698
87	0	0	2000	2000	2000	2000	2000	2000	2000	2000	2000
89	0	0	2000	2000	2000	2000	2000	2000	2000	2000	2000

(a) SiO₂

(b) AC

	10	20	40	79	158	316	630	1257	2507	5000	
65	0	0	15	164	222	246	325	243	184	222	
67	0	0	39	273	327	337	378	258	243	236	
69	0	0	38	265	379	402	422	331	307	256	
71	0	0	54	362	461	545	488	412	359	332	
73	0	0	41	235	1304	562	571	510	450	431	
75	0	0	91	532	700	763	676	614	606	486	
77	0	0	106	675	810	842	800	691	870	570	
79	0	0	324	817	1084	982	948	934	1138	801	
81	0	0	457	1043	845	1191	1159	1111	1397	1056	
83	0	0	730	1313	1439	1428	1334	1385	1582	1402	
85	0	0	1399	1775	1849	1828	1760	1703	1795	1696	
87	0	0	1945	1993	1991	1987	1983	1975	1968	1871	
89	0	0	1977	1996	2000	1998	2000	1999	1993	1997	

(c) PS

Figure 3.24: Number of scattered ions with energies above the threshold energy (35 eV) for SiO₂, AC, and PS. Total number of incident ions is 2000, table row names are θ_{in} in degree and column names are E_{in} in eV.

considered in such cases.

It is worth noting the fitting parameters (a, b, c, d) presented in Table 3.2 were calculated based on results in which the threshold energy (35 eV) has already been taken into account.

CHAPTER

4

FLUOROCARBON POLYMER FORMATION

4.1 Abstract

During a plasma etching process using fluorocarbon gases such as CF_4 and C_4F_8 , the formation of fluorocarbon polymers can occur due to chemical reactions and modifications of the reactive radicals in the plasma with the substrate material being etched, usually on its surface. These polymer films typically consist of a complex mixture of chemical compounds, primarily containing carbon and fluorine with a PTFE-like structure, but may also include other elements from the substrate materials, such as silicon, oxygen, and hydrogen. The fluorocarbon polymer that forms on the substrate material surface can have both positive and negative effects. On one hand, it can act as a protective layer to protect the underlying material from being etched. On the other hand, the buildup of excessive unwanted polymers can result in process contamination, reduce etch selectivity, slow down the etch rate, and negatively impact the final feature profile. With the help of reactive molecular dynamics simulations, the impact of different conditions on the formation of the fluorocarbon polymer can be investigated in nanoscale, the atomic structure of the formed polymer film can be well captured, and the accuracy of modeling chemical reactions in plasma-

surface interactions can be improved. In this chapter, we discuss results from reactive MD simulations of fluorocarbon polymer formation on HAR sidewalls in plasma etching processes by depositing CF_x ($x = 1 \sim 3$) radicals onto amorphous SiO_2 and Si substrates. ReaxFF interatomic potential was used and a parameter file for Si/O/C/F systems was prepared. Validation and verification tests were carried out for the parameter file. The MD simulation results show that the film thickness strongly depends on the incident species as fluorine deficient species tend to grow thicker polymers. The film thickness also strongly depends on the substrate materials as polymer on Si crystal can grow much thicker than on amorphous SiO_2 . It was also found that carbon could potentially play a role in forming thicker polymer films. The MD simulations were performed using LAMMPS primarily with ReaxFF potential, and ZBL potential was also used for modeling the interaction of energetic Ar^+ ions with other atoms.

4.2 Prepare ReaxFF parameter set

Modeling fluorocarbon polymer formation in a plasma etching process using ReaxFF potential requires a system (parameter set) which at least is able to describe the interactions among atoms of Si/O/C/F simultaneously. However, a full Si/O/C/F system (parameter set) cannot be found in the literature for ReaxFF potential at the time this work was performed.

As mentioned in Chapter 2, ReaxFF potential was designed to be expendable, meaning that different ReaxFF parameter sets can be directly combined as long as they are on the same development branch, see Fig. 4.1 for an illustration of the ReaxFF development tree made in 2016 (Senftle et al. 2016).

Although a full Si/O/C/F system cannot be found for ReaxFF, several sub-systems (parameter sets containing parameters for three of the desired atoms types) can be found in the literature, and these systems have individually passed rigorous verification and validation (V&V) tests both in the original papers and in the following papers which cited these works. Therefore the accuracy of these sub-systems can be ensured. The main sub-systems referenced in this work are listed below, where the ReaxFF parameter sets were obtained either from the corresponding Supporting Information or from the authors directly.

- **Ref.3: C/O/F** - (Singh et al. 2013) - Singh, Sandeep Kumar, et al. "Thermal properties of fluorinated graphene." Physical Review B 87.10 (2013): 104114.
- **Ref.2: C/O/Si** - (Newsome et al. 2012) - Newsome, David A., et al. "Oxidation of silicon

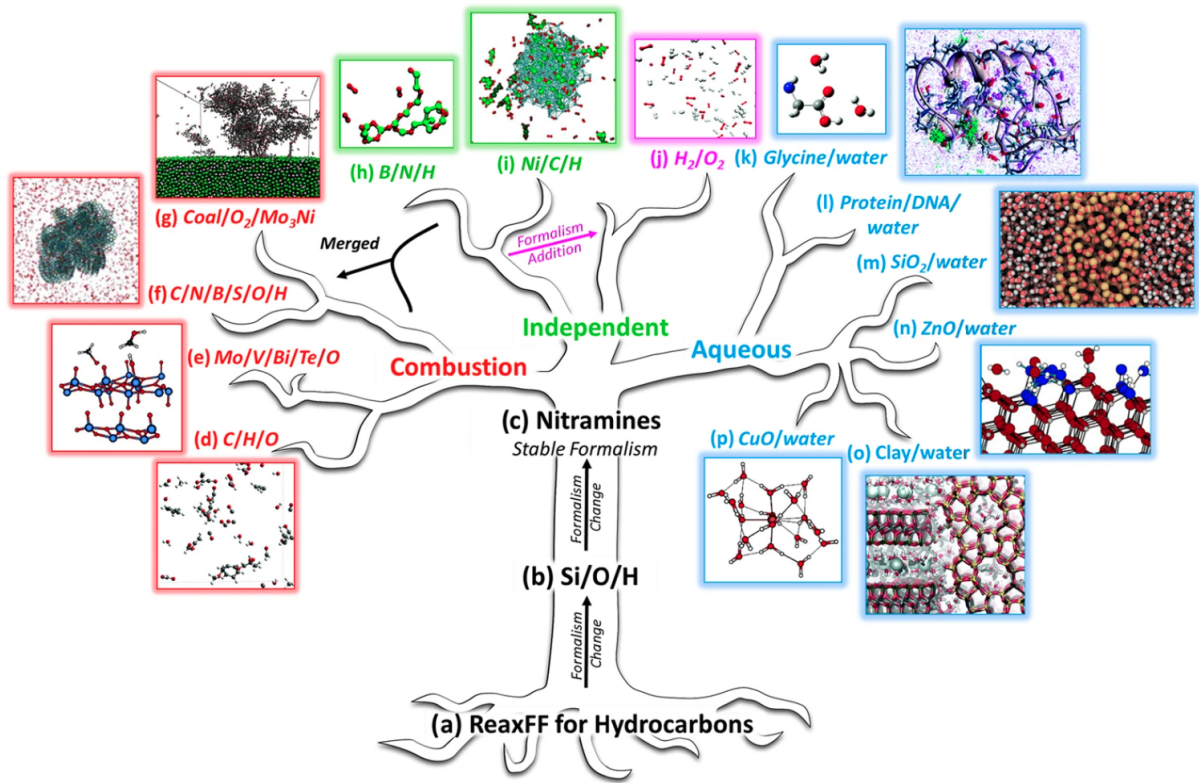


Figure 4.1: ReaxFF development tree, where parameter sets on the same development branch can be directly combined. (Figure taken from Senftle et al. (2016) and permission gained from Creative Commons Attribution 4.0 International License.)

carbide by O₂ and H₂O: a ReaxFF reactive molecular dynamics study, Part I." The Journal of Physical Chemistry C 116.30 (2012): 16111-16121.

- **Ref.4: Si/O/F** - (Kim et al. 2021) - Kim, Dong Hyun, et al. "Molecular Dynamics Simulation of Silicon Dioxide Etching by Hydrogen Fluoride Using the Reactive Force Field." ACS omega 6.24 (2021): 16009-16015.
- **Ref.7: Si/F** - (Rahnamoun and Van Duin 2014) - Rahnamoun, A., and A. C. T. Van Duin. "Reactive molecular dynamics simulation on the disintegration of Kapton, POSS polyimide, amorphous silica, and teflon during atomic oxygen impact using the ReaxFF reactive force-field method." The Journal of Physical Chemistry A 118.15 (2014): 2780-2787.

Since these sub-systems are all in the same *Combustion* branch as shown in Fig. 4.1, they can be combined into a full Si/O/C/F system. However, several precautions need to be taken into account prior to and during actually conducting the combining process.

Firstly, the general parameters of all the sub-systems should be the same so that they don't conflict with each other, which is a suggestion given by the original author of ReaxFF from an email discussion. For ReaxFF potential, there are 39 general parameters which are required for any ReaxFF parameter set and are often listed at the beginning of each parameter file, see Appendix A for an example. These general parameters do not specifically define the interactions between atoms, instead, they are usually within correction terms such as overcoordination and stabilisation. The general parameters of all the ReaxFF parameter sets referenced in this work are listed and compared in Table 4.1, where the column names are consistent with the references listed above and the last column performs logical operation to determine if the value of a general parameter is identical for all the four sub-systems. Out of the 39 general parameters, it was found that most of them are identical for all the four sub-systems. For those that are not equal, the two "*!Triple bond stabilisation parameter*" terms and the "*!Triple bond stabilization energy*" term only affect the triple bond for the C-O bonded pair in carbon monoxide, the "*!C2-correction*" term only affects the triple bond in a C₂ molecule, and the two "*!Double bond/angle parameter: overcoord*" terms only affect the molecule in which two double bonds share an atom in a valency angle. The detailed explanations can be found in the Supporting Information of Chenoweth et al. (2008). In summary, for all the general parameters with discrepancy, not only their values are quite close among different sub-systems but also they will not play major roles for the chemistry concerned within the scope of this work. Therefore the

sub-systems can be combined without significant consistency issues.

Secondly, there are some overlappings for the specific parameters in different ReaxFF sub-systems which need to be taken care of. The specific parameters uniquely define properties for different atom types, bond pairs, angle pairs, and torsion pairs, and are generally located right below the general parameters in any ReaxFF parameter file, see Appendix A for examples. It is possible that two different ReaxFF parameter files have parameters defined for one same atom type but the values are slightly different. For example, almost all ReaxFF parameter files include C/O/H atom types since the first ever ReaxFF model was proposed for hydrocarbon compounds (Van Duin et al. 2001), and both *Ref.2* and *Ref.4* have parameters for Si atom and the corresponding Si-X(-Y-Z) interactions. Different combining strategies were tested, it was found that the one shown in Eq. 4.1 gives the overall most satisfying performance,

$$\boxed{\text{Ref.3: C/O/F}} + \boxed{\text{Ref.2: Si-(C/O)}} + \boxed{\text{Ref.4 or 7: Si-F}} = \boxed{\text{C/O/F/Si}} \quad (4.1)$$

where the parameter set from *Ref.3* was used as the base system since it is already available in LAMMPS official versions and has passed tests performed by LAMMPS developers. *Ref.3* has parameters for C/O/F system which means that only the parameters for Si and the corresponding interaction terms need to be added to the base system. The parameters for Si as well as the interaction terms (including bond, angle, torsion, etc.) between Si and other atoms (except F atom) were taken from *Ref.2* and added to the base system. The reasons to choose *Ref.2* over *Ref.4* are not only *Ref.2* is well established but also *Ref.2* gives a better performance in describing Si-O compounds in tests. The parameters for Si-F interaction terms were then added to the base system to form a complete C/O/F/Si system. This work originally used parameters for Si-F interaction terms from *Ref.4*, but it was later found that *Ref.4* cannot predict the tetrahedral structure of SiF_4 correctly while *Ref.7* can fix that. This is less of a concern for fluorocarbon deposition simulations but can be important for calculating the sticking coefficient of SiF_x ($x = 1 \sim 4$) radicals in next chapter. In fact, parameters for Si-F interaction terms from both *Ref.4* and *Ref.7* were tested for fluorocarbon deposition simulations, and the results do not show significant difference. Therefore, parameters from *Ref.4* were mainly used for the fluorocarbon deposition simulations in this chapter and parameters from *Ref.7* were mainly used for the sticking coefficients simulations in next chapter. Both two versions of the combined systems (parameter sets) are listed in Appendix A for reference purpose.

Table 4.1: Comparison of the general parameters of all the ReaxFF parameter sets referenced in this work

General parameter item	Ref.3: C/O/F	Ref.2: C/O/Si	Ref.4: Si/O/F	Ref.7: Si/F	If equal?
!Overcoordination parameter	50	50	50	50	TRUE
!Overcoordination parameter	9.5469	9.5469	9.5469	9.5469	TRUE
!Valency angle conjugation parameter	26.5405	26.5405	26.5405	26.5405	TRUE
!Triple bond stabilisation parameter	1.7224	1.5105	1.7224	1.7224	FALSE
!Triple bond stabilisation parameter	6.8702	6.663	6.8702	6.8702	FALSE
!C2-correction	60.485	0	60.485	60.485	FALSE
!Undercoordination parameter	1.0588	1.0588	1.0588	1.0588	TRUE
!Triple bond stabilisation parameter	4.6	4.6	4.6	4.6	TRUE
!Undercoordination parameter	12.1176	12.1176	12.1176	12.1176	TRUE
!Undercoordination parameter	13.3056	13.3056	13.3056	13.3056	TRUE
!Triple bond stabilization energy	-70.5044	-70.1292	-70.5044	-70.5044	FALSE
!Lower Taper-radius	0	0	0	0	TRUE
!Upper Taper-radius	10	10	10	10	TRUE
!Not used	2.8793	2.8793	2.8793	2.8793	TRUE
!Valency undercoordination	33.8667	33.8667	33.8667	33.8667	TRUE
!Valency angle/lone pair parameter	6.0891	6.0891	6.0891	6.0891	TRUE
!Valency angle	1.0563	1.0563	1.0563	1.0563	TRUE
!Valency angle parameter	2.0384	2.0384	2.0384	2.0384	TRUE
!Not used	6.1431	6.1431	6.1431	6.1431	TRUE
!Double bond/angle parameter	6.929	6.929	6.929	6.929	TRUE
!Double bond/angle parameter: overcoord	0.3842	0.3989	0.3989	0.3989	FALSE
!Double bond/angle parameter: overcoord	2.9294	3.9954	3.9954	3.9954	FALSE
!Not used	-2.4837	-2.4837	-2.4837	-2.4837	TRUE
!Torsion/BO parameter	5.7796	5.7796	5.7796	5.7796	TRUE
!Torsion overcoordination	10	10	10	10	TRUE
!Torsion overcoordination	1.9487	1.9487	1.9487	1.9487	TRUE
!Conjugation 0 (not used)	-1.2327	-1.2327	-1.2327	-1.2327	TRUE
!Conjugation	2.1645	2.1645	2.1645	2.1645	TRUE
!vdWaals shielding	1.5591	1.5591	1.5591	1.5591	TRUE
!Cutoff for bond order (*100)	0.1	0.1	0.1	0.1	TRUE
!Valency angle conjugation parameter	2.1365	2.1365	2.1365	2.1365	TRUE
!Overcoordination parameter	0.6991	0.6991	0.6991	0.6991	TRUE
!Overcoordination parameter	50	50	50	50	TRUE
!Valency/lone pair parameter	1.8512	1.8512	1.8512	1.8512	TRUE
!Not used	0.5	0.5	0.5	0.5	TRUE
!Not used	20	20	20	20	TRUE
!Molecular energy (not used)	5	5	5	5	TRUE
!Molecular energy (not used)	0	0	0	0	TRUE
!Valency angle conjugation parameter	2.6962	2.6962	2.6962	2.6962	TRUE

4.3 Validation of combined ReaxFF parameter set

Several V&V tests need to be performed on the combined ReaxFF parameter set prior to using it in the fluorocarbon polymer formation simulation. The general idea is to compare the C/O/F/Si combined system with the three sub-systems (see Eq. 4.1) respectively. For each comparison group, a unique test case(s) will be used, meaning that the test case should be representative for the part of parameters incorporated into the combined system from this particular sub-system (tests of F-C for *Ref.3*, Si-C for *Ref.2* and Si-F for *Ref.4* or *Ref.7*). For each comparison group, properties such as radial distribution functions (RDF), bond length distributions and bond angle distributions will be measured and the properties should be similar using both the combined system and the sub-system, which indicates no syntax/format mistake was made when performing the combining operations as well as no significant inconsistency was induced during this process. These properties should also be compared with experimental measurements, and good match will suggest that the combined ReaxFF system can describe the tested materials very well.

4.3.1 Si-C system

To test the performance of the combined ReaxFF parameter set in describing Si-C interactions, a Si-C system was constructed and the results were compared against *Ref.2*. Specifically, among the numerous polymorphs of silicon carbide crystal (Shaffer 1969), 3C-SiC was selected as test material due to its high symmetry in molecular structure which makes it fairly easy to reproduce in a MD simulation.

The molecular structure of 3C-SiC crystal is similar to diamond with half of the C atoms in a lattice replaced by Si atoms at the same positions. The 3C-SiC crystal can be conveniently created using LAMMPS diamond lattice with lattice constant of 4.376 Å, see Fig. 4.2.

The constructed material was then thermally equilibrated under NPT ensemble at 300 K and 0 pressure, using parameter sets from both the combined system and *Ref.2*. The timestep was 0.2 fs and the simulation ran for 10^6 steps (0.2 ns). It was found that in both cases the material reached thermal equilibrium almost instantaneously and the crystalline structure was well maintained, indicating that both systems were able to accurately describe the Si-C interactions in this 3C-SiC crystal. However, there are some discrepancy in the results. By tracking the trajectories of all the atoms in within the whole simulation duration, it was found that the material modeled using *Ref.2* parameter set appeared to be "softer"

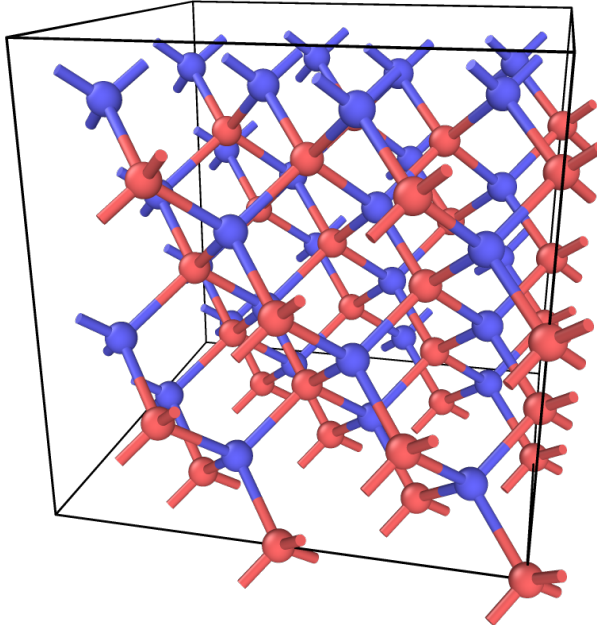


Figure 4.2: Molecular structure of 3C-SiC crystal (red=Si, blue=C) in a 8.752 Å long (2 times lattice constant) cubic simulation box

than using the combined parameter set, meaning that the amplitudes of all atoms oscillating around their center positions in the *Ref.2* system are slightly larger, while the oscillation frequencies are slightly lower than in the combined system therefore the thermal energy of the whole system can still match the temperature of 300 K in both cases. This discrepancy was also reflected in the RDFs, see Fig. 4.3 for the partial RDFs from both test cases. It can be seen that the peak positions for all three curves as well as the relative magnitude for different curves match well across two test cases, while the peaks from the test case of *Ref.2* are generally wider than the corresponding peaks from the test case of the combined parameter set except the first major peak of Si-C pair. This can be explained since the Si-C and Si-Si interaction parameters are almost identical for the two parameter sets while the C-C interaction parameters are slightly different. As shown in Fig. 4.2, the only type of bond existed in 3C-SiC crystal is Si-C bond, which is represented in the RDF as the first major peak of the Si-C curve. The Si-C bonded potential plays a major role when calculating the overall system energy and thus the major peaks are similar due to similarity in Si-C interaction parameters. On the other hand, although the C-C pairs are not bonded, they can also contribute to the overall system energy through other type of potentials such as angle, torsion and non-bonded potentials, and the difference in C-C interaction parameters could possibly affect the relative positions of the Si/C atoms which are not directly bonded and

cause the broadening of other minor peaks in the RDF.

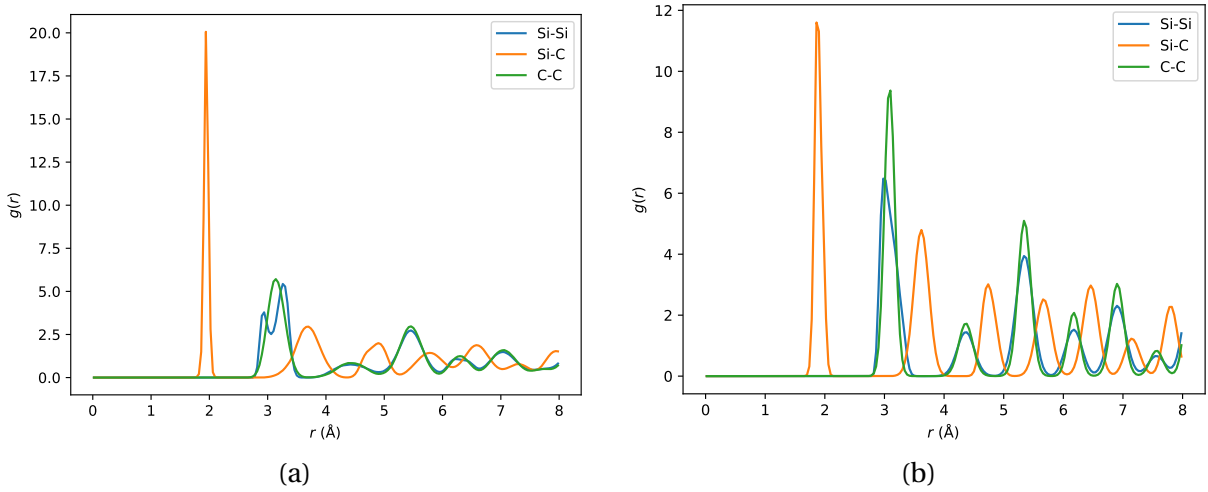


Figure 4.3: Comparison of partial RDFs for 3C-SiC crystal, using ReaxFF parameters from (a) Ref.2, (b) the combined parameter set

The bond analysis was also performed for both test cases. Here the bonds were defined using a cutoff radius of 2.5 Å (a bond will be created for any atom pairs with interatomic distance less than the cutoff radius). The value of the cutoff radius is arbitrary as long as it can accurately reflect the actual physics. In our case, a cutoff radius of 2.5 Å will ensure that only the Si-C bonds can be created and will be created for any neighboring Si-C pairs, and the effectiveness was already shown in Fig. 4.2.

The results of the bond analysis are summarized as the bond length distributions as well as the bond angle distributions, presented in Fig. 4.4 for comparison. Since only the Si-C bonds were created, the bond length distributions are for Si-C bonds only and the bond angle distributions are for Si-C-Si and C-Si-C pairs (middle atom being the vertex of the angle), as shown in Fig. 4.2. It can be seen from Fig. 4.4 that the bond length distributions are similar for both test cases with the distribution for the combined parameter set being slightly wider. For the bond angle distributions, more discrepancies can be found such as the shape of the distribution for the *Ref.2* parameter set is less symmetrical and wider. These findings support our conclusions from the RDF results since the difference in C-C interaction parameters should affect the distribution bond angle more than for the bond length, and the discrepancy in bond angles would introduce more variations to the relative positions of the atoms which not directly bonded and therefore cause broadening of these

long-range minor peaks in RDFs.

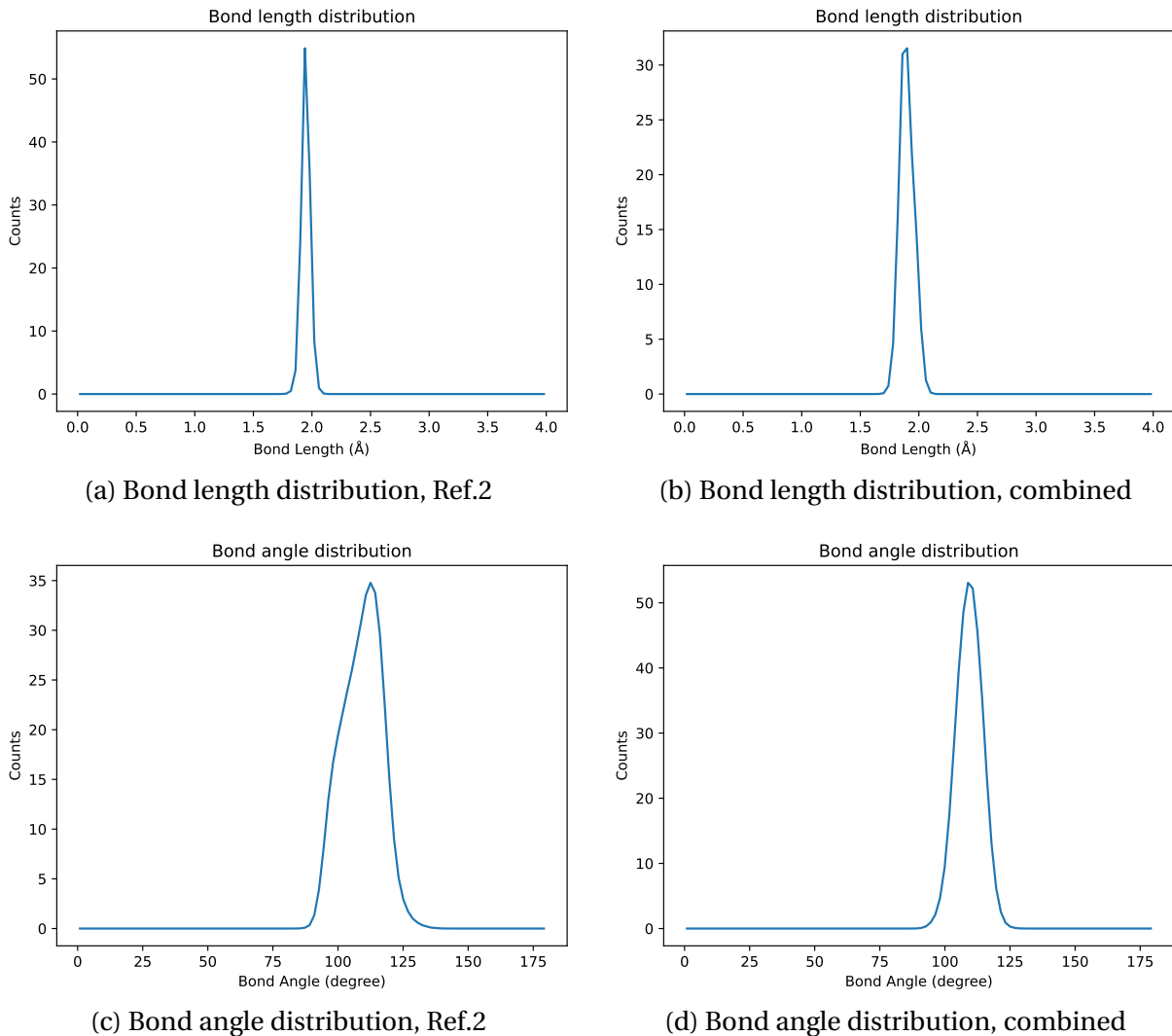


Figure 4.4: Comparison of results from bond analysis for 3C-SiC crystal, using ReaxFF parameters from both Ref.2 and the combined parameter set

The results were also compared to published data. It was found that in experiment the Si-C bond length was measured to be 1.89 Å (Ayalew 2004), while our results predicted 1.94 Å for the *Ref.2* parameter set and 1.90 Å for the combined parameter set. The bond angle of both Si-C-Si and C-Si-C pairs was measured to be 109° in another MD work using different interatomic potentials (Vashishta et al. 2007), while our work predicted 112.5° for the *Ref.2* parameter set and 109.0° for the combined parameter set. Thus, the results from this work

match published data very well and the combined parameter set performs even better than the *Ref.2* parameter set.

Overall, satisfying performance of the combined ReaxFF parameter set was achieved since it not only matched the performance of the *Ref.2* parameter set but also accurately predicted bond properties matching some published data. Thus, the combined ReaxFF parameter set passed the Si-C system test.

4.3.2 F-C system

To test the performance of the combined ReaxFF parameter set in describing F-C interactions, F-C systems were constructed and the results were compared against *Ref.3*. Specifically, fluorographene was first tested since a test case for it is already available in LAMMPS release version. Apart from that, CF_4 molecules were also selected as the test material since the majority of this work is related to CF_4 and its corresponding CF_x ($x = 1 \sim 3$) radicals. The results for the tests of both materials are presented in two separate subsections following below.

Fluorographene

The molecular structure of fluorographene is similar to graphene where a two dimensional carbon sheet of sp^3 carbons is located in the middle with each carbon atom connected to one fluorine atom, and the material was first created in 2010 (Robinson et al. 2010). The initial structure of fluorographene was first prepared, presented in Fig. 4.5, where the middle carbon layer is surrounded by two layers of fluorine atoms with one on each side.

The prepared material was then thermally equilibrated under NVT ensemble with temperature of 100 K, using parameter sets from both the combined system and *Ref.3*. The timestep was 0.2 fs and the simulation ran for only 300 steps (60 fs) since the target of this test case can be achieved already. It was found that both parameter sets can well maintain the structure of fluorographene. Due to the short duration of the simulation, the system was not able to reach thermal equilibrium, and vertical oscillation of bonded C-F layers were observed in both cases.

In fact, the two parameter sets predicted exactly the same results for this fluorographene system, which is expected and can be further applied to any F-C system. Note in the combining strategy Eq. 4.1, *Ref.3* was used as the base system and other reference systems were additive, which means any interactions that are already existed in *Ref.3* should not be modified during the combining process and the combined system should use exactly the

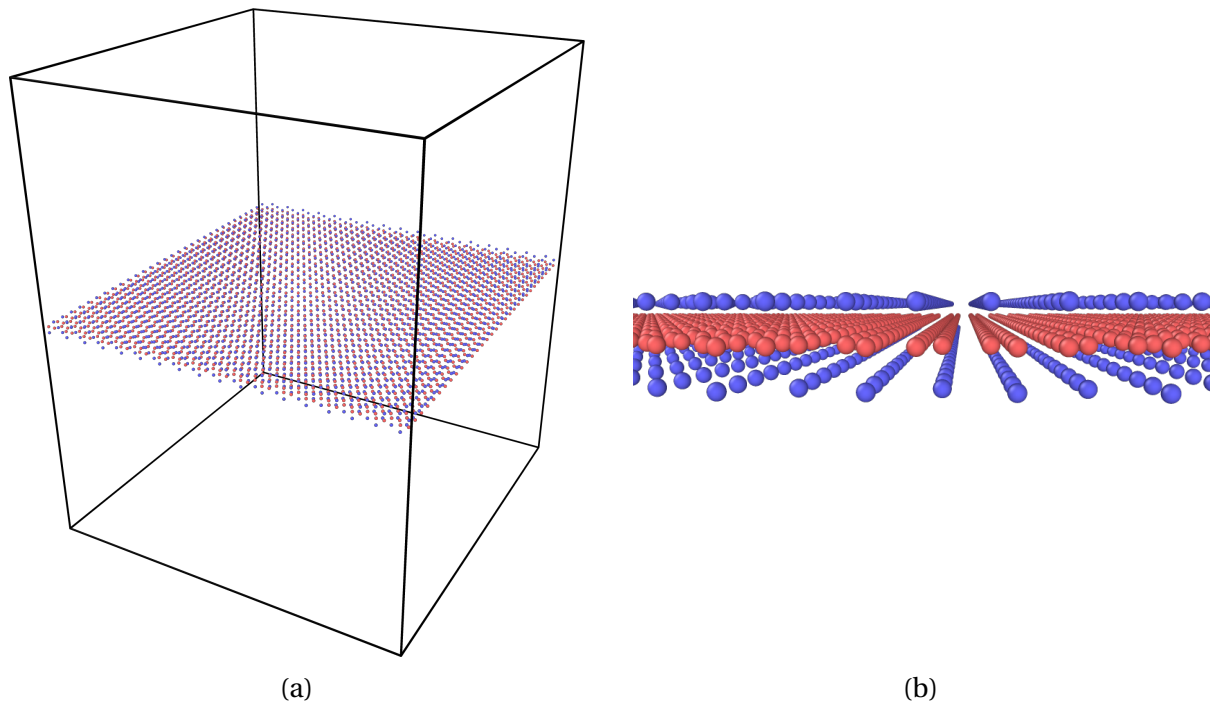


Figure 4.5: Molecular structure of fluorographene sheet (red=C, blue=F) (a) in a $81.1158(x) \times 82.1773(y) \times 100.032(z)$ Å³ horizontally periodical simulation box; (b) zoom-in front view.

same parameters for the same interactions. For any F-C system, only the interactions of F-F, F-C and C-C need to be calculated, and there should be no difference for the ReaxFF parameters involved in these interactions from both the two parameter sets.

The RDFs were also measured, see Fig. 4.6, and the results support the findings. Note the system was not able to reach thermal equilibrium, so the RDFs were not reaching steady state. Thus the partial RDFs were measured at the very last timestep $n_{\text{step}} = 300$ for both cases instead of a moving average of a range of time series. Therefore the RDFs appear to be spikier than the previous results. Despite that, the RDFs using the two parameter sets perfectly match each other, as shown in Fig. 4.6, indicating that no errors or inconsistencies were induced to the parameters of F-C interactions when performing the combining process. Note the goal in the first test was not to match the simulation results with any experimental work (which will be available in the next test), instead, it was to confirm that the combined parameter set is performing as well as *Ref.3* parameter set. Thus, the combined ReaxFF parameter set passed the first test of F-C system.

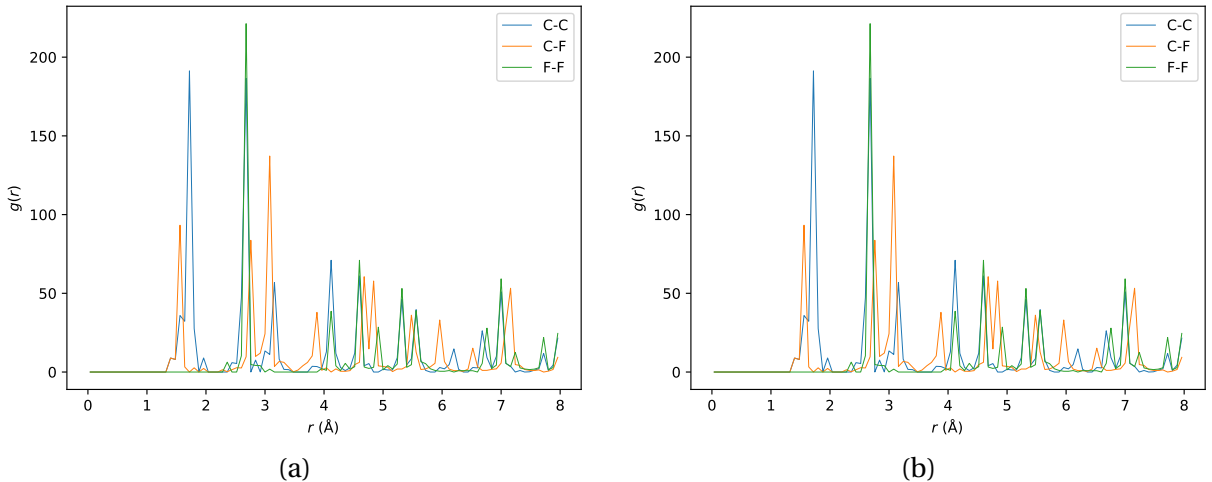


Figure 4.6: Comparison of partial RDFs for fluorographene, using ReaxFF parameters from (a) Ref.3, (b) the combined parameter set

CF₄ molecules

Since CF₄ molecule as well as its resulting radicals CF_x ($x = 1 \sim 3$) are heavily used in this work, the performance of the combined ReaxFF parameter set in modeling CF₄ molecules

are also tested here.

The molecular structure of CF_4 is simply tetrahedral with 1 carbon atom located at the center and 4 F atoms located symmetrically at 4 corners, and the angle of a F-C-F bond pair is generally 109.5° . Using these properties, a template (usually contains information of atom type and relative position of all atoms within a molecule) of a CF_4 molecule can be created, which can then be used as a data file for LAMMPS to generate multiple molecules in a simulation box. As shown in Fig. 4.7a, 10 CF_4 molecules were randomly placed in a cubic simulation box with 20 \AA in length, where periodical boundary conditions were applied for all three directions.

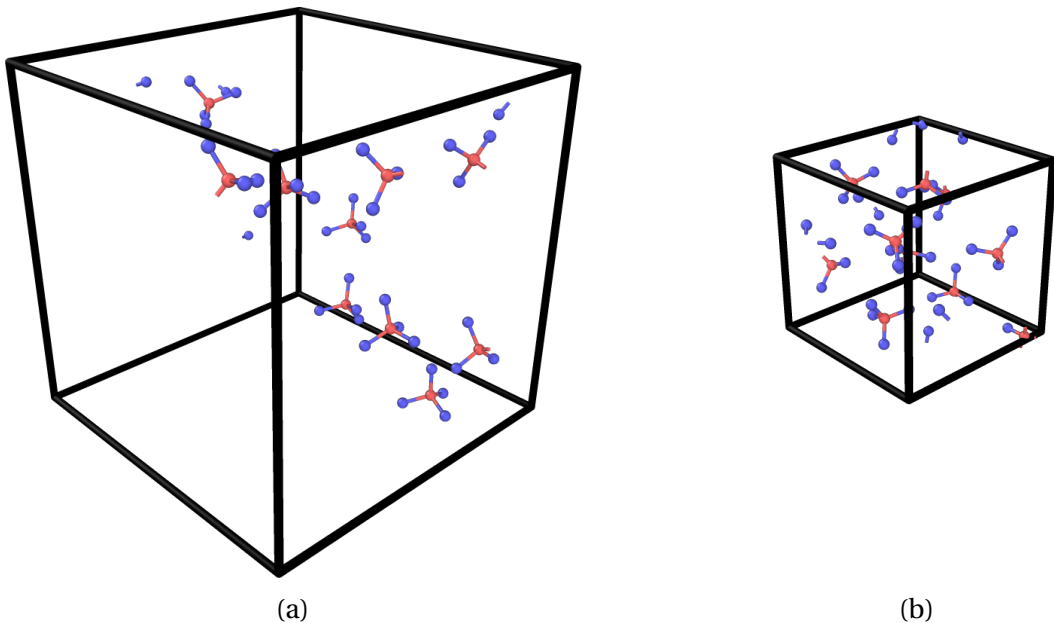


Figure 4.7: Molecular structure of CF_4 molecules, with 10 molecules in a periodical simulation box (red=C, blue=F): (a) initial setup with 20 \AA in cubic box length; (b) after 0.5 ns box shrank to 10.34 \AA in cubic box length.

The prepared material was then thermally equilibrated under NPT ensemble with temperature of 120 K and pressure of 1.0 atmosphere, using parameter sets from the combined system only. The timestep was 0.5 fs and the whole simulation ran for 10^6 steps (0.5 ns) in total. Note the low temperature condition was used in order to increase the density (decrease the box size) at equilibrium, otherwise the simulation box would grow too large (300 K was tested) so that it is difficult to visualize the molecule structures. Using damping parameters

of 50 fs for temperature and 500 fs for pressure respectively, the system shrank slightly and was able to reach thermal equilibrium after about 10^5 steps (50 ps), and the final system state is presented in Fig. 4.7b, where the cubic box length decreased to 10.34 Å. It was also found that the tetrahedral structure of all the 10 CF_4 molecules was well preserved, with no bond breaking and reforming during the whole process, indicating that the combined parameter set is also able to stably model the C-F interactions in CF_4 molecules, in addition to in fluorographene.

The RDF was also calculated, as shown in Fig. 4.8. The location of the first peak of the C-F pair curve was measured to be 1.40 Å, which matches the C-F bond length measurement in other DFT work (1.3841 Å) and ReaxFF work (~ 1.41 Å) (Singh et al. 2013). The C-F bond length was measured in experiments to be 1.34 Å (Project 2020), so all the MD models slightly overpredict the C-F bond length.

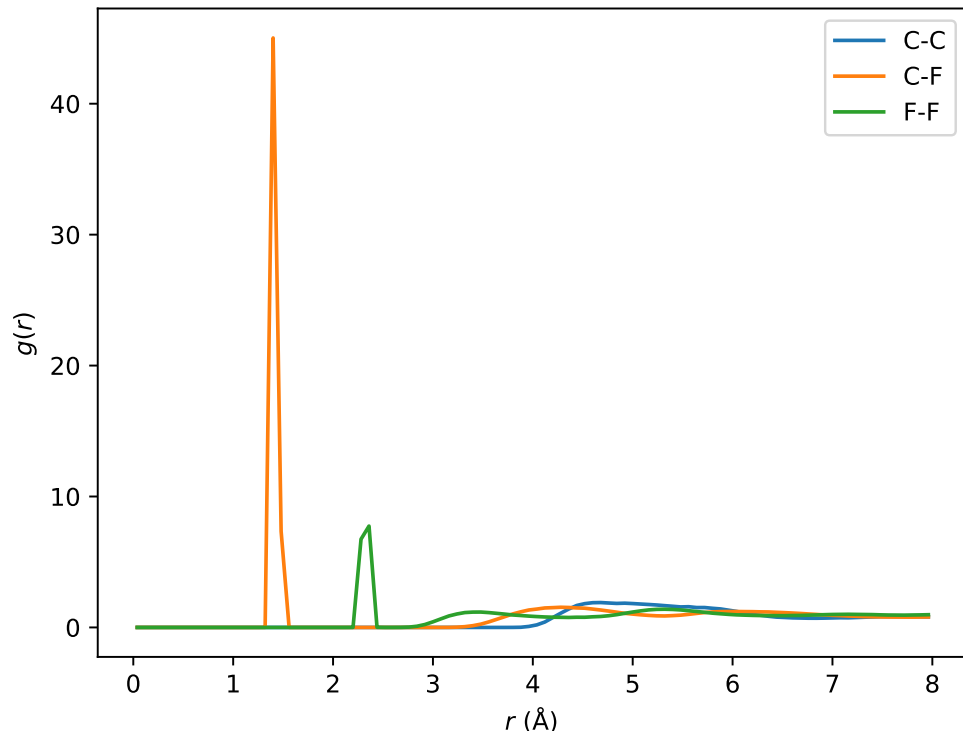


Figure 4.8: Partial RDF for CF_4 , using ReaxFF parameters from the combined parameter set

Overall, the combined ReaxFF parameter set showed satisfying performance in modeling F-C systems. Not only it exactly matched the performance of the *Ref.3* parameter

set but also it showed stability when describing different F-C systems. It also predicted C-F bond properties matching both other simulation results and published experimental efforts. Thus, the combined ReaxFF parameter set passed the F-C system test.

4.3.3 Si-F system

To test the performance of the combined ReaxFF parameter set in describing Si-F interactions, tests for Si-F system were constructed and the results were compared against both *Ref.4* and *Ref.7*. Specifically, a random system, which does not exist in reality but can be used for testing purpose, was first manufactured where many Si and F atoms were randomly placed into a periodical simulation box. Apart from that, SiF_4 molecules were also selected as the test material since it was heavily used in this work for estimating the sticking coefficients of different SiF_x ($x = 1 \sim 3$) radicals, presented in next chapter. The results for the tests of both materials are presented in two separate subsections following below.

Note it is expected to see more discrepancy in the tests for Si-F system than for previous Si-C and F-C systems, which is due to the least amount of parameters from either *Ref.4* or *Ref.7* were transferred to the combined system. As shown in Eq. 4.1, only the parameters for Si-F interactions from either *Ref.4* or *Ref.7* were incorporated into the combined parameter set, which means the parameters for standalone interactions of Si or F in the combined parameter set are independent from both references. Thus, some discrepancies could be expected.

Manufactured random system

The random Si-F system was manufactured by randomly placing 200 Si atoms and 800 F atoms in a periodical cubic simulation box (20 Å in length), using LAMMPS *create_atoms random* command. The same random seeds were used so that the initial state of the random system would be the same for different tests.

The manufactured system was then thermally equilibrated under NPT ensemble with temperature of 300 K and pressure of 1.0 atmosphere, using parameter sets from both the combined system and *Ref.7*. (Note the test based on *Ref.4* was also performed, however, the results did not match expectation, especially for the F-Si-F bond angles, which will be detailed in next section when discussing SiF_4 molecules.) The timestep was 0.5 fs and the whole simulation ran for 2×10^5 steps (0.1 ns) in total. Using damping parameters of 50 fs for temperature and 500 fs for pressure respectively, the system expanded slightly and was

able to reach thermal equilibrium after about 5×10^4 steps (25 ps), and the final system state is presented in Fig. 4.9 for both parameter sets.

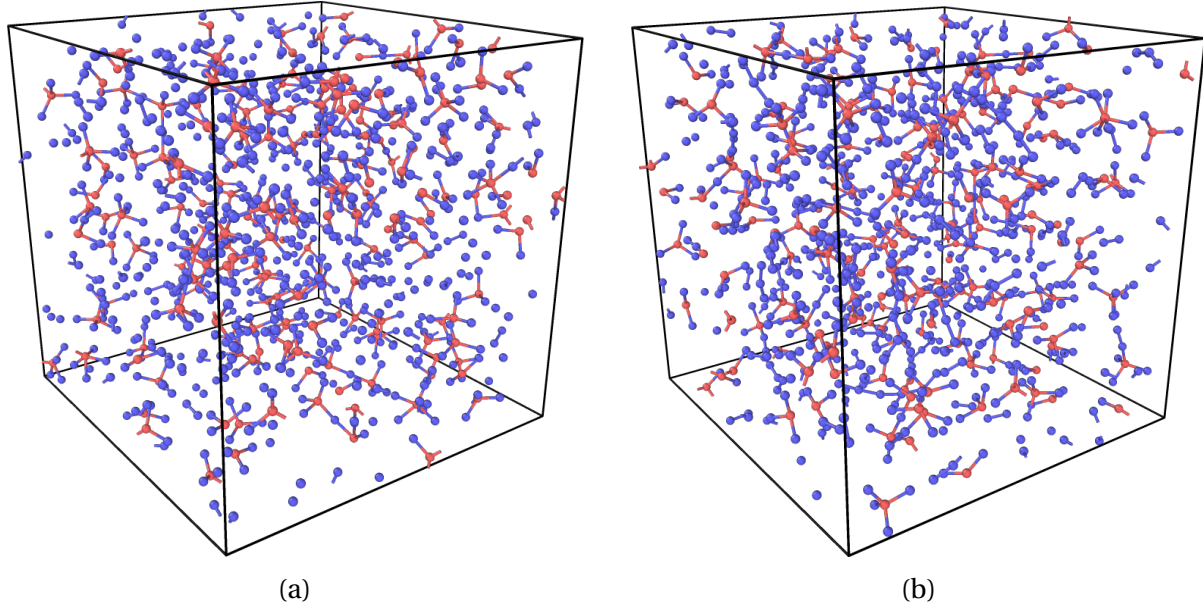


Figure 4.9: Molecular structure of the manufactured Si-F random system, using ReaxFF parameters from (a) Ref.7, (b) the combined parameter set

It was found that the two parameter sets gave similar final densities (1.680 g/cm^3 for the *Ref.7* parameter set and 1.693 g/cm^3 for the combined parameter set), indicating that they performed similarly in estimating the interatomic forces, especially for the non-bonded pairs. Using a cutoff radius of 2.0 \AA , the coordination numbers were estimated for Si atoms in both test cases and are listed in Table 4.2. It can be seen that both parameter sets gave similar results except the *Ref.7* parameter set predicted more Si atoms with coordination number equal to 4 (more SiF_4 and less SiF_3).

The partial RDFs were also calculated and are presented in Fig. 4.10 for both the two parameter sets. The Si-F pair curves in the two plots match each other very well, which is due to the two parameter sets share the same parameters for Si-F interactions. For the F-F pair, the curves match well except the first major peak in Fig. 4.10b shifted slightly towards the left, indicating shorter F-F bond length. For the Si-Si pair, however, more discrepancy can be found since the curve in Fig. 4.10b showed more significant bifurcation for the first major peak than in Fig. 4.10a. This is less of a concern since first the Si-Si pairs in this

Table 4.2: Comparison of coordination numbers for Si atoms in the manufactured Si-F random system, using both ReaxFF parameter sets

Coordination Number	Ref.7 parameter set	Combined parameter set
1	19	19
2	58	62
3	66	86
4	44	28

system are not really bonded, see Fig. 4.9, therefore their relative positions will be heavily affected by a lot of other interactions. Secondly, the Si-Si pairs will be more of a concern when modeling materials such as SiO_2 and crystal Si, and our later results will show that the combined parameter set is able to work with both materials very well.

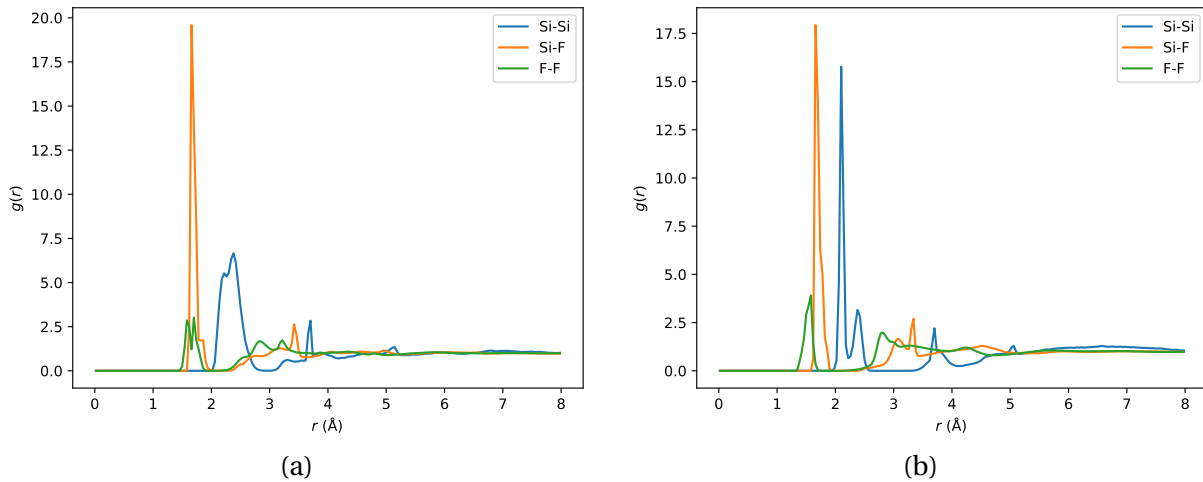


Figure 4.10: Comparison of partial RDFs for the manufactured Si-F random system, using ReaxFF parameters from (a) Ref.7, (b) the combined parameter set

Since the manufactured Si-F random system does not really exist in reality, the goal of this test was to perform cross comparison between two ReaxFF parameter sets rather than to compare with experiments (which will be covered in next section for testing SiF_4 molecules). Based on the comparison results, we conclude that the combined ReaxFF parameter set has passed the first test of Si-F system.

SiF_4 molecules

In order to estimate the sticking coefficients of SiF_4 molecules as well as SiF_x ($x = 1 \sim 3$) radicals, the performance of the combined ReaxFF parameter set as well as *Ref.4* and *Ref.7* in modeling SiF_4 molecules were also tested. In fact, as mentioned earlier, the performance in modeling SiF_4 molecules was also the main reason why we decided to take the parameters for Si-F interaction terms from *Ref.7* instead of from *Ref.4*, see Eq. 4.1.

The molecular structure of SiF_4 is almost identical to CF_4 : the geometry is also tetrahedral with 1 silicon atom located at the center and 4 F atoms located symmetrically at 4 corners; the angle of a F-Si-F bond pair is 109.5° , too; the only difference is that the Si-F bond is longer (1.58 \AA) than the C-F bond (1.34 \AA). Using these properties, a similar template of a SiF_4 molecule was created, and was then used as a data file for LAMMPS to generate multiple molecules in a simulation box. Similarly, 10 SiF_4 molecules were randomly placed in a cubic simulation box with 20 \AA in length, where periodical boundary conditions were applied for all three directions.

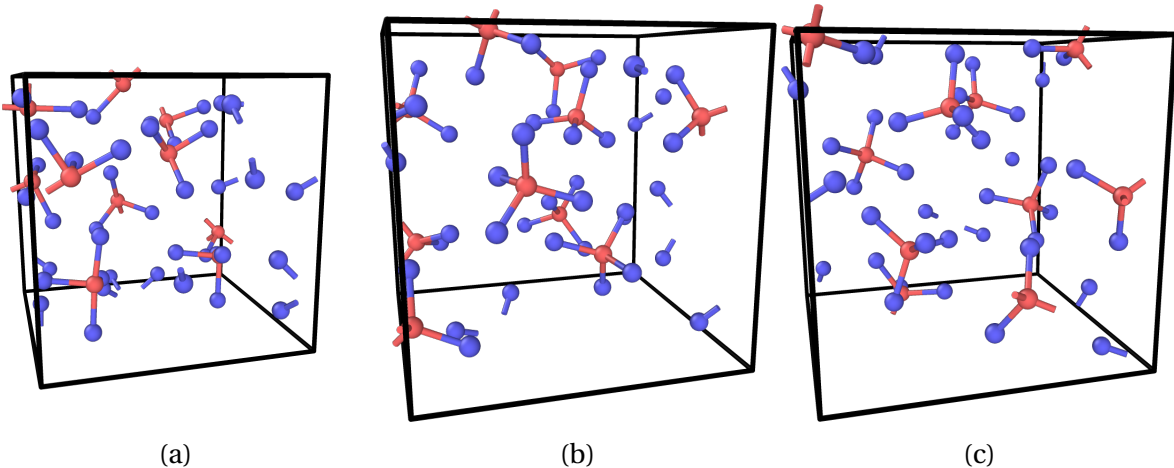


Figure 4.11: Molecular structure of thermally equilibrated SiF_4 molecules at 120 K , with 10 molecules in a periodical simulation box (red=Si, blue=F), using parameter set respectively from: (a) *Ref.4*; (b) *Ref.7*; (c) the combined system.

The prepared material was then thermally equilibrated under NPT ensemble with temperature of 120 K and pressure of 1.0 atmosphere , using parameter sets from the combined system, *Ref.4* and *Ref.7* respectively. The timestep was 0.5 fs and the whole simulation ran for 2×10^5 steps (0.1 ns) in total. Using damping parameters of 50 fs for temperature and

500 fs for pressure respectively, the system shrank slightly and was able to reach thermal equilibrium after about 5×10^4 steps (25 ps), and the final equilibrated system states are presented in Fig. 4.11. It was found that the tetrahedral structure of all the 10 SiF₄ molecules was well preserved using parameter sets from both *Ref.7* and the combined system, see Fig. 4.11b and Fig. 4.11c, with no bond breaking and reforming during the whole process. However, the *Ref.4* system gave an irregular SiF₄ structure, see Fig. 4.11a, where the bond angle of F-Si-F pair seems to be right angle rather than 109.5°. It was also found that the equilibrated density for the *Ref.7* system (≈ 1.75 g/cm³) matched the combined system (≈ 1.83 g/cm³), while the *Ref.4* system (≈ 2.52 g/cm³) significantly overpredicted it, which is possibly due to the inconsistency in SiF₄ molecular structures.

The discrepancy in *Ref.4* parameter set can be better recognized in bond analyses. Using a cutoff radius of 2.0 Å, the Si-F bonds were selectively defined and the bond length distributions as well as the bond angle distributions were calculated, presented in Fig. 4.12 for all three systems. It can be seen that both the bond length and the bond angle distributions match very well between the *Ref.7* system and the combined system. For the *Ref.4* system, the bond length distribution is slightly wider with an additional small peak located to the right. While for the bond angle distribution, there are two peaks where the major peak shifted to the left (below 100°) compared to its expected value, and the minor peak is located around 175°. The exact peak locations of all distributions were measured and compared against experimental measurements, as listed in Table 4.3. It can be seen that all three parameter sets were able to capture the Si-F bond length with a slight overprediction. The bond angle of F-Si-F pair was accurately captured by *Ref.7* and the combined system, but remained problematic in the *Ref.4* system.

Table 4.3: Comparison of the peak locations of the bond length and the bond angle distributions presented in Fig. 4.12 for the three ReaxFF parameter sets, and the corresponding experimental data are also included

Parameter sets	Length (Å)	Angle (°)
Ref.4	1.633	92.0 & 175.3
Ref.7	1.668	109.4
Combined	1.676	109.6
Experiments	1.58	109.5

Overall, the combined ReaxFF parameter set showed satisfying performance in model-

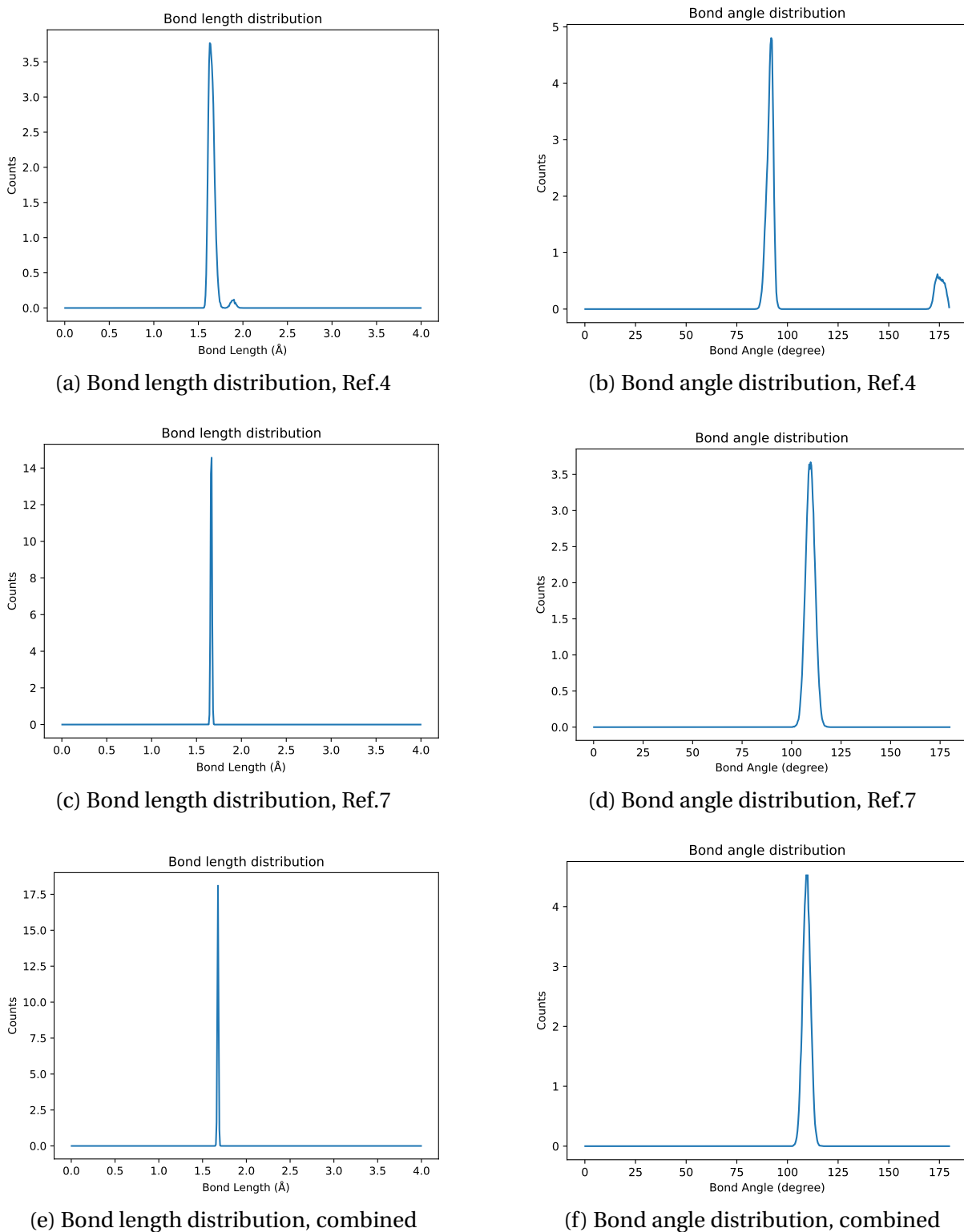


Figure 4.12: Comparison of results from bond analyses for SiF_4 molecules, using ReaxFF parameter sets from both Ref.4, Ref.7 and the combined system

ing Si-F systems. Due to the inconsistency of *Ref.4* parameter set in predicting the tetrahedral structure of SiF_4 molecules, *Ref.7* parameter set was used instead when incorporating Si-F interactions into the combined parameter set. This updated version of the combined parameter set was exclusively used in our later work when SiF_x ($x = 1 \sim 4$) molecules and radicals were involved. The updated combined parameter set not only exactly matched the performance of the *Ref.7* parameter set but also showed stability in describing different Si-F systems. It also predicted Si-F bond properties matching published experimental efforts. Thus, the combined ReaxFF parameter set passed the Si-F system test.

4.4 Deposition of CF_x radicals on amorphous SiO_2

After the combined ReaxFF parameter set has passed all the validation and verification tests, it was used for studying the formation of fluorocarbon polymer film on amorphous SiO_2 substrate. Several parametric studies of different input conditions, such as incident species, incident angles and energies, substrate temperature and the addition of energetic Ar^+ ions, were performed to investigate what factors could play a role in the fluorocarbon polymer formation process. Properties such as thickness and growth rate of the polymer films were mainly compared for each parametric study.

4.4.1 Material preparation and simulation setup

The preparation of amorphous SiO_2 was quite straightforward. The data file for amorphous SiO_2 generated by Tersoff potential in Chapter 3 was used here, but the interatomic forces were described by ReaxFF potential instead. The ideal situation is that the material with ReaxFF can stay stable, keeping its locally tetrahedral structure and globally amorphous structure, and the generally properties such as density and RDFs can remain the same as with Tersoff potential using the same conditions. And that was indeed observed, see Fig. 4.13. The material was almost instantly equilibrated (less than 500 timesteps, 500 fs) with ReaxFF using NPT ensemble at temperature of 300 K and pressure of 0, see Fig. 4.13a. The relative positions of all the atoms did not change, with only slightly shrinking in system sizes ($35.18\text{\AA} \rightarrow 33.95\text{\AA}$). The final density of the material was 2.55 g/cm^3 , which was higher than the density obtained from Tersoff potential (2.288 g/cm^3) and from experiments ($\sim 2.2 \text{ g/cm}^3$), indicating that the amorphous SiO_2 material generated by ReaxFF is slightly denser. The partial RDFs were also calculated, see Fig. 4.13b, and the general shape as well as relative magnitude and the position of the major peaks match previous results (see

Fig. 3.7) very well. It should be noted that the material preparation process can also be seen as a successful validation test of the combined ReaxFF parameter set for a Si-O system.

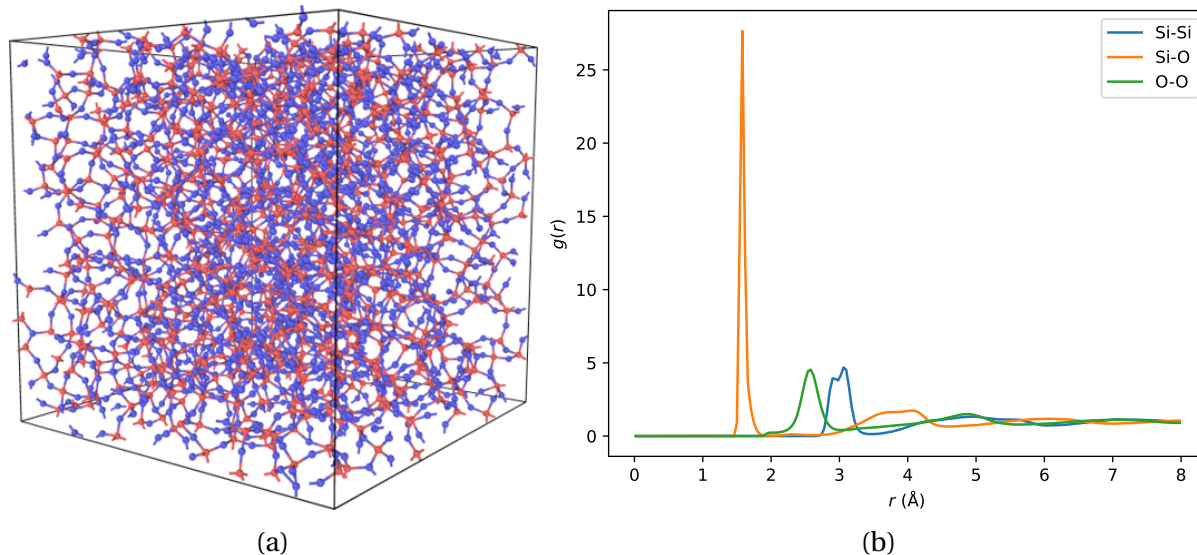


Figure 4.13: Preparation and validation of amorphous SiO_2 : (a) amorphous SiO_2 equilibrated at 300 K using ReaxFF potential; (b) correspondingly partial RDFs.

For the incident species, the general idea is that find data files containing the molecular structure information of the desired species from some online databases, and customize the files to get the corresponding radical structures. For example, the data files for CF_4 and C_4F_8 (Octafluorocyclobutane) can both be found in PubChem (2023), and the related radicals such as CF_2 and C_4F_4 can be obtained by removing some F atoms from the whole molecules, i.e., by adding or removing certain lines within the data files. The downloaded data files are not necessarily compatible with LAMMPS, thus certain efforts need to be performed, manually or using some Python scripts, in order to translate the data files into LAMMPS format.

After the data files for both the substrate materials and the incident species were well prepared and validated, they were both read by a LAMMPS input file to setup a deposition simulation. For all the simulation cases performed in this chapter, a time step of 0.25 fs was used. Due to the limited computational power we had at the time of performing these simulations, the substrate materials were downscaled laterally in order to have a reasonable run time. The ratio of the downscale were different for different cases, but were

generally between 0.5 (a quarter of the original volume) to 1 (no downscale) in length in x and y directions. The vertical dimension (in z direction) of the material was mostly kept the same since the incident species were inserted in z direction. Periodic boundary conditions were used in the lateral directions, and finite boundary condition was used in the vertical direction. Some empty space was added above the materials for the incident molecules to travel and for the polymer films to grow. The substrate materials were generally thermally equilibrated at temperature of 300 K, where a thin top layer (10% in thickness) was equilibrated using NVE ensemble so that they can properly leave the simulation box if get removed, a bottom layer (20% in thickness) was kept static so that the substrate would not have some unwanted bulk motions, and the rest of the substrate in the middle was equilibrated using NVT ensemble at 300 K in order to properly dissipate the introduced thermal energy. See Fig. 4.14 for a diagram illustration.

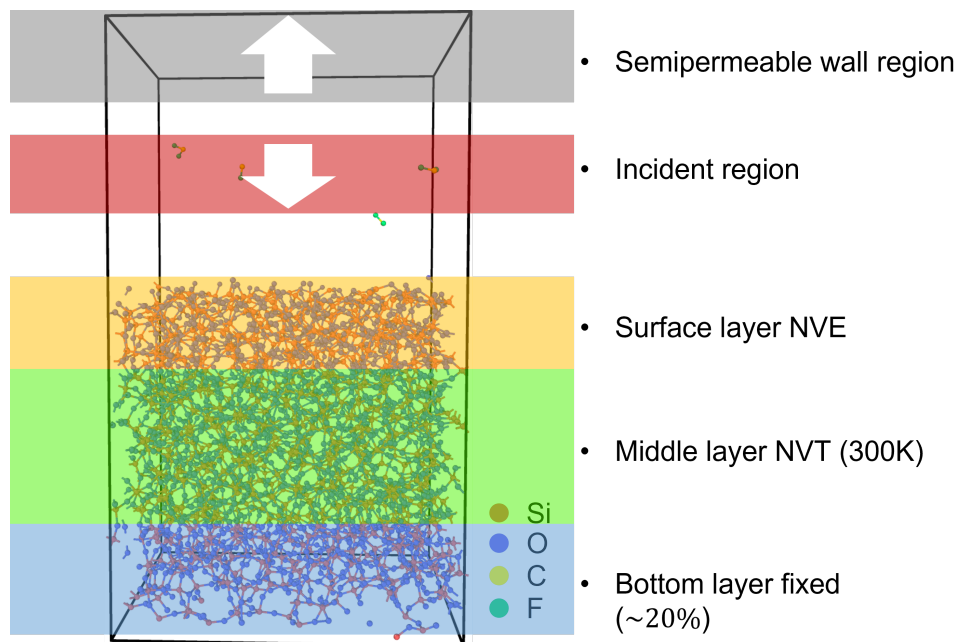


Figure 4.14: Diagram presenting the computational setup of the amorphous SiO_2 deposition simulations.

Constant flux of CF_x species were inserted within a thin layer above and parallel to the substrate top surface at predefined incident angles and energies, see Fig. 4.14, and the initial horizontal positions (x, y) of the inserted molecules were determined randomly with a minimum interatomic distance of 2 Å. There was another virtual region called "semiper-

meable wall region", see Fig. 4.14, which was used to ensure that all the reflected molecules that reached this region can then correctly leave the simulation box, by constraining that the velocity vectors of all the particles within this region can only point upwards.

During the simulation, the trajectories of all the atoms for the entire run were stored in a large data file for a single run case, and the data file can be visualized in some graphical softwares such as Ovito to intuitively understand the process or post-processed using some Python scripts to get the desired information.

In summary, the computational setup for modeling the deposition of CF_x radicals onto amorphous SiO_2 substrate has been built. Several parametric studies were then performed by adjusting the input parameters to investigate what factors could play a role in the fluorocarbon polymer formation process, and the results are discussed in the next few sections.

4.4.2 A general test case for CF_x radicals deposition

After the computational setup was prepared, a general test case for CF_x radicals deposition on amorphous SiO_2 substrate was performed. Since most of the details have already been introduced in Section 4.4.1, only the differences and customizations will be covered here. The size of the substrate material in this test was $(34.4 \text{ \AA})^3$. Both CF and CF_2 radicals were inserted at a ratio of $\text{CF}_2 : \text{CF} = 2$, where the ratio value was picked based on the fact that there is generally more CF_2 radicals than CF radicals in a low temperature fluorocarbon plasma. In total 400 CF radicals and 800 CF_2 radicals were inserted independently, where the number of timesteps between two consecutive incidences was 1000 for CF and 500 for CF_2 . The incident energies for both CF and CF_2 were thermal (0.0259 eV, 300 K), and the incident angles were normal with respect to the substrate surface. The whole simulation ran for 4E5 steps, and the deposition results are visualized in Fig. 4.15 at multiple timesteps.

It can be found from Fig. 4.15 that the CF_x radicals were able attach on the substrate surface and form a thin film. Due to their very low kinetic energies, the radicals did not introduce significant material damage. The growth rate of the film seems to be relatively high when the substrate was uncovered ($0 \rightarrow 2\text{E}5$ steps), but decreased significantly and almost saturated when the coverage ratio got higher ($2\text{E}5 \rightarrow 4\text{E}5$ steps). This can be better understood by plotting the number of attached atoms as a function of timestep, as shown in Fig. 4.16. It can be seen that the number of attached C and F atoms increased almost linearly when the substrate surface was less covered, but nearly reached saturation after around 1.5E5 timesteps. This saturated fluorocarbon film was only monolayer thick, with

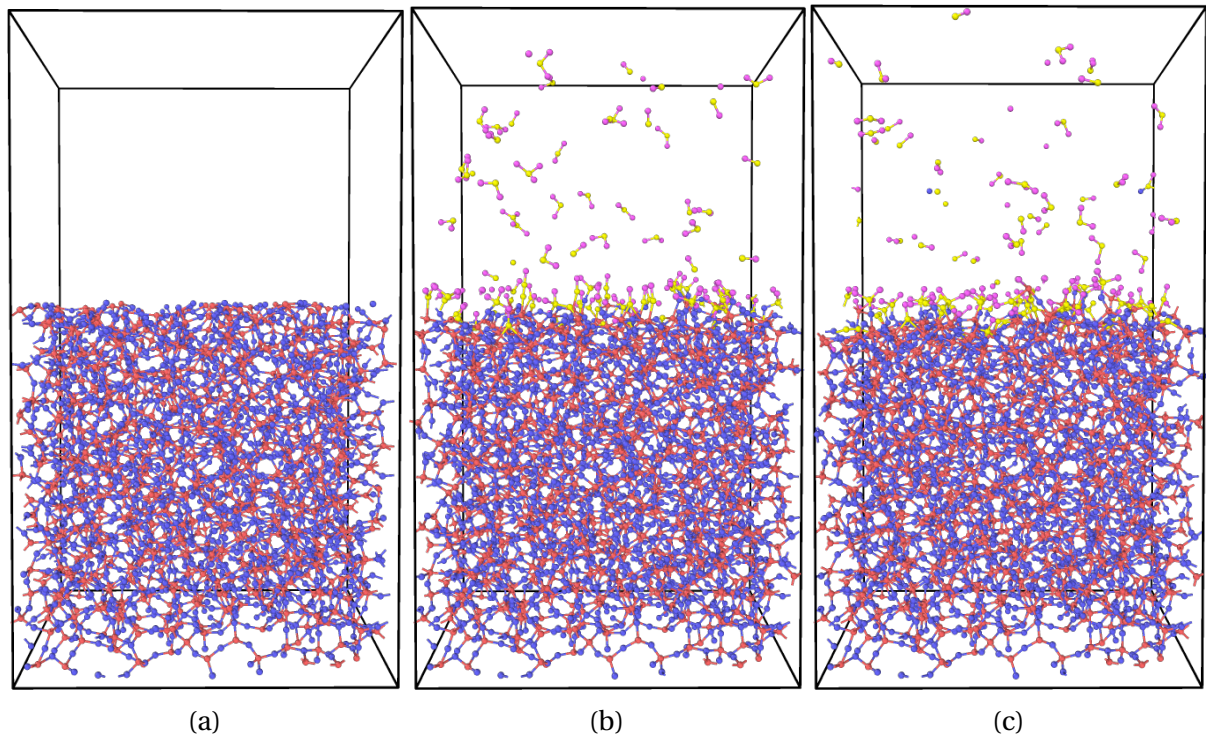


Figure 4.15: Deposition of CF_x radicals onto amorphous SiO_2 substrate (red=Si, blue=O, yellow=C, pink=F), presented here are snapshots at timestep of: (a) 0; (b) 2E5; (c) 4E5.

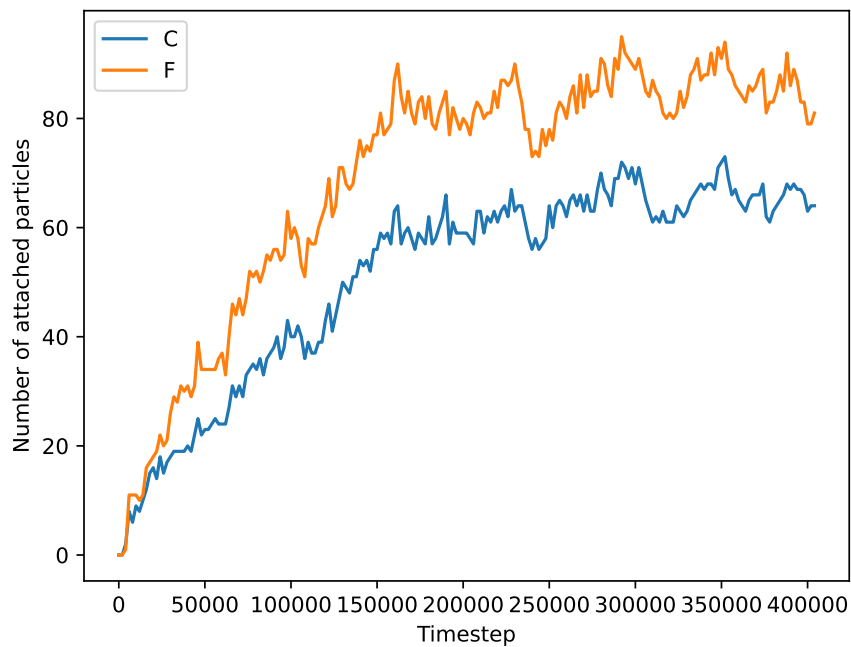


Figure 4.16: Number of attached C and F atoms on SiO₂ substrate as a function of timestep.

the highest F atom being at 37.87 \AA in z axis. Thus, this directed us to several parametric studies trying to figure out what factors could help in growing thick fluorocarbon polymer films.

4.4.3 Substrate temperature dependency

The first parametric study was based on the temperature of the SiO_2 substrate. The computational setup was similar to the test case in last section, except the lateral dimensions of the substrate material were decreased to $20 \times 20 \text{ \AA}^2$ due to the limited computational power we had for running multiple parallel simulation cases. CF and CF_2 radicals were still inserted at a ratio of $\text{CF}_2 : \text{CF} = 2$ and the total number of CF_x incidence was 3000. A parametric study of 6 independent cases was performed for substrate temperature of 200, 220, 240, 260, 280, and 300 K. The number of attached atoms on the substrate surface as a function of timestep was plotted for each case and are compared in Fig. 4.17.

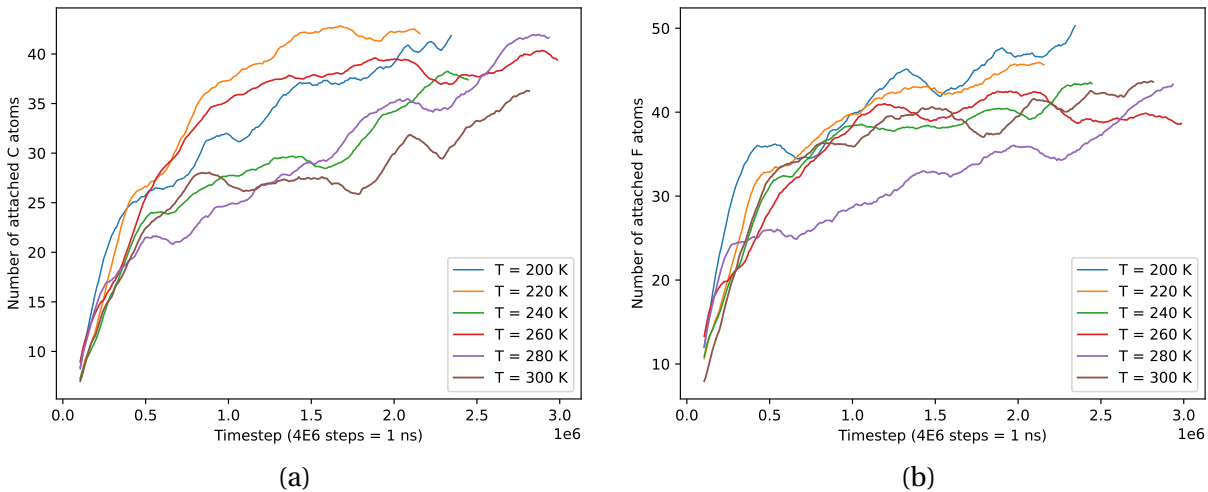


Figure 4.17: Comparison of number of attached atoms as a function of timestep for different substrate temperature, presented here are for: (a) C atoms; (b) F atoms.

It can be seen from Fig. 4.17 that there is no clear trend showing that the growth rate is monotonically related to the substrate temperature, and the number of attached atoms at the end of the deposition seems to be very close for different cases. Therefore, we conclude that the difference among these curves are still within the range of statistical errors and the formation of fluorocarbon polymer on amorphous SiO_2 substrate does not depend on the

substrate temperature, at least within the range of 200 K to 300 K.

4.4.4 CF_x incident energy and angle dependency

The effects of the incident energy and angle of the CF_x species were also tested. The dimension of the substrate ($20 \times 20 \times 34.4 \text{ \AA}^3$) was the same as in the temperature dependency test. CF and CF_2 radicals were inserted at a ratio of $\text{CF}_2 : \text{CF} = 3$ and the total number of CF_x incidence was 1000, where the number of timesteps between two consecutive incidences was 4000. A parametric study of 8 independent cases was performed for incident energy of 1, 5, 10, 25, 50, 75, 100 and 250 eV, in which the incident angle was normal with respect to the substrate surface. The number of attached atoms on the substrate surface as a function of timestep was plotted for each case and are compared in Fig. 4.18. Note only the results for incident energies below 25 eV were presented due to significant material damage was observed in the higher energy cases and the number of attached atoms was not well captured, which will be discussed later in this section.

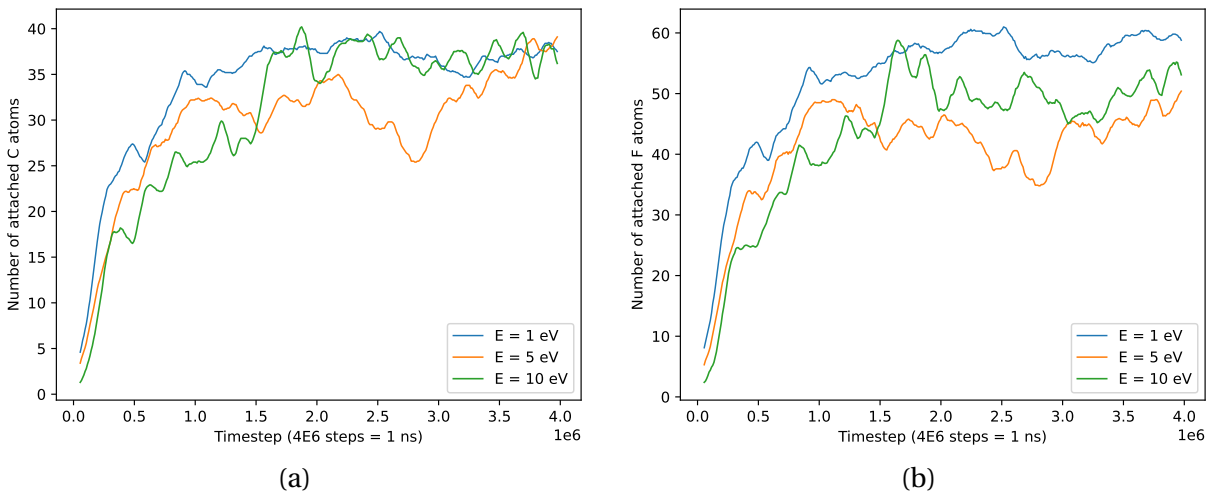


Figure 4.18: Comparison of number of attached atoms as a function of timestep for different CF_x incident energies, presented here are for: (a) C atoms; (b) F atoms.

It can be found that at the beginning of the deposition process, the case with lower incident energy seems to have higher growth rate, indicating that radicals with lower kinetic energy are more likely to attach on bare material surfaces. However, at the end of the process when the substrate was fully covered, all the curves seem to saturate at the same point,

suggesting that the saturated polymer thickness does not depend on the incident energy of the CF_x species.

For the cases with incident energies higher than 20 eV, the induced material damage was so significant that no constant polymer formation can be achieved. As shown in Fig. 4.19, a large portion of underlaying SiO_2 was etched after 4000 CF_x incidence even at 25 eV. For those cases we performed with incident energy of 50 eV or above, all the substrate material was etched at some point during the simulation, and the etch rate was positively related to the incident energy as expected.

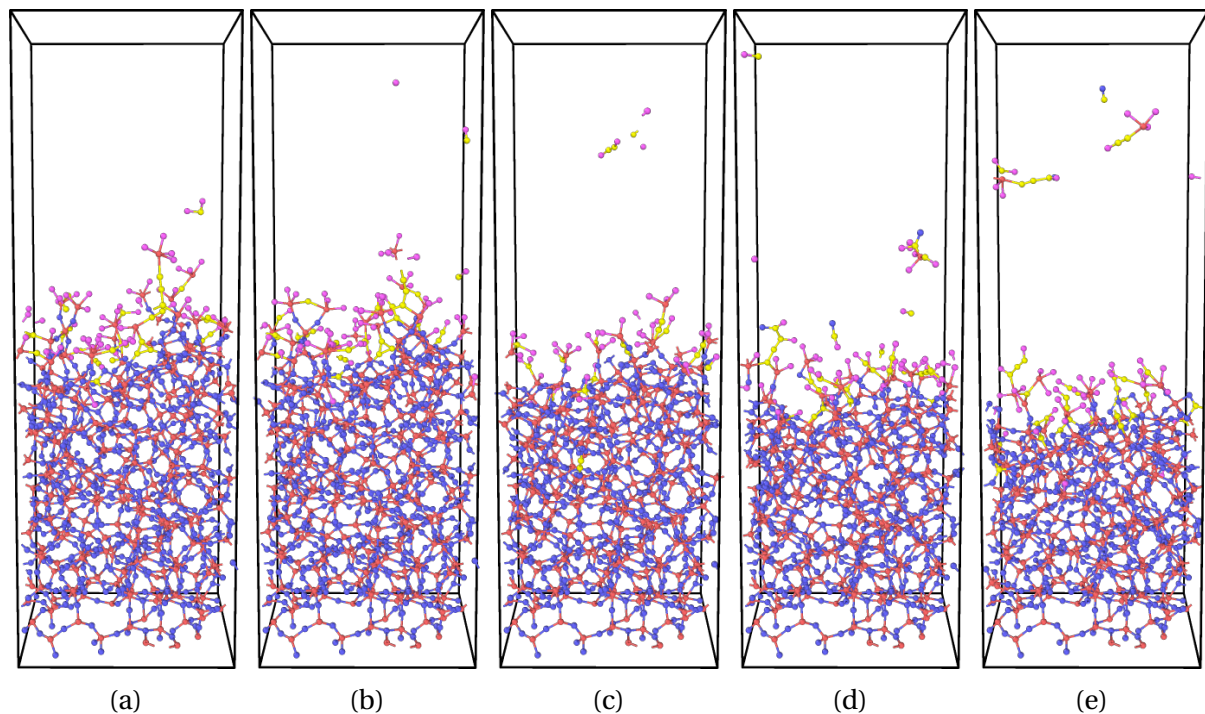


Figure 4.19: Deposition of 25 eV CF_x radicals onto amorphous SiO_2 substrate (red=Si, blue=O, yellow=C, pink=F), presented here are snapshots at timestep of: (a) 0; (b) 1E6; (c) 2E6; (d) 3E6; (e) 4E6

The effect of incident angle was tested by comparing normal incidence cases and random angle incidence cases. Specifically, the incident angle (with respect to surface normal) was randomly sampled from a uniform distribution ranging from 0° to 60° , where 0° points to the negative z direction. Therefore most of the radicals were obliquely inserted, and the center of the incidental solid angle was still normal to the substrate surface so

that all the inserted radicals can effectively reach the substrate. A parametric study of 6 independent cases was performed for incident energy of 1, 5, 10, 15, 20 and 25 eV, and the same Number of attached vs. Timestep plots were measured for each case, as shown in Fig. 4.20.

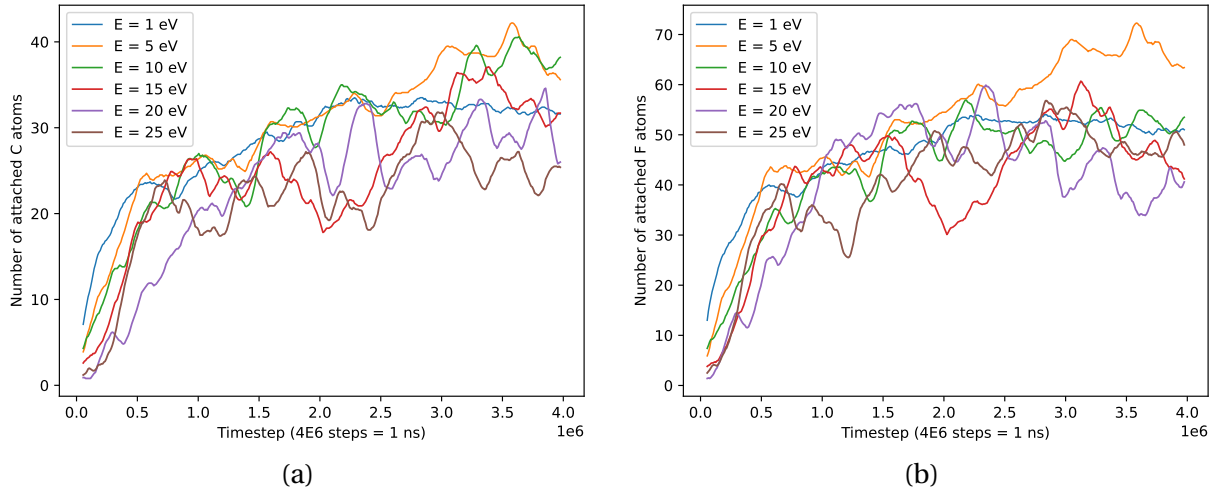


Figure 4.20: Comparison of number of attached atoms as a function of timestep for different CF_x incident energies where the incident angle was randomly sampled, presented here are for: (a) C atoms; (b) F atoms.

It can be seen that the results are similar to the normal incidence cases. Lower energy radicals were easier to attach when the substrate surface was less covered, and all the cases seem to reach saturation around the same level, where the saturation point is also very close to the normal incidence cases with the same energies in Fig. 4.18. Therefore we conclude that the saturated polymer thickness does not depend on the incident angle of the CF_x species.

4.4.5 Effects of energetic Ar ions

The effect of energetic Ar ions on fluorocarbon polymer formation was also investigated, with the expectation that the ions may modify the polymer surface condition by breaking existed bonds and creating more opening sites for more layers to grow on. The dimension of the substrate ($34.4 \times 34.4 \times 34.4 \text{ \AA}^3$) was the same as in previous sections. CF and CF_2 radicals were inserted at a ratio of $\text{CF}_2 : \text{CF} = 3$ and the total number of CF_x incidence was

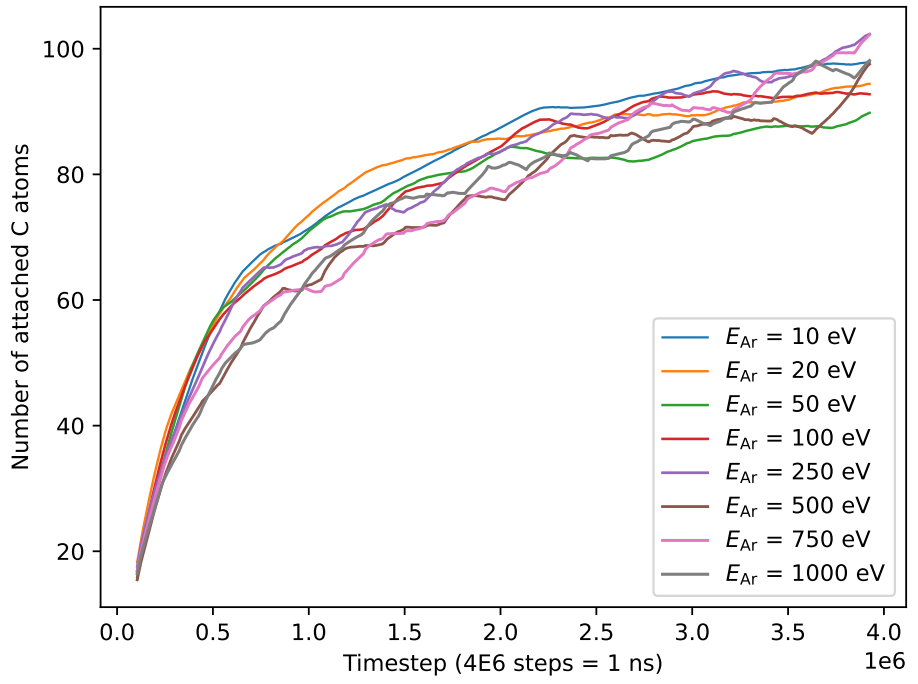
1000, where the number of timesteps between two consecutive incidences was 4000. The CF_x radicals were inserted with kinetic energy of 1 eV and at normal angle for all the cases performed in this test. Energetic Ar^+ ions were also inserted, with the flux being only 3/80 of the flux for CF_x (so total number of incidence was 37 and number of timesteps in-between was 106666). A parametric study was performed for Ar^+ incident energy of 10, 20, 50, 100, 250, 500, 750, and 1000 eV, and for Ar^+ incident angle of 75° (glancing-angle). To reduce the statistical errors, each incident energy case was repeated 3 times (3 same but independent simulation runs with different random seeds), and the results were averaged over the three repeated cases. Therefore, in total there were 24 independent cases (8 energies \times 3 repeats). It should be mentioned that in order to model the interaction between Ar atoms and other already existed atoms, the ZBL potential was used jointly with ReaxFF potential. The number of attached atoms on the substrate surface as a function of timestep was averaged over the three repeated runs and was plotted for each case in Fig. 4.21, for both C and F atoms.

It can be found from Fig. 4.21 that the kinetic energy of the Ar ions seems to slightly affect the number of attached atoms, especially around the beginning of the deposition process where the substrate surface was not fully covered. Specifically, the growth rate seems to be inversely dependent on the Ar energy, i.e., higher energy Ar ions tend to make the polymer growth slower. One possible explanation is that as the incident energy of Ar ions increases, the Ar ions would become so energetic that a significant portion of the already deposited polymer films could be removed. Another possible explanation is that the higher energy Ar ions would transfer more kinetic energy to the substrate surface and increase its temperature, where the higher temperature substrate generally gives lower growth rate when it is partially covered, as previously observed in Fig. 4.17.

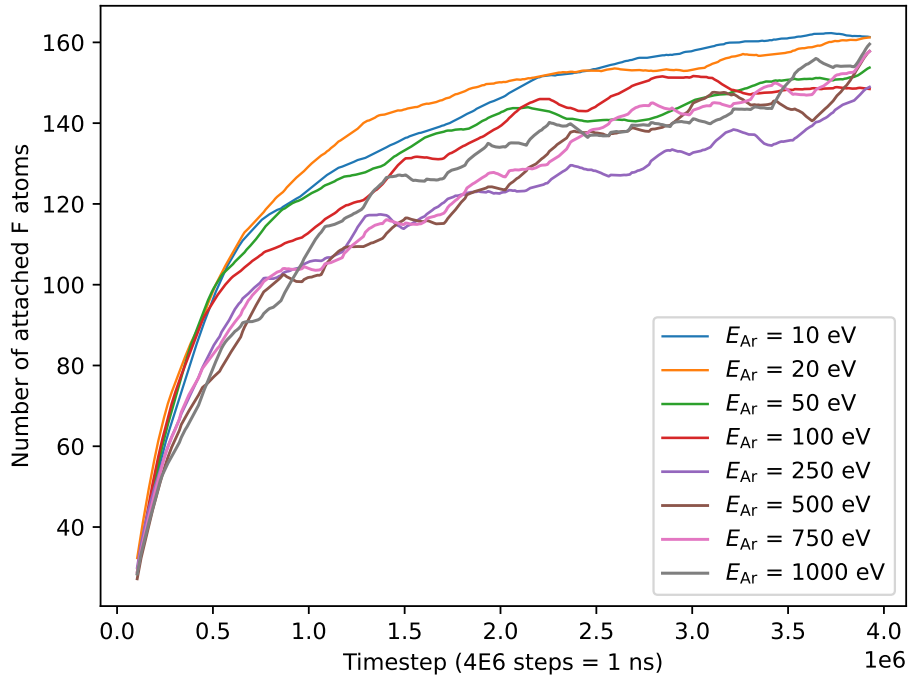
It can also be found that even though the Ar ions could potentially affect the number of attached C atoms, the overall thickness of the polymer film was still self-limiting, similar to the results in Fig. 4.20 where no Ar ions were added. Therefore we conclude that the saturated thickness of the fluorocarbon polymer film does not strongly depend on the addition of energetic Ar ions.

4.5 Effects of different incident species

The effect of different incident species on fluorocarbon polymer formation was also investigated. Instead of using mixed CF_x species as in the previous studies, multiple parametric



(a)



(b)

Figure 4.21: Comparison of number of attached atoms as a function of timestep for different Ar ions incident energies where the incident angles were 75° with respect to surface normal, presented here are for: (a) C atoms; (b) F atoms.

studies were performed using single incident species of CF, C₂F₄ and C₄F₄. The dimension of the substrate differs for each parametric study, where the lateral dimension was altered while the thickness was generally the same.

The first parametric study was for incident species of pure CF radicals. The dimension of the substrate ($20 \times 20 \times 34.4 \text{ \AA}^3$) was the same as in previous sections. 4000 CF radicals were inserted, and the number of timesteps between two consecutive incidences was 1500. The CF radicals were inserted at normal angle and the incident energy was controlled. Ar⁺ ions were also inserted with a $N_{\text{Ar}}/N_{\text{CF}}$ ratio of 3/80. The Ar⁺ ions were inserted at a glancing angle of 85° and the incident energy was also controlled. Therefore, a parametric study was performed for CF incident energy of 5 and 10 eV, and for Ar incident energy of 100, 200, 400, 700 and 1000 eV. In total, 13 independent cases were simulated, including 3 extra cases for CF incident energy of 1, 5 and 10 eV where no Ar ions were added. The number of attached atoms on the substrate surface as a function of timestep was plotted for each case and are compared in Fig. 4.22 for C atoms only.

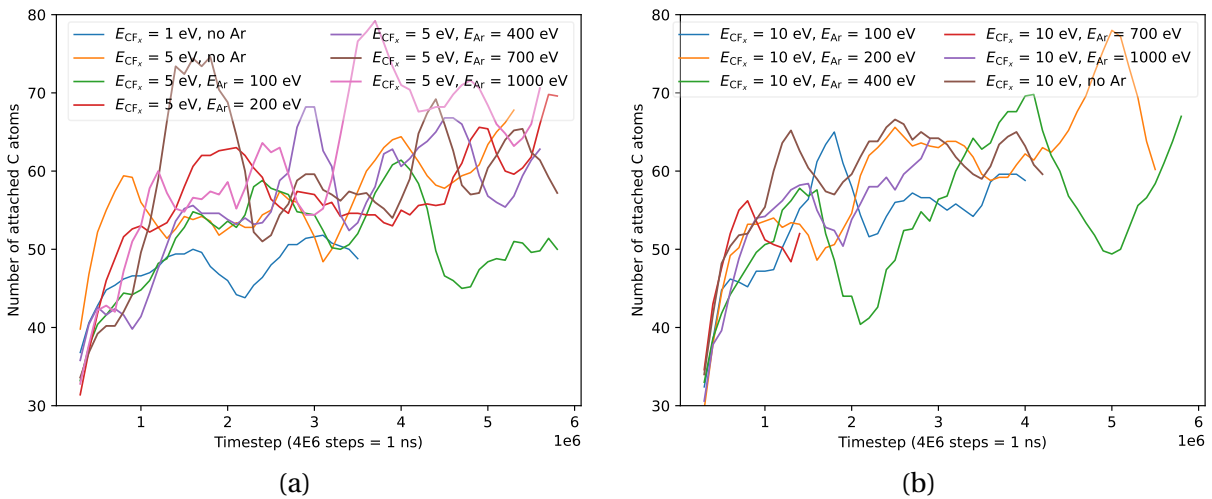


Figure 4.22: Comparison of number of attached C atoms as a function of timestep for different CF incident energies as well as different Ar ions incident energies, presented here are separated by CF incident energy of: (a) 1 and 5 eV; (b) 10 eV.

It can be found from Fig. 4.22 that the curves are still noisy although a moving average scheme has already been applied. The noise is due to the fairly low level of the base data, which can be reduced by increasing the surface area of the substrate. Another reason for the noise is that as the kinetic energies of CF_x and Ar⁺ increase, the significance of sputtering

also increases. The substrate surface condition is in a dynamic balance where each energetic ion incidence will cause a drop in the numbers of attached atoms, followed by a gradual increase as a result of the upcoming incident radicals. Therefore, it can be seen that the curves for the higher energy cases generally have larger fluctuations.

Despite the noise, it can be observed that all the curves generally reached saturation after timestep around 2E6, and the saturation position is approximately the same for different cases, where the results for $E_{Ar} = 200$ eV seem to be slightly higher for both the two CF incident energies. The results match the results from previous parametric studies for mixed CF and CF_2 incidence, where the number of attached C atoms is generally higher for the pure CF incidence cases.

The second parametric study was for incident species of C_2F_4 radicals. The simulation conditions, including the dimension of the substrate, the total number of incidence, the timesteps in between, etc., were generally the same as in previous CF incidence cases, and both C_2F_4 and Ar were inserted. A parametric study of 5 independent cases was performed for different incident energies of C_2F_4 and Ar, and the results are presented as the Number of attached vs. Timestep plots in Fig. 4.23.

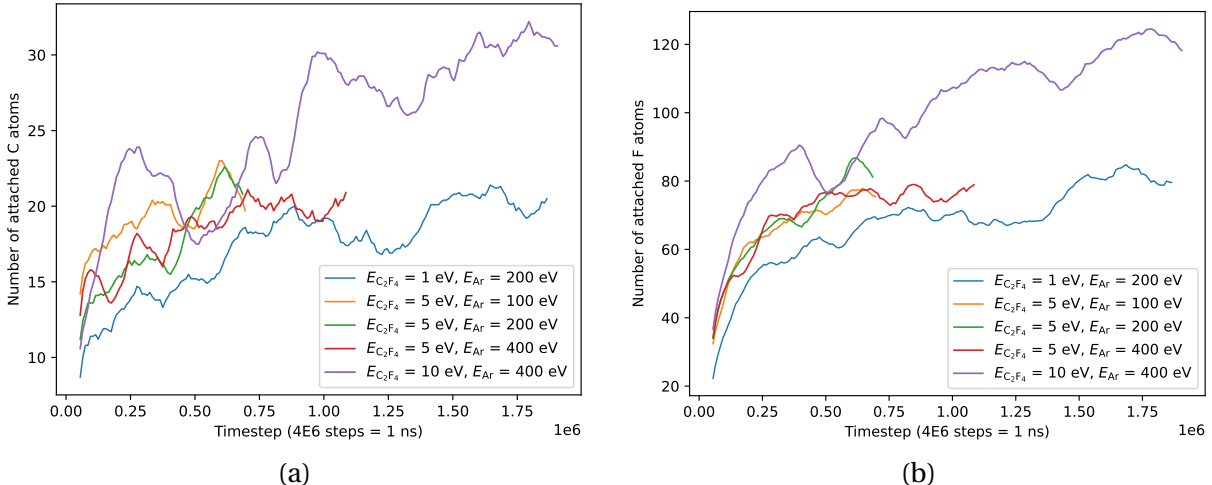


Figure 4.23: Comparison of number of attached atoms as a function of timestep for different incident energies of C_2F_4 and Ar, presented here are for: (a) C atoms; (b) F atoms.

It can be seen from Fig. 4.23 that the effect of incident energies is more prominent in this study. The (10 eV, 400 eV) case was the highest in both the plots for C and F atoms, which matches our observations in the previous studies for both the mixed CF_x incidence and

the pure CF incidence. However, most of the curves still seem to have reached saturation around the timestep of 5E5, which is earlier than the previous cases. The saturated number of attached C atoms is generally lower than the previous studies, possibly due to the high F:C ratio of C_2F_4 molecules and the attached F atoms can terminate the substrate surface from being attached by upcoming radicals.

Another study was for incident species of C_4F_4 radicals. A larger substrate was used with dimension of $34.4 \times 34.4 \times 34.4 \text{ \AA}^3$. 2000 CF radicals were inserted, and the number of timesteps between two consecutive incidences was 1500. The C_4F_4 radicals were inserted at normal angle and the incident energy was 1 eV. No Ar^+ ions were inserted. The same Number of attached vs. Timestep plot is presented in Fig. 4.24.

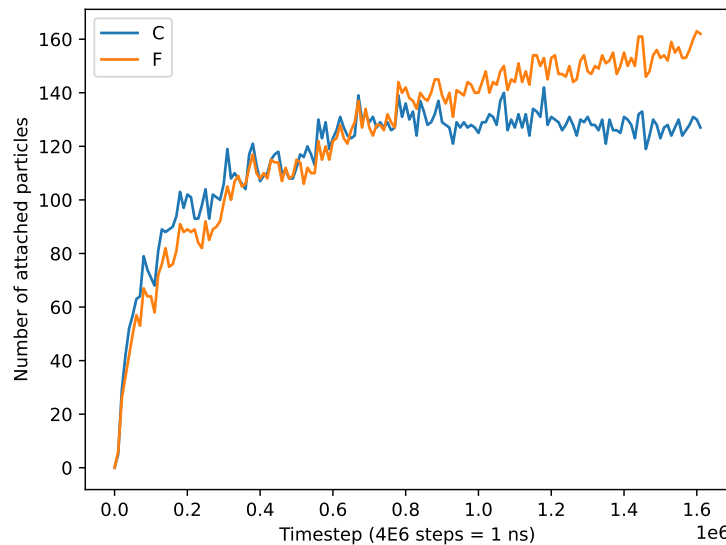


Figure 4.24: Number of attached C and F atoms as a function of timestep for C_4F_4 species incident on amorphous SiO_2 substrate.

It can be seen that the noise level was reduced due to both larger substrate size and lower kinetic energy. The curves follow the same trends as in previous studies, where the C atoms curve reached saturation around timestep of 7E5. The number of attached atoms is higher due to larger top surface of the substrate. In order to compare the results for different cases with different substrate sizes, the number of attached atoms should be normalized with respect to the surface area, which will be performed at the end of next section in Table 4.4 to incorporate the results for different substrate materials.

In summary, in this section we performed parametric studies using single incident

species of CF, C₂F₄ and C₄F₄. It was found that species with lower F:C ratio generally can stick more molecules onto the substrates. However, all the deposition cases studied have reached saturation at some point, indicating that only a thin fluorocarbon polymer film can be formed on top of amorphous SiO₂ substrate using only CF_x species deposition, with or without the addition of energetic Ar⁺ flux.

4.6 Effects of different substrate materials

The effect of different substrate materials on fluorocarbon polymer formation was also investigated. Specifically, CF and C₄F₄ radicals were deposited onto Si crystal substrates. The molecular structure of C₄F₄ was derived from C₄F₈ molecule (see Fig. 4.25), which is another common gas used in fluorocarbon plasma etching (Metzler et al. 2014).

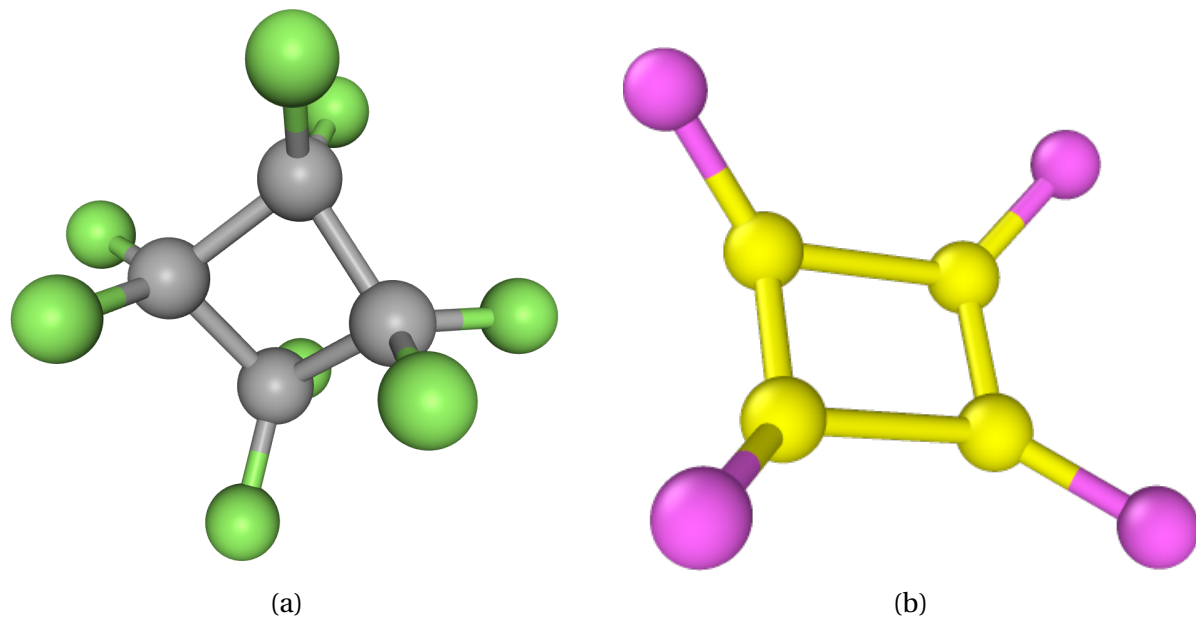


Figure 4.25: Molecular structures of: (a) C₄F₈ (gray=C, green=F; obtained from PubChem online database); (b) C₄F₄ (yellow=C, pink=F; generated from this work).

For the CF radicals deposition, the dimension of the Si crystal substrate was 30×30×30 Å³. 2000 CF radicals were inserted, and the number of timesteps between two consecutive incidences was 500. The CF radicals were inserted with kinetic energy of 1 eV and at normal angle. It was found that the polymer growth on Si was significantly different from on

amorphous SiO_2 , see Fig. 4.26 for an example.

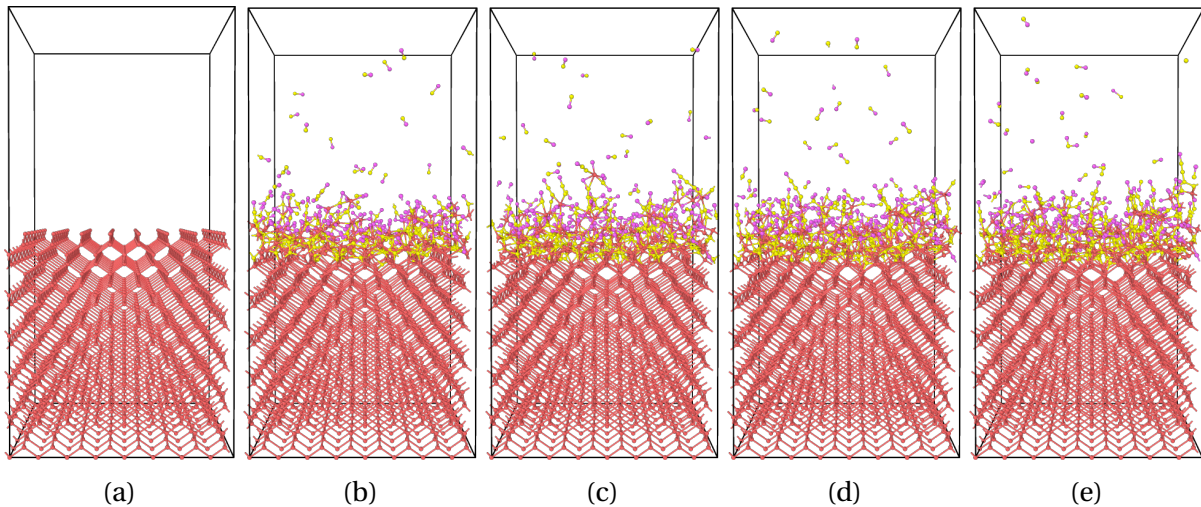


Figure 4.26: Deposition of 1 eV CF radicals onto Si crystal substrate (red=Si, yellow=C, pink=F), presented here are snapshots at timestep of: (a) 0; (b) 2.5E5; (c) 5E5; (d) 7.5E5; (e) 1E6.

It can be found that the incident CF species was able to attach on the Si surface at a much higher rate than on the SiO_2 , which can be better illustrated using the Number of attached atoms vs. Timestep plot, as shown in Fig. 4.27. The curves for C and F match very well for almost the entire simulation duration, indicating the Si surface was so reactive that the atoms barely left the surface after get attached, which can also be supported by the very low noise level on the curves compared to the results for SiO_2 . The numbers of attached atoms for Si are much higher than for SiO_2 , suggesting a thicker fluorocarbon polymer film. Although the growth rate significantly decreased after around 0.5E6 steps, the curves seem to show the potential of continuous growing. A much longer run is needed to show if the curves indeed reach saturation at some later point.

For the C_4F_4 radicals deposition, the dimension of the Si crystal substrate was $40 \times 40 \times 25 \text{ \AA}^3$ such that the substrate was wider in lateral direction. 2000 C_4F_4 radicals were inserted, and the number of timesteps between two consecutive incidences was 1000. The C_4F_4 radicals were inserted with kinetic energy of 5 eV and at normal angle. It was found that the polymer growth with C_4F_4 on Si was similar to the CF on Si case, and had much higher growth rate than on amorphous SiO_2 , see Fig. 4.28 for an example.

It can be found that the formed fluorocarbon polymer film is even thicker, and the

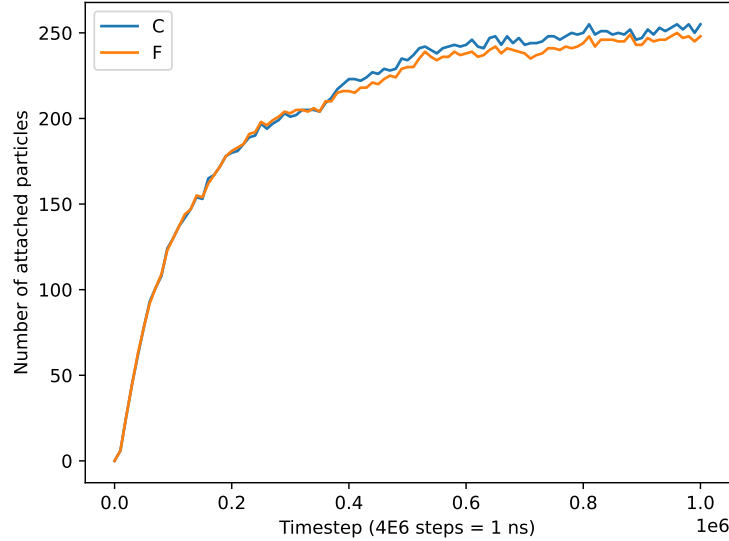


Figure 4.27: Number of attached C and F atoms as a function of timestep for CF species incident on Si crystal substrate.

same mixing layer can also be observed in which the Si, C and F atoms are correlated. The Number of attached atoms vs. Timestep plot was also plotted in Fig. 4.29. It can be seen that the curves for C and F still match very well and show slight de-fluorine towards the later half the simulation duration. The numbers of attached atoms are even higher, and clear trend of continuous growing can be observed.

In order to perform cross-comparison among different deposition cases with different substrate dimensions (i.e., different top surface areas), the number of attached C atoms at the final timestep of each deposition case was normalized with respect to the substrate surface area and is listed in Table 4.4, in which the 1 eV data from Fig. 4.18(a) was used for the parametric study of mixed CF_x on SiO_2 where $\text{CF}_2 : \text{CF} = 3$, the 1 eV data from Fig. 4.22(a) was used for CF on SiO_2 , and the 1 eV data from Fig. 4.23(a) was used for C_2F_4 on SiO_2 . The '+' sign in Table 4.4 indicates that the corresponding curve did not reach saturation at the end of the simulation, and the '++' sign indicates more significant trend of increase.

Table 4.4: Comparison of number of attached C atoms for different deposition cases, normalized with respect to the substrate surface area.

Num./Area (\AA^{-2})	$\text{CF}_2 : \text{CF} = 3$	CF	C_4F_4	C_2F_4
On SiO_2	0.0933	0.12	0.107	0.0483
On Si	NA	0.283+	0.299 ++	NA

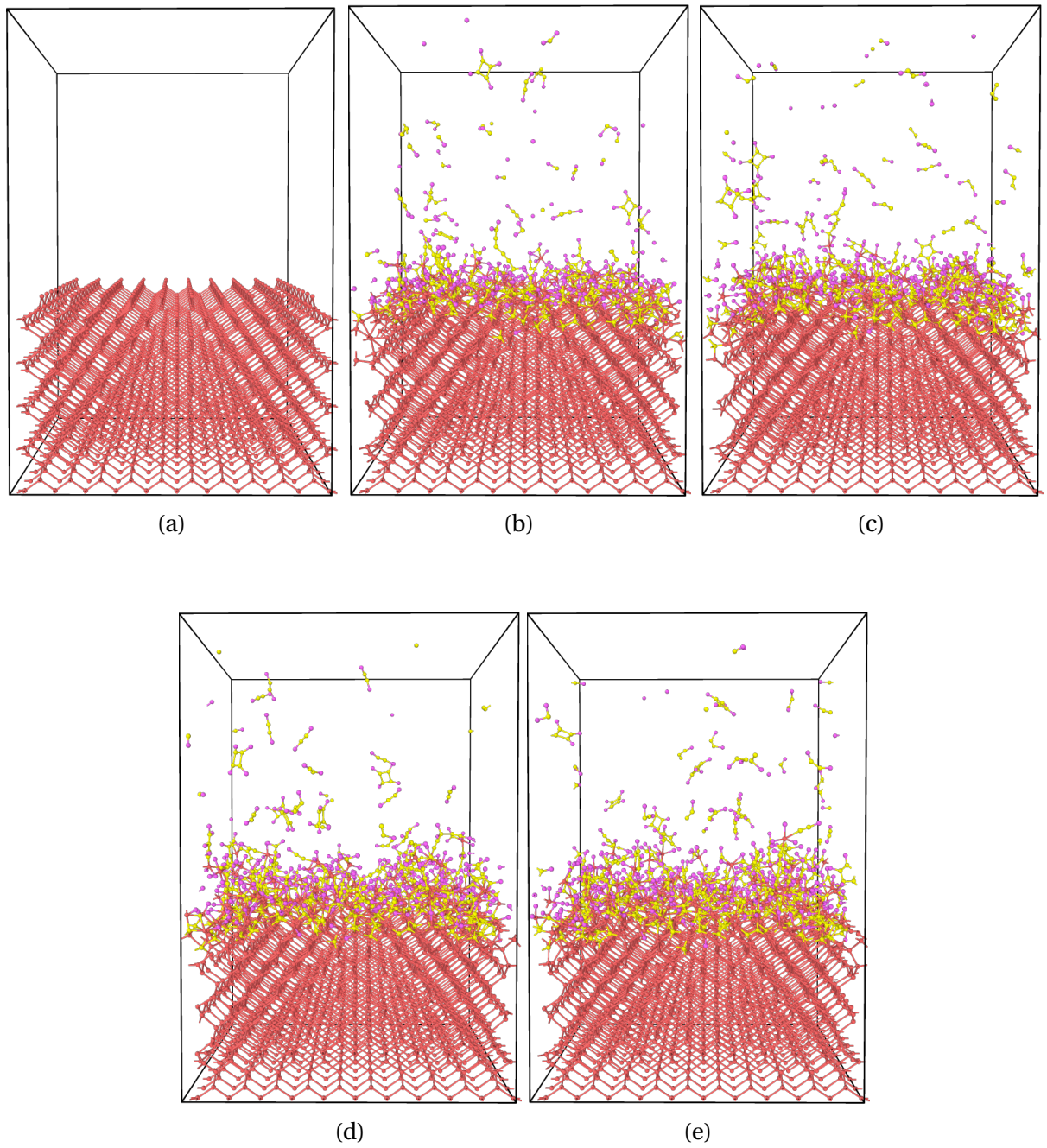


Figure 4.28: Deposition of 5 eV C_4F_4 radicals onto Si crystal substrate (red=Si, yellow=C, pink=F), presented here are snapshots at timestep of: (a) 0; (b) 4E5; (c) 8E5; (d) 1.2E6; (e) 1.6E6.

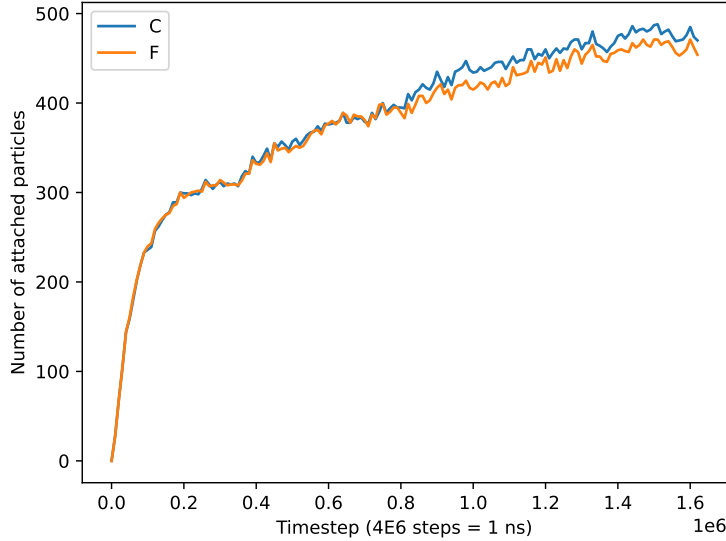


Figure 4.29: Number of attached C and F atoms as a function of timestep for C_4F_4 species incident on Si crystal substrate.

It can be seen that species with lower F:C ratio tend to attach more easily on the substrate. This can be expected since C atoms can form 4 covalent bonds while F atoms can only form 1. More C atoms can bond with each other to form long polymer chains, while more F atoms would occupy the available bonding electrons and resist bonding with upcoming radicals. We performed a test case mixing the incidence of CF_x species with F atoms, and the deposition reached saturation much faster than the CF_x only incidence case.

Another thing can be found from Table 4.4 is that the normalized number of attached C atoms is much higher on Si than on SiO_2 , and it shows clear trend of continuous growing to make the number even higher. This indicates that Si crystal is much more reactive than amorphous SiO_2 , possibly due to Si atoms can form more covalent bonds than O atoms (4 vs. 2). It can be expected that for the same condition of incident CF_x flux, the fluorocarbon polymer film can grow much faster and thicker on substrate of Si crystal than on amorphous SiO_2 .

4.7 Effects of adding carbon atoms

The results from last few sections suggest that species with lower F:C ratio tend to attach more easily on the substrate and form thicker polymers. In this section, we tested the effects of carbon atoms in polymer formation, by both depositing pure carbon atoms on the

substrate materials and mixing carbon atoms with CF_x radicals in the deposition process.

The first test case we performed was for C atoms deposition on amorphous SiO_2 substrate. The dimension of the substrate ($20 \times 20 \times 34.4 \text{ \AA}^3$) was the same as in previous sections. 2000 C atoms were inserted, where the number of timesteps between two consecutive incidences was 1500. All the C atoms were inserted with kinetic energy of 1 eV and at normal angle. It was found that C atoms were much more likely to attach on the substrate surface and form a low density chain-structure film, see Fig. 4.30 for an example. The deposited C atoms mostly had sp hybridization (2 bonding atoms), with only a small portion had sp^2 hybridization (3 bonding atoms). Therefore, sp hybridized C atoms generally form multiple carbon chains, and different chains are cross-linked by these sp^2 hybridized C atoms, as shown in Fig. 4.30. It is worth noting that the structure of the formed film is similar to the back-bone chains of carbon based polymers, except that no stem atoms are involved.

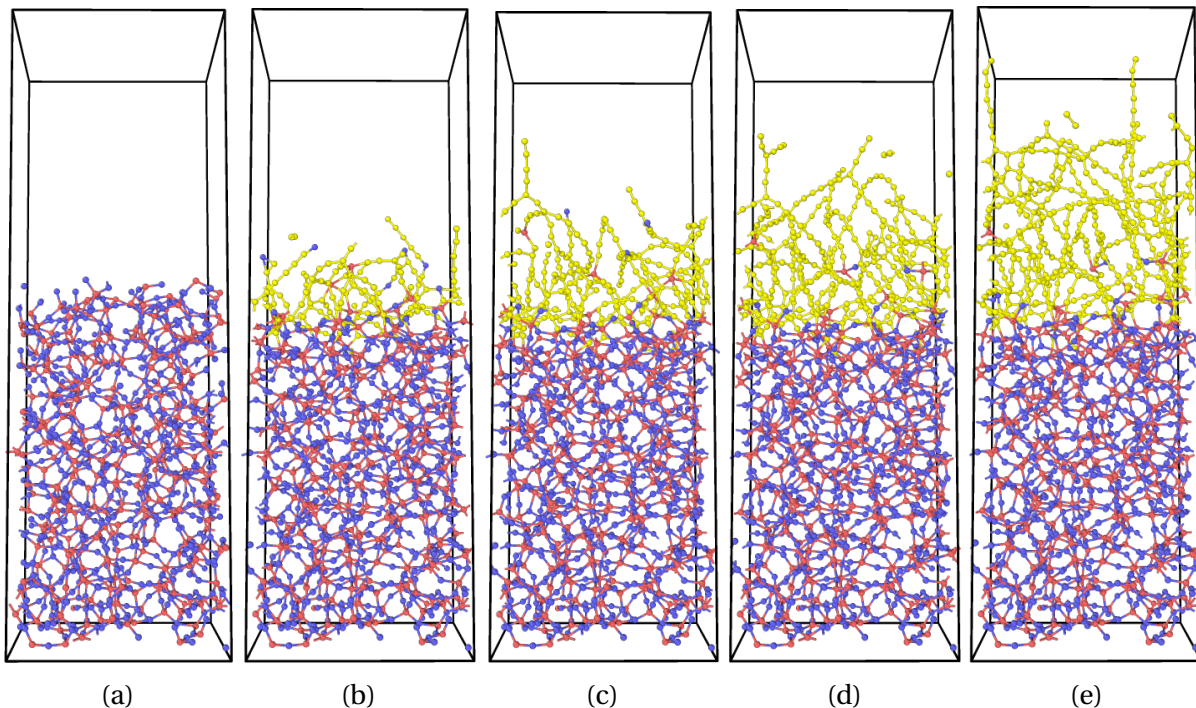


Figure 4.30: Deposition of 1 eV C atoms onto amorphous SiO_2 substrate (red=Si, blue=O, yellow=C), presented here are snapshots at timestep of: (a) 0; (b) 3E5; (c) 6E5; (d) 9E5; (e) 1.2E6.

4.7.1 Comparison of depositing carbon atoms on different substrate materials

The deposition of carbon atoms on amorphous SiO₂ and on Si crystal were simulated. Larger material sizes were used for both the two substrates. Specifically, the size of the SiO₂ substrate was $(34.4 \text{ \AA})^3$, and the size of the Si crystal was $30 \times 30 \times 34.4 \text{ \AA}^3$ so that both materials have roughly the same thickness. C atoms were inserted with kinetic energy of 1 eV and at normal angle for both cases, and the number of timesteps between two consecutive incidences was the same (500). The results are presented in Fig. 4.31.

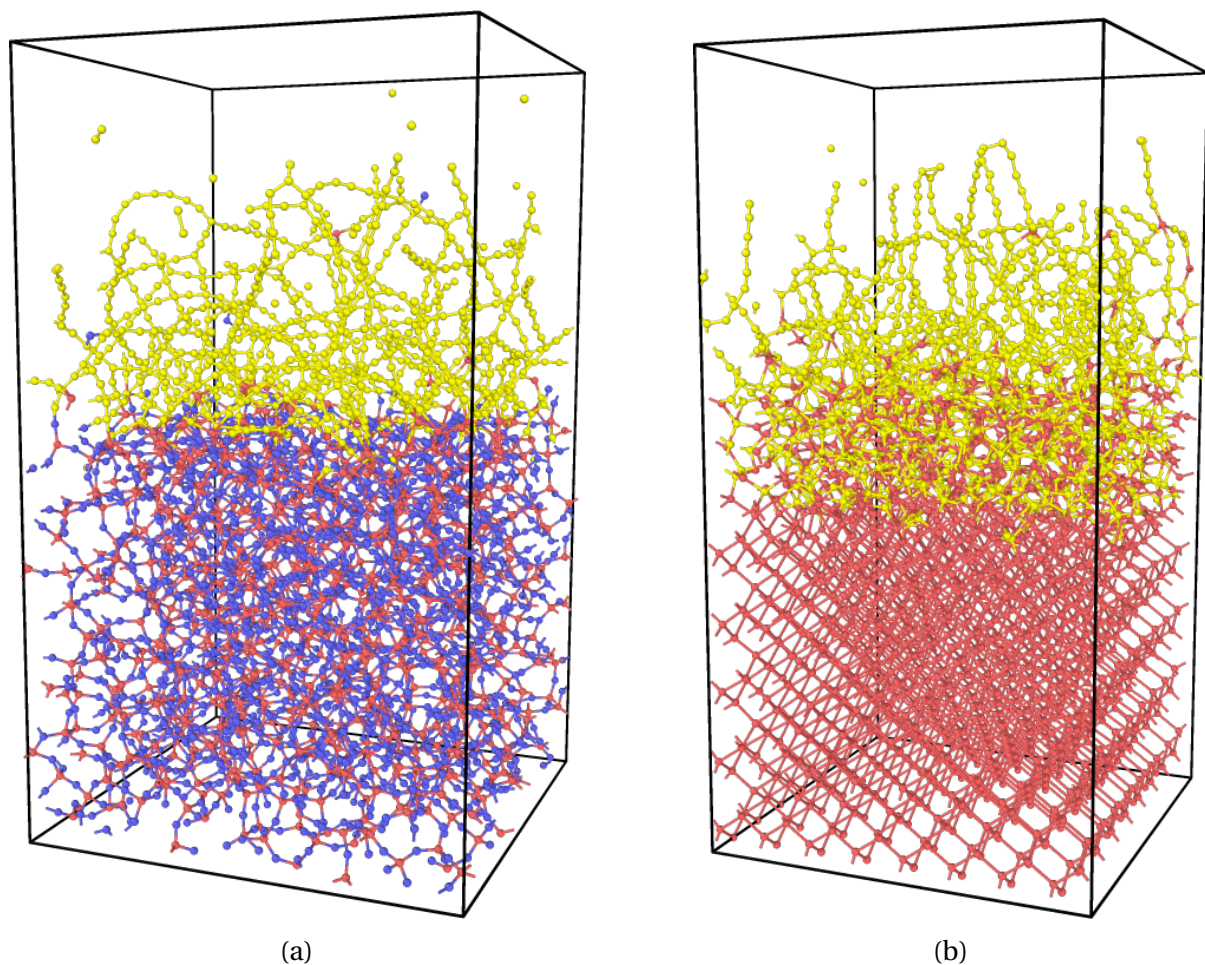


Figure 4.31: Deposition of 1 eV C atoms onto substrate materials of (red=Si, blue=O, yellow=C): (a) amorphous SiO₂; (b) Si crystal.

It can be seen that even though the same C flux was inserted, the formed films were significantly different for different substrate materials. On amorphous SiO_2 , it seems like the interface between the substrate and the carbon film is quite distinct (i.e., the C atoms do not migrate deeply into the substrate), and the formed carbon chains seem to exclusively attach to the Si atoms on the substrate surface. However, on Si crystal, there appears to be a mixing layer where both C and Si atoms greatly migrate towards each other and the number density seems to be much higher. This can be better illustrated by plotting a histogram of the z position of the attached C atoms on both substrates, see Fig. 4.32. It can be found that a much larger portion of the histogram for Si crystal substrate falls below the original substrate surface position (the vertical black dashed lines) compared to for amorphous SiO_2 substrate, indicating more significant migration. The histogram for Si also appears to be more symmetrical where it is more right skewed for SiO_2 , indicating the existence of thick mixing layer on the Si crystal substrate.

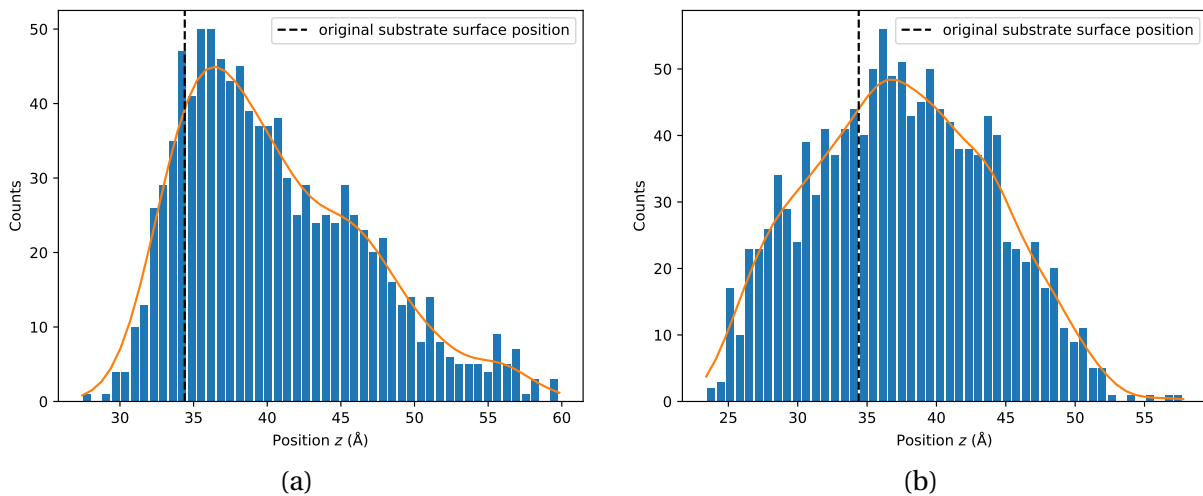


Figure 4.32: Histograms of the z position (with respect to substrate bottom plane where $z = 0$) of C atoms on substrates: (a) amorphous SiO_2 ; (b) Si crystal.

The very top region of the carbon film on the Si substrate seems to be similar to what on the amorphous SiO_2 , where most C atoms are sp hybridized. The number and percentage of different types of hybridization of the deposited C atoms on SiO_2 and Si substrates are listed in Table 4.5. The results show that most of the C atoms on SiO_2 have sp hybridization, while the percentages of the C atoms on Si crystal having sp hybridization or sp^2 hybridization are roughly the same, which matches our observation.

Table 4.5: Comparison of number and percentage of C hybridization on SiO₂ and Si substrates.

C hybridization	On SiO ₂	On Si
End (CN=1)	44 (4.41%)	30 (2.37%)
<i>sp</i> (CN=2)	811 (81.26%)	584 (46.17%)
<i>sp</i> ² (CN=3)	123 (12.32%)	503 (39.76%)
<i>sp</i> ³ (CN=4)	3 (0.30%)	145 (11.46%)
Total	998	1265

The effect of incident energy of the C atoms on Si crystal substrate was also investigated. A parametric study of 3 independent cases with incident energy of 1, 10 and 20 eV was performed, and the number and percentage of different types of hybridization of the deposited C atoms for cases with different incident energies are listed in Table 4.6.

Table 4.6: Comparison of number and percentage of C hybridization on Si substrate for different incident energies.

C hybridization	1 eV	10 eV	20 eV
End (CN=1)	30 (2.37%)	10 (0.95%)	10 (1.09%)
<i>sp</i> (CN=2)	584 (46.17%)	227 (21.64%)	195 (21.26%)
<i>sp</i> ² (CN=3)	503 (39.76%)	666 (63.49%)	592 (64.56%)
<i>sp</i> ³ (CN=4)	145 (11.46%)	143 (13.63%)	118 (12.87%)
Total	1265	1049	917

The results suggest that as the incident energy increases, the ratio of *sp*² hybridized C atoms also increases and the formed carbon film is more compact, which matches our results in modeling amorphous carbon using Tersoff potential in Chapter 3.

4.7.2 Combining incidence of CF_x radicals with carbon atoms

The results from C atoms deposition suggest that C atoms (or compounds of multiple C atoms) may play a role in forming thick fluorocarbon polymer films on the substrate surface during a fluorocarbon plasma etching process. Carbon compounds were found in previous experimental efforts in fluorocarbon plasma etching process, such as in Labelle et al. (2004) where C₃ and C₂ peaks were measured within the plasmas using optical emission spectra data, and in Metzler et al. (2014) where C-C peak was measured within the deposited films

using x-ray photoelectron spectroscopy data.

In this section, we tested the effects of combining the incidence of CF_x radicals with carbon atoms in fluorocarbon polymer film formation. The prepared amorphous SiO_2 with the original size ($34.4 \times 34.4 \times 34.4 \text{ \AA}^3$) was used as the substrate material. A total number of 1000 CF_x radicals (including both CF and CF_2 at a ratio of $\text{CF}_2 : \text{CF} = 2$) was inserted, and the number of timesteps between two consecutive CF_x incidences was 1000. C atoms were also uniformly inserted, where the $N_{\text{C}}/N_{\text{CF}_x}$ ratio was predefined and the number of timesteps between two consecutive C incidences was calculated correspondingly so that the durations of incidence for both CF_x and C were the same. Both CF_x radicals and C atoms were inserted with kinetic energy of 1 eV and at normal angle. A parametric study of 5 independent cases was performed for the $N_{\text{C}}/N_{\text{CF}_x}$ ratios of 0.1, 0.4, 0.6, 0.8 and 1.0, and the results are presented in Fig. 4.33 as snapshots at the same timestep of 1E6 for different $N_{\text{C}}/N_{\text{CF}_x}$ ratios. It can be found from Fig. 4.33 that carbon atoms do help in growing thick polymer films as expected. As the ratio of carbon flux increases, more carbon atoms appeared to be able to attach to the substrates, forming longer chains and thicker polymer films.

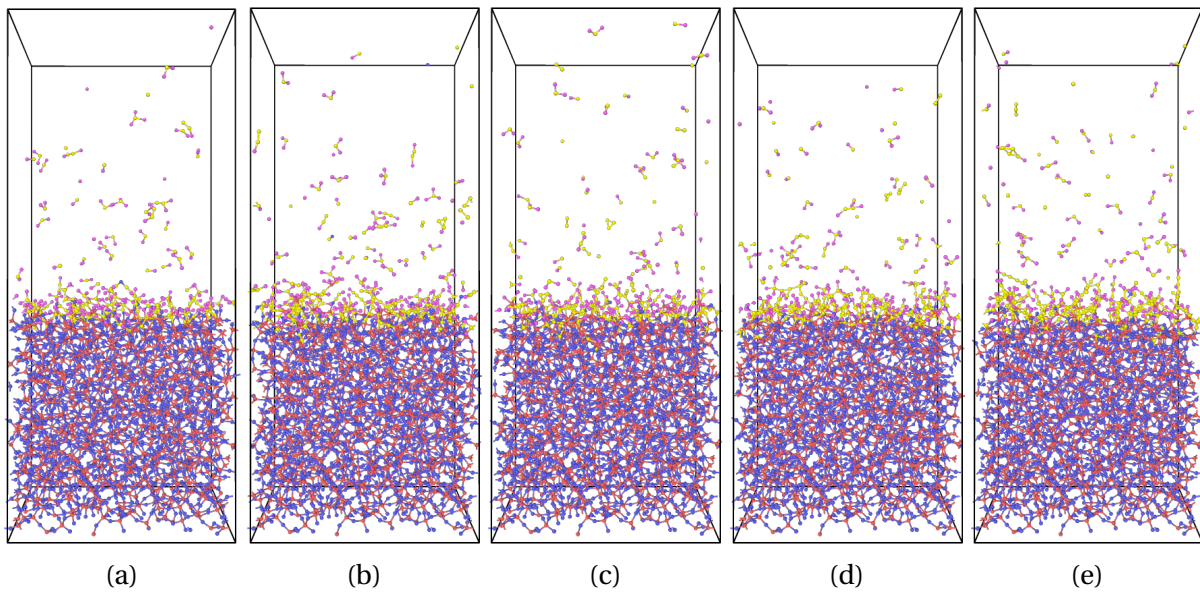


Figure 4.33: Deposition of combining CF_x and C flux onto amorphous SiO_2 substrate (red=Si, blue=O, yellow=C, pink=F), presented here are snapshots at the same timestep of 1E6 for different $N_{\text{C}}/N_{\text{CF}_x}$ ratios of: (a) 0.1; (b) 0.4; (c) 0.6; (d) 0.8; (e) 1.0.

The number of attached atoms on the substrate surface as a function of timestep was also plotted for each case and are compared in Fig. 4.34. It can be found that not only the number of attached C atoms increased with increasing C flux, but also all the curves do not seem to have reached a saturation state, which shows the potential for continuous growing. However, the number of attached F atoms seems to stay constant with increasing C flux, and this suggests that the increase in polymer film thickness was mainly due to C atoms and the probability for CF_x radicals to attach was roughly the same for different conditions. This could be explained by considering the very high ratio of *sp* hybridized carbon atoms on SiO_2 substrate, as shown in Table 4.5. Since most of the *sp* carbon are located in separate carbon chains without too much cross-linking, this indicates that only the end atom of each chain can easily form new bonds with upcoming molecules. Therefore, higher C flux results in longer carbon chains but the total number of carbon chains stays roughly the same, and the probability for CF_x radicals to attach stays the same.

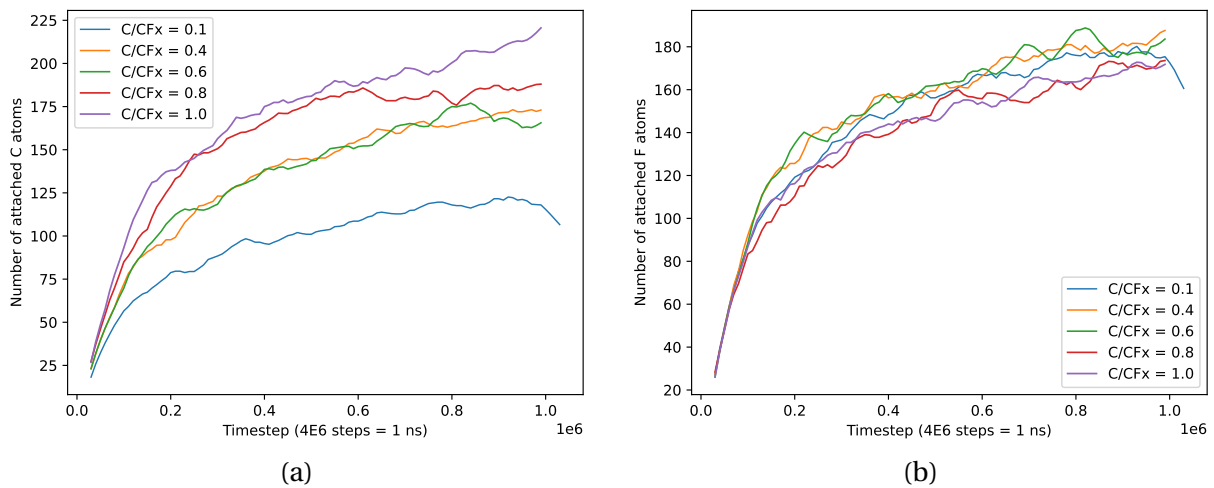


Figure 4.34: Comparison of number of attached atoms as a function of timestep for different $N_{\text{C}}/N_{\text{CF}_x}$ ratios, presented here are for: (a) C atoms; (b) F atoms.

In summary, in this section we show that by depositing pure C atoms onto amorphous SiO_2 substrate, a polymer-like low density carbon film can be formed without saturation, in which most of the C atoms have *sp* hybridization. The carbon films formed on amorphous SiO_2 substrate and on Si crystal substrate are significantly different, where a thick mixing layer of Si and C atoms can only be found in Si crystal deposition and the formed carbon film is denser. By combining the incidence of CF_x radicals with carbon atoms, the formed

fluorocarbon polymer film can grow much thicker. However, the growth in film thickness is mainly due to C atoms by forming longer carbon chains, the number of attached F atoms stays roughly the same. Further investigation is needed to figure out how to make the upcoming molecules to also connect to the middle C atoms on a carbon chain instead of only to the end C atoms, so that the formed fluorocarbon polymer film is not so F deficient.

4.8 Alternative approach: use PTFE as a surrogate

As mentioned previously in Chapter 1, it was reported in several findings that the passivation layer formed on HAR sidewalls during fluorocarbon plasma etching has a molecular structure similar to polytetrafluoroethylene (PTFE) (Booth 1999; d'Agostino et al. 1983; Millard and Kay 1982). Therefore instead of modeling the growth of the passivation layer by depositing CF_x radicals on Si/SiO_2 , an alternative approach could be that use manufactured PTFE as a surrogate and stack it on top of the target materials. The manufactured PTFE can be modified so that its properties can match some experimental measurements. For example, the F:C atoms ratio in a typical PTFE is around 2.0, while the ratio is generally between 1 and 2 for passivation layers formed during fluorocarbon plasma etching (Labelle et al. 2004). Therefore, some of the F atoms in the manufactured PTFE can be randomly deleted, using LAMMPS commands such as *delete_atoms random*, to lower the F:C ratio and match the experimental measurements. Additional thermal equilibration steps are still needed for the polymers to cross-link after the material modification, and the final structure need to be validated using some experimental data in addition to the F:C atoms ratio.

In preparing PTFE, a single chain of PTFE was first prepared, as shown in Fig. 4.35a. 10 such polymer chains with each chain having 40 monomers were then randomly oriented and placed into a simulation box with periodical boundaries in all three directions, as shown in Fig. 4.35b. The size of the simulation box (110 Å in length for the cubic box) was designed to match a lower density (0.05 g/cm³) so that no overlapping of atoms would happen and therefore simulation instability can be avoided. These initialization steps were all performed using the same online polymer builder (Haley et al. 2010) as used previously for preparing polystyrene.

Once the initial structure of PTFE were prepared, the same ReaxFF C/O/F/Si system was used to simulate the thermal equilibration of PTFE. The material was first heated up to 800 K and kept constant temperature for 150 ps (75 ps NVT followed by 75 ps NPT). This

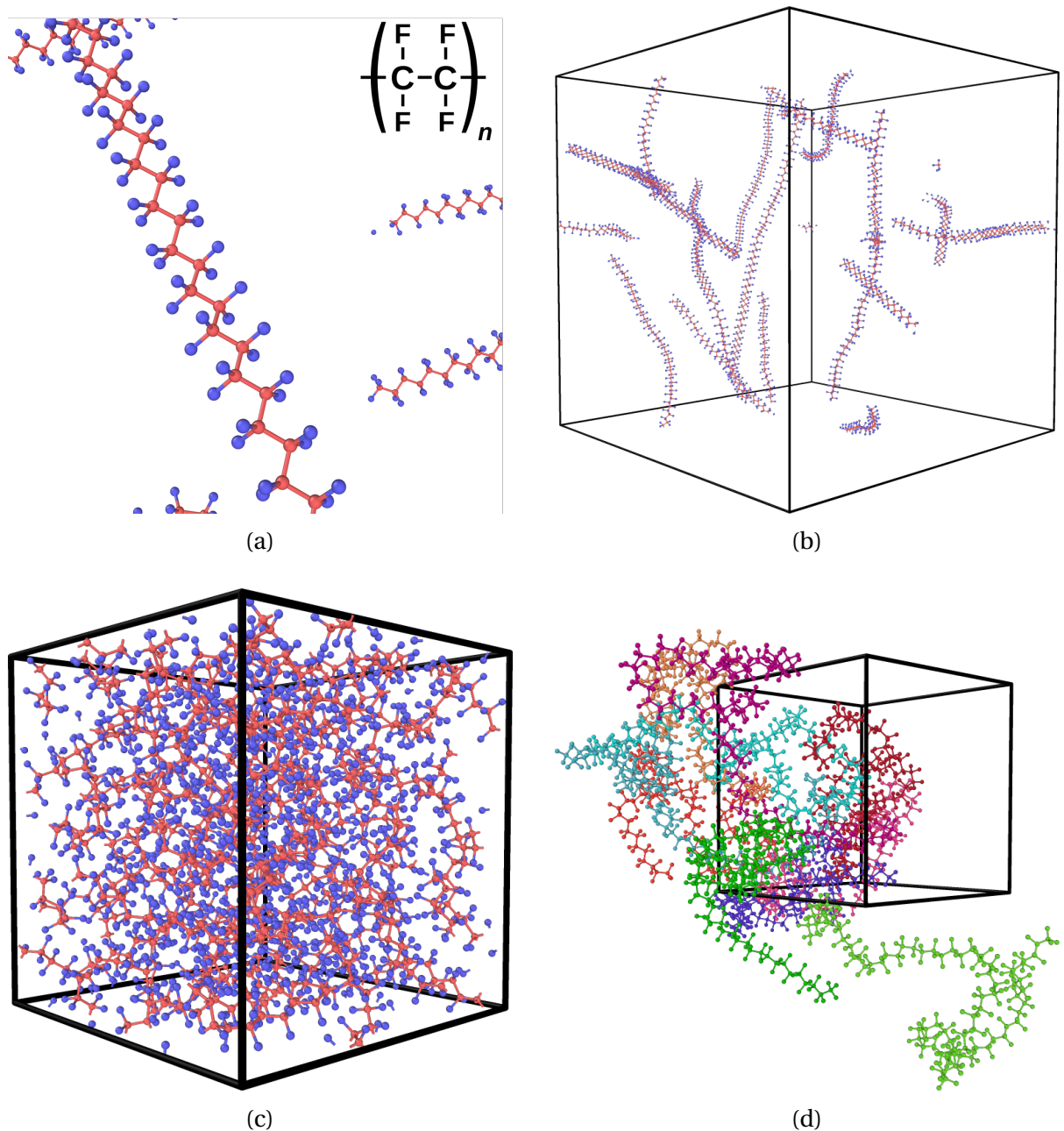


Figure 4.35: Preparation of PTFE using ReaxFF: (a) single polymer chain of PTFE; (b) 10 polymer chains of PTFE, where each chain has 40 monomers, are randomly oriented and placed into a simulation box with periodical boundaries in all three directions, and the initial density was 0.05 g/cm^3 ; (c) thermal equilibrated at 300 K and final density reached 2.2 g/cm^3 (d) same results as in (c) but chains are colored separately and unwrapped at periodical boundaries.

step was intended to sufficiently mix and relax the material so that an uniform material can be achieved, while the temperature should not be too high to break any existing bonds and do damage to the material. After the material showed stable properties such as density and radial distribution function, it was cooled down from 800 K to 300 K within another 75 ps (6.67 K/ps) using NPT ensemble. Once the material reached 300 K, a final relaxation step was performed using NPT ensemble for another 25 ps.

The aim of these thermal equilibration steps is to reach a target density of 2.2 g/cm³, which is a typical value measured in experiments for PTFE (Blumm et al. 2010). However, it seemed like ReaxFF was under-predicting the density after the pre-described steps at normal pressure. At the pressure of 1 atmosphere, ReaxFF predicted a density around 1.1 g/cm³ for PTFE equilibrated at 300K, which is 50% lower than the target value. Different procedures were also tested such as varying the order or duration of each thermal equilibration step, varying the cooling rate and varying the mixing temperature, however, the predicted density was still in the range of 1.1 ~ 1.3 g/cm³ for PTFE at 300 K and 1 atmosphere.

Therefore, in order to match the target density, high pressure was applied using NPT ensemble to compress the material. It was found that on average a much higher pressure (~ 20000 atm) was needed in order to reach the target density, which is not ideal since normally it would only require atmosphere pressure such as in previous simulation of polystyrene using TraPPE potential. One possible explanation for this inconsistency is that this particular combined ReaxFF C/O/F/Si system does not accurately describe the C-F interaction in a PTFE system. However, different ReaxFF parameter files (such as in Rahnamoun and Van Duin (2014)) containing C/F parameters were also tested and the under-prediction of density persists. Another possible explanation is that by observing the morphology of PTFE when increasing pressure, ReaxFF seems to be over-predicting the repulsive forces between the stem F atoms on different polymer chains, and the intermolecular distance of two neighbouring polymer chains is over-predicted therefore under-estimating the density. In one of the previous works using ReaxFF to model PTFE (Rahnamoun and Van Duin 2014), the author mentioned that they also compressed the system to achieve a target density of 2.2 g/cm³. Further investigation is needed to confirm if this inconsistency is intrinsic within ReaxFF potential in general.

Despite of the inconsistency, using the high pressure (~ 20000 atm) condition with NPT ensemble, the PTFE was able to reach the target density of 2.2 g/cm³ at 300 K, as shown in Fig. 4.35c. To better visualize the chain structure, different chains were colored separately and unwrapped at periodical boundaries, meaning that a long chain that extends through multiple periodical boxes as multiple segments will be combined into one whole chain and

stretch outside the simulation box, as shown in Fig. 4.35d. The chain structure of PTFE was preserved very well during these thermal equilibration steps since the same 10 chains were observed in the end.

Radial distribution function (RDF) was also used to validate the manufactured PTFE with some published results, as shown in Fig. 4.36, where the partial RDFs were categorized by different types of atom pairs and were shifted upwards to avoid overlapping. The short-range RDF, mainly describing the local structure within short distance thus atoms on the same chain for polymer structure, for the C-C pair in Fig. 4.36a matches the RDF of the intra-molecular C-C pair in [Zuo et al. (2015)] very well for both the peak positions and the general shapes. The long-range RDFs, mainly describing the local structure within longer distance thus atoms on different chains for polymer structure, for all three pairs in Fig. 4.36b match the inter-molecular RDFs in [Tsige et al. (2008)] for both the peak positions and the general shapes. Thus, despite that the high pressure condition needed to be applied, ReaxFF was able to reproduce the local structures of PTFE very well. If the over-prediction of the repulsive forces between the stem F atoms on different polymer chains can be fixed, the intermolecular distance between different polymer chains can be reduced and the target density can be reached for PTFE at 1 atmosphere and 300 K.

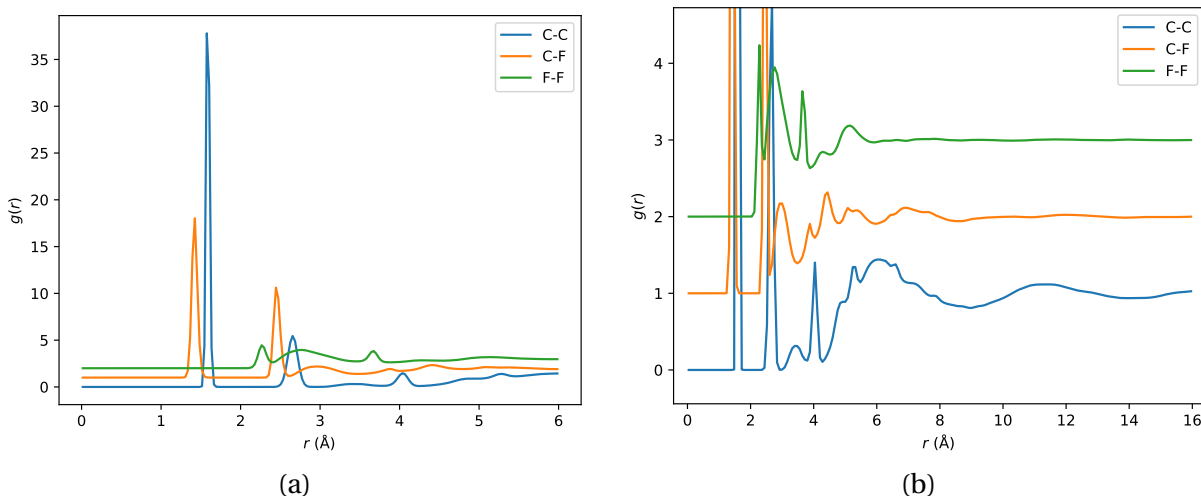


Figure 4.36: Partial RDF for PTFE, categorized by different types of atom pairs: (a) short-range part; (b) zoomed in to emphasize the long-range part.

Using the modeled PTFE in Fig. 4.35c and the SiO_2 obtained previously, the passivation layer can be represented by stacking the PTFE on top of the SiO_2 , as shown in Fig. 4.37. It

should be noted that periodical boundary conditions were applied for both x and y directions and finite boundary condition was applied for z direction, therefore the simulated material represents an infinite large layered structure. In order to attach the PTFE to the SiO_2 more stably, the interface region (about 4 Å thick centered around the interface) was modified to become more reactive, which was done by randomly removing 80% of the F and O atoms within that region using LAMMPS command. The whole material was then relaxed using partial NPT ensemble (in x and y directions) at 300 K and 1 atmosphere, with a timestep of 0.25 fs, as shown in Fig. 4.37. The same ReaxFF parameter set was used for describing the interatomic potentials.

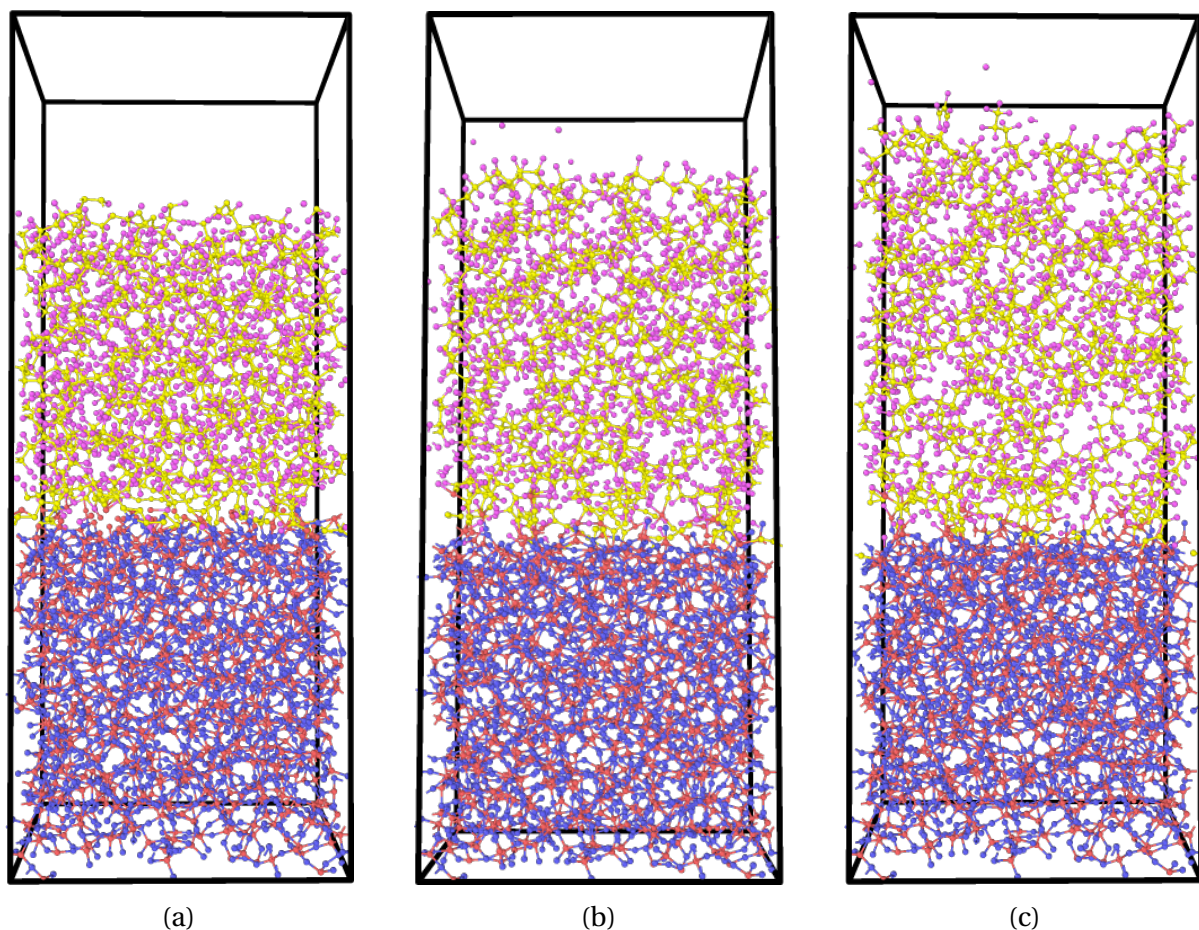


Figure 4.37: Stack PTFE (yellow=C, pink=F) on top of SiO_2 (red=Si, blue=O): (a) initial structure; (b) PTFE swollen vertically after 2.5 ps; (c) after 5 ps

As expected, the material did not stay as compact as desired. The PTFE swelled vertically,

resulting in an increase in thickness as well as a decrease in density, while the SiO₂ was quite stable. This is due to the attached PTFE was generated under high pressure, meaning that this high pressure was applied on all six periodical boundaries in Fig. 4.35c. However, in the configuration as shown in Fig. 4.37, the top face of the PTFE was facing vacuum (0 pressure), therefore the reduction in pressure caused the swell in *z* direction.

In summary, the combined ReaxFF parameter set is partially compatible with modeling PTFE. Under high pressure around 20000 atmosphere, the model can generate PTFE at desired density, and the RDFs match published results, indicating that the local structures can be accurately predicted. However, the inconsistency will cause swell when stacking PTFE on top of SiO₂, resulting in a manufactured passivation layer which has less density than a typical PTFE. Further investigation is needed to validate this manufactured passivation layer prior to taking any actual data upon it. For example, even if the manufactured passivation layer has less density than a typical PTFE, the density could still be in a valid range for an actual passivation layer since it is generally porous. The molecular weight of the manufactured passivation layer should also match the actual material since it is less likely to form a very long carbon chain due to ion bombardment. Furthermore, the current model has individual equal-length polymer chains but it is expected to see cross-linking of polymer chains in the actual passivation layer, which could be achieved by randomly (or selectively) removing some C and F atoms in the thermal equilibration steps. These are some ideas slightly tested in this project but can be fulfilled in future works.

CHAPTER

5

STICKING COEFFICIENT

5.1 Abstract

Measuring sticking coefficients for various plasma species on different HAR feature materials in fluorocarbon plasma etching processes is a natural outcome of studying the fluorocarbon polymer formation. Measuring sticking coefficients on varying substrate surface conditions as a function of time can help in understanding the time-dependent behavior of polymer growth on substrate surfaces. On the other hand, measuring sticking coefficients can also benefit computational models such as feature profile simulations, by delivering more accurate and more flexible parameters which are essential to these rigorous models. It can be expected that in experimental works, sticking coefficients are generally difficult to measure, and are usually estimated indirectly from other results such as feature profile shape and radicals' density within the plasma. With the help of MD simulations, the sticking coefficients can be measured directly at atomistic scale, and the conditions of the incident species as well as the substrate surfaces can be precisely manipulated so that the effect of each factor can be measured independently. In this chapter, the sticking coefficients of molecules CF_x ($x = 0 \sim 4$) and SiF_x ($x = 0 \sim 4$) on substrate materials such

as amorphous SiO_2 and Si crystal were measured using molecular dynamics simulation with the aforementioned ReaxFF potential. The sticking coefficients were measured both on the bare material surfaces, by resetting the material every five incidences, and on the material surfaces with growing polymer layer, in a dynamic manner similar to fluorocarbon polymer formation. The number of attached molecules were measured as a function of the number of incidence, and the sticking coefficients were measured from the slope of the curves. An analytical model was also derived and fitted to the measured data using two-segment regression, and good match was achieved between the analytical model and the measured data, which makes it possible to incorporate the simple analytical model into any rigorous models to conveniently predict the variation in sticking coefficients as a function of surface conditions.

5.2 Material preparation and simulation setup

In this chapter, the sticking coefficients of molecules CF_x ($x = 0 \sim 4$) and SiF_x ($x = 0 \sim 4$) on substrate materials amorphous SiO_2 and Si crystal were measured. The atomic structures of CF_4 and SiF_4 were already validated in Section 4.3 of Chapter 4, and the data files for the corresponding radicals CF_x and SiF_x can be generated by removing the desired number of F atoms from CF_4 or SiF_4 respectively. For the substrate materials, since the preparation of both amorphous SiO_2 and Si crystal were already introduced in previous chapters and the prepared materials were carefully validated, the same data files or LAMMPS commands were used here. For all the simulation cases performed in this chapter, a time step of 0.25 fs was used and the substrate materials (both the amorphous SiO_2 and the Si crystal) were designed to have a cubic shape with a length of 34 Å on each side. Since the number density of amorphous SiO_2 is higher than Si crystal, the initial system of amorphous SiO_2 has 1000 Si atoms and 2000 O atoms, while the initial system of Si crystal has 2106 Si atoms. Periodic boundary conditions were used in the x and y (lateral) directions, while finite boundary condition was used in the z (vertical) direction. Some empty space was added above the materials, which need to be at least larger than the cutoff distance of the interatomic potential, so that the incident molecules can be assumed to have travelled from a very large distance. The substrate materials were thermally equilibrated under NVT ensemble at 300 K, in order to reproduce the physical conditions in reality. However, the temperature of the top layer of the substrate materials were generally higher than 300 K, which was expected due to the transfer of the kinetic energy of the incoming fluxes to thermal energy.

The incident molecules were equilibrated under NVE ensemble (no applied constrains) so that LAMMPS can properly model the trajectory of these molecules at the desired kinetic energy.

5.3 Sticking coefficients measurements

The sticking coefficients were measured in two ways:

- In a static manner where the substrate material was reset to its initial state after several incidence events so that no accumulation can happen and the incident molecules can be assumed to interact with the substrate material independently. In such cases the sticking coefficients can be assumed to be constant for each species;
- In a dynamic manner where the substrate material was deposited with constant flux of molecules without being reset, therefore the substrate surface condition varied dynamically as more and more molecules attached to the material surface. In such cases the sticking coefficients could be varying as a function of time or more essentially as a function of surface coverage.

5.3.1 On bare surface - static

A parametric study of 10 different species, CF_x ($x = 0 \sim 4$) and SiF_x ($x = 0 \sim 4$), was performed. These species are commonly seen within the plasma or as the etch byproducts for a fluorocarbon plasma etching. The sticking coefficients of these species are important since the reactive radicals and the etch byproducts can modify surface conditions when attached to the substrates, which would in turn affect the parameters of quantifying etch performance such as etch rate, selectivity and feature profile.

The simulation box has a size of $34 \times 34 \times 50 \text{ \AA}^3$, and both the two substrate materials, amorphous SiO_2 and Si crystal, have a size of $(34 \text{ \AA})^3$, resulting in enough empty space above the substrate for the incident molecules to travel through. All the incident molecules were inserted within a thin layer 10 \AA above and parallel to the substrate top surface. The horizontal positions (x, y) of the inserted molecules were determined randomly while a minimum interatomic distance of 8 \AA was enforced so that the molecules inserted simultaneously can be assumed to do not interfere with each other. See Fig. 5.1 for examples of measuring sticking coefficients of CF_3 radicals on Si crystal as well as SiF_4 molecules on

amorphous SiO_2 . Note that periodic boundary conditions were used for lateral directions so that some molecules may extend across the boundaries.

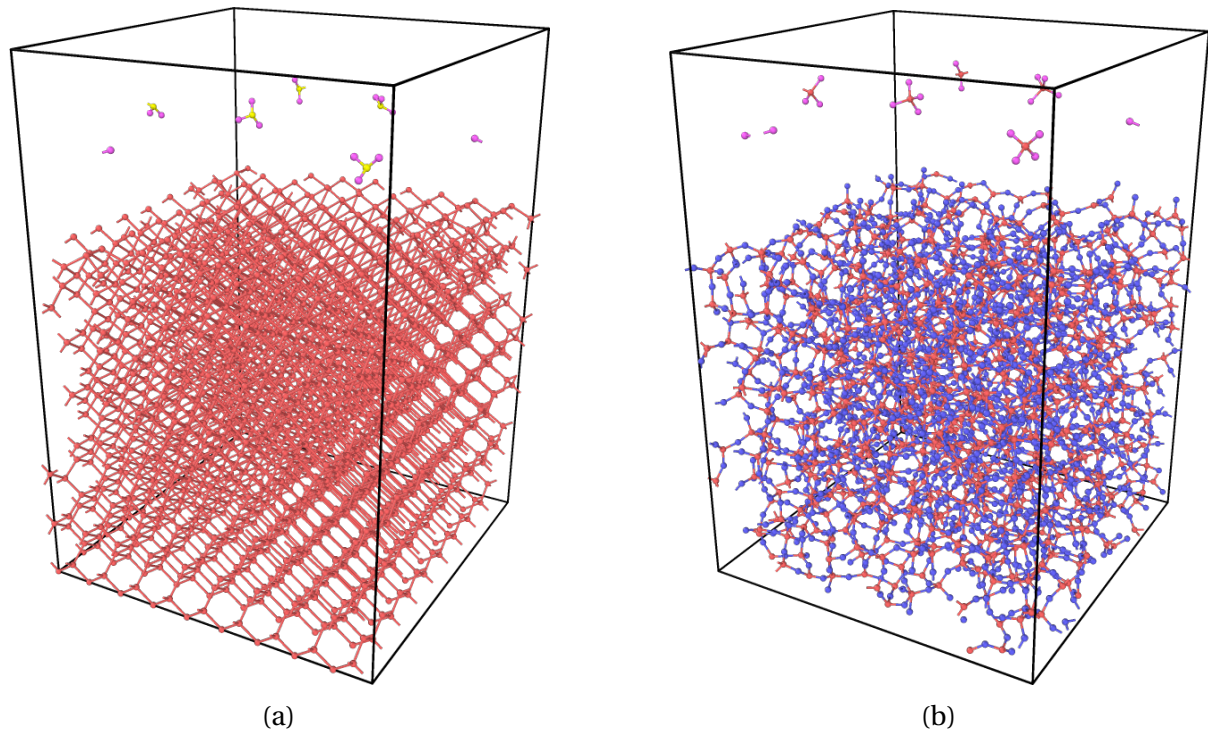


Figure 5.1: Measure sticking coefficient on bare surface (red=Si, blue=O, yellow=C, pink=F): (a) CF_3 radicals incident on Si crystal; (b) SiF_4 molecules incident on amorphous SiO_2 .

As a result of the limitation of the minimum interatomic distance and the system size, 5 molecules were inserted simultaneously for a single independent run. The kinetic energies of all the incident molecules were 0.0259 eV (300 K), and all the molecules were inserted normal to the substrate top surface. The substrate materials were equilibrated at 300 K using NVT ensemble. The number of timesteps of each run was determined by the molecules' molecular mass. A Python script was written to quantify it for different species. Generally, each run would take from 13,000 steps for light molecules to 37,000 steps for heavy molecules to ensure that all the inserted molecules would happen enough time to reach and interact with the substrate surface. At the end of the each independent run, the substrate materials were reset to their initial states, allowing the next independent run to take place. The independent run was repeated for 400 times with varying random number

seeds so that there were 2000 molecules sampled in total, ensuring good statistical accuracy but not requiring too much computational resources.

The final state of each run, with the position and velocity information of all the particles, was recorded in a single separate data file, and a Python script was used to collect the data from all 400 data files and to post-process the data to extract the desired information. In this work, the number of attached molecules on the substrate materials surface was measured at the end of each run. It should be noted that it was actually the number of C or Si atoms that was measured rather than the whole molecule, and the reasons were: (a) the bonds are determined internally and dynamically for LAMMPS using ReaxFF potential, which means that in the recorded data file the molecules are stored as individual atoms without the bond information, and therefore measuring the centering atoms C or Si would be a good and convenient estimate of the whole molecules; (b) the incident molecules did not necessarily keep their molecular structure after interacting with the substrate materials, especially for CF_x radicals incident on Si crystal (see Fig. 5.2 for an example), and therefore tracking atoms such as C or Si would be representative for measuring the whole sticking events.

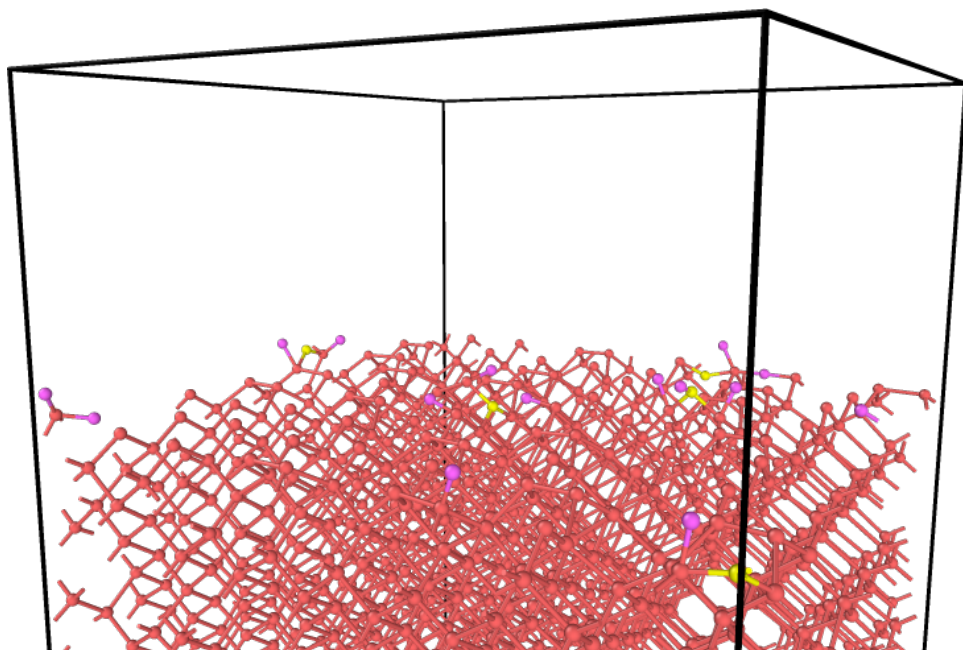


Figure 5.2: Incident CF_3 radicals attached to Si crystal with molecules dissociation (red=Si, yellow=C, pink=F)

In order to accurately define if a particular atom is attached to the substrate surface or not, a Python script was written with multiple filtering schemes to count the number of attached C or Si atoms. Firstly, as mentioned earlier, the bond information does not exist in the recorded data files, therefore bonds were manually generated between the corresponding atom pairs with the help of Ovito Python library. The cutoff values for generating different bond types are listed in Table 5.1, in which the experimentally measured bond lengths are also listed for comparison. The idea is that the cutoff values should be only slightly larger than the actually bond length so that all the physically existed bonds can be captured without creating some pseudo bonds, and different cutoff values were tested multiple times and the final values were selected as shown in Table 5.1. After the bonds were generated, only the specified type of atoms with the specified type of bonds (atoms with type Carbon and with the bond type C-Si and/or C-O for an example) were kept to be the potential candidates. Secondly, since it is possible that an incident molecule can rip off some substrate atoms and form some volatile compounds (for example it was observed some carbon atoms left the surface in the form of CO or CO₂), leaving the substrate surface but still with the specified bond type, only those incident atoms that were within 4 Å distance from the substrate surface were kept as the attached atoms. The 4 Å distance was adequate since the incident energy was low (0.0259 eV) and only 5 molecules were inserted in a single run.

Table 5.1: The experimentally measured bond length (Chemist 2023) and the characteristic cutoff values used for different bond types

Bond type	Bond length (Å)	Bond cutoff (Å)
Si–Si	2.33	2.5
Si–C	1.85	2.2
Si–F	1.6	1.83
C–F	1.35	1.5
C–O	≈ 1.43	1.6
Si–O	1.63	1.9

After designing the schemes to accurately define sticking events, the Python script was used to count the number of attached molecules for all the 10 incident species on the 2 substrate materials, and the results are listed in Table 5.2.

It can be found from Table 5.2 that the sticking coefficient of the same incident species

Table 5.2: Number of attached molecules on the substrate materials surface with a total incidence of 2000 molecules

Incident molecules	Crystal Si	Amorphous SiO ₂
C	2000	851
CF	2000	1210
CF ₂	1999	568
CF ₃	1998	36
CF ₄	1996	0
Si	1998	1995
SiF	1853	1983
SiF ₂	1693	752
SiF ₃	1208	35
SiF ₄	12	0

has a strong dependence on the type of the substrate material. It can be concluded that the Si crystal is much more reactive than the amorphous SiO₂ since almost all the sticking coefficients measured on the Si crystal are greater than the corresponding sticking coefficients measured on the amorphous SiO₂. The material dependence could possibly be explained by comparing the bond energies. The experimentally measured bond energies (Chemist 2023) for different bond types related to this work are listed in Table 5.3, where it can be found that the bond energy for Si–O is twice of the bond energy for Si–Si, meaning that Si–O bond is much stronger than Si–Si bond, which makes it easier for the incident species to react with the Si crystal and form new bonds. Another possible explanation is related to the molecular structure of the top surface of the two substrate materials. As shown in Fig. 5.3, the top surface of the Si crystal contains Si atoms uniformly. While Si atoms can generally form 4 covalent bonds, the Si atoms within the top monolayer only have formed 2 bonds, which means these atoms are undercoordinated and have a higher chance to form new bonds with the incident molecules. On the other hand, for amorphous SiO₂, the top surface contains Si and O atoms with a ratio of 1:2. Not only these Si atoms appear to be less undercoordinated (have more bonds) compared to Si crystal, but also those O atoms are either already saturated (with 2 bonds) or connected with 1 bond (could possibly form another bond to reach saturation). Thus, it can be expected that overall there are more sites on the crystal Si surface for the incident species to connect to, resulting in higher sticking coefficients.

It can also be found from Table 5.2 that the sticking coefficient also has a strong dependence on the incident species for the same substrate material. Generally, it can be

Table 5.3: The experimentally measured bond energies (Chemist 2023) for different bond types related to this work

Bond type	Bond energy (kJ/mol)
Si–Si	222
Si–O	452
C–Si	318
Si–F	565
C–F	485
C–O	358
C=O	799
C≡O	1072

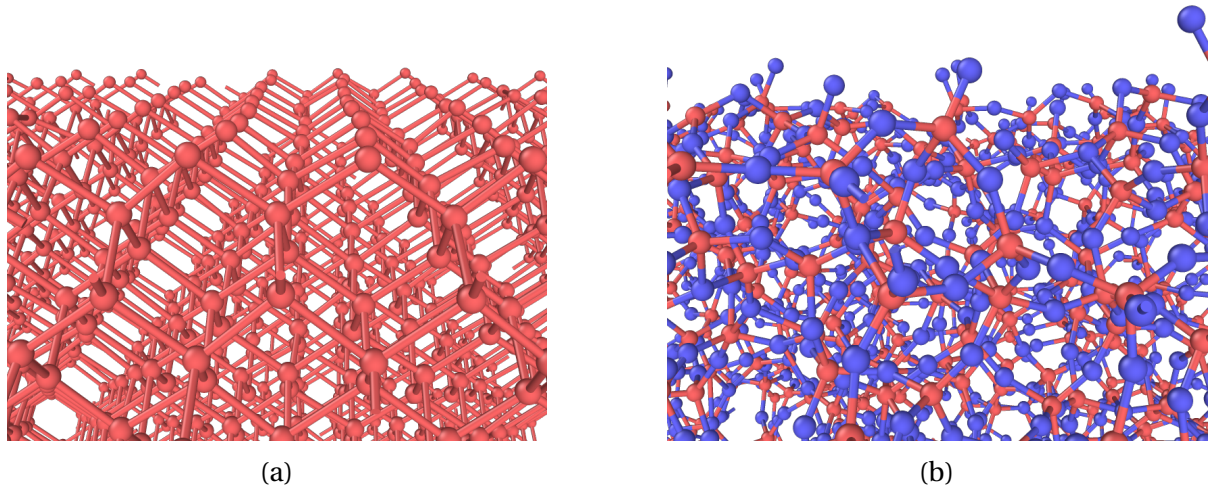


Figure 5.3: Top layer zoom in view of (red=Si, blue=O): (a) Si crystal; (b) amorphous SiO_2 .

concluded that for the same substrate material, the sticking coefficient gets lower when the incident species gets more fluorine rich, especially for the incident species of SiF_x , see Fig. 5.4. It can also be found that the sticking coefficient does not decrease linearly with the number of fluorine atoms within the molecule. There are some regions where the sticking coefficient decrease drastically and those regions seem to be material dependent. For example, for SiF_x , the sticking coefficient decreases from 0.6 to 0.006 within the region of SiF_3 to SiF_4 for Si crystal, while it decreases from 0.376 to 0.018 within the region of SiF_2 to SiF_3 for amorphous SiO_2 . Therefore, it could be difficult to predict the sticking coefficient as a function of the number of the monovalent(corner) atoms within a molecule.

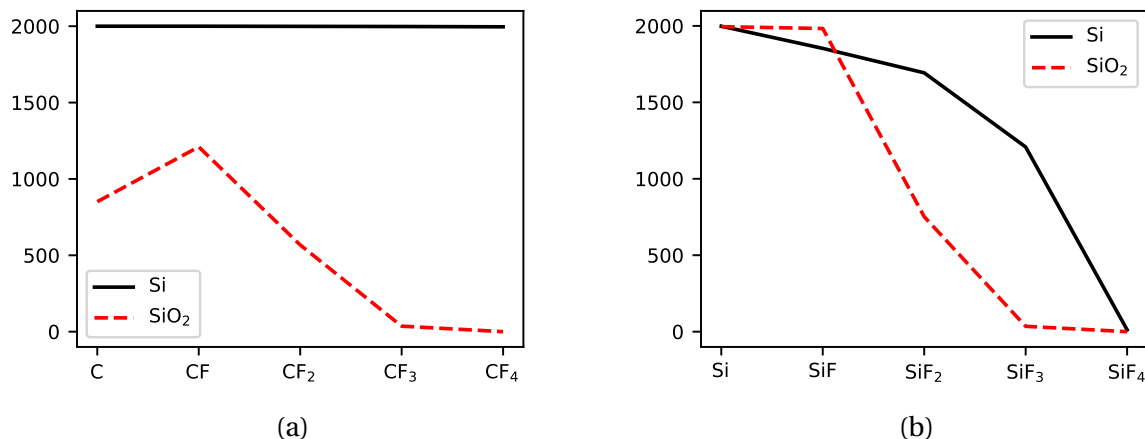


Figure 5.4: Plots of the data in Table 5.2, categorized by incident species as: (a) CF_x ; (b) SiF_x

One exception for the monotonic decrease in sticking coefficient can be located in the region of C to CF for substrate material SiO_2 , see Fig. 5.4a. This can be explained by monitoring the full trajectory of all the particles for the related incidence events. It was found that actually almost all the incident C atoms were able to attach to the SiO_2 surface at some point and form bonds with Si and(or) O atoms, which is expected since C atoms are assumed to be the most reactive species among all CF_x . However, the attached C atoms did not always reside stably on the substrate, in fact, if a C atom was connected to an O atom(s) only, there was a significant chance that the C atom would rip off the O atom(s) from the substrate and leave the substrate in the form of CO or CO_2 , see Fig. 5.5 for an example. A large portion of the incident C atoms was observed to leave the simulation

box in the form of CO_x and therefore was not counted in the total number of attached molecules. In contrast, it was observed that incident species such as CF and CF_2 produce much less volatile CO_x and thus the sticking coefficient measured for C atoms was lower than expected.

In this work, due to the purpose of saving hard drive space, only the final state of most of the independent runs were stored (the full trajectory of the first 20 runs was kept), and therefore the number of CO_x leaving the simulation box cannot be measured. It is possible to take the CO_x into account for measuring the sticking coefficients if the full trajectory of all the independent runs are retained.

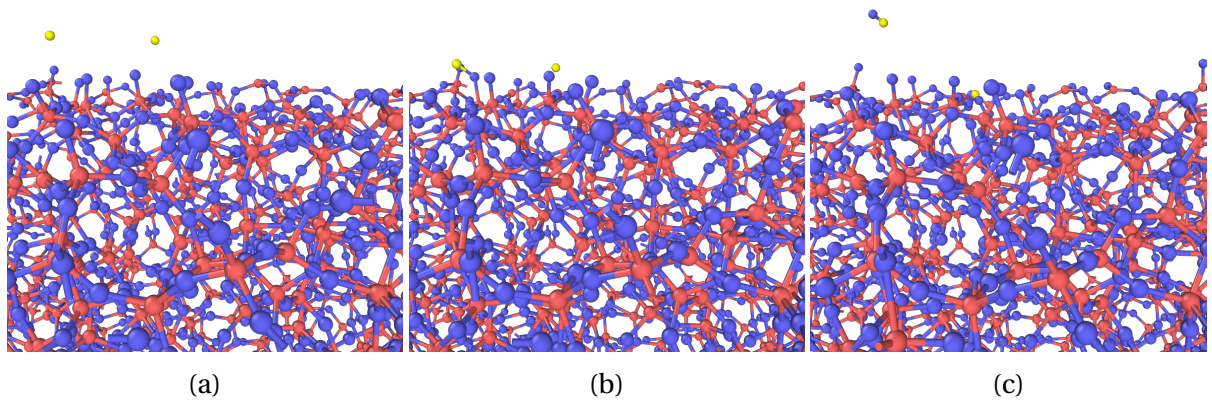


Figure 5.5: Trajectory plots showing that an attached C atom left the SiO_2 substrate surface in the form of CO (red=Si, blue=O, yellow=C), presented here are snapshots at timesteps of: (a) 5000; (b) 5700; (c) 6800.

Another exception for the monotonic decrease in sticking coefficient is for CF_x species incident on Si crystal substrate, see Fig. 5.4a. It can be found that the sticking coefficient was constantly 1.0 no matter which CF_x species was inserted. This can be better understood by taking the dissociation of molecules into account, as shown in Fig. 5.2 for CF_3 incident on Si crystal. In fact, it was found that no matter how stable the molecular structure look like (for example CF_4 is generally stable), the interaction between CF_x molecules and Si atoms were strong enough to break the C-F bonds and dissociate the whole molecules into individual atoms with newly formed Si-C and(or) Si-F bonds. See Fig. 5.6 for an example. This is not the case for SiF_x molecules as their molecular structures were mostly retained, see Fig. 5.7 for an example. The difference in CF_x and SiF_x molecules incident on Si crystal can also

be possibly explained by comparing the bond energy of the related bonds, see Table 5.3. The bond energy of all the related bonds are in the order of [Si-F] > [C-F] > [C-Si] > [Si-Si], therefore breaking C-F bonds and forming Si-F bonds would overall produce energy and direct the whole system to a lower energy (more stable) state. However, this explanation is not so solid since the difference in bond energies for C-F bonds (485 kJ/mol) and Si-F bonds (565 kJ/mol) is not so significant, therefore further investigation could be used in order to better understand the phenomenon.

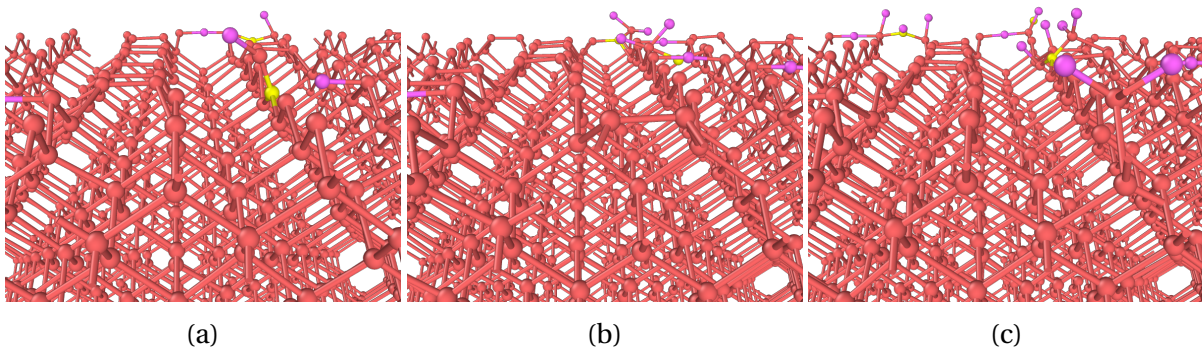


Figure 5.6: CF_x molecules dissociated on Si crystal (red=Si, yellow=C, pink=F), presented here are: (a) CF_2 ; (b) CF_3 ; (c) CF_4 .

It should be worth noting that the whole procedure for measuring sticking coefficients as well as the corresponding LAMMPS input files and Python scripts can be conveniently applied to other incident species and substrate materials as long as the related element types and bond types are supported by the ReaxFF parameter file (see Chapter 2 and Appendix A for details), which generally would require parameter files combination and extension as well as validation and verification, similar to what we performed in Chapter 4.

5.3.2 On growing surface - dynamic

A parametric study of 4 different species, CF_x ($x = 1 \sim 4$) was performed on the substrate materials of Si crystal and amorphous SiO_2 . Unlike the previous study on the static surface, only the CF_x species were evaluated since these are the main species that contribute the polymer growth on the surface. Measuring the sticking coefficients on a polymer growing

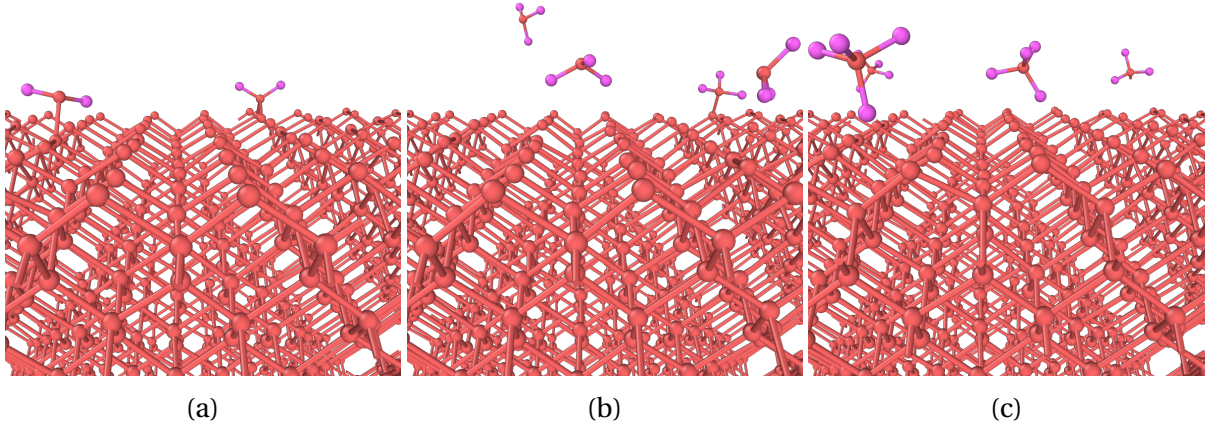


Figure 5.7: SiF_x molecules retained molecular structure on Si crystal (red=Si, pink=F), presented here are: (a) SiF_2 ; (b) SiF_3 ; (c) SiF_4 .

surface is important since it is expected to see that the growth rate, which is proportional to the sticking coefficient, strongly depends on the surface conditions of the substrate. For example, the sticking coefficient for a given species with the same incident angle and energy on a bare substrate surface is generally constant as we previously measured. As the incident species accumulates on the substrate and grows a thin film, the sticking coefficient gradually transitions to and approaches another constant value which can be estimated by the steady state growth rate. During the transition process, it can be assumed that the sticking coefficient (growth rate) depends on the surface coverage θ , which is dimensionless quantity generally used to characterize how much of the target material is covered by the incident species.

The sizes of the materials are identical to what we used for bare surface incidence simulations, while the simulation box size ($34 \times 34 \times 80 \text{ \AA}^3$) is slightly different as more empty space was added above the material in order to have enough space for the polymer to grow. All the molecules were inserted within a thin horizontal plane 10 \AA below the top surface of the simulation box, and the horizontal positions (x, y) were randomly sampled with a minimum interatomic distance of 3 \AA . Periodic boundary conditions were used for the lateral directions x and y , while finite boundary condition was applied to the vertical direction z . It should be noted that the top surface of the simulation box was set as open so that the reflected molecules can properly leave the simulation box, and at the bottom of the substrate, a thin layer of the material (about 20% by volume) was kept static so that the substrate material would not have some unwanted bulk motions. The rest of the substrate

was thermally equilibrated at 300 K using NVT ensemble. It should also be noted that there were some occasions where the reflected molecules were leaving the simulation box through the top surface while self rotating. What could happen was that a part of the molecules left the box first, and the rest atoms returned back and went downwards because those atoms actually had velocity vectors pointing downwards at the moment due to self rotating and the restraining forces (bonds) were nullified when the first part of the molecules left the box. This phenomenon is definitely not desired and was resolved by creating a thin layer region (5 Å thick) right below the top exit where all atoms can only go upwards and any downwards motions will be reflected, using LAMMPS *fix oneway* command.

Unlike the previous study on the static surface, constant flux of CF_x species was introduced to the substrate surface and no material reset was performed. The incident energy (1 eV) was slightly higher than previous (0.0259 eV) due to the limitation of time scale and system size scale, i.e., a very low energy would result in a small interatomic distance between two consecutive incidences and therefore there would be too many incident molecules reside simultaneously within the simulation box which results in significant interference between "older" reflected molecules and "newer" incident molecules. The incident angle was normal to the substrate surface. The incident molecules were introduced at a constant pace with 1000 timesteps (250 fs) between two consecutive incidences, and the total number of incidence was 3000. Therefore a whole simulation would run for roughly 3 million timesteps where some extra timesteps were added to the end in order to give the last few incident molecules enough time to travel. The whole simulation was quite computationally expensive so that compromise among factors such as flux, incident energy and total number of incidence was taken into account.

The trajectories of all the atoms during the full time length were recorded for each simulation case and stored in a single separate data file. Ovito was used to visualize the data file, and a Python script was used to collect the data and post-process it to extract the desired information. See Fig. 5.8 for an example of measuring sticking coefficient of CF radicals incident on Si crystal surface. In this work, the number of attached molecules on the substrate materials surface was measured as a function of time, and the slope of the number vs. time curve can be used to measure the growth rate and more importantly estimate the sticking coefficient since constant fluxes were used.

The scheme used to count the number of attached molecules at a given time was different from the one previously used for the bare surfaces. For the bare surfaces, since only 5 incidences were introduced for one run and only the results for the final state were recorded, the counting scheme need to be as accurate as possible and thus we introduced

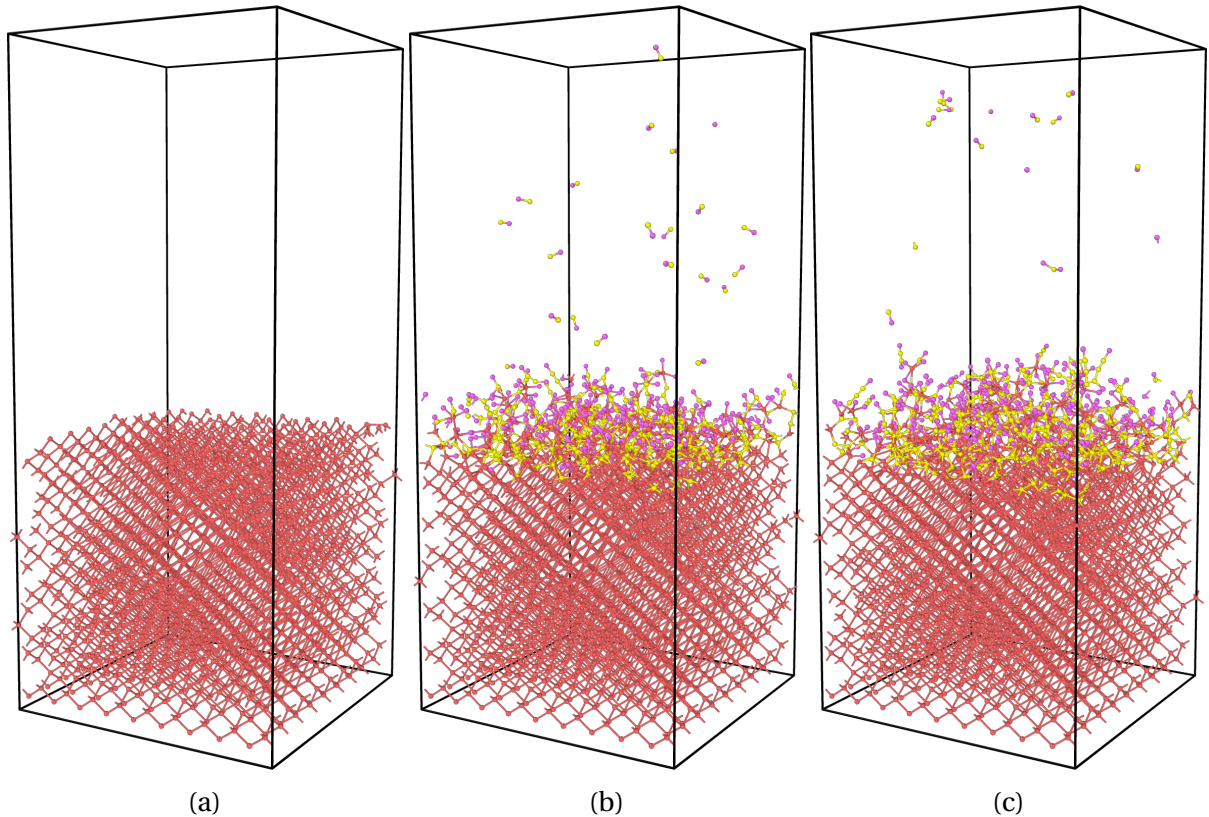


Figure 5.8: Measure sticking coefficient on growing surface (CF radicals incident on Si crystal; red=Si, yellow=C, pink=F): (a) after 0 molecules incidence; (b) after 1000 radicals incidence; (c) after 3000 radicals incidence.

multiple layer of filtering schemes to correctly build the bonds and derive the number of attachment from the bond information. However, for the growing surfaces, such schemes would be too time consuming to measure the time dependent data and the schemes might not be as accurate due to much complex surface conditions. Since what we really interested is the averaged data within a time bin (moving average) to reduce noises and statistical errors, it is possible to use a simple scheme for counting numbers which is less accurate but on moving average it can track the true values. Therefore, we counted the number of C and F atoms within a layer that was right above the substrate surface. The thickness of this layer depends on the case. For example, if it was measured that in the end of the simulation the polymer grew 5 Å thick, then a 5 Å thick layer could be used to contain the whole polymer growth process during the simulation. It can be seen that this layer would also contain those passing particles which are either just inserted or already reflected at the moment of measurement, but it can be safely assumed that by taking a moving average, those noises can be canceled out and the true number of attached particles can be revealed. Therefore, a Python script was used to count the number of C and F atoms within the layer and the layer thickness was determined manually for each simulation case.

The number of attached C and F atoms was measured as a function of timestep for all CF_x ($x = 1 \sim 4$) incident species on two substrate materials and are plotted in Fig. 5.9 for Si crystal and Fig. 5.10 for amorphous SiO_2 respectively. It can be seen that in all cases, the F:C ratio in the polymer layer matches the F:C ratio of the incident species very well, indicating that without the effect of the incidence of other energetic species, the 1 eV incident species tend to attach or get reflected as a whole molecule. This could because of that the kinetic energy transfer during the interaction was not high enough to break the bonds, or the interaction was so reactive that all the parts can be fully absorbed even though the molecule was dissociated, as we observed for CF_x species incident on bare Si crystal surface.

It can also be found that the shape of the curves generally matches our assumption that the sticking coefficients gradually transition from one steady state to another steady state, where the two steady states both have constant sticking coefficients due to uniformity in surface conditions. In our particular cases, since constant flux species was used for all cases, the growth rate (slope of the curve) is proportional to the corresponding sticking coefficient. And since the CF_x species have higher sticking coefficient on the bare surface compared to on the fluorocarbon polymer layer, for most of the curves in Fig. 5.9 and Fig. 5.10, the curves seem to initially increase linearly at a higher rate, and gradually transitions to another linear region with a slower increase rate (or 0) where the transition region is generally smooth

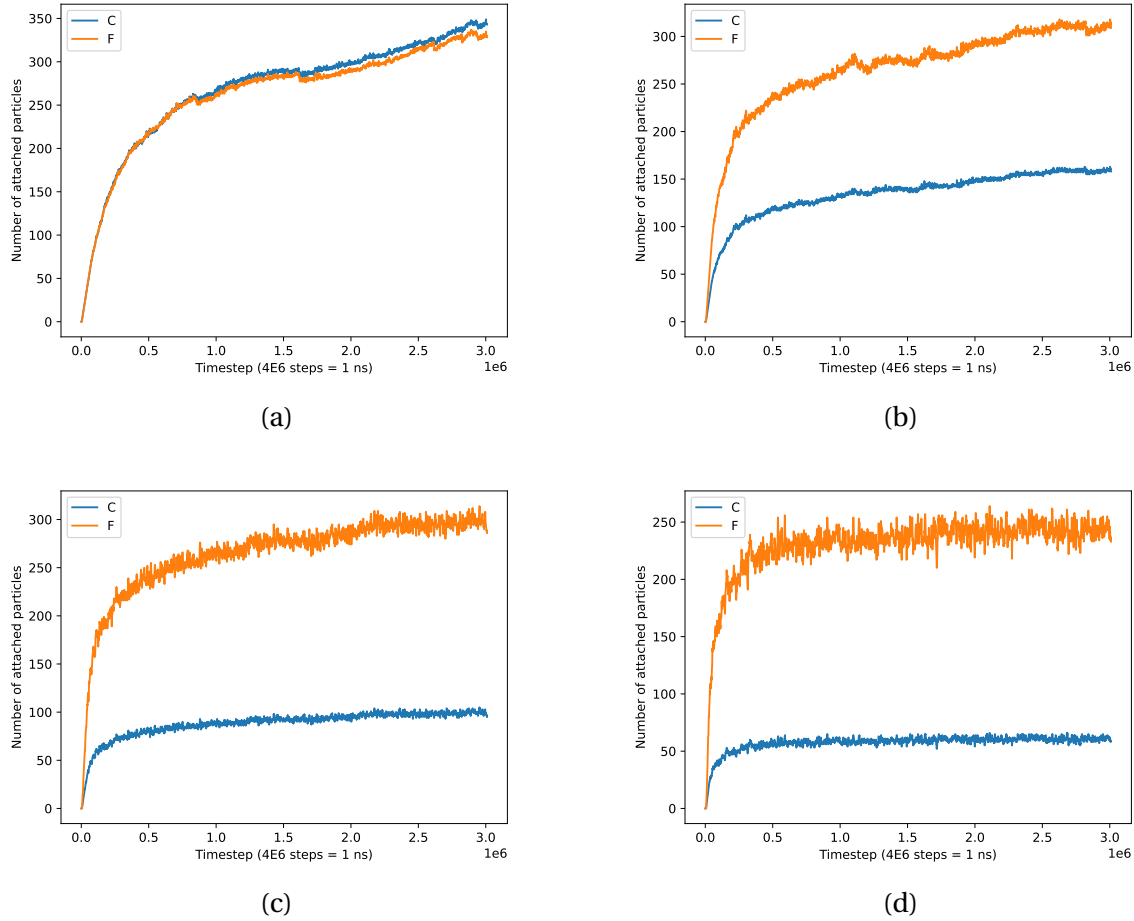
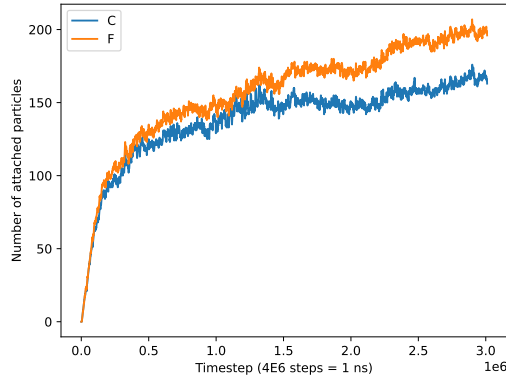
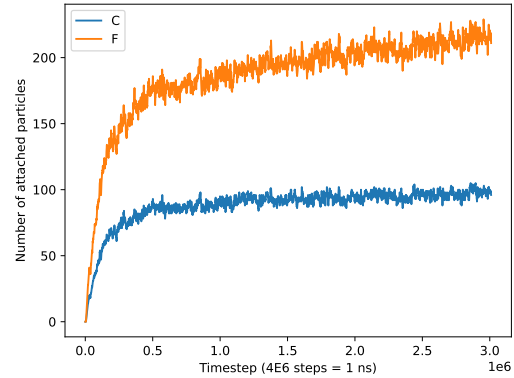


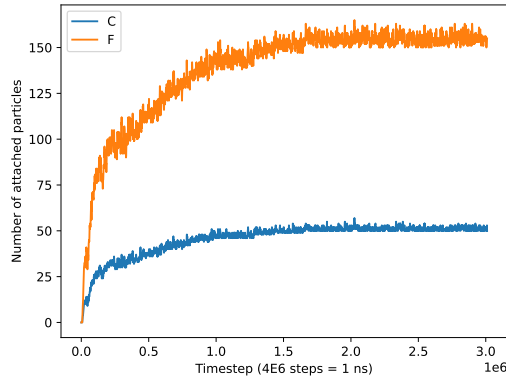
Figure 5.9: Number of attached C and F atoms as a function of timestep, for substrate material of Si crystal and incident species of: (a) CF; (b) CF₂; (c) CF₃; (d) CF₄



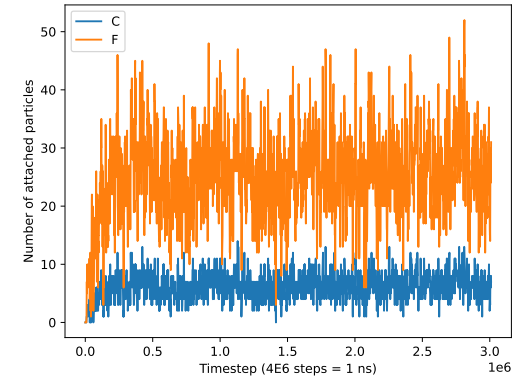
(a)



(b)



(c)



(d)

Figure 5.10: Number of attached C and F atoms as a function of timestep, for substrate material of amorphous SiO₂ and incident species of: (a) CF; (b) CF₂; (c) CF₃; (d) CF₄

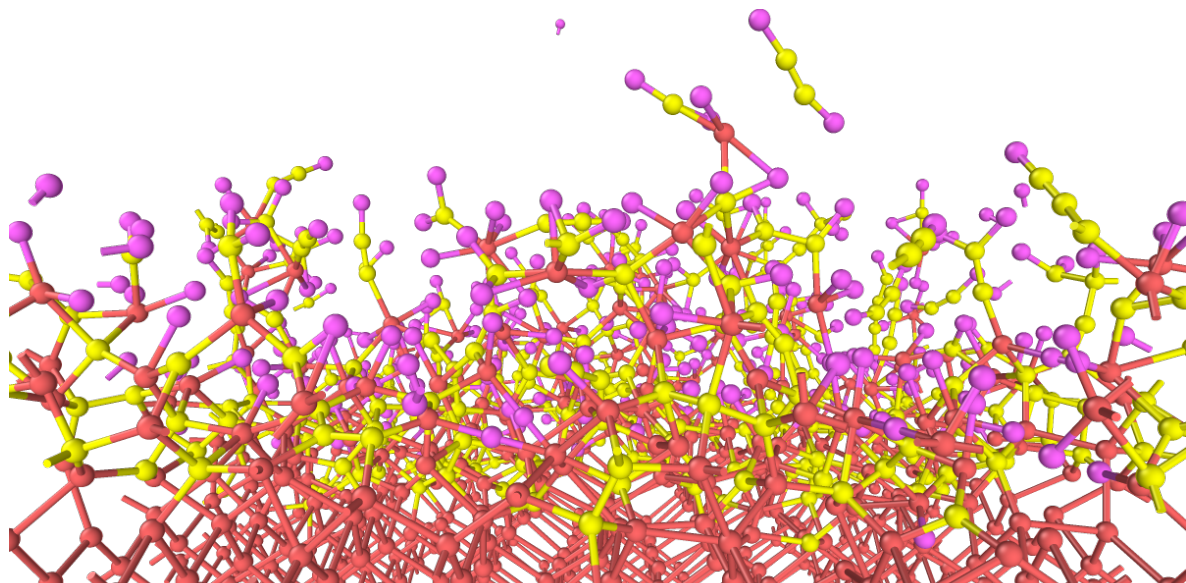
and the width of the transition region seems to negatively related to the F:C ratio of the incident species. Therefore the shape of all the curves matches our expectation.

Some of the polymer growth were saturated (i.e., showing a plateau in the curves) and the likelihood of reaching saturation seems to be related to the F:C ratio of the incident species. It can be found that incident species with higher F:C ratio generally leads to faster saturation. This can be expected since higher F:C ratio means that the incident molecule is more saturated (less electrons to pair and form bonds) and thus the formed polymer film is more fluorine rich and less likely to form new bonds.

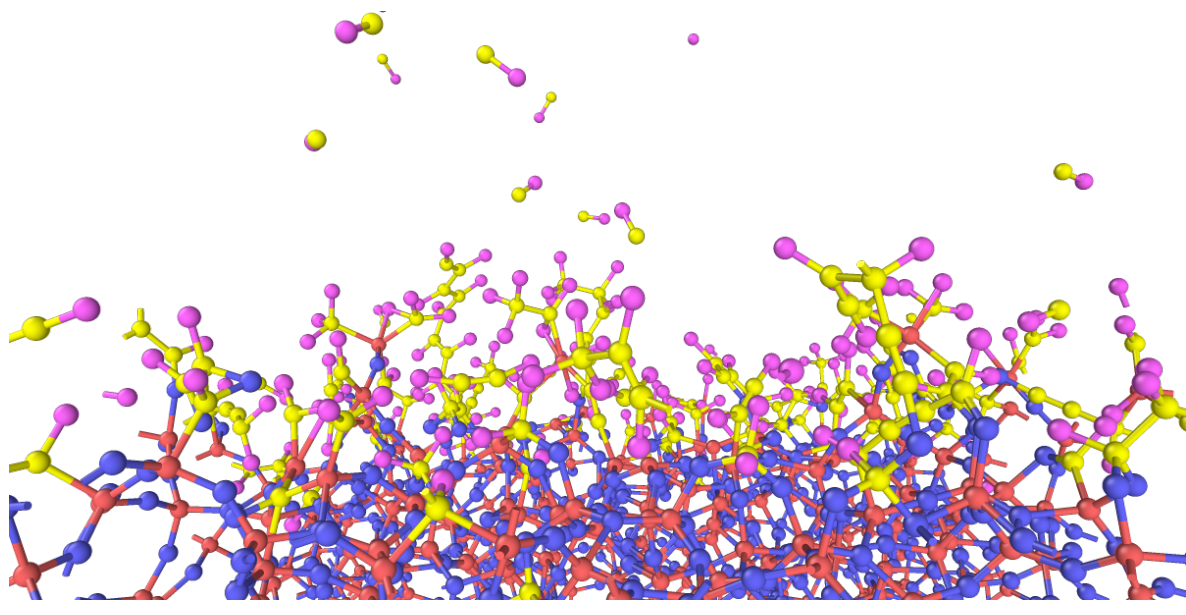
The saturation also depends on the substrate material. It can be observed that for the same incident species, it was less likely to reach saturation on the Si crystal compared to on the amorphous SiO_2 . On the Si crystal, not only the number of attached atoms for the same incident species at the same timestep was higher than on the amorphous SiO_2 , but also the growth rate after reaching steady state was slightly higher. This matches the results on the bare surface since it was found that Si crystal was more reactive than amorphous SiO_2 , therefore it is expected to see more molecules attached to the Si surface at least for the first a few monolayers.

Furthermore, the difference in growth rates after reaching steady state for the two substrate materials also suggests that even for the same incident species, after the substrate materials are fully covered, the formed polymer layers are still slightly different for different substrate materials. This can be better understood by visualizing the molecular structures, see Fig. 5.11 for an example of CF radicals deposited on Si crystal and amorphous SiO_2 . It can be observed that not only the polymer formed on the Si crystal is thicker than the on amorphous SiO_2 , the mixing of the substrate layer with the polymer layer is also more significant on the Si crystal, i.e., there are much more Si atoms migrating to the polymer layer region and forming multiple bonds, even on the very top surface of polymer film. The migration of Si atoms is possibly due to their high reactivity. And by comparing the bond energies, see Table 5.3, the bond energy of Si-Si (222 kJ/mol) is significantly lower than Si-O (452 kJ/mol) and other related bonds, which could also contribute to the migration of Si atoms. Thus, more Si atoms in the formed polymer layer on Si crystal than on amorphous SiO_2 could lead to higher growth rate as more bonds can be formed.

One exception in the matching of the F:C ratio in the polymer layer with in the incident species can be found in Fig. 5.10 for CF radicals incident on amorphous SiO_2 . The C atoms were slightly less likely to attach on the substrate than the F atoms, instead of equally attached. This could be better understood by taking into account the de-oxygen effect, as we observed previously for C atoms incident on bare SiO_2 surfaces. As shown in Table 5.4, the



(a)



(b)

Figure 5.11: Zoom-in view of the top layer of CF radicals deposited on substrate materials (red=Si, blue=O, yellow=C, pink=F): (a) Si crystal; (b) amorphous SiO₂.

number of Si atoms and O atoms left in the system at the end of the simulation for different incident species are measured. It can be found that fluorine rich molecules generally are less likely to remove O atoms from the substrate surface, which matches our previous observation for the bare surfaces that a large portion of C atoms left the simulation box in the form of CO_x . Since some attached C atoms left the substrate while the F atoms did not, it is expected to see an offset when counting the numbers, especially for those low F:C ratio incidences.

Table 5.4: Number of Si atoms and O atoms left in the system at the end of the simulation for different incident cases

Incident molecules	Number of Si atoms	Number of O atoms
CF	1000	1953
CF ₂	1000	1990
CF ₃	1000	2000
CF ₄	1000	2000

Another exception in the smoothness of these Number vs. Timestep curves in Fig. 5.9 and Fig. 5.10 can be located within the plot for CF₄ molecules incident on amorphous SiO₂. The curves seem to be extremely noisy and this is because of the counting scheme. Actually, no CF₄ molecules were able to attach on the SiO₂ substrate, see Fig. 5.12. Therefore, the data on the curves only represent the atoms passing the counting region and therefore only the noises were plotted.

5.4 Analytical model

In the last section a parametric study of CF_x ($x = 1 \sim 4$) species was performed on the substrate materials of Si crystal and amorphous SiO₂. Polymer growth was observed and the number of attached atoms was measured as a function of timestep. Since for all the simulation cases, the species was directed to the substrate surface at constant flux, the sticking coefficients can be measured by calculating the time-dependent slopes of the Number vs. Timestep curves.

For most of the measured curves, it was found that they all follow a similar rule: the growth rate gradually transitions from one steady state (linear) region to another steady state (linear) region, where in the two regions the growth rate seems to be constant. This

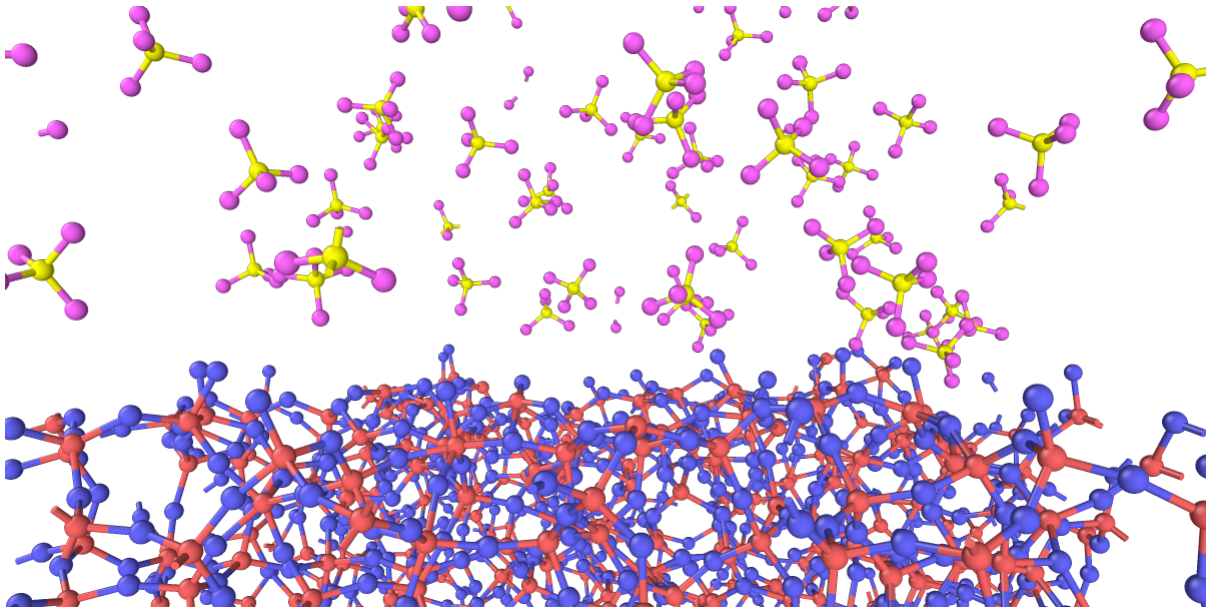


Figure 5.12: Zoom-in view of the top layer of CF_4 molecules incident on amorphous SiO_2 (red=Si, blue=O, yellow=C, pink=F).

generality could lead to an empirical model, and the model should have the same functional form for all the different incident cases, with some fitting parameters which can be used to uniquely characterize different cases. The idea is the same for what we have done for the scattering matrices for different HAR sidewall materials in Chapter 3. If the empirical analytical model can be constructed properly and intuitively, not only it can help us to extract the deep information from the curves and compare the results directly across different incident cases, but also it makes it possible to conveniently reproduce and reuse the data in rigorous models such as feature profile simulators.

5.4.1 Model derivation

In order to derive the empirical analytical model, assumptions first need to be made based on the shape of the Number vs. Timestep curves as well as on the understanding of the deposition process in general. The assumptions are listed below:

- When the incident molecules first reach the substrate surface, the growth rate is constant due to uniformity and it depends on the sticking coefficient on the bare surfaces;

- As the incident molecules accumulate on the substrate, the surface is partially covered. When the next molecules come in, depending on which part of the surface the molecules see, the sticking coefficient has two different values. The total growth rate depends on the surface coverage ratio and gradually transitions from one steady state to another steady state, shown as the blue line region in Fig. 5.13;
- When the incident molecules have fully covered the substrate surface, the surface condition is also assumed to be uniform. The polymer growth reaches steady state as the growth rate is constant and depends on the sticking coefficient on the surface of the polymer film, shown as the red line region in Fig. 5.13.

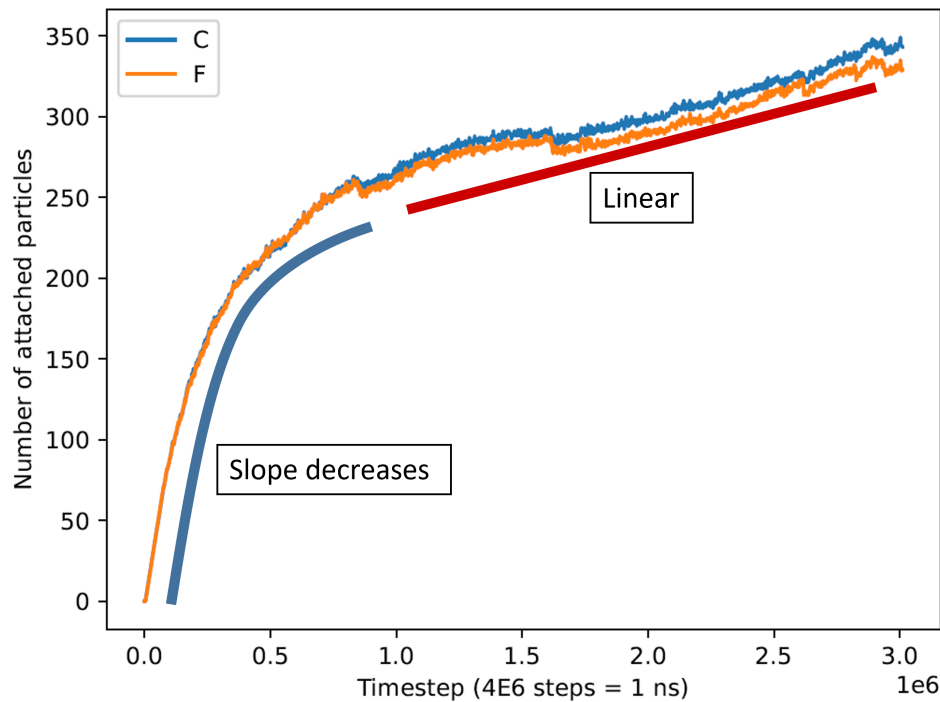


Figure 5.13: Diagram showing that there are two characteristic regions where the polymer growth behaves differently.

Using these assumptions, an analytical model describing the polymer growth can be derived in a differential form, as shown in Eq. 5.1

$$\frac{dn}{dt} = \begin{cases} \left(1 - \frac{n}{b}\right)r_L + \frac{n}{b}r_H & n \leq b \\ r_H & n > b \end{cases} \quad (5.1)$$

where n is the number of attached particles at time t , and $\frac{dn}{dt}$ gives the growth rate. Note in the derivation, we actually normalized t by the value of the flux so that t now represents the total number of incidence at that time and $\frac{dn}{dt}$ gives the sticking coefficient. b is used to quantify when the substrate is fully covered and has the same units as n , therefore $\frac{n}{b}$ is the surface coverage ratio. b is also the y value of the intersection point of the blue and the red regions in Fig. 5.13. r_L is the growth rate (sticking coefficient) of the incident species on bare substrate surfaces, while r_H is the growth rate (sticking coefficient) on fully covered polymer films. Linear combination is used to calculate the growth rate on partially covered surfaces as a function of surface coverage ratio $\frac{n}{b}$, as shown in Eq. 5.1 for $n \leq b$. Note it is possible to use different combination rules if the current model does not fit the data well.

The two ordinary differential equations (ODE) in Eq. 5.1 are generally simple to solve. For $n > b$, the ODE is at 0th order and the solution is a linear function shown as

$$n = r_H(t - t_b) + b \quad (5.2)$$

where t_b is the time where $n = b$ and is also the x value of the intersection point of the blue and the red regions in Fig. 5.13. For $n \leq b$, the ODE is at first order and the solution is an exponential function shown as

$$\begin{aligned} n &= r_L \cdot \frac{b}{r_L - r_H} \left[1 - \exp\left(-t \left| \frac{b}{r_L - r_H} \right.\right) \right] \\ &= r_L \cdot \tau \left[1 - \exp\left(-\frac{t}{\tau}\right) \right] \end{aligned} \quad (5.3)$$

where the initial condition of $n = 0$ at $t = 0$ was applied and the introduced auxiliary variables are defined/correlated as

$$\tau = \frac{b}{r_L - r_H} \quad (5.4a)$$

$$t_b = \tau \ln\left(\frac{r_L}{r_H}\right) \rightarrow r_H = r_L \exp\left(-\frac{t_b}{\tau}\right) \quad (5.4b)$$

Therefore, now the problem becomes to find the optimal values of these characteristic parameters which can best reproduce the original $n(t)$ curves. It should be noted that this analytical model is not perfect as the fundamental assumptions may not be valid in some extreme cases. For example, this model does not take into account the loss term, i.e., when a large chunk of the attached molecules leave the substrate surface in a compound form,

which was observed in the MD simulations, especially for those cases with high incident energies. Moreover, this model is based on the assumption that the surface condition is uniform for both the bare substrate and the fully covered surface, which could be valid for dense materials such as Si crystal and amorphous SiO₂, but might not be true for the deposited polymer films. However, since in this work the reactive species were introduced to the substrate materials at fairly low energies and normal angles, those effects might be negligible when modeling sticking events. The proposed analytical model need to be tested by fitting it to the measured $n(t)$ curves in order to see how it performs without including those effects.

5.4.2 Regression scheme

The derived analytical model is summarized here as

$$n(t) = \begin{cases} r_L \cdot \tau [1 - \exp(-t/\tau)] & n \leq b \\ r_H(t - t_b) + b & n > b \end{cases} \quad (5.5)$$

and a two-segment regression scheme was used to find the optimal values for these characteristic parameters in Eq. 5.5. The idea is that the value of t_b is first predefined by doing a full sweep of it within a reasonable range. For the transition region ($t \leq t_b$, $n \leq b$), we do a regression using the exponential function as shown in Eq. 5.3, the optimal values for r_L and τ can be determined and the corresponding sum of squared errors (SSE) can be calculated. And for the steady state region , we do a linear regression using Eq. 5.2, the optimal values for r_H and b can be determined as well as the corresponding SSE. Finally, the total SSEs is evaluated for different t_b values, and the optimal values for (t_b, r_L, τ, r_H, b) can be determined which gives the least SSE.

One thing need to be taken care of is the "boundary" conditions at the intersection point ($t = t_b$, $n = b$) for the two solutions, i.e., how the two fitting lines should be connected at the intersection point. Generally, there are four options: (a) no constrain; (b) match value; (c) match derivative; (d) match both. Ideally we want to have the two fitting lines match both the values and the derivatives at the intersection point. However, it was found that it was unrealistic to do so since it would introduce significant statistical errors. Since the sticking coefficient is the primary quantity to capture by the model and it is represented by the derivative of the curve, we decided to choose option (c), match derivative, so that the value of the sticking coefficient is continuous across the intersection point.

By matching the derivative, we introduce one more constraint to the problem so that

the total degrees of freedom is reduced by one, i.e., now the value of r_H is determined by other variables as shown in Eq. 5.4b rather than by the regression scheme directly. The final regression scheme is listed in Algorithm 2.

Algorithm 2 A two-segment regression scheme

```

 $SSE_{min} \leftarrow \infty$ 
for all  $t_b$  within a predefined range do

    Do regression for  $t \leq t_b$  part of  $n(t)$ :
    • Get the value of  $[r_L, \tau]$ 
    • Calculate sum of squared errors ( $SSE_L$ )

    Calculate  $r_H$  based on the values of  $[t_b, r_L, \tau]$ 
    Do regression for  $t > t_b$  part of  $n(t)$ :
    • Get the value of  $[b]$ 
    • Calculate sum of squared errors ( $SSE_H$ )

     $SSE = SSE_L + SSE_H$ 
    if  $SSE < SSE_{min}$  then
         $SSE_{min} = SSE$ 
         $params_{min} = [t_b, r_L, \tau, r_H, b]$ 
    end if
end for
Output  $[t_b, r_L, \tau, r_H, b]$ 

```

5.4.3 Regression results

A Python script was used to apply Algorithm 2 to all the measured $n(t)$ curves to obtain the optimal parameter values. The number of attached C atoms was used as $n(t)$ and the normalized timestep (with respect to flux) was used as variable t so that the slope $\frac{dn(t)}{dt}$ gives the sticking coefficient. The obtained fitting parameters are presented in Table 5.5 for Si crystal and in Table 5.6 for amorphous SiO₂, in which the row for CF₄ on SiO₂ is left as "NA" since no valid data was measured in Fig. 5.10. Since r_L is defined as the growth rate (sticking coefficient) for the initial surface where no incident molecules have been

attached, it should match the sticking coefficients obtained previously for the bare surfaces. However, it can be seen that the obtained r_L values generally overpredict the actual sticking coefficients on the bare surfaces, which is possibly an artifact introduced by the scheme used for counting attached atoms. Since the counting scheme actually measures the total number of specified atoms within a thin layer above the substrate surface rather than the attached atoms, what could possibly happen is that for a given constant flux, the number of atoms within the thin layer actually includes both the attached atoms and a finite number of passing atoms. The number of passing atoms is constant for a given constant flux and contributes to the full $n(t)$ curve as a constant offset. This offset is generally negligible when performing the two-segment regression and calculating derivatives for the full curves. However, it can significantly affect the fitting results at the starting point of the curves ($n \approx 0$), where $n(t)$ almost instantly increase from 0 to the offset value and therefore the slope significantly overpredicts the true sticking coefficient value.

Table 5.5: Fitting parameters obtained from the two-segment regression for CF_x species incident on Si crystal

Incident molecules	t_b	r_L	τ	b	r_H	SSE
CF	822	1.043	247.44	228.5	0.03762	67304
CF_2	448	1.056	107.62	114.32	0.01644	19067
CF_3	312	1.142	62.556	78.992	0.00779	22834
CF_4	318	0.974	52.253	55.659	0.00222	14434

Table 5.6: Fitting parameters obtained from the two-segment regression for CF_x species incident on amorphous SiO_2

Incident molecules	t_b	r_L	τ	b	r_H	SSE
CF	599	0.8507	145.04	124.66	0.01369	69545
CF_2	640	0.6807	126.12	85.52	0.00426	30669
CF_3	805	0.3074	129.58	48.796	0.00062	14598
CF_4	NA	NA	NA	NA	NA	NA

Another finding is that the fully coverage number b seems to be inversely proportional to the F:C ratio of the incident species ($r_{\text{F/C}} \times b \approx \text{const}$), especially for the Si crystal cases.

This makes sense since it was observed that the F:C ratio within the polymer film matched the F:C ratio of the incident species, and therefore the inverse proportionality suggests that the total numbers of F atoms within the polymer film for fully covered surfaces using different incident species are approximately the same.

In order to visualize the accuracy of the analytical model, the two fitting lines are overlaid on the original curves and all the plots are presented in Fig. 5.14 for both Si crystal and amorphous SiO_2 . It can be seen that for all the curves, the analytical model were able to capture the shape of the curves very well, indicating that the fundamental assumptions behind the model are indeed solid and valid for the concerned conditions. Due to only matching derivatives, a discontinuity can be observed at the intersection point for all curves and its magnitude seems to differ from case to case. However, since measuring sticking coefficients is the primary goal in this work, the small gap is acceptable as long as the derivatives are continuous when the fitting lines pass the intersection point.

It should also be noted that the derived analytical model for predicting sticking coefficients on growing surfaces as well as the corresponding LAMMPS input files and Python scripts can be conveniently extended to other simulation cases with different incident species and substrate materials. The general function form of the model (see Eq. 5.5), together with the characteristic parameters for the desired pair of incident species and substrate materials, is complete for predicting sticking coefficients on growing surfaces and can be easily incorporated into any rigorous models such as feature profile simulators.

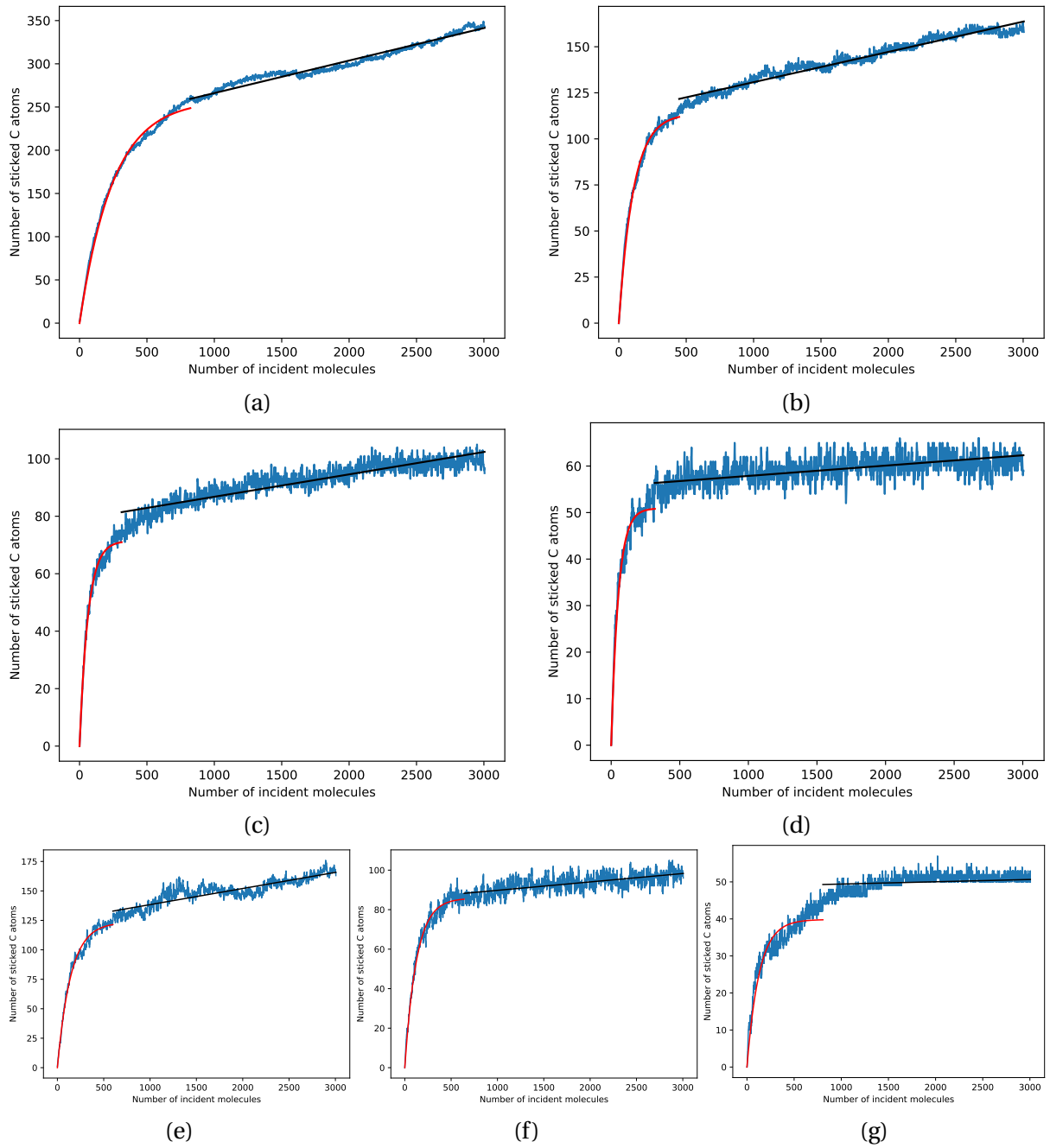


Figure 5.14: Number of attached C atoms as a function of number of inserted molecules, with fitting lines overlaid. Presented here are curves for simulation cases as: (a) CF on Si; (b) CF₂ on Si; (c) CF₃ on Si; (d) CF₄ on Si; (e) CF on SiO₂; (f) CF₂ on SiO₂; (g) CF₃ on SiO₂.

CHAPTER

6

CONCLUSIONS AND FUTURE WORK

6.1 Conclusions

This dissertation explores plasma-surface interactions in high-aspect-ratio plasma etching using Molecular dynamics simulations. In particular, three topics have been selected and investigated in individual chapters.

Glancing-angle scatterings were discussed in Chapter 3. In this work, we have performed MD simulations of glancing-angle scattering on different sidewall materials typically exposed to energetic ions during HAR processes, including SiO₂, AC and PS. The results of this study indicate a transition from predominantly specular scattering to more diffusive scattering as the incident ion angle becomes more normal and as the incident ion energy increases. This transition to diffusive scattering is accompanied by increased ion energy loss and a higher likelihood of implanting into the material or a near-total ion energy loss. The angles over which this transition occurs are very relevant for typical HAR processes, particularly when the faceting of the mask due to ion erosion is considered. These trends in scattering are consistent with current practice in HAR processing in which greater incident ion energies are used to achieve higher aspect ratios. These trends also suggest that ion

energy loss could contribute to RIE (reactive ion etching) lag and etch stop at higher aspect ratios where a large number of sidewall collisions are expected as the ion traverses from the top to the bottom of an HAR feature. To be able to incorporate the MD measured data into any rigorous models, an empirical analytical function was also proposed, which can be used to predict the scattering distribution as a function of incident angle and incident energy. Cross comparisons between the measured distributions and the predicted distributions were performed, and good agreement was generally achieved for all the sidewall materials studied.

Fluorocarbon polymer formation was discussed in Chapter 4. In this work, we discussed results from reactive MD simulations of fluorocarbon polymer formation on HAR sidewalls in plasma etching processes by depositing CF_x ($x = 1 \sim 3$) radicals onto amorphous SiO_2 and Si crystal substrates. ReaxFF interatomic potential was used and a parameter file for Si/O/C/F systems was prepared. Validation and verification tests were carried out for the parameter file. The MD simulation results show that the growth of fluorocarbon polymer film on amorphous SiO_2 surface generally saturates very quickly. Only a few monolayers of polymer film can form on the surface, and the thickness weakly depends on the incident energy and angle of the CF_x species, as well as the addition of energetic Ar ions. The results also show that the film thickness strongly depends on the incident species as fluorine deficient species tend to grow thicker polymers. The film thickness also strongly depends on the substrate materials as polymers on substrate of Si crystal can grow much thicker than on amorphous SiO_2 . It was also found that carbon species could potentially play a positive role in forming thicker polymer films. However, the long carbon chains formed on the substrate surface, especially on amorphous SiO_2 , are mostly *sp* hybridized which do not actively cross-link with other carbon chains or with other CF_x species. With the help of other energetic incidence, these *sp* carbons may be activated to be more *sp*² hybridized and form more graphene-like structures.

Sticking coefficients were discussed in Chapter 5. In this work, the sticking coefficients of molecules CF_x ($x = 0 \sim 4$) and SiF_x ($x = 0 \sim 4$) on substrate materials of amorphous SiO_2 and Si crystal were measured using reactive MD simulations with the aforementioned ReaxFF potential. The sticking coefficients were measured both on the bare material surfaces and on the material surfaces with growing polymer layers. The number of attached molecules were measured as a function of the number of incidence, and the sticking coefficients were measured from the slope of these curves. An empirical analytical model was also derived and fitted to the MD measured data using a two-segment regression scheme, and good match was achieved between the analytical model predicted results and the measured data,

which makes it possible to incorporate the analytical model into any rigorous models to conveniently predict the variation in sticking coefficients as a function of surface conditions.

6.2 Future Work

6.2.1 Refinement of the ReaxFF parameter set

The ReaxFF parameter set used in this work was prepared by combining three different ReaxFF parameter sets from three well validated journal papers. Although we have already conducted tons of verification and validation tests and the combined ReaxFF parameter set performed very well, there are still some minor inconsistencies as a result of this direct combination approach. The ideal way of obtaining such combined parameter set in ReaxFF is to perform the related quantum mechanics calculations and re-fit the parameters using the specific software developed by the Penn State group (Senftle et al. 2016). Due to the limited time and the lack of knowledge, we were not able to perform such quantum mechanics calculations but may be able to do so in the future.

6.2.2 Use available polymer structures as surrogates

As mentioned in Chapter 4.8, the passivation layer formed on HAR sidewalls during fluorocarbon plasma etching has a molecular structure similar to polytetrafluoroethylene (PTFE). Therefore instead of modeling the growth of fluorocarbon polymer layer by depositing CF_x radicals onto substrates, an alternative approach could be that use manufactured PTFE as a surrogate and stack it on top of the substrates. As proposed in Chapter 4.8, the F:C ratio in the PTFE film can be modified to match the experimentally measured F:C ratio within a fluorocarbon polymer film. However, as tested in the final part of Chapter 4.8, the current ReaxFF parameter set tends to under-predict the density of the PTFE at atmosphere pressure, resulting swelling when stacked on top of the substrate. Moreover, only matching the F:C ratio may not be adequate to accurately reproduce the polymer film, detailed experimental data containing structural information would definitely benefit the computational efforts. Future work should address on solving such issues in order to conveniently use PTFE as a surrogate for fluorocarbon polymer film.

6.2.3 Expand the dataset to include other molecules and materials

As mentioned previously, both the empirical analytical models for glancing-angle scattering and for sticking coefficients have the potential to be expanded to include other incident species and substrate materials. For example, the scattering distribution for Cl^- ions may be able to use the same functional form as for Ar^+ ions, with some adjustments to the fitting value of the characteristic parameters. Similarly, silicon nitride is also a common material in plasma etching. Measuring the sticking coefficients of reactive species or etch byproducts on silicon nitride, and predict the sticking coefficients related to silicon nitride using the analytical model would also be needed by some other researches.

6.2.4 Larger scale parametric studies on more powerful HPC

Some of the MD simulations performed in this work was limited (in material size and/or in simulation length) by the available computational resources, especially for the simulation cases using ReaxFF since ReaxFF is much more computationally expensive than the other traditional interatomic potentials such as Tersoff and ZBL. Even though these simulation cases were ran on the NCSU HPC, the computational power was still not enough, mostly due to the available CPUs were quite old and low in single core frequency, and the maximum duration for each simulation case was limited. Moreover, the HPC was found to be very non-uniform, i.e., the speed of running two same cases using the same number of the same CPU can sometimes be significantly different, which makes it harder to perform parametric studies. Therefore, running larger scale parametric studies on more powerful HPC is definitely necessary. Not only can it reduce the noise level as shown in the plots in Chapter 4, but also longer runs could reveal the saturation status much better.

6.2.5 More investigations in modeling carbon systems using ReaxFF

As discussed in Chapter 4.7, adding atomic carbon species could potentially help the growth of fluorocarbon polymer films. However, the results from the pure carbon deposition cases, see Fig. 4.31, show that the carbon atoms within the very top layer are mostly sp hybridized and form some stringy structures. Although this was also observed in other MD works (Li et al. 2019) using different ReaxFF parameter sets, it is still not clear if it is a general ReaxFF artifact or it actually exists. More tests should be performed to validate the combined ReaxFF parameter set against other pure carbon systems such as carbon graphitization (Li et al. 2018) and carbon nanoparticle formation (Orekhov et al. 2020).

REFERENCES

- Abrams, C. F and Graves, D. B. (1998). Energetic ion bombardment of sio 2 surfaces: Molecular dynamics simulations. *Journal of Vacuum Science & Technology A: Vacuum, Surfaces, and Films*, 16(5):3006–3019.
- Armacost, M., Hoh, P. D., Wise, R., Yan, W., Brown, J. J., Keller, J. H., Kaplita, G. A., Halle, S. D., Muller, K. P., Naeem, M. D., et al. (1999). Plasma-etching processes for ulsi semiconductor circuits. *IBM journal of research and development*, 43(1.2):39–72.
- Ayalew, T. (2004). *SiC Semiconductor Devices Technology, Modeling, and Simulation*. PhD thesis, Vienna University of Technology.
- Bhattarai, B. and Drabold, D. (2017). Amorphous carbon at low densities: An ab initio study. *Carbon*, 115:532–538.
- Blumm, J., Lindemann, A., Meyer, M., and Strasser, C. (2010). Characterization of ptfe using advanced thermal analysis techniques. *International Journal of Thermophysics*, 31(10):1919–1927.
- Booth, J.-P. (1999). Optical and electrical diagnostics of fluorocarbon plasma etching processes. *Plasma Sources Science and Technology*, 8(2):249.
- Cardinaud, C., Peignon, M.-C., and Tessier, P.-Y. (2000). Plasma etching: principles, mechanisms, application to micro-and nano-technologies. *Applied Surface Science*, 164(1-4):72–83.
- Chemist, W. (2023). Common bond energies and bond lengths. https://www.wiredchemist.com/chemistry/data/bond_energies_lengths.html. Accessed: 2023-01-29.
- Chenoweth, K., Van Duin, A. C., and Goddard, W. A. (2008). Reaxff reactive force field for molecular dynamics simulations of hydrocarbon oxidation. *The Journal of Physical Chemistry A*, 112(5):1040–1053.
- Coburn, J. W. and Winters, H. F. (1979). Plasma etching—a discussion of mechanisms. *Journal of vacuum Science and Technology*, 16(2):391–403.
- Conrads, H. and Schmidt, M. (2000). Plasma generation and plasma sources. *Plasma Sources Science and Technology*, 9(4):441.
- Cunge, G., Vempaire, D., Ramos, R., Touzeau, M., Joubert, O., Bodard, P., and Sadeghi, N. (2010). Radical surface interactions in industrial silicon plasma etch reactors. *Plasma Sources Science and Technology*, 19(3):034017.
- Donnelly, V. M. and Kornblit, A. (2013). Plasma etching: Yesterday, today, and tomorrow. *Journal of Vacuum Science & Technology A: Vacuum, Surfaces, and Films*, 31(5):050825.

- d'Agostino, R., Cramarossa, F., Colaprico, V., and d'Ettore, R. (1983). Mechanisms of etching and polymerization in radiofrequency discharges of cf4–h₂, cf4–c2f4, c2f6–h₂, c3f8–h₂. *Journal of Applied Physics*, 54(3):1284–1288.
- Engelmann, S., Bruce, R., Kwon, T., Phaneuf, R., Oehrlein, G., Bae, Y., Andes, C., Graves, D., Nest, D., Hudson, E., et al. (2007). Plasma-surface interactions of model polymers for advanced photoresists using c 4 f 8/ ar discharges and energetic ion beams. *Journal of Vacuum Science & Technology B: Microelectronics and Nanometer Structures Processing, Measurement, and Phenomena*, 25(4):1353–1364.
- Erhart, P. and Albe, K. (2005). Analytical potential for atomistic simulations of silicon, carbon, and silicon carbide. *Physical Review B*, 71(3):035211.
- Eriguchi, K., Takao, Y., and Ono, K. (2014). A new aspect of plasma-induced physical damage in three-dimensional scaled structures—sidewall damage by stochastic straggling and sputtering. In *2014 IEEE International Conference on IC Design & Technology*, pages 1–5. IEEE.
- Evans, D. J. and Holian, B. L. (1985). The nose–hoover thermostat. *The Journal of chemical physics*, 83(8):4069–4074.
- Flamm, D. L. and Manos, D. M. (1989). *Plasma Etching: An Introduction*. Academic Press.
- Gabriel, E., Fagg, G. E., Bosilca, G., Angskun, T., Dongarra, J. J., Squyres, J. M., Sahay, V., Kambadur, P., Barrett, B., Lumsdaine, A., Castain, R. H., Daniel, D. J., Graham, R. L., and Woodall, T. S. (2004). Open MPI: Goals, concept, and design of a next generation MPI implementation. In *Proceedings, 11th European PVM/MPI Users' Group Meeting*, pages 97–104, Budapest, Hungary.
- Gou, F., Kleyn, A., and Gleeson, M. (2008). The application of molecular dynamics to the study of plasma–surface interactions: Cf x with silicon. *International Reviews in Physical Chemistry*, 27(2):229–271.
- Graves, D. B. and Brault, P. (2009). Molecular dynamics for low temperature plasma–surface interaction studies. *Journal of Physics D: Applied Physics*, 42(19):194011.
- Haley, B. P., Wilson, N., Li, C., Arguelles, A., Jaramillo, E., and Strachan, A. (2010). Polymer modeler.
- Han, J. and Boyd, R. H. (1996). Molecular packing and small-penetrant diffusion in polystyrene: a molecular dynamics simulation study. *Polymer*, 37(10):1797–1804.
- Harmandaris, V., Adhikari, N., van der Vegt, N. F., and Kremer, K. (2006). Hierarchical modeling of polystyrene: From atomistic to coarse-grained simulations. *Macromolecules*, 39(19):6708–6719.

- Helmer, B. and Graves, D. (1998). Molecular dynamics simulations of ar+ and cl+ impacts onto silicon surfaces: Distributions of reflected energies and angles. *Journal of Vacuum Science & Technology A: Vacuum, Surfaces, and Films*, 16(6):3502–3514.
- Ho, C. Y., Lien, C., Sakamoto, Y., Yang, R. J., Fijita, H., Liu, C., Lin, Y., Pittikoun, S., and Aritome, S. (2008). Improvement of interpoly dielectric characteristics by plasma nitridation and oxidation for future nand flash memory. *IEEE electron device letters*, 29(11):1199–1202.
- Hua, X., Engelmann, S., Oehrlein, G., Jiang, P., Lazzeri, P., Iacob, E., and Anderle, M. (2006). Studies of plasma surface interactions during short time plasma etching of 193 and 248 nm photoresist materials. *Journal of Vacuum Science & Technology B: Microelectronics and Nanometer Structures Processing, Measurement, and Phenomena*, 24(4):1850–1858.
- Huang, S., Huard, C., Shim, S., Nam, S. K., Song, I.-C., Lu, S., and Kushner, M. J. (2019). Plasma etching of high aspect ratio features in sio₂ using ar/c4f8/o₂ mixtures: A computational investigation. *Journal of Vacuum Science & Technology A: Vacuum, Surfaces, and Films*, 37(3):031304.
- Huard, C. M., Sriraman, S., Paterson, A., and Kushner, M. J. (2018). Transient behavior in quasi-atomic layer etching of silicon dioxide and silicon nitride in fluorocarbon plasmas. *Journal of Vacuum Science & Technology A: Vacuum, Surfaces, and Films*, 36(6):06B101.
- Inc., G. (2021). Polystyrene material information. <http://www.goodfellow.com/E-Polystyrene.html>. Accessed: 2021-09-12.
- Izawa, M., Negishi, N., Yokogawa, K., and Momonoi, Y. (2007). Investigation of bowing reduction in sio₂ etching taking into account radical sticking in a hole. *Japanese Journal of Applied Physics*, 46(12R):7870.
- Jin, W. and Sawin, H. H. (2003). Feature profile evolution in high-density plasma etching of silicon with cl₂. *Journal of Vacuum Science & Technology A: Vacuum, Surfaces, and Films*, 21(4):911–921.
- Johnson, P.A., Wright, A. C., and Sinclair, R. N. (1983). Neutron scattering from vitreous silica ii. twin-axis diffraction experiments. *Journal of non-crystalline solids*, 58(1):109–130.
- Kammara, K. K., Kumar, R., and Donbosco, F. S. (2016). Reconsideration of metal surface sputtering due to bombardment of high-energy argon ion particles: a molecular dynamics study. *Computational Particle Mechanics*, 3(1):3–13.
- Kanarik, K. J. (2020). Inside the mysterious world of plasma: A process engineer's perspective. *Journal of Vacuum Science & Technology A: Vacuum, Surfaces, and Films*, 38(3):031004.
- Kim, D. H., Kwak, S. J., Jeong, J. H., Yoo, S., Nam, S. K., Kim, Y., and Lee, W. B. (2021). Molecular dynamics simulation of silicon dioxide etching by hydrogen fluoride using the reactive force field. *ACS omega*, 6(24):16009–16015.

- Kim, H., Ahn, S.-J., Shin, Y. G., Lee, K., and Jung, E. (2017). Evolution of nand flash memory: From 2d to 3d as a storage market leader. In *2017 IEEE International Memory Workshop (IMW)*, pages 1–4. IEEE.
- Kim, J. K., Cho, S. I., Kim, N. G., Jhon, M. S., Min, K. S., Kim, C. K., and Yeom, G. Y. (2013). Study on the etching characteristics of amorphous carbon layer in oxygen plasma with carbonyl sulfide. *Journal of Vacuum Science & Technology A: Vacuum, Surfaces, and Films*, 31(2):021301.
- Kim, M., Moon, J., Choi, J., Park, S., Lee, B., and Cho, M. (2018). Multiscale simulation approach on sub-10 nm extreme ultraviolet photoresist patterning: Insights from nanoscale heterogeneity of polymer. *Macromolecules*, 51(17):6922–6935.
- Kouza, M. (2013). Numerical simulation of folding and unfolding of proteins. *arXiv preprint arXiv:1308.2380*.
- Labelle, C. B., Donnelly, V. M., Bogart, G. R., Opila, R. L., and Kornblit, A. (2004). Investigation of fluorocarbon plasma deposition from c-c 4 f 8 for use as passivation during deep silicon etching. *Journal of Vacuum Science & Technology A: Vacuum, Surfaces, and Films*, 22(6):2500–2507.
- Laermer, F. and Schilp, A. (1996). Method of anisotropically etching silicon. US Patent 5,501,893.
- LAMMPS (2022). Lammps documentation (23 jun 2022 version). <https://docs.lammps.org/Manual.html>. Accessed: 2022-07-07.
- Lee, C. G., Kanarik, K. J., and Gottscho, R. A. (2014). The grand challenges of plasma etching: a manufacturing perspective. *Journal of Physics D: Applied Physics*, 47(27):273001.
- Lee, J.-K., Jang, I.-Y., Lee, S.-H., Kim, C.-K., and Moon, S. H. (2010). Mechanism of sidewall necking and bowing in the plasma etching of high aspect-ratio contact holes. *Journal of The Electrochemical Society*, 157(3):D142.
- Li, K., Zhang, H., Li, G., Zhang, J., Bouhadja, M., Liu, Z., Skelton, A. A., and Barati, M. (2018). Reaxff molecular dynamics simulation for the graphitization of amorphous carbon: a parametric study. *Journal of chemical theory and computation*, 14(5):2322–2331.
- Li, X., Hua, X., Ling, L., Oehrlein, G. S., Barela, M., and Anderson, H. M. (2002). Fluorocarbon-based plasma etching of sio 2: comparison of c 4 f 6/ar and c 4 f 8/ar discharges. *Journal of Vacuum Science & Technology A: Vacuum, Surfaces, and Films*, 20(6):2052–2061.
- Li, X., Mizuseki, H., Pai, S. J., and Lee, K.-R. (2019). Reactive molecular dynamics simulation of the amorphous carbon growth: Effect of the carbon triple bonds. *Computational Materials Science*, 169:109143.

- Lieberman, M. A. and Lichtenberg, A. J. (2005). *Principles of plasma discharges and materials processing*. John Wiley & Sons.
- Lyulin, A. V. and Michels, M. (2002). Molecular dynamics simulation of bulk atactic polystyrene in the vicinity of t g. *Macromolecules*, 35(4):1463–1472.
- Martin, M. G. and Siepmann, J. I. (1998). Transferable potentials for phase equilibria. 1. united-atom description of n-alkanes. *The Journal of Physical Chemistry B*, 102(14):2569–2577.
- Martyna, G. J., Tobias, D. J., and Klein, M. L. (1994). Constant pressure molecular dynamics algorithms. *The Journal of chemical physics*, 101(5):4177–4189.
- MATSCI (2022). Materials science community discourse. <https://matsci.org/>. Accessed: 2022-07-10.
- McCulloch, D., McKenzie, D., and Goringe, C. (2000). Ab initio simulations of the structure of amorphous carbon. *Physical Review B*, 61(3):2349.
- Metzler, D., Bruce, R. L., Engelmann, S., Joseph, E. A., and Oehrlein, G. S. (2014). Fluorocarbon assisted atomic layer etching of sio₂ using cyclic ar/c4f₈ plasma. *Journal of Vacuum Science & Technology A: Vacuum, Surfaces, and Films*, 32(2):020603.
- Millard, M. and Kay, E. (1982). Difluorocarbene emission spectra from fluorocarbon plasmas and its relationship to fluorocarbon polymer formation. *Journal of The Electrochemical Society*, 129(1):160.
- Min, J.-H., Lee, G.-R., Lee, J.-K., Moon, S. H., and Kim, C.-K. (2005). Effect of sidewall properties on the bottom microtrench during si o₂ etching in a cf₄ plasma. *Journal of Vacuum Science & Technology B: Microelectronics and Nanometer Structures Processing, Measurement, and Phenomena*, 23(2):425–432.
- Mori, M., Irie, S., Osano, Y., Eriguchi, K., and Ono, K. (2021). Model analysis of the feature profile evolution during si etching in hbr-containing plasmas. *Journal of Vacuum Science & Technology A: Vacuum, Surfaces, and Films*, 39(4):043002.
- MPICH (2022). Mpich homepage. <https://www.mpich.org>. Accessed: 2022-07-07.
- Munetoh, S., Motooka, T., Moriguchi, K., and Shintani, A. (2007). Interatomic potential for si-o systems using tersoff parameterization. *Computational Materials Science*, 39(2):334–339.
- Nakano, A., Kalia, R. K., and Vashishta, P. (1995). Dynamics and morphology of brittle cracks: A molecular-dynamics study of silicon nitride. *Physical Review Letters*, 75(17):3138.
- Nakazaki, N., Takao, Y., Eriguchi, K., and Ono, K. (2014). Molecular dynamics simulations of silicon chloride ion incidence during si etching in cl-based plasmas. *Japanese Journal of Applied Physics*, 53(5):056201.

- Newsome, D. A., Sengupta, D., Foroutan, H., Russo, M. F., and Van Duin, A. C. (2012). Oxidation of silicon carbide by o₂ and h₂o: a reaxff reactive molecular dynamics study, part i. *The Journal of Physical Chemistry C*, 116(30):16111–16121.
- Nose, S. (1990). Constant-temperature molecular dynamics. *Journal of Physics: Condensed Matter*, 2(S):SA115.
- Oehrlein, G. S., Phaneuf, R. J., and Graves, D. B. (2011). Plasma-polymer interactions: A review of progress in understanding polymer resist mask durability during plasma etching for nanoscale fabrication. *Journal of Vacuum Science & Technology B, Nanotechnology and Microelectronics: Materials, Processing, Measurement, and Phenomena*, 29(1):010801.
- OpenMP (2022). Openmp homepage. <https://www.openmp.org>. Accessed: 2022-07-07.
- Orekhov, N., Ostroumova, G., and Stegailov, V. (2020). High temperature pure carbon nanoparticle formation: Validation of airebo and reaxff reactive molecular dynamics. *Carbon*, 170:606–620.
- O'Malley, B., Snook, I., and McCulloch, D. (1998). Reverse monte carlo analysis of the structure of glassy carbon using electron-microscopy data. *Physical Review B*, 57(22):14148.
- Project, T. M. (2020). Materials data on cf4 by materials project.
- Prskalo, A.-P., Schmauder, S., Ziebert, C., Ye, J., and Ulrich, S. (2010). Molecular dynamics simulations of the sputtering of sic and si3n4. *Surface and Coatings Technology*, 204(12-13):2081–2084.
- PubChem (2023). Pubchem compound summary for cid 6393, carbon tetrafluoride. <https://pubchem.ncbi.nlm.nih.gov/compound/Carbon-tetrafluoride>. Accessed: 2023-02-08.
- Rahnamoun, A. and Van Duin, A. (2014). Reactive molecular dynamics simulation on the disintegration of kapton, poss polyimide, amorphous silica, and teflon during atomic oxygen impact using the reaxff reactive force-field method. *The Journal of Physical Chemistry A*, 118(15):2780–2787.
- Rauf, S., Sparks, T., Ventzek, P., Smirnov, V., Stengach, A., Gaynullin, K., and Pavlovsky, V. (2007). A molecular dynamics investigation of fluorocarbon based layer-by-layer etching of silicon and si o 2. *Journal of applied physics*, 101(3):033308.
- Robertson, J. (2002). Diamond-like amorphous carbon. *Materials science and engineering: R: Reports*, 37(4-6):129–281.
- Robinson, J. T., Burgess, J. S., Junkermeier, C. E., Badescu, S. C., Reinecke, T. L., Perkins, F. K., Zalalutdinov, M. K., Baldwin, J. W., Culbertson, J. C., Sheehan, P. E., et al. (2010). Properties of fluorinated graphene films. *Nano letters*, 10(8):3001–3005.

- Ruixue, D., Yintang, Y., and Ru, H. (2009). Microtrenching effect of sic icp etching in sf₆/o₂ plasma. *Journal of Semiconductors*, 30(1):016001.
- Ryckaert, J.-P., Ciccotti, G., and Berendsen, H. J. (1977). Numerical integration of the cartesian equations of motion of a system with constraints: molecular dynamics of n-alkanes. *Journal of computational physics*, 23(3):327–341.
- Sarkar, A., Eapen, J., Raj, A., Murty, K., and Burchell, T. D. (2016). Modeling irradiation creep of graphite using rate theory. *Journal of Nuclear Materials*, 473:197–205.
- Scheer, H.-C., Bogdanski, N., and Wissen, M. (2005). Issues in nanoimprint processes: the imprint pressure. *Japanese journal of applied physics*, 44(7S):5609.
- Senftle, T. P., Hong, S., Islam, M. M., Kyłasa, S. B., Zheng, Y., Shin, Y. K., Junkermeier, C., Engel-Herbert, R., Janik, M. J., Aktulga, H. M., et al. (2016). The reaxff reactive force-field: development, applications and future directions. *npj Computational Materials*, 2(1):1–14.
- Shaffer, P. (1969). A review of the structure of silicon carbide. *Acta Crystallographica Section B: Structural Crystallography and Crystal Chemistry*, 25(3):477–488.
- Shinoda, W., Shiga, M., and Mikami, M. (2004). Rapid estimation of elastic constants by molecular dynamics simulation under constant stress. *Physical Review B*, 69(13):134103.
- Singh, S. K., Srinivasan, S. G., Neek-Amal, M., Costamagna, S., Van Duin, A. C., and Peeters, F. (2013). Thermal properties of fluorinated graphene. *Physical Review B*, 87(10):104114.
- Srivastava, A. (2010). *A Molecular Dynamics Based Study of Bulk and Finite Polystyrene-carbon Dioxide Binary Systems*. PhD thesis, The Ohio State University.
- Standaert, T., Hedlund, C., Joseph, E., Oehrlein, G., and Dalton, T. (2004). Role of fluoro-carbon film formation in the etching of silicon, silicon dioxide, silicon nitride, and amorphous hydrogenated silicon carbide. *Journal of Vacuum Science & Technology A: Vacuum, Surfaces, and Films*, 22(1):53–60.
- Stubbs, J. M., Potoff, J. J., and Siepmann, J. I. (2004). Transferable potentials for phase equilibria. 6. united-atom description for ethers, glycols, ketones, and aldehydes. *The Journal of Physical Chemistry B*, 108(45):17596–17605.
- Subramanian, S., Hosseini, M., Chiarella, T., Sarkar, S., Schuddinck, P., Chan, B., Radisic, D., Mannaert, G., Hikavyy, A., Rosseel, E., et al. (2020). First monolithic integration of 3d complementary fet (cfet) on 300mm wafers. In *2020 IEEE Symposium on VLSI Technology*, pages 1–2. IEEE.
- Sycheva, A. A., Voronina, E. N., Rakhimova, T. V., and Rakhimov, A. T. (2018). Argon clustering in silicon under low-energy irradiation: Molecular dynamics simulation with different ar-si potentials. *Journal of Vacuum Science & Technology A: Vacuum, Surfaces, and Films*, 36(6):061303.

- Tersoff, J. (1988). New empirical approach for the structure and energy of covalent systems. *Physical review B*, 37(12):6991.
- Tersoff, J. (1989). Modeling solid-state chemistry: Interatomic potentials for multicomponent systems. *Physical review B*, 39(8):5566.
- Thompson, A. P., Aktulga, H. M., Berger, R., Bolintineanu, D. S., Brown, W. M., Crozier, P. S., in't Veld, P. J., Kohlmeyer, A., Moore, S. G., Nguyen, T. D., et al. (2021). Lammps-a flexible simulation tool for particle-based materials modeling at the atomic, meso, and continuum scales. *Computer Physics Communications*, page 108171.
- Tinacba, E. J. C., Isobe, M., Karahashi, K., and Hamaguchi, S. (2019). Molecular dynamics simulation of si and sio₂ reactive ion etching by fluorine-rich ion species. *Surface and Coatings Technology*, 380:125032.
- Tinacba, E. J. C., Ito, T., Karahashi, K., Isobe, M., and Hamaguchi, S. (2021). Molecular dynamics simulation for reactive ion etching of si and sio₂ by sf 5+ ions. *Journal of Vacuum Science & Technology B, Nanotechnology and Microelectronics: Materials, Processing, Measurement, and Phenomena*, 39(4):043203.
- Tsige, M., Curro, J. G., and Grest, G. S. (2008). Packing of poly (tetrafluoroethylene) in the liquid state: Molecular dynamics simulation and theory. *The Journal of chemical physics*, 129(21):214901.
- Van Duin, A. C., Dasgupta, S., Lorant, F., and Goddard, W. A. (2001). Reaxff: a reactive force field for hydrocarbons. *The Journal of Physical Chemistry A*, 105(41):9396–9409.
- Vashishta, P., Kalia, R. K., Nakano, A., and Rino, J. P. (2007). Interaction potential for silicon carbide: A molecular dynamics study of elastic constants and vibrational density of states for crystalline and amorphous silicon carbide. *Journal of applied physics*, 101(10):103515.
- Vegh, J., Nest, D., Graves, D., Bruce, R., Engelmann, S., Kwon, T., Phaneuf, R., Oehrlein, G., Long, B., and Willson, C. (2007). Near-surface modification of polystyrene by ar+: Molecular dynamics simulations and experimental validation. *Applied Physics Letters*, 91(23):233113.
- Végh, J. J. (2007). *Molecular Dynamics Simulations of Plasma-Surface Interactions*. PhD thesis, University of California, Berkeley.
- Wang, S. and Komvopoulos, K. (2020). Structure evolution during deposition and thermal annealing of amorphous carbon ultrathin films investigated by molecular dynamics simulations. *Scientific reports*, 10(1):1–12.
- Wick, C. D., Martin, M. G., and Siepmann, J. I. (2000). Transferable potentials for phase equilibria. 4. united-atom description of linear and branched alkenes and alkylbenzenes. *The Journal of Physical Chemistry B*, 104(33):8008–8016.

- Wu, B., Kumar, A., and Pamarthi, S. (2010). High aspect ratio silicon etch: A review. *Journal of applied physics*, 108(5):9.
- Zhang, Y., Huard, C., Sriraman, S., Belen, J., Paterson, A., and Kushner, M. J. (2017). Investigation of feature orientation and consequences of ion tilting during plasma etching with a three-dimensional feature profile simulator. *Journal of Vacuum Science & Technology A: Vacuum, Surfaces, and Films*, 35(2):021303.
- Zhang, Y., Kushner, M. J., Sriraman, S., Marakhtanov, A., Holland, J., and Paterson, A. (2015). Control of ion energy and angular distributions in dual-frequency capacitively coupled plasmas through power ratios and phase: Consequences on etch profiles. *Journal of Vacuum Science & Technology A: Vacuum, Surfaces, and Films*, 33(3):031302.
- Zhigilei, L. V., Yingling, Y. G., Itina, T. E., Schoolcraft, T. A., and Garrison, B. J. (2003). Molecular dynamics simulations of matrix-assisted laser desorption—connections to experiment. *International Journal of Mass Spectrometry*, 226(1):85–106.
- Ziegler, J. F. and Biersack, J. P. (1985). The stopping and range of ions in matter. In *Treatise on heavy-ion science*, pages 93–129. Springer.
- Zuo, Z., Yang, Y., and Song, L. (2015). Miscibility analysis of polyethersulfone and polytetrafluoroethylene using the molecular dynamics method. *Fibers and Polymers*, 16(3):510–521.

APPENDICES

APPENDIX

A

REAXFF PARAMETER FILES

Here we list the combined ReaxFF parameters files for a Si/O/C/F system used in this work.

```
1 DATE: 2013-06-28 UNITS: real . Expanded based on reference 3, added reference 2
2   first and reference 4 later. Parameters for O-Si in reference 2 was used
3   instead of reference 3
4
5   39 ! Number of general parameters
6     50.0000 !Overcoordination parameter
7     9.5469 !Overcoordination parameter
8     26.5405 !Valency angle conjugation parameter
9     1.7224 !Triple bond stabilisation parameter
10    6.8702 !Triple bond stabilisation parameter
11    60.4850 !C2-correction
12    1.0588 !Undercoordination parameter
13    4.6000 !Triple bond stabilisation parameter
14    12.1176 !Undercoordination parameter
15    13.3056 !Undercoordination parameter
16    -70.5044 !Triple bond stabilization energy
17    0.0000 !Lower Taper-radius
18    10.0000 !Upper Taper-radius
19    2.8793 !Not used
20    33.8667 !Valency undercoordination
21    6.0891 !Valency angle/lone pair parameter
22    1.0563 !Valency angle
23    2.0384 !Valency angle parameter
```

```

21   6.1431 !Not used
22   6.9290 !Double bond/angle parameter
23   0.3842 !Double bond/angle parameter: overcoord
24   2.9294 !Double bond/angle parameter: overcoord
25   -2.4837 !Not used
26   5.7796 !Torsion/B0 parameter
27   10.0000 !Torsion overcoordination
28   1.9487 !Torsion overcoordination
29   -1.2327 !Conjugation 0 (not used)
30   2.1645 !Conjugation
31   1.5591 !vdWaals shielding
32   0.1000 !Cutoff for bond order (*100)
33   2.1365 !Valency angle conjugation parameter
34   0.6991 !Overcoordination parameter
35   50.0000 !Overcoordination parameter
36   1.8512 !Valency/lone pair parameter
37   0.5000 !Not used
38   20.0000 !Not used
39   5.0000 !Molecular energy (not used)
40   0.0000 !Molecular energy (not used)
41   2.6962 !Valency angle conjugation parameter
42   8    ! Nr of atoms; cov.r; valency;a.m;Rvdw;Evdw;gammaEEM;cov.r2;#
43   alfa;gammavdW;valency;Eunder;Eover;chiEEM;etaEEM;n.u.
44   cov r3;Elp;Heat inc.;n.u.;n.u.;n.u.;n.u.
45   ov/un;val1;n.u.;val3,vval4
46   C   1.3831   4.0000   12.0000   1.8814   0.1923   0.9000   1.1363   4.0000
47   9.7821   2.1317   4.0000   30.0000   79.5548   5.9666   7.0000   0.0000
48   1.2071   0.0000   186.1720   9.0068   34.9357   13.5366   0.8563   0.0000
49   -2.8983   2.5675   1.0564   4.0000   2.9663   0.0000   0.0000   0.0000
50   H   0.8873   1.0000   1.0080   1.5420   0.0598   0.6883   -0.1000   1.0000
51   8.1910   30.9706   1.0000   0.0000   121.1250   3.5768   10.5896   1.0000
52   -0.1000   0.0000   54.0596   1.3986   2.1457   0.0003   1.0698   0.0000
53   -15.7683   2.1488   1.0338   1.0000   2.8793   0.0000   0.0000   0.0000
54   O   1.2477   2.0000   15.9990   1.9236   0.0904   1.0503   1.0863   6.0000
55   10.2127   7.7719   4.0000   36.9573   116.0768   8.5000   8.9989   2.0000
56   0.9088   1.0003   60.8726   20.4140   3.3754   0.2702   0.9745   0.0000
57   -3.6141   2.7025   1.0493   4.0000   2.9225   0.0000   0.0000   0.0000
58   N   1.2333   3.0000   14.0000   1.9324   0.1376   0.8596   1.1748   5.0000
59   10.0667   7.8431   4.0000   32.2482   100.0000   6.8418   6.3404   2.0000
60   1.0433   13.7673   139.9837   2.1961   3.0696   2.7683   0.9745   0.0000
61   -4.3875   2.6192   1.0183   4.0000   2.8793   0.0000   0.0000   0.0000
62   S   1.9405   2.0000   32.0600   2.0677   0.2099   1.0336   1.5479   6.0000
63   9.9575   4.9055   4.0000   52.9998   112.1416   5.6210   8.2545   2.0000
64   1.4601   9.7177   71.1843   5.7487   23.2859   12.7147   0.9745   0.0000
65   -11.0000   2.7466   1.0338   6.2998   2.8793   0.0000   0.0000   0.0000
66   F   1.2100   1.0000   18.9984   1.8601   0.1200   0.3000   -0.1000   7.0000
67   11.5000   7.5000   4.0000   9.2533   0.2000   9.0000   15.0000   0.0000
68   -1.0000   35.0000   33.1268   6.9821   4.1799   1.0561   0.0000   0.0000
69   -7.3000   2.6656   1.0493   4.0000   2.9225   0.0000   0.0000   0.0000
70   Si  2.0291   4.0000   28.0600   2.0043   0.1247   0.8218   1.5023   4.0000

```

71		13.0000	2.0618	4.0000	11.8211	136.4845	1.8038	7.3852	0.0000
72		-1.0000	0.0000	126.5182	3.6038	8.5961	0.2368	0.8563	0.0000
73		-3.5163	4.2105	1.0338	6.2998	2.5791	0.0000	0.0000	0.0000
74	X	-0.1000	2.0000	1.0080	2.0000	0.0000	1.0000	-0.1000	6.0000
75		10.0000	2.5000	4.0000	0.0000	0.0000	8.5000	1.5000	0.0000
76		-0.1000	0.0000	-2.3700	8.7410	13.3640	0.6690	0.9745	0.0000
77		-11.0000	2.7466	1.0338	2.0000	2.8793	0.0000	0.0000	0.0000
78	27	! Nr of bonds; Edis1;LPpen;n.u.;pbe1;pbo5;13corr;pbo6 pbe2;pbo3;pbo4;n.u.;pbo1;pbo2;ovcorr							
79		1 1 143.3883	96.3926	76.4404	-0.7767	-0.4710	1.0000	34.9900	0.5108
80		0.4271	-0.1116	9.0638	1.0000	-0.0840	6.7452	1.0000	0.0000
81	1 2 181.9084	0.0000	0.0000	-0.4768	0.0000	1.0000	6.0000	0.7499	
82		12.8085	1.0000	0.0000	1.0000	-0.0608	6.9928	0.0000	0.0000
83	2 2 168.2342	0.0000	0.0000	-0.2191	0.0000	1.0000	6.0000	1.0062	
84		6.1152	1.0000	0.0000	1.0000	-0.0889	6.0000	0.0000	0.0000
85	1 3 158.6946	107.4583	23.3136	-0.4240	-0.1743	1.0000	10.8209	1.0000	
86		0.5322	-0.3113	7.0000	1.0000	-0.1447	5.2450	0.0000	0.0000
87	3 3 60.1463	176.6202	51.1430	-0.2802	-0.1244	1.0000	29.6439	0.9114	
88		0.2441	-0.1239	7.6487	1.0000	-0.1302	6.2919	1.0000	0.0000
89	1 4 134.1215	140.2179	79.9745	0.0163	-0.1428	1.0000	27.0617	0.2000	
90		0.1387	-0.3681	7.1611	1.0000	-0.1000	5.0825	1.0000	0.0000
91	3 4 130.8596	169.4551	40.0000	0.3837	-0.1639	1.0000	35.0000	0.2000	
92		1.0000	-0.3579	7.0004	1.0000	-0.1193	6.8773	1.0000	0.0000
93	4 4 157.9384	82.5526	152.5336	0.4010	-0.1034	1.0000	12.4261	0.5828	
94		0.1578	-0.1509	11.9186	1.0000	-0.0861	5.4271	1.0000	0.0000
95	2 3 163.1043	0.0000	0.0000	-0.4155	0.0000	1.0000	6.0000	0.3607	
96		1.9380	1.0000	0.0000	0.0000	-0.0778	4.3082	0.0000	0.0000
97	2 4 231.8173	0.0000	0.0000	-0.3364	0.0000	1.0000	6.0000	0.4402	
98		8.8910	1.0000	0.0000	1.0000	-0.0327	6.5754	0.0000	0.0000
99	1 5 128.7959	56.4134	39.0716	0.0688	-0.4463	1.0000	31.1766	0.4530	
100		0.1955	-0.3587	6.2148	1.0000	-0.0770	6.6386	1.0000	0.0000
101	2 5 136.1049	0.0000	0.0000	-0.4669	0.0000	1.0000	6.0000	0.3803	
102		10.5730	1.0000	0.0000	1.0000	-0.1000	7.0000	1.0000	0.0000
103	3 5 165.3308	220.0000	40.0000	0.7131	-0.2406	1.0000	22.1005	0.2000	
104		0.8027	-0.2748	8.3393	1.0000	-0.1043	5.6108	1.0000	0.0000
105	4 5 130.0000	180.0000	0.0000	0.5000	-0.2000	1.0000	40.0000	0.3000	
106		0.4000	-0.2500	9.0000	1.0000	-0.1000	6.0000	1.0000	0.0000
107	5 5 96.1871	93.7006	68.6860	0.0955	-0.4781	1.0000	17.8574	0.6000	
108		0.2723	-0.2373	9.7875	1.0000	-0.0950	6.4757	1.0000	0.0000
109	1 6 237.8781	0.0000	0.0000	-0.7438	-0.5000	1.0000	35.0000	1.0460	
110		3.6661	-0.2500	15.0000	1.0000	-0.0800	5.4719	1.0000	0.0000
111	2 6 0.0000	0.0000	0.0000	-0.4643	0.0000	1.0000	6.0000	0.6151	
112		12.3710	1.0000	0.0000	1.0000	-0.1008	8.5980	0.0000	0.0000
113	3 6 0.0000	0.0000	0.0000	0.2500	-0.5000	1.0000	45.0000	0.6000	
114		0.4000	-0.2500	15.0000	1.0000	-0.1000	10.0000	1.0000	0.0000
115	4 6 0.0000	0.0000	0.0000	-0.4643	0.0000	1.0000	6.0000	0.6151	
116		12.3710	1.0000	0.0000	1.0000	-0.0098	8.5980	0.0000	0.0000
117	5 6 0.0000	0.0000	0.0000	0.2500	-0.5000	1.0000	45.0000	0.6000	
118		0.4000	-0.2500	15.0000	1.0000	-0.1000	10.0000	1.0000	0.0000
119	6 6 250.0765	0.0000	0.0000	0.2298	-0.3500	1.0000	25.0000	0.8427	

121		0.1167	-0.2500	15.0000	1.0000	-0.1506	7.3516	1.0000	0.0000	
122	1	7	90.6281	6.3660	0.0000	0.3176	-0.5558	1.0000	17.2117	0.5577
123		0.7223	-0.2118	7.7440	1.0000	-0.1039	5.4442	1.0000	0.0000	
124	2	7	137.1002	0.0000	0.0000	-0.1902	0.0000	1.0000	6.0000	0.4256
125		17.7186	1.0000	0.0000	1.0000	-0.0377	6.4281	0.0000	0.0000	
126	3	7	230.7615	93.6959	43.3991	-0.3617	-0.3000	1.0000	36.0000	0.3161
127		0.9856	-0.3882	4.6686	1.0000	-0.3960	4.5499	1.0000	0.0000	
128	4	7	119.7136	41.2405	43.3991	-0.2060	-0.3000	1.0000	36.0000	0.7957
129		0.8189	-0.2614	9.4060	1.0000	-0.1245	6.1856	1.0000	0.0000	
130	6	7	242.0786	0.0000	0.0000	-0.2499	-0.3500	1.0000	25.0000	0.3295
131		9.9995	-0.2500	15.0000	1.0000	-0.2000	5.4855	1.0000	0.0000	
132	7	7	72.8867	50.0318	30.0000	0.9983	-0.3000	1.0000	16.0000	0.1000
133		1.0538	-0.0447	10.6176	1.0000	-0.1452	8.0404	0.0000	0.0000	
134	17		! Nr of off-diagonal terms; Ediss;Ro;gamma;rsigma;rpi;rpi2							
135	1	2	0.1188	1.4017	9.8545	1.1203	-1.0000	-1.0000		
136	2	3	0.0299	1.3153	10.9102	0.9093	-1.0000	-1.0000		
137	2	4	0.1059	1.8290	9.7818	0.9598	-1.0000	-1.0000		
138	1	3	0.1156	1.8520	9.8317	1.2854	1.1352	1.0706		
139	1	4	0.1447	1.8766	9.7990	1.3436	1.1885	1.1363		
140	3	4	0.1048	2.0003	10.1220	1.3173	1.1096	1.0206		
141	1	5	0.1408	1.8161	9.9393	1.7986	1.3021	1.4031		
142	2	5	0.0895	1.6239	10.0104	1.4640	-1.0000	-1.0000		
143	3	5	0.2250	1.7911	10.2423	1.4546	1.4011	-1.0000		
144	4	5	0.1505	1.9000	10.5104	1.8000	1.4000	-1.0000		
145	1	6	0.1071	1.6243	11.0402	1.3176	-1.0000	-1.0000		
146	2	6	0.0431	1.7204	10.3632	0.5386	-1.0000	-1.0000		
147	1	7	0.0250	1.7695	12.4753	1.5866	1.4409	-1.0000		
148	2	7	0.0291	1.6805	12.5137	1.3429	-1.0000	-1.0000		
149	3	7	0.1958	1.7958	11.1207	1.6105	1.1632	-1.0000		
150	4	7	0.1297	1.9384	10.9856	1.6175	1.4045	-1.0000		
151	6	7	0.2144	1.2971	13.9999	1.8607	-1.0000	-1.0000		
152	97		! Nr of angles;at1;at2;at3;Thetao,o;ka;kb;pv1;pv2							
153	1	1	1	72.7917	38.5829	0.7209	0.0000	0.1409	17.4509	1.0670
154	1	1	2	72.1533	14.2108	6.2512	0.0000	0.0100	0.0000	1.1022
155	2	1	2	73.2608	24.9703	3.7807	0.0000	0.1335	0.0000	3.0461
156	1	2	2	0.0000	0.0000	6.0000	0.0000	0.0000	0.0000	1.0400
157	1	2	1	0.0000	7.5000	5.0000	0.0000	0.0000	0.0000	1.0400
158	2	2	2	0.0000	27.9213	5.8635	0.0000	0.0000	0.0000	1.0400
159	1	1	3	49.6811	7.1713	4.3889	0.0000	0.7171	10.2661	1.0463
160	3	1	3	77.7473	40.1718	2.9802	-25.3063	1.6170	-46.1315	2.2503
161	1	1	4	66.1305	12.4661	7.0000	0.0000	3.0000	50.0000	1.1880
162	3	1	4	73.9544	12.4661	7.0000	0.0000	3.0000	0.0000	1.1880
163	4	1	4	64.1581	12.4661	7.0000	0.0000	3.0000	0.0000	1.1880
164	2	1	3	65.0000	13.8815	5.0583	0.0000	0.4985	0.0000	1.4900
165	2	1	4	74.2929	31.0883	2.6184	0.0000	0.0755	0.0000	1.0500
166	1	2	4	0.0000	0.0019	6.3000	0.0000	0.0000	0.0000	1.0400
167	1	3	1	73.5312	44.7275	0.7354	0.0000	3.0000	0.0000	1.0684
168	1	3	3	79.4761	36.3701	1.8943	0.0000	0.7351	67.6777	3.0000
169	1	3	4	82.4890	31.4554	0.9953	0.0000	1.6310	0.0000	1.0783
170	3	3	3	80.7324	30.4554	0.9953	0.0000	1.6310	50.0000	1.0783

171	3	3	4	84.3637	31.4554	0.9953	0.0000	1.6310	0.0000	1.0783
172	4	3	4	89.7071	31.4554	0.9953	0.0000	1.6310	0.0000	1.1519
173	1	3	2	70.1880	20.9562	0.3864	0.0000	0.0050	0.0000	1.6924
174	2	3	3	75.6935	25.0000	2.0000	0.0000	1.0000	0.0000	1.1680
175	2	3	4	75.6201	18.7919	0.9833	0.0000	0.1218	0.0000	1.0500
176	2	3	2	77.3619	4.8342	7.1628	0.0000	2.9933	0.0000	1.5948
177	1	4	1	66.0330	22.0295	1.4442	0.0000	1.6777	0.0000	1.0500
178	1	4	3	103.3204	33.0381	0.5787	0.0000	1.6777	0.0000	1.0500
179	1	4	4	104.1335	8.6043	1.6495	0.0000	1.6777	0.0000	1.0500
180	3	4	3	74.1978	42.1786	1.7845	-18.0069	1.6777	0.0000	1.0500
181	3	4	4	74.8600	43.7354	1.1572	-0.9193	1.6777	0.0000	1.0500
182	4	4	4	75.0538	14.8267	5.2794	0.0000	1.6777	0.0000	1.0500
183	1	4	2	69.1106	25.5067	1.1003	0.0000	0.0222	0.0000	1.0369
184	2	4	3	81.3686	40.0712	2.2396	0.0000	0.0222	0.0000	1.0369
185	2	4	4	83.0104	43.4766	1.5328	0.0000	0.0222	0.0000	1.0500
186	2	4	2	70.8687	12.0168	5.0132	0.0000	0.0222	0.0000	1.1243
187	1	2	3	0.0000	25.0000	3.0000	0.0000	1.0000	0.0000	1.0400
188	1	2	4	0.0000	0.0019	6.0000	0.0000	0.0000	0.0000	1.0400
189	1	2	5	0.0000	0.0019	6.0000	0.0000	0.0000	0.0000	1.0400
190	3	2	3	0.0000	4.4124	2.5758	0.0000	0.0000	0.0000	2.9884
191	3	2	4	0.0000	0.0019	6.0000	0.0000	0.0000	0.0000	1.0400
192	4	2	4	0.0000	0.0019	6.0000	0.0000	0.0000	0.0000	1.0400
193	2	2	3	0.0000	15.0000	2.2970	0.0000	0.0000	0.0000	1.3268
194	2	2	4	0.0000	0.0019	6.0000	0.0000	0.0000	0.0000	1.0400
195	1	1	5	74.4180	33.4273	1.7018	0.1463	0.5000	0.0000	1.6178
196	1	5	1	79.7037	28.2036	1.7073	0.1463	0.5000	0.0000	1.6453
197	2	1	5	63.3289	29.4225	2.1326	0.0000	0.5000	0.0000	3.0000
198	1	5	2	85.9449	38.3109	1.2492	0.0000	0.5000	0.0000	1.1000
199	1	5	5	85.6645	40.0000	2.9274	0.1463	0.5000	0.0000	1.3830
200	2	5	2	83.8555	5.1317	0.4377	0.0000	0.5000	0.0000	3.0000
201	2	5	5	97.0064	32.1121	2.0242	0.0000	0.5000	0.0000	2.8568
202	3	5	3	81.0957	22.5308	7.4511	-2.3089	2.8609	0.0000	2.0914
203	1	5	3	70.0000	35.0000	3.4223	0.0000	1.3550	0.0000	1.2002
204	1	3	5	58.9977	36.2016	1.7948	0.0000	0.4304	0.0000	3.0000
205	3	3	5	83.9753	31.0715	3.5590	0.0000	0.8161	0.0000	1.1776
206	2	3	5	90.0000	17.5000	3.5000	0.0000	1.9770	0.0000	3.0000
207	1	1	6	74.0446	35.8484	6.6125	0.0000	0.9453	0.0000	3.0000
208	6	1	6	77.8443	49.0744	5.9913	0.0000	0.7835	0.0000	2.3020
209	1	6	1	0.0000	19.9962	3.2299	0.0000	2.1012	0.0000	1.1537
210	1	6	6	0.0000	25.0000	1.0000	0.0000	1.0000	0.0000	1.0400
211	6	1	2	69.6421	10.0000	2.0000	0.0000	1.0000	0.0000	1.0400
212	3	1	6	70.0000	35.0000	2.0000	0.0000	1.0000	0.0000	1.2500
213	5	1	6	70.0000	35.0000	3.4223	0.0000	1.3550	0.0000	1.2002
214	7	7	7	71.6771	13.0081	3.6376	0.0000	0.2384	0.0000	1.3185
215	2	7	7	89.1207	11.7566	1.1579	0.0000	0.0100	0.0000	1.2975
216	2	7	2	26.3763	5.5393	0.9656	0.0000	2.3381	0.0000	1.1704
217	3	7	7	85.6335	17.1826	6.5759	0.0000	0.4105	0.0000	1.6398
218	2	7	3	59.6558	6.8748	7.0452	0.0000	4.0000	0.0000	1.0400
219	3	7	3	72.7359	17.5203	2.4434	0.0000	0.0100	0.0000	1.7374
220	7	3	7	18.3653	5.7702	3.4915	0.0000	4.0000	0.0000	1.9438

221	2	3	7	57.5894	40.0000	8.0000	0.0000	3.8263	0.0000	1.0534
222	3	3	7	54.5893	38.8349	7.6245	0.0000	2.7656	0.0000	3.0000
223	2	2	7	0.0000	47.1300	6.0000	0.0000	1.6371	0.0000	1.0400
224	7	2	7	0.0000	31.5209	6.0000	0.0000	1.6371	0.0000	1.0400
225	3	2	7	0.0000	31.0427	4.5625	0.0000	1.6371	0.0000	1.0400
226	1	1	7	63.8858	35.1811	0.6236	0.0000	2.6344	0.0000	2.3890
227	1	7	1	71.6429	31.1160	0.5107	0.0000	0.0100	0.0000	1.9113
228	7	1	7	63.2523	33.3810	2.2952	0.0000	0.0201	0.0000	1.7191
229	1	7	7	70.9876	29.7098	1.0210	0.0000	0.0100	0.0000	1.8242
230	2	1	7	96.9319	10.9008	1.4627	0.0000	2.4557	0.0000	1.5109
231	1	7	2	73.9320	16.6559	3.0433	0.0000	0.7961	0.0000	1.4005
232	1	3	7	91.5678	5.9243	2.4284	0.0000	2.9840	0.0000	1.0400
233	1	7	3	96.3796	36.5757	0.8505	0.0000	3.6964	0.0000	1.6527
234	3	1	7	42.5553	40.0000	1.5855	0.0000	1.0802	0.0000	1.1584
235	4	7	7	60.6199	17.7559	1.0576	0.0000	2.1459	0.0000	1.0400
236	4	7	4	74.1294	20.6494	2.1244	0.0000	0.7689	0.0000	1.0400
237	4	7	3	57.0650	9.4985	0.3423	0.0000	0.7689	0.0000	1.0400
238	7	4	7	24.1137	1.7457	0.2198	0.0000	4.1125	0.0000	1.0400
239	2	7	4	68.7410	15.5851	1.8545	0.0000	0.8613	0.0000	1.0400
240	2	4	7	80.9040	4.0560	1.2284	0.0000	1.6982	0.0000	1.0400
241	4	4	7	60.0000	10.0000	0.7500	0.0000	1.0000	0.0000	1.0400
242	3	4	7	69.8728	32.7155	1.5875	0.0000	2.2466	0.0000	1.0400
243	4	3	7	69.8728	27.1273	1.5875	0.0000	2.2466	0.0000	1.0400
244	4	2	7	0.0000	31.0427	4.5625	0.0000	1.6371	0.0000	1.0400
245	6	7	7	79.7014	16.9791	1.6839	0.0000	1.0944	0.0000	1.0500
246	6	7	6	90.9986	68.2397	4.5675	0.0000	4.0451	0.0000	1.0000
247	7	6	7	0.0000	42.3353	7.1082	0.0000	1.3635	0.0000	1.0840
248	6	6	7	0.0000	10.0000	2.0000	0.0000	1.0000	0.0000	1.2500
249	6	7	3	28.9834	39.9921	1.2589	0.0000	2.1212	0.0000	1.0000
250	42	! Nr of torsions;at1;at2;at3;at4;;V1;V2;V3;V2(B0);vconj;n.u;n								
251	1	1	1	-0.5000	53.0886	-0.1335	-6.2875	-1.9524	0.0000	0.0000
252	1	1	1	2	-0.4614	29.0459	0.2551	-4.8555	-2.7007	0.0000
253	2	1	1	2	-0.2833	31.2867	0.2965	-4.8828	-2.4652	0.0000
254	1	1	1	3	-0.3495	22.2142	-0.2959	-2.5000	-1.9066	0.0000
255	2	1	1	3	0.0646	24.3195	0.6259	-3.9603	-1.0000	0.0000
256	3	1	1	3	-0.5456	5.5756	0.8433	-5.1924	-1.0180	0.0000
257	1	1	3	1	1.7555	27.9267	0.0072	-2.6533	-1.0000	0.0000
258	1	1	3	2	-1.4358	36.7830	-1.0000	-8.1821	-1.0000	0.0000
259	2	1	3	1	-1.3959	34.5053	0.7200	-2.5714	-2.1641	0.0000
260	2	1	3	2	-2.5000	70.0597	1.0000	-3.5539	-2.9929	0.0000
261	1	1	3	3	0.6852	11.2819	-0.4784	-2.5000	-2.1085	0.0000
262	2	1	3	3	0.1933	80.0000	1.0000	-4.0590	-3.0000	0.0000
263	3	1	3	1	-1.9889	76.4820	-0.1796	-3.8301	-3.0000	0.0000
264	3	1	3	2	0.2160	72.7707	-0.7087	-4.2100	-3.0000	0.0000
265	3	1	3	3	-2.5000	71.0772	0.2542	-3.1631	-3.0000	0.0000
266	1	3	3	1	2.5000	-0.6002	1.0000	-3.4297	-2.8858	0.0000
267	1	3	3	2	-2.5000	-3.3822	0.7004	-5.4467	-2.9586	0.0000
268	2	3	3	2	2.5000	-4.0000	0.9000	-2.5000	-1.0000	0.0000
269	1	3	3	3	1.2329	-4.0000	1.0000	-2.5000	-1.7479	0.0000
270	2	3	3	3	0.8302	-4.0000	-0.7763	-2.5000	-1.0000	0.0000

```

271 3 3 3 3 -2.5000 -25.0000 1.0000 -2.5000 -1.0000 0.0000 0.0000
272 0 1 2 0 0.0000 0.0000 0.0000 0.0000 0.0000 0.0000 0.0000
273 0 2 2 0 0.0000 0.0000 0.0000 0.0000 0.0000 0.0000 0.0000
274 0 2 3 0 0.0000 0.1000 0.0200 -2.5415 0.0000 0.0000 0.0000
275 0 1 1 0 0.0000 50.0000 0.3000 -4.0000 -2.0000 0.0000 0.0000
276 0 3 3 0 0.5511 25.4150 1.1330 -5.1903 -1.0000 0.0000 0.0000
277 0 1 4 0 -2.4242 128.1636 0.3739 -6.6098 -2.0000 0.0000 0.0000
278 0 2 4 0 0.0000 0.1000 0.0200 -2.5415 0.0000 0.0000 0.0000
279 0 3 4 0 1.4816 55.6641 0.0004 -7.0465 -2.7203 0.0000 0.0000
280 0 4 4 0 -0.3244 27.7086 0.0039 -2.8272 -2.0000 0.0000 0.0000
281 4 1 4 4 -5.5181 8.9706 0.0004 -6.1782 -2.0000 0.0000 0.0000
282 0 1 5 0 3.3423 30.3435 0.0365 -2.7171 0.0000 0.0000 0.0000
283 0 5 5 0 -0.0555 -5.0000 0.1515 -2.2056 0.0000 0.0000 0.0000
284 0 2 5 0 0.0000 0.0000 0.0000 0.0000 0.0000 0.0000 0.0000
285 1 1 1 6 0.5000 0.1000 0.4683 -11.5274 -1.7255 0.0000 0.0000
286 2 1 1 6 0.0000 49.3871 0.2000 -10.5765 -1.7255 0.0000 0.0000
287 6 1 1 6 -0.5000 95.4727 -0.2080 -4.8579 -1.7255 0.0000 0.0000
288 0 1 6 0 4.0000 45.8264 0.9000 -4.0000 0.0000 0.0000 0.0000
289 0 6 6 0 4.0000 45.8264 0.9000 -4.0000 0.0000 0.0000 0.0000
290 2 3 5 3 2.5000 2.5000 0.2237 -10.0000 -1.0000 0.0000 0.0000
291 0 3 5 0 -2.5000 50.0000 -0.5000 -10.0000 -1.0000 0.0000 0.0000
292 0 4 7 0 0.0000 0.0000 0.0000 -2.4426 0.0000 0.0000 0.0000
293 ! Nr of hydrogen bonds;at1;at2;at3;Rhb;Dehb;vhb1
294 3 2 3 2.1845 -2.3549 3.0582 19.1627
295 3 2 4 1.6658 -3.8907 3.0582 19.1627
296 4 2 3 1.8738 -3.5421 3.0582 19.1627
297 4 2 4 1.8075 -4.1846 3.0582 19.1627
298 3 2 5 1.5000 -2.0000 3.0582 19.1627
299 4 2 5 1.5000 -2.0000 3.0582 19.1627
300 5 2 3 1.5000 -2.0000 3.0582 19.1627
301 5 2 4 1.5000 -2.0000 3.0582 19.1627
302 5 2 5 1.5000 -2.0000 3.0582 19.1627

```

Listing A.1: Combined ReaxFF parameters set for a Si/O/C/F system

```

1 DATE: 2022-09-12 UNITS: real . Expanded based on reference 3, added reference 2
2 first and ffield_Kapton later. Parameters for O-Si in reference 2 was used
3 39 ! Number of general parameters
4 50.0000 !Overcoordination parameter
5 9.5469 !Overcoordination parameter
6 26.5405 !Valency angle conjugation parameter
7 1.7224 !Triple bond stabilisation parameter
8 6.8702 !Triple bond stabilisation parameter
9 60.4850 !C2-correction
10 1.0588 !Undercoordination parameter
11 4.6000 !Triple bond stabilisation parameter
12 12.1176 !Undercoordination parameter
13 13.3056 !Undercoordination parameter
14 -70.5044 !Triple bond stabilization energy
15 0.0000 !Lower Taper-radius

```

```

15   10.0000 !Upper Taper-radius
16   2.8793 !Not used
17   33.8667 !Valency undercoordination
18   6.0891 !Valency angle/lone pair parameter
19   1.0563 !Valency angle
20   2.0384 !Valency angle parameter
21   6.1431 !Not used
22   6.9290 !Double bond/angle parameter
23   0.3842 !Double bond/angle parameter: overcoord
24   2.9294 !Double bond/angle parameter: overcoord
25   -2.4837 !Not used
26   5.7796 !Torsion/B0 parameter
27   10.0000 !Torsion overcoordination
28   1.9487 !Torsion overcoordination
29   -1.2327 !Conjugation 0 (not used)
30   2.1645 !Conjugation
31   1.5591 !vdWaals shielding
32   0.1000 !Cutoff for bond order (*100)
33   2.1365 !Valency angle conjugation parameter
34   0.6991 !Overcoordination parameter
35   50.0000 !Overcoordination parameter
36   1.8512 !Valency/lone pair parameter
37   0.5000 !Not used
38   20.0000 !Not used
39   5.0000 !Molecular energy (not used)
40   0.0000 !Molecular energy (not used)
41   2.6962 !Valency angle conjugation parameter
42   8     ! Nr of atoms; cov.r; valency;a.m;Rvdw;Evdw;gammaEEM;cov.r2;#
43   alfa;gammavdW;valency;Eunder;Eover;chiEEM;etaEEM;n.u.
44   cov r3;Elp;Heat inc.;n.u.;n.u.;n.u.;n.u.
45   ov/un;val1;n.u.;val3,vval4
46   C    1.3831  4.0000  12.0000  1.8814  0.1923  0.9000  1.1363  4.0000
47   9.7821  2.1317  4.0000  30.0000  79.5548  5.9666  7.0000  0.0000
48   1.2071  0.0000  186.1720  9.0068  34.9357  13.5366  0.8563  0.0000
49   -2.8983  2.5675  1.0564  4.0000  2.9663  0.0000  0.0000  0.0000
50   H    0.8873  1.0000  1.0080  1.5420  0.0598  0.6883  -0.1000  1.0000
51   8.1910  30.9706  1.0000  0.0000  121.1250  3.5768  10.5896  1.0000
52   -0.1000  0.0000  54.0596  1.3986  2.1457  0.0003  1.0698  0.0000
53   -15.7683  2.1488  1.0338  1.0000  2.8793  0.0000  0.0000  0.0000
54   O    1.2477  2.0000  15.9990  1.9236  0.0904  1.0503  1.0863  6.0000
55   10.2127  7.7719  4.0000  36.9573  116.0768  8.5000  8.9989  2.0000
56   0.9088  1.0003  60.8726  20.4140  3.3754  0.2702  0.9745  0.0000
57   -3.6141  2.7025  1.0493  4.0000  2.9225  0.0000  0.0000  0.0000
58   N    1.2333  3.0000  14.0000  1.9324  0.1376  0.8596  1.1748  5.0000
59   10.0667  7.8431  4.0000  32.2482  100.0000  6.8418  6.3404  2.0000
60   1.0433  13.7673  139.9837  2.1961  3.0696  2.7683  0.9745  0.0000
61   -4.3875  2.6192  1.0183  4.0000  2.8793  0.0000  0.0000  0.0000
62   S    1.9405  2.0000  32.0600  2.0677  0.2099  1.0336  1.5479  6.0000
63   9.9575  4.9055  4.0000  52.9998  112.1416  5.6210  8.2545  2.0000
64   1.4601  9.7177  71.1843  5.7487  23.2859  12.7147  0.9745  0.0000

```

65		-11.0000	2.7466	1.0338	6.2998	2.8793	0.0000	0.0000	0.0000	
66	F	1.2100	1.0000	18.9984	1.8601	0.1200	0.3000	-0.1000	7.0000	
67		11.5000	7.5000	4.0000	9.2533	0.2000	9.0000	15.0000	0.0000	
68		-1.0000	35.0000	33.1268	6.9821	4.1799	1.0561	0.0000	0.0000	
69		-7.3000	2.6656	1.0493	4.0000	2.9225	0.0000	0.0000	0.0000	
70	Si	2.0291	4.0000	28.0600	2.0043	0.1247	0.8218	1.5023	4.0000	
71		13.0000	2.0618	4.0000	11.8211	136.4845	1.8038	7.3852	0.0000	
72		-1.0000	0.0000	126.5182	3.6038	8.5961	0.2368	0.8563	0.0000	
73		-3.5163	4.2105	1.0338	6.2998	2.5791	0.0000	0.0000	0.0000	
74	X	-0.1000	2.0000	1.0080	2.0000	0.0000	1.0000	-0.1000	6.0000	
75		10.0000	2.5000	4.0000	0.0000	0.0000	8.5000	1.5000	0.0000	
76		-0.1000	0.0000	-2.3700	8.7410	13.3640	0.6690	0.9745	0.0000	
77		-11.0000	2.7466	1.0338	2.0000	2.8793	0.0000	0.0000	0.0000	
78	27	! Nr of bonds; Edis1;LPpen;n.u.;pbe1;pbo5;13corr;pbo6 pbe2;pbo3;pbo4;n.u.;pbo1;pbo2;ovcorr								
79										
80	1	1	143.3883	96.3926	76.4404	-0.7767	-0.4710	1.0000	34.9900	0.5108
81			0.4271	-0.1116	9.0638	1.0000	-0.0840	6.7452	1.0000	0.0000
82	1	2	181.9084	0.0000	0.0000	-0.4768	0.0000	1.0000	6.0000	0.7499
83			12.8085	1.0000	0.0000	1.0000	-0.0608	6.9928	0.0000	0.0000
84	2	2	168.2342	0.0000	0.0000	-0.2191	0.0000	1.0000	6.0000	1.0062
85			6.1152	1.0000	0.0000	1.0000	-0.0889	6.0000	0.0000	0.0000
86	1	3	158.6946	107.4583	23.3136	-0.4240	-0.1743	1.0000	10.8209	1.0000
87			0.5322	-0.3113	7.0000	1.0000	-0.1447	5.2450	0.0000	0.0000
88	3	3	60.1463	176.6202	51.1430	-0.2802	-0.1244	1.0000	29.6439	0.9114
89			0.2441	-0.1239	7.6487	1.0000	-0.1302	6.2919	1.0000	0.0000
90	1	4	134.1215	140.2179	79.9745	0.0163	-0.1428	1.0000	27.0617	0.2000
91			0.1387	-0.3681	7.1611	1.0000	-0.1000	5.0825	1.0000	0.0000
92	3	4	130.8596	169.4551	40.0000	0.3837	-0.1639	1.0000	35.0000	0.2000
93			1.0000	-0.3579	7.0004	1.0000	-0.1193	6.8773	1.0000	0.0000
94	4	4	157.9384	82.5526	152.5336	0.4010	-0.1034	1.0000	12.4261	0.5828
95			0.1578	-0.1509	11.9186	1.0000	-0.0861	5.4271	1.0000	0.0000
96	2	3	163.1043	0.0000	0.0000	-0.4155	0.0000	1.0000	6.0000	0.3607
97			1.9380	1.0000	0.0000	0.0000	-0.0778	4.3082	0.0000	0.0000
98	2	4	231.8173	0.0000	0.0000	-0.3364	0.0000	1.0000	6.0000	0.4402
99			8.8910	1.0000	0.0000	1.0000	-0.0327	6.5754	0.0000	0.0000
100	1	5	128.7959	56.4134	39.0716	0.0688	-0.4463	1.0000	31.1766	0.4530
101			0.1955	-0.3587	6.2148	1.0000	-0.0770	6.6386	1.0000	0.0000
102	2	5	136.1049	0.0000	0.0000	-0.4669	0.0000	1.0000	6.0000	0.3803
103			10.5730	1.0000	0.0000	1.0000	-0.1000	7.0000	1.0000	0.0000
104	3	5	165.3308	220.0000	40.0000	0.7131	-0.2406	1.0000	22.1005	0.2000
105			0.8027	-0.2748	8.3393	1.0000	-0.1043	5.6108	1.0000	0.0000
106	4	5	130.0000	180.0000	0.0000	0.5000	-0.2000	1.0000	40.0000	0.3000
107			0.4000	-0.2500	9.0000	1.0000	-0.1000	6.0000	1.0000	0.0000
108	5	5	96.1871	93.7006	68.6860	0.0955	-0.4781	1.0000	17.8574	0.6000
109			0.2723	-0.2373	9.7875	1.0000	-0.0950	6.4757	1.0000	0.0000
110	1	6	237.8781	0.0000	0.0000	-0.7438	-0.5000	1.0000	35.0000	1.0460
111			3.6661	-0.2500	15.0000	1.0000	-0.0800	5.4719	1.0000	0.0000
112	2	6	0.0000	0.0000	0.0000	-0.4643	0.0000	1.0000	6.0000	0.6151
113			12.3710	1.0000	0.0000	1.0000	-0.1008	8.5980	0.0000	0.0000
114	3	6	0.0000	0.0000	0.0000	0.2500	-0.5000	1.0000	45.0000	0.6000

115		0.4000	-0.2500	15.0000	1.0000	-0.1000	10.0000	1.0000	0.0000	
116	4	6	0.0000	0.0000	0.0000	-0.4643	0.0000	1.0000	6.0000	0.6151
117		12.3710	1.0000	0.0000	1.0000	-0.0098	8.5980	0.0000	0.0000	
118	5	6	0.0000	0.0000	0.0000	0.2500	-0.5000	1.0000	45.0000	0.6000
119		0.4000	-0.2500	15.0000	1.0000	-0.1000	10.0000	1.0000	0.0000	
120	6	6	250.0765	0.0000	0.0000	0.2298	-0.3500	1.0000	25.0000	0.8427
121		0.1167	-0.2500	15.0000	1.0000	-0.1506	7.3516	1.0000	0.0000	
122	1	7	90.6281	6.3660	0.0000	0.3176	-0.5558	1.0000	17.2117	0.5577
123		0.7223	-0.2118	7.7440	1.0000	-0.1039	5.4442	1.0000	0.0000	
124	2	7	137.1002	0.0000	0.0000	-0.1902	0.0000	1.0000	6.0000	0.4256
125		17.7186	1.0000	0.0000	1.0000	-0.0377	6.4281	0.0000	0.0000	
126	3	7	230.7615	93.6959	43.3991	-0.3617	-0.3000	1.0000	36.0000	0.3161
127		0.9856	-0.3882	4.6686	1.0000	-0.3960	4.5499	1.0000	0.0000	
128	4	7	119.7136	41.2405	43.3991	-0.2060	-0.3000	1.0000	36.0000	0.7957
129		0.8189	-0.2614	9.4060	1.0000	-0.1245	6.1856	1.0000	0.0000	
130	6	7	292.0773	0.0000	0.0000	0.0514	-0.3500	1.0000	25.0000	0.8000
131		0.0848	-0.2500	15.0000	1.0000	-0.1497	7.3978	1.0000	0.0000	
132	7	7	72.8867	50.0318	30.0000	0.9983	-0.3000	1.0000	16.0000	0.1000
133		1.0538	-0.0447	10.6176	1.0000	-0.1452	8.0404	0.0000	0.0000	
134	17		! Nr of off-diagonal terms; Ediss;Ro;gamma;rsigma;rpi;rpi2							
135	1	2	0.1188	1.4017	9.8545	1.1203	-1.0000	-1.0000		
136	2	3	0.0299	1.3153	10.9102	0.9093	-1.0000	-1.0000		
137	2	4	0.1059	1.8290	9.7818	0.9598	-1.0000	-1.0000		
138	1	3	0.1156	1.8520	9.8317	1.2854	1.1352	1.0706		
139	1	4	0.1447	1.8766	9.7990	1.3436	1.1885	1.1363		
140	3	4	0.1048	2.0003	10.1220	1.3173	1.1096	1.0206		
141	1	5	0.1408	1.8161	9.9393	1.7986	1.3021	1.4031		
142	2	5	0.0895	1.6239	10.0104	1.4640	-1.0000	-1.0000		
143	3	5	0.2250	1.7911	10.2423	1.4546	1.4011	-1.0000		
144	4	5	0.1505	1.9000	10.5104	1.8000	1.4000	-1.0000		
145	1	6	0.1071	1.6243	11.0402	1.3176	-1.0000	-1.0000		
146	2	6	0.0431	1.7204	10.3632	0.5386	-1.0000	-1.0000		
147	1	7	0.0250	1.7695	12.4753	1.5866	1.4409	-1.0000		
148	2	7	0.0291	1.6805	12.5137	1.3429	-1.0000	-1.0000		
149	3	7	0.1958	1.7958	11.1207	1.6105	1.1632	-1.0000		
150	4	7	0.1297	1.9384	10.9856	1.6175	1.4045	-1.0000		
151	6	7	0.2263	1.7693	12.0088	1.5090	-1.0000	-1.0000		
152	97		! Nr of angles;at1;at2;at3;Thetao,o;ka;kb;pv1;pv2							
153	1	1	1	72.7917	38.5829	0.7209	0.0000	0.1409	17.4509	1.0670
154	1	1	2	72.1533	14.2108	6.2512	0.0000	0.0100	0.0000	1.1022
155	2	1	2	73.2608	24.9703	3.7807	0.0000	0.1335	0.0000	3.0461
156	1	2	2	0.0000	0.0000	6.0000	0.0000	0.0000	0.0000	1.0400
157	1	2	1	0.0000	7.5000	5.0000	0.0000	0.0000	0.0000	1.0400
158	2	2	2	0.0000	27.9213	5.8635	0.0000	0.0000	0.0000	1.0400
159	1	1	3	49.6811	7.1713	4.3889	0.0000	0.7171	10.2661	1.0463
160	3	1	3	77.7473	40.1718	2.9802	-25.3063	1.6170	-46.1315	2.2503
161	1	1	4	66.1305	12.4661	7.0000	0.0000	3.0000	50.0000	1.1880
162	3	1	4	73.9544	12.4661	7.0000	0.0000	3.0000	0.0000	1.1880
163	4	1	4	64.1581	12.4661	7.0000	0.0000	3.0000	0.0000	1.1880
164	2	1	3	65.0000	13.8815	5.0583	0.0000	0.4985	0.0000	1.4900

165	2	1	4	74.2929	31.0883	2.6184	0.0000	0.0755	0.0000	1.0500
166	1	2	4	0.0000	0.0019	6.3000	0.0000	0.0000	0.0000	1.0400
167	1	3	1	73.5312	44.7275	0.7354	0.0000	3.0000	0.0000	1.0684
168	1	3	3	79.4761	36.3701	1.8943	0.0000	0.7351	67.6777	3.0000
169	1	3	4	82.4890	31.4554	0.9953	0.0000	1.6310	0.0000	1.0783
170	3	3	3	80.7324	30.4554	0.9953	0.0000	1.6310	50.0000	1.0783
171	3	3	4	84.3637	31.4554	0.9953	0.0000	1.6310	0.0000	1.0783
172	4	3	4	89.7071	31.4554	0.9953	0.0000	1.6310	0.0000	1.1519
173	1	3	2	70.1880	20.9562	0.3864	0.0000	0.0050	0.0000	1.6924
174	2	3	3	75.6935	25.0000	2.0000	0.0000	1.0000	0.0000	1.1680
175	2	3	4	75.6201	18.7919	0.9833	0.0000	0.1218	0.0000	1.0500
176	2	3	2	77.3619	4.8342	7.1628	0.0000	2.9933	0.0000	1.5948
177	1	4	1	66.0330	22.0295	1.4442	0.0000	1.6777	0.0000	1.0500
178	1	4	3	103.3204	33.0381	0.5787	0.0000	1.6777	0.0000	1.0500
179	1	4	4	104.1335	8.6043	1.6495	0.0000	1.6777	0.0000	1.0500
180	3	4	3	74.1978	42.1786	1.7845	-18.0069	1.6777	0.0000	1.0500
181	3	4	4	74.8600	43.7354	1.1572	-0.9193	1.6777	0.0000	1.0500
182	4	4	4	75.0538	14.8267	5.2794	0.0000	1.6777	0.0000	1.0500
183	1	4	2	69.1106	25.5067	1.1003	0.0000	0.0222	0.0000	1.0369
184	2	4	3	81.3686	40.0712	2.2396	0.0000	0.0222	0.0000	1.0369
185	2	4	4	83.0104	43.4766	1.5328	0.0000	0.0222	0.0000	1.0500
186	2	4	2	70.8687	12.0168	5.0132	0.0000	0.0222	0.0000	1.1243
187	1	2	3	0.0000	25.0000	3.0000	0.0000	1.0000	0.0000	1.0400
188	1	2	4	0.0000	0.0019	6.0000	0.0000	0.0000	0.0000	1.0400
189	1	2	5	0.0000	0.0019	6.0000	0.0000	0.0000	0.0000	1.0400
190	3	2	3	0.0000	4.4124	2.5758	0.0000	0.0000	0.0000	2.9884
191	3	2	4	0.0000	0.0019	6.0000	0.0000	0.0000	0.0000	1.0400
192	4	2	4	0.0000	0.0019	6.0000	0.0000	0.0000	0.0000	1.0400
193	2	2	3	0.0000	15.0000	2.2970	0.0000	0.0000	0.0000	1.3268
194	2	2	4	0.0000	0.0019	6.0000	0.0000	0.0000	0.0000	1.0400
195	1	1	5	74.4180	33.4273	1.7018	0.1463	0.5000	0.0000	1.6178
196	1	5	1	79.7037	28.2036	1.7073	0.1463	0.5000	0.0000	1.6453
197	2	1	5	63.3289	29.4225	2.1326	0.0000	0.5000	0.0000	3.0000
198	1	5	2	85.9449	38.3109	1.2492	0.0000	0.5000	0.0000	1.1000
199	1	5	5	85.6645	40.0000	2.9274	0.1463	0.5000	0.0000	1.3830
200	2	5	2	83.8555	5.1317	0.4377	0.0000	0.5000	0.0000	3.0000
201	2	5	5	97.0064	32.1121	2.0242	0.0000	0.5000	0.0000	2.8568
202	3	5	3	81.0957	22.5308	7.4511	-2.3089	2.8609	0.0000	2.0914
203	1	5	3	70.0000	35.0000	3.4223	0.0000	1.3550	0.0000	1.2002
204	1	3	5	58.9977	36.2016	1.7948	0.0000	0.4304	0.0000	3.0000
205	3	3	5	83.9753	31.0715	3.5590	0.0000	0.8161	0.0000	1.1776
206	2	3	5	90.0000	17.5000	3.5000	0.0000	1.9770	0.0000	3.0000
207	1	1	6	74.0446	35.8484	6.6125	0.0000	0.9453	0.0000	3.0000
208	6	1	6	77.8443	49.0744	5.9913	0.0000	0.7835	0.0000	2.3020
209	1	6	1	0.0000	19.9962	3.2299	0.0000	2.1012	0.0000	1.1537
210	1	6	6	0.0000	25.0000	1.0000	0.0000	1.0000	0.0000	1.0400
211	6	1	2	69.6421	10.0000	2.0000	0.0000	1.0000	0.0000	1.0400
212	3	1	6	70.0000	35.0000	2.0000	0.0000	1.0000	0.0000	1.2500
213	5	1	6	70.0000	35.0000	3.4223	0.0000	1.3550	0.0000	1.2002
214	7	7	7	71.6771	13.0081	3.6376	0.0000	0.2384	0.0000	1.3185

215	2	7	7	89.1207	11.7566	1.1579	0.0000	0.0100	0.0000	1.2975	
216	2	7	2	26.3763	5.5393	0.9656	0.0000	2.3381	0.0000	1.1704	
217	3	7	7	85.6335	17.1826	6.5759	0.0000	0.4105	0.0000	1.6398	
218	2	7	3	59.6558	6.8748	7.0452	0.0000	4.0000	0.0000	1.0400	
219	3	7	3	72.7359	17.5203	2.4434	0.0000	0.0100	0.0000	1.7374	
220	7	3	7	18.3653	5.7702	3.4915	0.0000	4.0000	0.0000	1.9438	
221	2	3	7	57.5894	40.0000	8.0000	0.0000	3.8263	0.0000	1.0534	
222	3	3	7	54.5893	38.8349	7.6245	0.0000	2.7656	0.0000	3.0000	
223	2	2	7	0.0000	47.1300	6.0000	0.0000	1.6371	0.0000	1.0400	
224	7	2	7	0.0000	31.5209	6.0000	0.0000	1.6371	0.0000	1.0400	
225	3	2	7	0.0000	31.0427	4.5625	0.0000	1.6371	0.0000	1.0400	
226	1	1	7	63.8858	35.1811	0.6236	0.0000	2.6344	0.0000	2.3890	
227	1	7	1	71.6429	31.1160	0.5107	0.0000	0.0100	0.0000	1.9113	
228	7	1	7	63.2523	33.3810	2.2952	0.0000	0.0201	0.0000	1.7191	
229	1	7	7	70.9876	29.7098	1.0210	0.0000	0.0100	0.0000	1.8242	
230	2	1	7	96.9319	10.9008	1.4627	0.0000	2.4557	0.0000	1.5109	
231	1	7	2	73.9320	16.6559	3.0433	0.0000	0.7961	0.0000	1.4005	
232	1	3	7	91.5678	5.9243	2.4284	0.0000	2.9840	0.0000	1.0400	
233	1	7	3	96.3796	36.5757	0.8505	0.0000	3.6964	0.0000	1.6527	
234	3	1	7	42.5553	40.0000	1.5855	0.0000	1.0802	0.0000	1.1584	
235	4	7	7	60.6199	17.7559	1.0576	0.0000	2.1459	0.0000	1.0400	
236	4	7	4	74.1294	20.6494	2.1244	0.0000	0.7689	0.0000	1.0400	
237	4	7	3	57.0650	9.4985	0.3423	0.0000	0.7689	0.0000	1.0400	
238	7	4	7	24.1137	1.7457	0.2198	0.0000	4.1125	0.0000	1.0400	
239	2	7	4	68.7410	15.5851	1.8545	0.0000	0.8613	0.0000	1.0400	
240	2	4	7	80.9040	4.0560	1.2284	0.0000	1.6982	0.0000	1.0400	
241	4	4	7	60.0000	10.0000	0.7500	0.0000	1.0000	0.0000	1.0400	
242	3	4	7	69.8728	32.7155	1.5875	0.0000	2.2466	0.0000	1.0400	
243	4	3	7	69.8728	27.1273	1.5875	0.0000	2.2466	0.0000	1.0400	
244	4	2	7	0.0000	31.0427	4.5625	0.0000	1.6371	0.0000	1.0400	
245	6	7	7	79.7014	16.9791	1.6839	0.0000	1.0944	0.0000	1.0500	
246	6	7	6	74.7778	38.2532	1.2522	0.0000	2.0453	0.0000	1.0500	
247	7	6	7	0.0000	42.3353	7.1082	0.0000	1.3635	0.0000	1.0840	
248	6	6	7	0.0000	10.0000	2.0000	0.0000	1.0000	0.0000	1.2500	
249	6	7	3	28.9834	39.9921	1.2589	0.0000	2.1212	0.0000	1.0000	
250	42	! Nr of torsions;at1;at2;at3;at4;;V1;V2;V3;V2(B0);vconj;n.u;n									
251	1	1	1	-0.5000	53.0886	-0.1335	-6.2875	-1.9524	0.0000	0.0000	
252	1	1	2	-0.4614	29.0459	0.2551	-4.8555	-2.7007	0.0000	0.0000	
253	2	1	1	2	-0.2833	31.2867	0.2965	-4.8828	-2.4652	0.0000	0.0000
254	1	1	1	3	-0.3495	22.2142	-0.2959	-2.5000	-1.9066	0.0000	0.0000
255	2	1	1	3	0.0646	24.3195	0.6259	-3.9603	-1.0000	0.0000	0.0000
256	3	1	1	3	-0.5456	5.5756	0.8433	-5.1924	-1.0180	0.0000	0.0000
257	1	1	3	1	1.7555	27.9267	0.0072	-2.6533	-1.0000	0.0000	0.0000
258	1	1	3	2	-1.4358	36.7830	-1.0000	-8.1821	-1.0000	0.0000	0.0000
259	2	1	3	1	-1.3959	34.5053	0.7200	-2.5714	-2.1641	0.0000	0.0000
260	2	1	3	2	-2.5000	70.0597	1.0000	-3.5539	-2.9929	0.0000	0.0000
261	1	1	3	3	0.6852	11.2819	-0.4784	-2.5000	-2.1085	0.0000	0.0000
262	2	1	3	3	0.1933	80.0000	1.0000	-4.0590	-3.0000	0.0000	0.0000
263	3	1	3	1	-1.9889	76.4820	-0.1796	-3.8301	-3.0000	0.0000	0.0000
264	3	1	3	2	0.2160	72.7707	-0.7087	-4.2100	-3.0000	0.0000	0.0000

265	3	1	3	3	-2.5000	71.0772	0.2542	-3.1631	-3.0000	0.0000	0.0000
266	1	3	3	1	2.5000	-0.6002	1.0000	-3.4297	-2.8858	0.0000	0.0000
267	1	3	3	2	-2.5000	-3.3822	0.7004	-5.4467	-2.9586	0.0000	0.0000
268	2	3	3	2	2.5000	-4.0000	0.9000	-2.5000	-1.0000	0.0000	0.0000
269	1	3	3	3	1.2329	-4.0000	1.0000	-2.5000	-1.7479	0.0000	0.0000
270	2	3	3	3	0.8302	-4.0000	-0.7763	-2.5000	-1.0000	0.0000	0.0000
271	3	3	3	3	-2.5000	-25.0000	1.0000	-2.5000	-1.0000	0.0000	0.0000
272	0	1	2	0	0.0000	0.0000	0.0000	0.0000	0.0000	0.0000	0.0000
273	0	2	2	0	0.0000	0.0000	0.0000	0.0000	0.0000	0.0000	0.0000
274	0	2	3	0	0.0000	0.1000	0.0200	-2.5415	0.0000	0.0000	0.0000
275	0	1	1	0	0.0000	50.0000	0.3000	-4.0000	-2.0000	0.0000	0.0000
276	0	3	3	0	0.5511	25.4150	1.1330	-5.1903	-1.0000	0.0000	0.0000
277	0	1	4	0	-2.4242	128.1636	0.3739	-6.6098	-2.0000	0.0000	0.0000
278	0	2	4	0	0.0000	0.1000	0.0200	-2.5415	0.0000	0.0000	0.0000
279	0	3	4	0	1.4816	55.6641	0.0004	-7.0465	-2.7203	0.0000	0.0000
280	0	4	4	0	-0.3244	27.7086	0.0039	-2.8272	-2.0000	0.0000	0.0000
281	4	1	4	4	-5.5181	8.9706	0.0004	-6.1782	-2.0000	0.0000	0.0000
282	0	1	5	0	3.3423	30.3435	0.0365	-2.7171	0.0000	0.0000	0.0000
283	0	5	5	0	-0.0555	-5.0000	0.1515	-2.2056	0.0000	0.0000	0.0000
284	0	2	5	0	0.0000	0.0000	0.0000	0.0000	0.0000	0.0000	0.0000
285	1	1	1	6	0.5000	0.1000	0.4683	-11.5274	-1.7255	0.0000	0.0000
286	2	1	1	6	0.0000	49.3871	0.2000	-10.5765	-1.7255	0.0000	0.0000
287	6	1	1	6	-0.5000	95.4727	-0.2080	-4.8579	-1.7255	0.0000	0.0000
288	0	1	6	0	4.0000	45.8264	0.9000	-4.0000	0.0000	0.0000	0.0000
289	0	6	6	0	4.0000	45.8264	0.9000	-4.0000	0.0000	0.0000	0.0000
290	2	3	5	3	2.5000	2.5000	0.2237	-10.0000	-1.0000	0.0000	0.0000
291	0	3	5	0	-2.5000	50.0000	-0.5000	-10.0000	-1.0000	0.0000	0.0000
292	0	4	7	0	0.0000	0.0000	0.0000	-2.4426	0.0000	0.0000	0.0000
293	9	! Nr of hydrogen bonds;at1;at2;at3;Rhb;Dehb;vhb1									
294	3	2	3	2.1845	-2.3549	3.0582	19.1627				
295	3	2	4	1.6658	-3.8907	3.0582	19.1627				
296	4	2	3	1.8738	-3.5421	3.0582	19.1627				
297	4	2	4	1.8075	-4.1846	3.0582	19.1627				
298	3	2	5	1.5000	-2.0000	3.0582	19.1627				
299	4	2	5	1.5000	-2.0000	3.0582	19.1627				
300	5	2	3	1.5000	-2.0000	3.0582	19.1627				
301	5	2	4	1.5000	-2.0000	3.0582	19.1627				
302	5	2	5	1.5000	-2.0000	3.0582	19.1627				

Listing A.2: Combined ReaxFF parameters set for a Si/O/C/F system

APPENDIX

B

LAMMPS INPUT FILES AND PYTHON SCRIPTS

The input files and Python scripts are publicly available on Github at <https://github.com/shannon-lab/input.examples.LAMMPS>.